Indian Ocean Dipole Asymmetry, Pattern and Climatic Impacts across Observations, Historical Simulations and Future Projections

ZHENG, Yiling

A Thesis Submitted in Partial Fulfillment

of the Requirements for the Degree of

Doctor of Philosophy

in

Earth and Atmospheric Sciences

The Chinese University of Hong Kong

July 2024

Thesis Assessment Committee

Professor LIU Lin (Chair)

Professor TAM Chi Yung Francis (Thesis Supervisor)

Professor ZHAI Shixian (Committee Member)

Professor XU Kang (External Examiner)

Abstract of thesis entitled:

Indian Ocean Dipole Asymmetry, Pattern and Climatic Impacts across Observations, Historical Simulations and Future Projections
Submitted by ZHENG, Yiling
for the degree of Doctor of Philosophy
at The Chinese University of Hong Kong in July 2024

The Indian Ocean Dipole (IOD) stands as a prominent year-to-year climate phenomenon within the tropical Indian Ocean (TIO), arising from the complex interaction between the ocean and the atmosphere. IOD influences the atmospheric circulation and weather dynamics across many countries bordering the Indian Ocean and beyond, with far-reaching environmental and societal consequences. IOD oscillates irregularly between the positive (pIOD) and negative (nIOD) phases, characterized by warming (cooling) of western (eastern) TIO and a reversed ocean temperature change pattern, respectively. Also, pIOD generally has a larger amplitude compared to nIOD. This study evaluates the IOD asymmetry, pattern and climatic impacts based on observations, historical simulations and future projections from the Coupled Model Intercomparison Project (CMIP) Phase 5/6 models.

Observed IOD events are associated with notable negative sea surface temperature anomaly (SSTA) skewness in the eastern TIO (ETIO), which is due to negative nonlinear dynamic heating. When examining CMIP models, almost all CMIP5 models tend to simulate less asymmetric IOD compared to observations. As for the 20 selected CMIP6 models, six are able to reproduce realistic IOD asymmetry. Further analysis shows that weaker IOD asymmetry is related to biases in the ocean mean state, which can be traced back to models' weaker Indian summer monsoon. These mean-state biases result in a reduced convective response to warm SSTA in western TIO, thus weaker zonal wind anomalies and reduced negative nonlinear zonal advection during pIOD. Besides, ETIO stratification also influences the IOD skewness: stronger stratification leads to larger mixed-layer temperature response to thermocline changes, contributing to larger anomalous vertical temperature gradient, larger nonlinear vertical advection, and thus stronger IOD asymmetry. These findings emphasize the critical importance of

addressing the Indian summer monsoon and ETIO stratification biases in Earth System Models to properly represent IOD characteristics.

Future projections under the Shared Socio-economic Pathway 5 (SSP5-8.5) scenario indicate a notable reduction in IOD asymmetry and northward shift of its pattern, with ~10% decrease in SSTA amplitude near the Sumatra coast and 10% increase along the equatorial ETIO. Reduced IOD asymmetry points to an increased frequency of extreme nIOD events and a decreased frequency of extreme pIOD events under global warming. The primary cause is weaker negative nonlinear dynamical heating in future simulations, especially the nonlinear zonal advection. Under global warming, increased atmospheric static stability weakens the large-scale atmospheric response to SSTA forcing, leading to reduced strength of nonlinear zonal advection, thus resulting in weaker pIOD and decreased IOD asymmetry. Moreover, the drier mean state over ETIO leads to decreased thermodynamic air-sea feedback efficiency, further weakening pIOD. This weaker pIOD primarily contributes to the SSTA amplitude decrease near the Sumatra coast. Despite projections indicating weakening pIOD, larger SSTA amplitude along the equatorial ETIO is projected, driven by the increased zonal advection of the anomalous temperature gradient by the mean current; this can be traced back to the IOD-like warming pattern. Regarding nIOD, increased variance is expected across ETIO, except near South Sumatra and Java. This is due to enhanced zonal advection and Ekman pumping in relation to more stratified upper ocean; along with reduced inhibition of nonlinear zonal advection, nIOD development is favoured, leading to an increased frequency of extreme nIOD events. Emergent constraint-corrected results predict even stronger reduction in IOD asymmetry, suggesting a higher frequency of extreme nIOD events and their impacts.

These changes underscore the potential risks associated with nIOD events in a warming world. Eastern Africa experiences significant impacts from the IOD, particularly on its short-rain precipitation characteristics, with increased (suppressed) rainfall during pIOD (nIOD). Most CMIP6 models overestimate the precipitation responses to IOD, especially during nIOD. This is found to be due to positive bias in moisture transport, related to the larger simulated IOD amplitude and the overestimated mean-state short-rain precipitation. Under global warming, the IOD climatic impacts on the Horn of Africa are projected to intensify while Southeastern Africa's IOD precipitation variability is expected to be reduced. These changes can be attributed to IOD-related wind circulation changes and the mean-state moisture changes. Due to the

increased extreme nIOD events, the frequency as well as severity of droughts in the Horn of Africa are projected to increase. Finally, IOD significantly impacts Australia's climate via stationary Rossby waves during the winter crop season: the anomalous upper-air anticyclone (cyclone) south of Australia can lead to warming (cooling) in Southwestern Australia and drier (wetter) than normal conditions in Southeastern Australia during pIOD (nIOD). However, CMIP6 models can only partially replicate these anomalies due to weaker simulations of IOD-induced Rossby wave trains. Under the SSP5-8.5 scenario, climatic responses to IOD events are projected to intensify, particularly in Southeastern Australia, potentially due to the amplified eddy-driven jet. These projections underscore the imperative to improve the simulations of IOD teleconnections to Australia.

摘要

鄭依玲

香港中文大學

印度洋偶極子（IOD）是發生在熱帶印度洋的年際海氣相互作用現象，顯著影響印度洋周邊國家乃至全球的天氣氣候過程，對經濟社會產生不可忽視的影響。IOD 包括正事件和負事件。在正事件期間，熱帶東印度洋海域（ETIO）出現顯著的冷海溫異常，而熱帶西印度洋海域（WTIO）則是暖海溫異常。負事件與正事件相反且正事件的振幅通常大於負事件。本研究主要討論 IOD 的非對稱性、模態分佈和氣候影響在 CMIP5/6 模式中的模擬情況，及其在 SSP5-8.5 情景模擬中的變化。

觀測結果表明 ETIO 的海表溫度異常在 IOD 期間呈現明顯的負偏度。該負偏度主要與該海域的負非線性海洋平流有關。幾乎所有的CMIP5 模式都低估了 IOD 非對稱性。而在 CMIP6 中，有 6 個模式可以模擬出較爲準確的 IOD 非對稱性。研究表明，低估的 IOD 非對稱性主要與海洋平均態的模擬偏差有關。該模擬偏差可追溯到印度洋夏季風的模擬。這些平均態偏差使得 WTIO 對暖海溫異常的響應變弱，進一步造成正事件期間更弱的緯向風異常和非線性緯向平流，不利於 IOD 非對稱性的發展。此外，ETIO 的上層海洋層化模擬也會影響 IOD 非對稱性模擬。上層海洋層化增強可通過增加混合層溫度對溫躍層變化的響應，加強非線性垂向平流，更有利於 IOD 非對稱性的發展。該結果闡釋了提高印度洋夏季風模擬和上層海洋層化模擬的重要性。

在 SSP5-8.5 情景模擬中，IOD 非對稱性顯著降低，IOD 模態會略微向北移動。IOD 模態北移主要表現爲海表溫度振幅在蘇門答臘附近海域減少 10%，而在赤道 ETIO 海域增加 10%。IOD 非對稱性降低意味着全球變暖可能導致更多的極端負事件和更少的極端正事件。IOD 非對稱性減少主要與未來更弱的非線性平流有關，特別是非線性緯向平流。全球變暖導致大氣穩定度增加，大尺度環流對海表溫度異常的響應變弱，造成更弱的非線性緯向平流，使得正事件減弱和 IOD 非對稱性降低。此外，ETIO 海域的平均態降水在全球變暖背景下將減少，使得熱力學海氣反饋機制的有效性降低，進一步減弱正事件。蘇門答臘附近海域海表溫

度振幅減少主要由正事件減弱有關。儘管正事件整體振幅減弱，但是赤道 ETIO 海域海表溫度振幅將在正事件期間有所增強，主要與類 IOD 增暖模態導致的線性緯向平流（緯向溫度異常乘以平均態海流）增強有關。相反地，除了南蘇門答臘和爪哇附近海域，ETIO 的海表溫度異常在負事件期間將有所增強。更弱的非線性平流，更強的線性緯向平流和埃克曼抽吸反饋均有利於負事件的發展，由此將引發更多的極端負事件。觀測約束的校正結果顯示 IOD 非對稱性應進一步降低，未來可能出現比模擬結果更多的極端負事件。

這些變化凸顯了全球變暖導致的與負事件相關的潛在風險。IOD 顯著影響東非雨季，正事件期間東非降雨增加，負事件則減少。然而，CMIP6 模式高估了 IOD 對東非降水的影響，特別是在負事件期間。這主要與 IOD 振幅模擬和東非氣候態降雨模擬偏大所導致的水汽輸送異常增強有關。全球變暖背景下，IOD 對索馬里半島的氣候影響將有所增強，但對非洲東南部的降水影響則有所減弱。這主要受 IOD 環流變化和平均態水汽增加影響。此外，由於極端負事件增加，索馬里半島的乾旱程度和頻率均有所增加。此外，IOD 通過準靜止羅斯貝波影響澳大利亞的氣候，特別是在冬季作物季節。在正（負）事件期間，羅斯貝波所引起的異常反氣旋（氣旋）使得西南澳大利亞的氣溫增加（減少）和東南澳大利亞的降水量減少（增加）。然而，CMIP6 模式僅能部分模擬出由 IOD 引起的澳大利亞氣候異常。在 SSP5-8.5 情景下，IOD 對澳大利亞的氣候影響將進一步增強，特別是東南澳大利亞地區，這可能與極地急流增強有關。該研究強調了提升 IOD 與澳大利亞大氣遙相關模擬的重要性。

Acknowledgment

I extend my sincere gratitude to my supervisor, Chi-Yung Francis Tam, whose kindness, rigor, and virtue have significantly enriched my academic journey. His provision of resources, patience, and space for growth, as well as his support for my international exchanges and conferences, have been invaluable. My appreciation also extends to Prof. Mat Collins for his unwavering support and Prof. Kang Xu for his insightful suggestions. Their dedication to teaching and preaching has played a pivotal role in my academic development. Reflecting on my journey, I acknowledge the challenges and stubbornness I encountered. However, my educators taught me to embrace uncertainty, remain vigilant against ignorance, and perceive the multifaceted nature of things. I wish them abundant enthusiasm, health, and well-being. My gratitude also goes to the professors who dedicated their time and expertise to reviewing this thesis.

I express my heartfelt gratitude to my group colleagues and those within our division who have provided guidance and assistance over the past three years. I am indebted to my family for their unconditional love and support. I am inspired by Yujia's unwavering commitment to societal improvement and Wenshan's zest for life and introduction to the world of reptiles. I appreciate my roommates, Xin in Hong Kong and Mengyan in Exeter, for their shared experiences. I acknowledge the women who have been part of my journey, awakening me to new perspectives. Indeed, a hearty thank you to the hurdles I've encountered, for gifting me an unparalleled tour of the wonderfully bizarre and often breathless theme park that is humanity. Lastly, I am grateful to myself for facing challenges, rebuilding my identity, and preserving goodness throughout my journey.

Table of Contents

1. Introduction 1
   1.1. Mean state in the Indian Ocean 1
   1.2. Physics of IOD 4
      1.2.1. Triggering mechanisms 4
      1.2.2. IOD life cycle 7
      1.2.3. Asymmetry mechanisms 8
   1.3. Present-day simulations of IOD in CMIP models 10
   1.4. IOD Projections in CMIP models 11
   1.5. Climatic impacts of IOD 13
      1.5.1. Eastern Africa 14
      1.5.2. Australia 16
   1.6. Objectives and framework 17
2. Data and methods 20
   2.1. Observation/Reanalysis datasets 20
   2.2. CMIP datasets 21
   2.3. Methods 22
   2.4. Model selection 28
      2.4.1. IOD identification in observations 28
      2.4.2. IOD identification in CMIP models 31
3. IOD asymmetry in observations 38
   3.1. Performances of IOD asymmetry 38
   3.2. Nonlinear dynamical heating 40
   3.3. Barrier Layer Thickness 45
   3.4. Thermodynamic process 47
   3.5. Summary 48
4. Historical simulations of IOD in CMIP5/6 models 50
   4.1. IOD asymmetry 50
      4.1.1. Simulated IOD asymmetry 50
      4.1.2. Simulated dynamics of IOD asymmetry 53
   4.2. Model biases in nonlinear zonal advection 56

4.3. Model biases in nonlinear vertical advection 62
4.4. Nonlinear meridional advection 66
5. Projections of IOD asymmetry by CMIP6 models 68
5.1. Reduction of IOD asymmetry due to global warming 68
5.2. Oceanic contribution to reduced IOD asymmetry 70
5.3. Increased extreme nIOD events 79
5.4. Constrained IOD asymmetry changes 86
6. Projections of IOD pattern by CMIP6 models 89
6.1. Alterations in IOD pattern due to global warming 89
6.2. Reduced SSTA amplitude near the Sumatra coast 91
6.3. Increased SSTA amplitude along the equatorial ETIO 96
7. IOD impacts on Eastern Africa and Australia 105
7.1. Observed IOD climatic impacts 105
7.2. Historical rainfall responses in Eastern Africa 106
7.2.1. Model selection 106
7.2.2. Overestimated rainfall responses in Eastern Africa 107
7.2.3. Contributions from simulated IOD biases 109
7.2.4. Contributions from mean state biases 111
7.3. Projected rainfall responses in Eastern Africa 113
7.3.1. Enhancement in Somali Peninsula and reduction in Southeastern Africa 113
7.3.2. Contributions from IOD circulation changes 116
7.3.3. Contributions from mean-state changes 118
7.3.4. Future rainfall response to extreme nIOD 120
7.4. IOD impacts on Australia 122
7.4.1. Underestimated IOD impacts on Australia 122
7.4.2. Weaker simulated Rossby waves 124
7.4.3. Projected changes in IOD impacts on Australia 127
8. Conclusions and discussions 129
8.1. Major conclusions 129
8.1.1. Underestimated IOD asymmetry in historical simulations 129
8.1.2. Reduced IOD asymmetry due to global warming 130
8.1.3. Projected northward shift of IOD pattern 131
8.1.4. Overestimated Eastern Africa rainfall responses to IOD 133

8.1.5. Enhanced IOD impacts on the Horn of Africa under global warming 133
8.1.6. Historical and projected climatic impacts of IOD on Australia 135
8.2. Study limitations 136
8.3. Future directions 140
Bibliography 145
Appendix 171

List of Figures

Figure 1.1. Mean-state SST (shading; unit: ℃), precipitation (contours in intervals of 3 mm day^{-1}) and 850 hPa wind (vector; unit: m s^{-1}) during March to May (MAM), June to August (JJA), September to November (SON), and December to February (DJF). 2

Figure 1.2. Mean-state thermocline (Z20; shading; unit: m), wind stress curl (contour; interval: 2×10^{-8} N m^{-3}) and 850 hPa wind stress (see scale vector in lower right; unit: N m^{-2}) during MAM, JJA, SON, and DJF. 3

Figure 1.3. Mean-state MLD (shading; unit: m) and surface current (see scale vector in lower right; unit: m s^{-1}) during MAM, JJA, SON, and DJF. 4

Figure 1.4. (a) Neutral phase, (b) negative phase and (c) positive phase of IOD. Source: https://snowbrains.com/noaa-march-enso-update-meet-ensos-neighbor-the-indian-ocean-dipole/. 5

Figure 2.1. Standardized IOD indices. (a) DMI (black line; dataset: ERSST), zonal wind index (green line; dataset: NCEP/NCAR), and SLA index (yellow line; dataset: GODAS). (b) DMI (black line, dataset: ERSST), PC2 of SST (green line, dataset: ERSST), and PC1 of SLA (yellow line, dataset: GODAS). Red (blue) shading is that the DMI is larger (smaller) than 1 (–1) STD. 29

Figure 2.2. EOF1 to EOF3 patterns of (a, b, c) SSTA (ERSST, 1950–2020) and (d, e, f) SLA (dataset: GODAS, 1980–2020). The dashed box is 5°S–5°N, 60°–90°E. The solid box in the western (eastern) Indian Ocean is 10°S–10°N, 50°–70°E (10°S–0°, 90°–110°E). 29

Figure 2.3. (a, b, c) S-EOF1 to 3 patterns of SSTA during JJASON and (d, e, f) their estimates of power spectra (dataset: GODAS, 1980–2020). The dotted red line in the estimate of power spectra is the 95% significant test and the dotted pink line is the red noise. 31

Figure 2.4. SST STD (unit: ℃) in observation (dataset: GODAS, 1980–2020) and 31 CMIP6 models using historical experiments. The solid box in the western (eastern) Indian Ocean is 10°S–10°N, 50°–70°E (10S°–0°, 90°–110°E). 32

Figure 2.5. The same as Fig. 2.4, but for STD of SLA (unit: m). 32

Figure 2.6. (a, b, c) EOF1 and (d, e, f) EOF2 of SST (unit: ℃) in (a, d) MRI-ESM2-0, (b, e) FGOALS-g3 and (c, f) EC-Earth3 models using historical experiments. 32

Figure 2.7. EOF1 of SLA (unit: m) in (a) BCC-CSM2-MR, (b) EC-Earth3, (c) EC-Earth-CC, (d) CAMS-CSM1-0, (e) FGOALS-f3-L and (f) INM-CM5-0 models using historical experiment. (g, h, i, j, k, l) EOF1 of SLA during JJASON. 33

Figure 2.8. S-EOF1 of SST (unit: ℃) during JJASON based on (a) ACCESS-ESM1-5, (b) FIO-ESM-2-0 and (c) INM-CM5-0 models. 34

Figure 2.9. Spatial correlation of S-EOF1 pattern between observations (dataset: GODAS) and each (a) CMIP6 or (b) CMIP5 model. Orange (blue) bars denote models with IOD well (poorly) simulated. 35

Figure 2.10. Composite pIOD during August to October of SST (shading; unit: ℃), precipitation (contours in intervals of 1 mm day^{-1}) and 850 hPa wind (vector; unit: m s^{-1}) anomalies in observations and CMIP6 historical runs. IOD is identified by the PC1 of S-EOF. 35

Figure 2.11. The same as Fig. 2.10, but for nIOD. 35

Figure 2.12. The same as Fig. 2.9, but using DMI. 36

Figure 2.13. The same as Fig. 2.12, but for nIOD. 36

Figure 2.14. Skewness of PC1 for representing IOD skewness (orange and yellow bars) and SSTA STD over ETIO (85°E–100°E, 8°S–2°N) during JJASON (blue and green bars) in (a) CMIP6 and (b) CMIP5 models. Orange and blue (yellow and green) bars denote selected (non-selected) models. Models with PC1 skewness larger than the observed are marked by grey circles above the skewness bars. Orange (blue) line denotes the observed skewness (STD) value (dataset: GODAS). 37

Figure 3.1. (a) Seasonal skewness of DMI and SSTA (multiplied by –1) averaged over the ETIO (8°S–2°N, 85°–100°E). (b) Phase development of DMI during the IOD cases from 1980 to 2020. SST data is from GODAS (1980–2020). 38

Figure 3.2. Lead-lag correlation between (a) DMI (unit: ℃) and zonal wind index (unit: m s^{-1}), (b) zonal wind index and SLA index (unit: m), (c) SLA index and DMI. (d) Monthly DMI vs zonal wind index. (e) Monthly zonal wind index vs SLA index. (f) Monthly SLA index vs DMI. Grey + is the monthly anomaly. Red (Blue) dot is the anomaly during JASO in pIOD (nIOD). Purple (Green) line is the

least squares linear fit of pIOD (nIOD). The r and slope values are the correlation coefficient and the slope between the two indices, respectively.....39

Figure 3.3. Composite (a) zonal wind stress (blue curve; unit: N m^{-2}), (b) zonal temperature (shading; unit: ℃) and current (see scale vector in lower right; unit: u in m s^{-1}, w in 10^{-4} m s^{-1}) anomalies along the equator (2°S–2°N), (c) meridional wind stress, (d) meridional temperature and current (v in m s^{-1}, w in 10^{-4} m s^{-1}) anomalies averaged in the ETIO (85°E–100°E) during JASO in pIOD. (e, f, g, h) is the same as (a, b, c, d) but for nIOD. The black circle means passing the 95% significant test. The yellow (green) line is MLD (20 °C isotherm) (dotted: mean state, solid: IOD). White stippling indicates the 95% significance level based on Student's t-test. 40

Figure 3.4. Seasonal changes of (a) MLT tendency (unit: ℃ $month^{-1}$), (b) NDH, (c) LDH, (d) net heat flux, (e) subsurface entrainment, (f) residual term, (g) nonlinear zonal advection, (h) nonlinear vertical advection and (i) nonlinear meridional advection in super pIODs (1994, 1997, 2019), normal pIOD, and normal nIOD averaged over the ETIO (8°S–2°N, 85°–100°E). 42

Figure 3.5. Time series of NDH (red line; unit: ℃ $month^{-1}$), nonlinear zonal advection (blue line), nonlinear meridional advection (yellow line), nonlinear vertical advection (green line), and DMI (grey shading; unit: ℃) from 1980 to 2020. 42

Figure 3.6. (a) SSTA (unit: ℃) vs surface zonal wind anomaly (unit: m s^{-1}) averaged over the ETIO (8°S–2°N, 85°–100°E). (b) Surface zonal wind anomaly vs zonal mixed-layer current anomaly (unit: m s^{-1}). (c) Surface zonal wind anomaly vs zonal MLT gradient anomaly (unit: ℃ m^{-1}). (d) Zonal current anomaly vs nonlinear zonal advection (unit: ℃ $month^{-1}$) within MLD. (e) Zonal MLT gradient anomaly vs nonlinear zonal advection within MLD. (f) Nonlinear zonal advection vs SSTA.....43

Figure 3.7. (a) Surface zonal wind anomaly (unit: m s^{-1}) vs vertical velocity anomaly (unit: m s^{-1}) at the base of mixed layer averaged over the ETIO (8°S–2°N, 85°–100°E). (b) Surface zonal wind anomaly vs vertical temperature gradient anomaly (unit: ℃ m^{-1}) at the base of mixed layer. (c, d) are the same as (a, b), but for surface meridional wind anomaly (unit: m s^{-1}). (e) Vertical velocity anomaly vs nonlinear vertical advection (unit: ℃ $month^{-1}$). (f) Vertical temperature gradient

anomaly vs nonlinear vertical advection. (g) Nonlinear vertical advection vs SSTA (unit: ℃).....44

Figure 3.8. (a) SSTA (unit: ℃) vs surface meridional wind anomaly (unit: m s^{-1}) averaged over the ETIO (8°S–2°N, 85°–100°E). (b) Surface meridional wind anomaly vs meridional mixed-layer current anomaly (unit: m s^{-1}). (c) Surface meridional wind anomaly vs meridional MLT gradient anomaly (unit: ℃ m^{-1}). (d) Meridional current anomaly vs nonlinear meridional advection (unit: ℃ $month^{-1}$) within MLD. (e) Meridional MLT gradient anomaly vs nonlinear meridional advection within MLD. (f) Nonlinear meridional advection vs SSTA.....45

Figure 3.9. The definition of BLT. Source: https://cerweb.ifremer.fr/deboyer/mld/Subsurface_Barrier_Layer_Thickness.php. 46

Figure 3.10. (a, b, c) Mean state, (d, e, f) composite pIOD and (g, h, i) composite nIOD of (a, d, g) BLT (unit: m), (b, e, h) ILD and (c, f, i) MLD anomalies. 47

Figure 3.11. (a) BLT anomaly (unit: m) vs SSTA (unit: ℃) averaged over the ETIO (85°E–100°E, 8°S–2°N). (b) ILD anomaly vs SSTA. (c) MLD anomaly vs SSTA. 47

Figure 3.12. (a) Precipitation anomaly (unit: mm day^{-1}) vs shortwave radiation anomaly (unit: W m^{-2}) during JASO averaged over the ETIO (8°S–2°N, 85°–100°E). (b) Shortwave radiation anomaly vs SSTA (unit: ℃). (c) and (d) are shortwave radiation anomalies per SSTA (unit: W m^{-2} $℃^{-1}$) in pIOD and nIOD, respectively. (e) Surface wind speed anomaly (unit: m s^{-1}) vs latent heat flux anomaly (unit: W m^{-2}). (f) Latent heat flux anomaly vs SSTA.....48

Figure 4.1. Skewness of PC1 for representing IOD skewness (orange bars) and SSTA STD over ETIO (8°S–2°N, 85°–100°E) during JJASON (blue bars) in (a) CMIP6 and (b) CMIP5 models. Orange (blue) line denotes the observed skewness (STD) value. Models with PC1 skewness larger than the observed are marked by grey circles above the skewness bars.....50

Figure 4.2. JJASON skewness (shading) and STD (contour) of (a, d, g, f) SSTA, anomalous ocean temperature averaged over (b. e. h. k) 5°S to 5°N and (c, f, i, l) 15°S to 5°S, based on (a, b, c) observations, (d, e, f) less-skewed CMIP6 model group, (g, h, i) more-skewed CMIP6 model group and (j, k, l) CMIP5 models. The observed and model-simulated 24, 22 and 20 ℃ isotherms (dash-dot contours) are

also shown in the ocean vertical cross sections. White stippling indicates the 95% significance level based on Student's t-test. 52

Figure 4.3. Composite (a, b, c, d) positive and (e, f, g, h) negative IOD for SST (shading; unit: ℃), precipitation (contour, in intervals of 1 mm day^{-1}) and 850 hPa wind anomalies (see scale vector in lower right; unit: m s^{-1}) during JASO, based on (a, e) observations, (b, f) less-skewed CMIP6 model group, (c, g) more-skewed CMIP6 model group and (d, h) CMIP5 models. Anomalies of SST (white stippling), precipitation and wind are shown when exceeding the 95% significance level based on Student's t-test. 53

Figure 4.4. Composite mixed-layer heat budget during positive and negative IODs during JASO within the ETIO (8°S–2°N, 85°–100°E) in (a) observations, (b) less-skewed CMIP6 model group, (c) CMIP5 models and (d) more-skewed CMIP6 model group. Error bar is based on one STD. Circle over the bar indicates signals passing the 95% significance level. 54

Figure 4.5. Long-term mean (a, b, c, d) NDH (unit: ℃ $month^{-1}$), (e, f, g, h) nonlinear zonal advection, (i, j, k, l) nonlinear vertical advection and (m, n, o, p) nonlinear meridional advection within the mixed layer during JASO based on (a, e, i, m) observations, (b, f, j, n) less-skewed CMIP6 model group, (c, g, k, o) more-skewed CMIP6 model group and (d, h, l, p) CMIP5 models. White stippling indicates the 95% significance level based on Student's t-test. 56

Figure 4.6. Positive IOD composites during JASO for (a, b, c, d) nonlinear zonal advection (unit: ℃ $month^{-1}$), (e, f, g, h) zonal mixed-layer current anomalies (unit: cm s^{-1}), (i, j, k, l) zonal temperature gradient anomalies within the mixed layer (unit: 10^{-6} ℃ m^{-1}) and (m, n, o, p) surface wind anomalies (see scale vector in lower right; unit: m s^{-1}; shading is surface zonal wind anomaly), based on (a, e, i, m) observations, (b, f, j, n) less-skewed CMIP6 model group, (c, g, k, o) more-skewed CMIP6 model group and (d, h, l, p) CMIP5 models. White stippling indicates the 95% significance level based on Student's t-test. Wind vectors in m, n, o, and p are shown when exceeding the 95% significance level based on Student's t-test. 57

Figure 4.7. Same as Fig. 4.6, but for negative IOD. 57

Figure 4.8. (a, b, c, d) Average precipitation (unit: mm day^{-1}) with respect to SST (unit: ℃) and (e, f, g, h) precipitation responses to SST changes (unit: mm day^{-1}

0.5°C^{-1}), based on (a, e) observations, (b, f) less-skewed CMIP6 model group, (c, g) more-skewed CMIP6 model group and (d, h) CMIP5 models. Red (blue) line gives precipitation change due to a 0.5°C increase (decrease) in SST and black bar is net precipitation response. (i) Mean-state SST (shading; unit: °C), precipitation (contour, in intervals of 3 mm day^{-1}) and 850 hPa wind (see scale vector in lower right; unit: m s^{-1}) and (m) net precipitation response (unit: mm day^{-1} 0.5°C^{-1}) during JASO in observations. (j, k, l) Mean state biases of SST, precipitation and 850 hPa wind and (n, o, p) net precipitation response, based on (j, n) less-skewed CMIP6 model group, (k, o) more-skewed CMIP6 model group and (l, p) CMIP5 models. White stippling indicates the 95% significance level based on Student's t-test. (q) Schematic diagram illustrating how mean-state positive IOD-like biases affect atmospheric response to SSTA. In observation, WTIO (ETIO) captures larger precipitation response to positive (negative) SSTA than to negative (positive) SSTA, favoring the pIOD with stronger atmospheric response. In models with mean-state positive IOD-like biases, warmer WTIO results in less (more) precipitation response to positive (negative) SSTA and colder ETIO causes less negative net precipitation response, leading to weaker atmospheric response during pIOD, less favor of pIOD and less IOD asymmetry. 58

Figure 4.9. Mean state in observations and CMIP6 models. (a) SST gradient (unit: °C; 45°–60°E minus 80°–100°E, 5°S–5°N; JASO) vs IOD skewness. (b) Surface zonal wind (unit: m s^{-1}; 5°S–5°N, 60°–90°E; JASO) vs IOD skewness. (c) Net convective response gradient (unit: mm day^{-1} 0.5°C^{-1}; 45°–60°E minus 80°–100°E, 5°S–5°N; JASO) vs IOD skewness. (d) Surface meridional wind (unit: m s^{-1}; 5°S–5°N, 45°–60°E; JJA) vs SST gradient (unit: °C; 45°–60°E minus 80°–100°E, 5°S–5°N; JJA). (e) SST gradient (unit: °C; 45°–60°E minus 80°–100°E, 5°S–5°N; JJA) vs surface zonal wind (unit: m s^{-1}; 5°S–5°N, 60°–90°E; SON). (f) Surface meridional wind (unit: m s^{-1}; 5°S–5°N, 45°–60°E; JJA) vs surface zonal wind (unit: m s^{-1}; 5°S–5°N, 60°–90°E; SON). (g) Surface meridional wind (unit: m s^{-1}; 10°S–0°, 90°–100°E; JJA) vs SST gradient (unit: °C; 45°–60°E minus 80°–100°E, 5°S–5°N; JJA). (h) Surface meridional wind (unit: m s^{-1}; 10°S–0°, 90°–100°E; JJA) vs surface zonal wind (unit: m s^{-1}; 5°S–5°N, 60°–90°E; SON). Blue line is the least square linear fit. The r value is the correlation coefficient. 61

Figure 4.10. (a, b, c, d, e) Mean-state SST (shading; unit: ℃), precipitation (contours in intervals of 3 mm day^{-1}) and 850 hPa wind (see scale vector in lower right; unit: m s^{-1}) from June to October in observations. Mean-state biases of SST, precipitation, 850 hPa wind based on (f, g, h, i, j) less-skewed CMIP6 model group, (k, l, m, n, o) more-skewed CMIP6 model group and (p, q, r, s, t) CMIP5 models. Biases of SST (white stippling), precipitation and wind are shown when exceeding the 95% significance level based on Student's t-test. 62

Figure 4.11. Positive IOD composites during JASO for (a, b, c, d) nonlinear vertical advection (unit: ℃ month^{-1}), (e, f, g, h) vertical velocity anomalies (unit: 10^{-3} cm s^{-1}) and (i, j, k, l) vertical temperature gradient anomalies at the base of mixed layer (unit: ℃ m^{-1}), based on (a, e, i) observations, (b, f, j) less-skewed CMIP6 model group, (c, g, k) more-skewed CMIP6 model group and (d, h, l) CMIP5 models. White stippling indicates the 95% significance level based on Student's t-test. 63

Figure 4.12. Same as Fig.4.11, but for negative IOD. 63

Figure 4.13. Standardized monthly SLA (8°S–2°N, 85°–110°E) vs SSTA (8°S–2°N, 85°–110°E) based on (a) observations, (b) less-skewed CMIP6 model group, (c) more-skewed CMIP6 model group and (d) CMIP5 models. Red (blue) crosses refer to positive (negative) IOD during JJASON. (b) to (d) consist of data during IOD events only. Black curve gives a quadratic fit of SLA and SST, and α is the nonlinear coefficient. 64

Figure 4.14. Mean ocean state in observations and CMIP6 models. (a) Ocean stratification (unit: ℃; 8°S–2°N, 85°–110°E; JASO) vs IOD skewness. (b) Thermocline (Z20; unit: m; 8°S–2°N, 85°–110°E; JASO) vs IOD skewness. Blue line is the least square linear fit. The r value is the correlation coefficient. The ocean stratification is calculated as the difference between the mean temperature over the upper 60 m and the temperature averaged from 90 m to 120 m. 65

Figure 4.15. (a, b, c, d, e) Mean-state vertical cross sections of temperature (unit: ℃) averaged over 8°S–2°N from June to October in observations. Temperature biases based on (f, g, h, i, j) less-skewed CMIP6 model group, (k, l, m, n, o) more-skewed CMIP6 model group and (p, q, r, s, t) CMIP5 models. Asterisk (circle) denotes observed (simulated) MLD. Black dash-dot (solid) contour is observed

(simulated) Z20. White stippling indicates the 95% significance level based on Student's t-test. 66

Figure 4.16. Positive IOD composites during JASO for (a, b, c, d) nonlinear meridional advection (unit: ℃ $month^{-1}$), (e, f, g, h) meridional mixed-layer current anomalies (unit: cm s^{-1}) and (i, j, k, l) meridional temperature gradient anomalies within the mixed layer (unit: 10^{-6} ℃ m^{-1}), based on (a, e, i) observations, (b, f, j) less-skewed CMIP6 model group, (c, g, k) more-skewed CMIP6 model group and (d, h, l) CMIP5 models. 67

Figure 4.17. Same as Fig. 4.16, but for negative IOD. 67

Figure 5.1. Multi-model averaged SSTA skewness during JJASON in the (a) historical and (b) SSP5-8.5 scenario simulations. Shading in (c) donates its greenhouse-warming-induced change with historical results shown by contours. White stippling indicates the 95% significance level based on Student's t-test. Seasonal fluctuations of SSTA skewness (multiplied by –1) within the ETIO (8°S–2°N, 85°–100°E) in the (d) historical and (e) SSP5-8.5 scenario simulations. Boxplot shows their median (red dash), interquartile range (blue box), lower and upper 1.5 times the interquartile range (black dash), and outlier (red + sign). The bold black solid line is the observed skewness. Skewness of (f) PC1 and (g) ETIO SSTA (multiplied by –1) during JJASON in the historical (blue bars) and SSP5-8.5 scenario (orange bars) simulations, with the black line denoting the observed skewness. Models with larger skewness in the SSP5-8.5 than the historical run are marked by a grey circle above the bar. 69

Figure 5.2. Changes in SSTA skewness during JJASON in 20 CMIP6 models. 70

Figure 5.3. IOD composite during JASO for mixed-layer heat budget within the ETIO (8°S–2°N, 85°–100°E) in the (a) historical, (b) SSP5-8.5 scenario simulations and (c) their greenhouse-warming-induced changes. The error bar is based on one STD. A circle over the bar indicates signals that are statistically significant at the 95% significance level. Long-term mean (d) nonlinear zonal advection (units: ℃ $month^{-1}$), (e) nonlinear vertical advection and (f) nonlinear meridional advection during JASO based on historical simulations. (g, h, i) are the same as (d, e, f), but for the SSP5-8.5 scenario simulations. (j, k, l) are the same as (d, e, f), but for changes. Shading values are shown when exceeding the 95% significance level based on the Student's t-test. 71

Figure 5.4. IOD composites during JASO for (a, b, c, j, k, l) nonlinear zonal advection (units: ℃ month^{-1}), (d, e, f, m, n, o) zonal current anomalies (units: cm s^{-1}) and (g, h, i, p, q, r) zonal MLT gradient anomalies (units: ℃ m^{-1}) based on (a, d, g) historical pIOD, (b, e, h) SSP5-8.5 pIOD, (c, f, i) pIOD changes, (j, m, p) historical nIOD, (k, n, q) SSP5-8.5 nIOD and (l, o, r) nIOD changes. White stippling is shown when exceeding the 95% significance level based on Student's t-test. 74

Figure 5.5. IOD composites during JASO for surface wind anomalies (see scale vector in lower right; units: m s^{-1}; shading is surface zonal wind anomaly) based on (a) historical pIOD, (b) SSP5-8.5 pIOD, (c) pIOD changes, (d) historical nIOD, (e) SSP5-8.5 nIOD and (f) nIOD changes. White stippling and vectors are shown when exceeding the 95% significance level based on Student's t-test. 74

Figure 5.6. STD of (a) nonlinear zonal advection (units: ℃ month^{-1}; 8°S–2°N, 85°–100°E; JASO) and (b) surface zonal wind anomaly (units: m s^{-1}; 5°S–5°N, 60°–90°E; JASO) during 1950–1999 vs 2050–2099. The black star and error bar denote the ensemble mean and one STD of inter-model variability, respectively. (c) SSTA gradient (units: ℃; 5°S–5°N, 45°–60°E minus 85°–100°E; JASO) vs surface zonal wind stress anomalies (units: 10^{-2} N m^{-2}; 5°S–5°N, 60°–90°E; JASO). The blue (red) line is the least squares linear fit of historical (SSP5-8.5 scenario) simulations. The k(–) [k(+)] values are the slope between two indices when SSTA gradients are smaller (larger) than zero. (d) Vertical average mean-state lapse rate change (units: ℃ km^{-1}; 30°E–120°E, 5°S–5°N; JASO) vs PC1 skewness change. (e) Vertical average mean-state lapse rate change vs SSTA skewness change (multiplied by –1) within ETIO (8°S–2°N, 85°–100°E; JASO). (f, g) are the same as (d, e), but for mean-state surface zonal wind change (units: m s^{-1}; 5°S–5°N, 60°–90°E; JASO). The blue line is the least squares linear fit and the r value is the correlation coefficient. (h) Historical mean state, (i) SSP5-8.5 mean state and (j) mean-state change of atmospheric potential temperature (units: K) averaged over 5°S–5°N during JASO. White stippling indicates the 95% significance level based on Student's t-test. 76

Figure 5.7. IOD composites during JASO for (a, b, c, j, k, l) nonlinear vertical advection (units: ℃ month^{-1}), (d, e, f, m, n, o) vertical velocity anomalies (units: cm s^{-1}) and (g, h, i, p, q, r) vertical temperature gradient anomalies at the base of

mixed layer (units: ℃ m^{-1}), based on (a, d, g) historical pIOD, (b, e, h) SSP5-8.5 pIOD, (c, f, i) pIOD changes, (j, m, p) historical nIOD, (k, n, q) SSP5-8.5 nIOD and (l, o, r) nIOD changes. White stippling indicates the 95% significance level based on Student's t-test. 78

Figure 5.8. Mean-state temperature (shading, units: ℃) averaged over 5°S–5°N during JASO in the (a) historical and (b) SSP5-8.5 scenario simulations. The circle (black solid contours) denotes climatological MLD (20℃, 22℃ and 24℃ isotherms). The bold solid line is the thermocline defined as the depth of the maximum vertical temperature gradient. (c) is the mean-state temperature change (shading). The circle (asterisk) denotes historical (SSP5-8.5) MLD. The black solid (dash-dot) contours are 20℃, 22℃ and 24℃ isotherms in historical (SSP5-8.5) simulation. The bold solid (dash-dot) line represents the historical (SSP5-8.5) thermocline. (d, e, f) are the same as (a, b, c), but for salinity (shading, units: PSU; contour, 34-35 PSU isohalines). White stippling indicates exceeding the 95% significance level based on Student's t-test. 79

Figure 5.9. (a) Multi-model ensemble histograms of standardized PC1 during the historical (1950–1999; green shading bar) and climate change (2050–2099; black bar) periods. (b) is the same as (a), but for SSTA (multiplied by –1) in the ETIO (units: ℃; 8°S–2°N, 85°–100°E) during JASO. (c) is the same as (a), but for DMI (units: ℃) during JASO. (d, e, f) are the same as (a, g, c), but for nIOD events only. The darker green shading bar (blue bar) denotes the extreme nIOD events in the historical (SSP5-8.5) simulations. The green (black) dash-dot and solid lines indicate the nIOD mean and the extreme nIOD mean in historical (SSP5-8.5) simulations, respectively. Composite extreme nIOD of SST (shading; unit: ℃), precipitation (contours in intervals of 1 mm day^{-1}; green: positive; pink: negative) and 850 hPa wind (see scale vector in lower right; unit: m s^{-1}) anomalies during JASO in the (g) historical and (h) SSP5-8.5 simulations. (i) is their greenhouse-warming-induced changes. Anomalies of SST (white stippling), precipitation and 850 hPa wind are shown when exceeding the 95% significance level based on Student's t-test. 81

Figure 5.10. Standardized monthly SLA vs SSTA (8°S–2°N, 85°–100°E) during IOD based on (a) historical and (b) SSP5-8.5 scenario simulations. The black curve gives a quadratic fit, and α is the nonlinear coefficient. The yellow (purple) line is

the least squares linear fit of pIOD with negative SLA (nIOD with positive SLA). 85

Figure 5.11. Emergent constraint on the IOD skewness. (a) Present-day PC1 skewness vs its change. (b) Present-day surface zonal wind (unit: m s^{-1}; 5°S–5°N, 60°–90°E; JASO) in the mean state vs PC1 skewness change. (c) Present-day surface zonal wind (unit: m s^{-1}; 5°S–5°N, 60°–90°E; JASO) in the mean state vs its change. (d) Present-day SSTA skewness (multiplied by –1) within ETIO (8°S–2°N, 85°–100°E; JASO) vs its change. (e) Present-day surface zonal wind (unit: m s^{-1}; 5°S–5°N, 60°–90°E; JASO) in the mean state vs change in ETIO SSTA skewness (multiplied by –1). The blue line indicates the best-fit regression line across the models. The black line represents the observation value. The intersection of the blue and black lines is the constrained value. 88

Figure 6.1. Multi-model averaged STD of SSTA (unit: ℃) during JJASON in the (a) historical and (b) SSP5-8.5 scenario simulations. Shading in (c) donates the greenhouse-warming-induced changes with historical simulation shown by contours. White stippling indicates the 95% significance level based on the Student's t-test. Seasonal fluctuations of SSTA STD within the ETIO (8°S–2°N, 85°–100°E) in the (d) historical and (e) SSP5-8.5 scenario simulations. Boxplot shows their median (red dash), interquartile range (blue box), lower and upper 1.5 times the interquartile range (black dash), and outlier (red + sign). The bold black solid line is the observed result. (f) SSTA STD over the ETIO during JJASON in the historical (blue bars) and SSP5-8.5 scenario (orange bars) simulations. The black line denotes the observed value. Models with larger STD under the SSP5-8.5 than the historical simulation are marked by grey circles above the bars.....89

Figure 6.2. (a, b, c) are the same as Fig. 6.1 (a, b, c), but for pIOD only. (d, e, f) are for nIOD only. The SSTA STD for pIOD is calculated by $\sqrt{\sum_1^N (SSTA_P)^2/N}$, where $SSTA_P$ is the SSTA during pIOD and N is the number of pIOD. The same goes for nIOD. 91

Figure 6.3. Composite pIOD of SST (shading; unit: ℃), precipitation (contours in intervals of 1 mm day^{-1}; green: positive; pink: negative) and 850 hPa wind (see scale vector in lower right; unit: m s^{-1}) anomalies during JASO in (a) historical and (b) SSP5-8.5 scenario simulations. (c) is their greenhouse-warming-induced changes. (d, e, f) are the same as (a, b, c), but for nIOD. Anomalies of SST (white

stippling), precipitation and 850 hPa wind are shown when exceeding the 95% significance level based on Student's t-test. 92

Figure 6.4. Composite pIOD of 500 hPa omega anomalies (unit: –0.01 Pa s^{-1}) during JASO in (a) historical and (b) SSP5-8.5 scenario simulations. (c) is its greenhouse-warming-induced change. (d, e, f) is the same as (a, b, c), but for nIOD. White stippling indicates the 95% significance level based on Student's t-test. 93

Figure 6.5. Composite pIOD of surface wind stress curl (shading, unit: N m^{-3}) and surface wind stress (vector, unit: N m^{-2}) anomalies during JASO in (a) historical and (b) SSP5-8.5 scenario simulations. (c) is their greenhouse-warming-induced changes. (d, e, f) is the same as (a, b, c), but for nIOD. White stippling and vector are shown when exceeding the 95% significance level based on Student's t-test. 94

Figure 6.6. Multi-model averaged JASO precipitation STD (unit: mm day^{-1}) in (a) historical and (b) SSP5-8.5 scenario simulations. Shading in (c) donates its changes with historical results shown by contours. (d, e, f) are the same as (a, b, c), but for mean-state precipitation. (g, h, i) are the same as (a, b, c), but for mean-state SST (shading; unit: ℃), precipitation [contours in intervals of 3 mm day^{-1} in (g, h) and 1 mm day^{-1} in (i)] and 850 hPa wind (see scale vector in lower right; unit: m s^{-1}). White stippling indicates the 95% significance level based on the Student's t-test. 95

Figure 6.7. (a) Mean-state precipitation changes (unit: mm day^{-1}) vs its STD changes during JASO within 10°S–3°S, 90°–110°E. (b) Mean-state precipitation changes vs SSTA STD for pIOD only (unit: ℃). The SSTA STD for pIOD is calculated by $\sqrt{\sum_1^N (SSTA_P)^2/N}$. The blue line is the least square linear fit. The r value is the correlation coefficient. 96

Figure 6.8. IOD composite during JASO for mixed-layer heat budget within 3°S–3°N, 70°–100°E in (a) historical, (b) SSP5-8.5 scenario simulations and (c) their greenhouse-warming-induced changes. The error bar is based on one STD. Circle over the bar indicates signals that are statistically significant at the 95% significance level.....98

Figure 6.9. Composite (a) pIOD $-\bar{u}(\partial T'/\partial x)$ (unit: ℃ $month^{-1}$), (d) pIOD $\partial T'/\partial x$ (unit: ℃ m^{-1}), (g) nIOD $-\bar{u}(\partial T'/\partial x)$, (j) nIOD $\partial T'/\partial x$, (m) $\bar{u}$ (unit: cm s^{-1}),

and (p) mean-state surface zonal wind (unit: m s^{-1}) during JASO in the historical simulations. (b, e, h, k, n, q) are the same as (a, d, g, j, m, p), but for SSP5-8.5 scenario. (c, f, i, l, o, r) are the same as (a, d, g, j, m, p), but for greenhouse-warming-induced changes. White stippling indicates the 95% significance level based on Student's t-test. 100

Figure 6.10. (a) $\bar{u}$ changes (unit: m s^{-1}) vs $-\bar{u}(\partial T'/\partial x)$ STD changes (unit: ℃ $month^{-1}$) during JASO within 3°S–3°N, 70°–100°E. (b) $-\bar{u}(\partial T'/\partial x)$ STD changes vs SSTA STD changes (unit: ℃). The blue line is the least square linear fit. The r value is the correlation coefficient. 101

Figure 6.11. Mean-state squared buoyancy frequency (shading; unit: s^{-2}) and MLD (circle) during JASO in the (a) historical and (b) SSP5-8.5 scenario simulations. (c) is the mean-state change. The circle (asterisk) denotes historical (SSP5-8.5) MLD. 102

Figure 6.12. Composite (a) pIOD $-w'\overline{(T-T_{-h})/h}$ (unit: ℃ $month^{-1}$), (d) pIOD w' (unit: cm s^{-1}), (g) nIOD $-w'\overline{(T-T_{-h})/h}$, (j) nIOD w', and (m) $\overline{(T-T_{-h})/h}$ (unit: ℃ m^{-1}) during JASO. (b, e, h, k, n) are the same as (a, d, g, j, m), but for SSP5-8.5 scenario. (c, f, i, l, o) are the same as (a, d, g, j, m), but for greenhouse-warming-induced changes. White stippling indicates the 95% significance level based on Student's t-test. 103

Figure 6.13. Composite (a) pIOD $-\bar{w}[(T-T_{-h})/h]'$ (unit: ℃ $month^{-1}$), (d) pIOD $[(T-T_{-h})/h]'$ (unit: ℃ m^{-1}), (g) nIOD $-\bar{w}[(T-T_{-h})/h]'$, (j) nIOD $[(T-T_{-h})/h]'$, and (m) $\bar{w}$ (unit: cm s^{-1}) during JASO. (b, e, h, k, n) are the same as (a, d, g, j, m), but for SSP5-8.5 scenario. (c, f, i, l, o) are the same as (a, d, g, j, m), but for greenhouse-warming-induced changes. White stippling indicates the 95% significance level based on Student's t-test. 104

Figure 7.1. Partial least squares regression of (a, b, c, d, e) 3-month SPEI, (f, g, h, i, j) precipitation anomalies (unit: mm day^{-1}) and (k, l, m, n, o) surface air temperature anomalies (unit: K) onto DMI with the influences of Niño 3.4 index removed during (a, f, k) JJA, (b, g, l) JAS, (c, h, m) ASO, (d, i, n) SON and (e, j, o) OND in observations. Stippling indicates the 95% significance level based on Student's t-test. 106

Figure 7.2. (a) Monthly climatological precipitation (unit: mm day^{-1}) pattern in observations. (b) Monthly climatological precipitation averaged over Eastern Africa (10°S–12°N, 30°–52°E) in observations and CMIP6 models. (c) RMSE vs spatial correlation of monthly climatological precipitation over Eastern Africa between observation and CMIP6 models.....107

Figure 7.3. Composite precipitation (unit: mm day^{-1}) and 850 hPa wind anomalies (see scale vector in lower right; unit: m s^{-1}) during (a, d, g, j) ASO, (b, e, h, k) SON and (c, f, i, l) OND based on (a, b, c) observed pIOD, (b, e, f) historical pIOD, (g, h, i) observed nIOD and (j, k, l) historical nIOD. The black box is 10°S–12°N, 30°–52°E. Shading values and black vectors are displayed upon surpassing the 95% significance level (Student's t-test). 108

Figure 7.4. Biases of IOD composite biases for precipitation anomalies and water vapor budget terms (unit: mm day^{-1}) averaged over Eastern Africa (10°S–12°N, 30°–52°E) during OND. Error bar is based on one STD. Circle over the bar indicates signals passing the 95% significance level. 109

Figure 7.5. The same as Fig. 7.3, but for SSTA (unit: ℃) and 850 hPa wind anomalies (see scale vector in lower right; unit: m s^{-1}). 110

Figure 7.6. The same as Fig. 7.3, but for 250 hPa velocity potential (unit: 10^6 m^2 s^{-1}) and divergent wind anomalies (see scale vector in lower right; unit: m s^{-1}). 110

Figure 7.7. (a) Composite pIOD for SSTA gradient in the TIO (unit: ℃; 5°S–5°N, 45°–60°E minus 80°–100°E; OND) vs precipitation anomalies in Eastern Africa (unit: mm day^{-1}; 10°S–12°N, 30°–52°E). (b) is the same as (a), but for nIOD. The purple line is the least square linear fit. The r value is the correlation coefficient. 111

Figure 7.8. (a, b) Mean-state precipitation (shading; unit: mm day^{-1}) and 850 hPa wind (see scale vector in lower right; unit: m s^{-1}), and (d, e) mean-state omega (shading; 0.01 Pa s^{-1}; multiplied by –1), and atmospheric zonal (m s^{-1})–vertical (–0.01 Pa s^{-1}) vectors averaged in 5°S–5°N during OND in (a, d) observations and (b, e) historical simulations. Mean-state biases of (e) precipitation and 850 hPa wind, and (f) Walker Circulation. Biases of omega (white stippling), precipitation and wind are shown when exceeding the 95% significance level based on Student's t-test. (g) Mean-state precipitation (unit: mm day^{-1}; 10°S–12°N, 30°–52°E; OND) vs its STD. (h) Mean-state 500 hPa omega (unit: Pa s^{-1}; 5°S–5°N,

30°–60°E; OND) vs mean-state precipitation. (i) Mean-state surface zonal wind (unit: m s^{-1}; 5°S–5°N, 60°–90°E; OND) vs mean-state 500 hPa omega. The purple line is the least square linear fit. The r value is the correlation coefficient. 112

Figure 7.9. Composite precipitation (unit: mm day^{-1}) and 850 hPa wind anomalies (see scale vector in lower right; unit: m s^{-1}) during OND in (a, b) pIOD and (d, e) nIOD based on (a, d) historical and (b, e) SSP5-8.5 simulations. Values exceeding the 95% significance level (Student's t-test) are shown. Their greenhouse-warming-induced changes during (c) pIOD and (f) nIOD with stippling and black vector for statistical significance. 114

Figure 7.10. Changes of IOD composite for precipitation anomalies and water vapor budget terms (unit: mm day^{-1}) averaged over (a) Somali Peninsula (2°S–12°N, 40°–52°E) and (b) Southeastern Africa (15°S–2°N, 30°–40°E) during OND. Error bar is based on one STD. Circle over the bar indicates signals passing the 95% significance level.....116

Figure 7.11. The same as Fig. 7.10, but for SSTA (unit: ℃) and 850 hPa wind anomalies (see scale vector in lower right; unit: m s^{-1}). 117

Figure 7.12. Inter-model EOF1 of 850 hPa wind anomaly changes during OND in (a) pIOD and (b) nIOD. (c) Inter-model PC1 of pIOD vs precipitation anomaly changes in Somali Peninsula (unit: mm day^{-1}; 2°S–12°N, 40°–52°E; OND). (d) is the same as (c), but for nIOD. (e, f) are the same as (c, d), but for Southeastern Africa (unit: mm day^{-1}; 15°S–2°N, 30°–40°E; OND). The blue line is the least square linear fit. The r value is the correlation coefficient. 117

Figure 7.13. Mean-state precipitation (unit: mm day^{-1}) and 850 hPa wind (see scale vector in lower right; unit: m s^{-1}) during OND in the (a) historical and (b) SSP5-8.5 scenario simulations. (c) donates its greenhouse-warming-induced changes. (d, e, f) are the same as (a, b, c), but for specific humidity (shading) and atmospheric zonal (m s^{-1})–vertical (–0.01 Pa s^{-1}) vectors averaged in 5°S–5°N during OND. Changes in specific humidity (white stippling), precipitation and wind are shown when exceeding the 95% significance level based on Student's t-test. 118

Figure 7.14. (a) Mean-state precipitation changes (unit: mm day^{-1}; 2°S–12°N, 40°–52°E; OND) vs its STD changes. (b) Mean-state 500 hPa omega changes (unit: Pa s^{-1}; 2°S–12°N, 40°–52°E; OND) vs mean-state precipitation changes. (c) Mean-state surface zonal wind changes (unit: m s^{-1}; 5°S–5°N, 60°–90°E; OND) vs

mean-state 500 hPa omega changes. The blue line is the least square linear fit. The r value is the correlation coefficient. 119

Figure 7.15. Emergent constraint on the precipitation STD changes in the Somali Peninsula. Present-day mean-state precipitation (unit: mm day^{-1}; 2°S–12°N, 40°–52°E; OND) vs its STD changes. The blue line indicates the best-fit regression line across the models. The black line represents the observation value. The intersection of the blue and black lines is the constrained value. 120

Figure 7.16. Composite extreme nIOD for precipitation (unit: mm day^{-1}) and 850 hPa wind anomalies (see scale vector in lower right; unit: m s^{-1}) during OND in the (a) historical and (b) SSP5-8.5 scenario simulations. Values exceeding the 95% significance level (Student's t-test) are shown. (c) is the precipitation anomaly change with stippling for statistical significance. Multi-model ensemble histograms of precipitation anomalies averaged over the Somali Peninsula (unit: mm day^{-1}; 2°S–12°N, 40°–52°E; OND) during the historical (1950–1999; green shading bar) and climate change (2050–2099; black bar) periods for (d) nIOD samples and (e) extreme nIOD samples, respectively. (f, g) is the same as (d, e), but for surface air temperature anomalies (unit: K). The multi-model mean for the historical (climate change) period is indicated by the red (black) line. 122

Figure 7.17. Composite surface air temperature anomalies (unit: K) in (a) observed pIOD, (b) observed nIOD, (e) historical pIOD and (f) historical nIOD during ASO. (i) Inter-model composite of surface air temperature anomalies in Southwestern Australia (33°–21°S, 115°–135°E; ASO). The red (blue) line denotes observed pIOD (nIOD) composite. Stippling indicates the 95% significance level based on Student's t-test. (c, d, g, h, j) are the same as (a, b, e, f, i), but for precipitation (unit: mm day^{-1}). (j) is for Southeastern Australia (43°–30°S, 135°–152°E). Anomalies have been adjusted to exclude the effects of the Niño 3.4 index. 123

Figure 7.18. Partial least squares regression of (a) SLP (unit: hPa) and 850 hPa wind (see scale vector in lower right; unit: m s^{-1}) anomalies onto DMI with the influences of Niño 3.4 index removed during JAS, ASO and SON in observations. Composite SLP and 850 hPa wind anomalies in (b) observed pIOD, (c) historical pIOD, (d) observed nIOD and (e) historical nIOD. Stippling and vector are shown when exceeding the 95% significance level based on Student's t-test. 125

Figure 7.19. The same as Fig. 7.18, but for 300 hPa streamfunction (unit: 10^6 m^2 s^{-1}) and rotational wind anomalies (see scale vector in lower right; unit: m s^{-1}). 125

Figure 7.20. The same as Fig. 7.18, but for Rossby wave source (unit: 10^{-10} s^{-1}). ... 126

Figure 7.21. The same as Fig. 7.18, but for 300 hPa velocity potential (unit: 10^6 m^2 s^{-1}) and divergent wind anomalies (see scale vector in lower right; unit: m s^{-1}).... 127

Figure 7.22. Composite surface air temperature anomalies (unit: K) of (a) historical pIOD, (b) historical nIOD, (e) SSP5-8.5 pIOD, (f) SSP5-8.5 nIOD, (i) pIOD change and (j) nIOD change during ASO. (c, d, g, h, k, l) are the same as (a, b, e, f, i, j), but for precipitation anomalies (unit: mm day^{-1}). Stippling indicates the 95% significance level based on Student's t-test. Anomalies have been adjusted to exclude the effects of the Niño 3.4 index..... 128

Figure 7.23. Composite 300 hPa streamfunction (unit: 10^6 m^2 s^{-1}) and rotational wind anomalies (see scale vector in lower right; unit: m s^{-1}) during JAS, ASO and SON in (a) historical pIOD, (b) SSP5-8.5 pIOD (c) historical nIOD and (d) SSP5-8.5 nIOD. 128

Figure 7.24. (a) Historical mean-state 300 hPa zonal wind, (b) SSP5-8.5 mean-state 300 hPa zonal wind and (c) its changes induced by greenhouse warming. Stippling indicates the 95% significance level based on Student's t-test. 128

Figure 8.1. Mean-state BLT (unit: m) in (a) observations, (b) historical and (c) SSP5-8.5 simulations. 141

Figure 8.2. Mean-state SST (unit: ℃; 2°S–2°N, 150°–240°E; JASO) vs 850 hPa zonal wind (unit: m s^{-1}; 5°S–5°N, 60°–90°E; JASO)..... 142

Figure A1. (a, b, c, d) Mean-state latent heat flux (shading; units: W m^{-2}) and sea surface wind (see scale vector in lower right; units: m s^{-1}) during JASO in observations, less-skewed CMIP6 model group, more-skewed CMIP6 model group and CMIP5 models. (e, f, g, h) Positive IOD composites during JASO for latent heat flux forcing anomalies (shading; unit: ℃ $month^{-1}$) and sea surface wind anomalies (see scale vector in lower right; units: m s^{-1}). (i, j, k, l) are the same as (e, f, g, h), but for negative IOD. 171

Figure A2. Skewness of Niño3.4 index versus IOD skewness defined by the PC1 skewness. 171

List of Tables

Table 2.1. The selected CMIP6 models. 22

Table 5.1. Composite mixed-layer advection terms (unit: ℃ month^{-1}) in pIOD and nIOD during JASO within 8°S–2°N, 85°–100°E, including their historical values, SSP5-8.5 scenario values and greenhouse-warming-induced changes. 73

Table 5.2. Frequency of nIOD using different indices. A normal (extreme) nIOD event is defined as when the PC1 of each model is negative and greater than 0.8 (1.5) STD in amplitude. As for the ETIO SSTA, a normal (extreme) nIOD event is defined as when the ETIO SSTA during JASO of each model is positive and greater than 1 (1.5) STD. In terms of DMI, a normal (extreme) nIOD event is defined as when the DMI of each model is negative and greater than 1 (2) STD. Model names in italics and bold indicate well-skewed models that capture comparable IOD skewness to observations in the historical run. Bold numbers indicate an increase in extreme nIOD events, and numbers in italics indicate no change from the historical (1950–1999) to climate change (2050–2099) periods. 83

Table 5.3. The same as Table 5.2, but for pIOD. 84

Table 5.4. The same as Table 5.1, but for extreme nIOD only. 86

Table 6.1. Composite mixed-layer advection terms (unit: ℃ month^{-1}) in pIOD and nIOD during JASO within 3°S–3°N, 70°–100°E, including their historical values, SSP5-8.5 scenario values and greenhouse-warming-induced changes. 99

Table A1. The same as Table 5.2, but for periods of 1900–1949 and 2050–2099. ... 172

1. Introduction

1.1. Mean state in the Indian Ocean

Among the three great oceans (Pacific, Atlantic, and Indian Oceans), the Indian Ocean is the youngest and smallest in terms of geology. It is also the ocean with the most complicated geophysical processes. The Indian Ocean extends from Africa in the west to Australia in the east, the Asian continent in the north, and Antarctica in the south, with a total area of about 7.34×10^8 km^2, occupying about 1/5 of the global ocean, and an average depth of about 3960 m (Talley et al. 2011). Since the Indian Ocean is landlocked to the north, this unusual distribution of land and sea generates the strongest monsoon system in the Indian Ocean, which has significant effects on the nearby regions, and therefore Indian Ocean rim countries are concerned about the forecast of the monsoon and its resulting climatic impacts (Ding and Chan 2005; Schott et al. 2009; Han et al. 2014).

The Indo-Pacific warm pool, which is typically above 28°C, is located in the upper western Pacific and eastern Indian Ocean, causing the warmer sea surface temperature (SST) in the eastern tropical Indian Ocean (ETIO) than the western tropical Indian Ocean (WTIO) (Fig. 1.1). Thus, the Walker Circulation in the Indian Ocean differs from the other two oceans, with rising branch in the eastern part and sinking branch in the western part (Talley et al. 2011; Cai et al. 2013). The corresponding precipitation in the ETIO is abundant, contributing to dense tropical rainforests over the maritime continent. Africa is largely arid because of the WTIO's sinking branch, which prefers bright days and little rain. The Indian Ocean exhibits notable seasonal fluctuations as a result of the monsoon (Fig. 1.1) (Schott and McCreary 2001; Wu et al. 2020). The Indian Ocean monsoon is typically separated into the northeast monsoon and the southwest monsoon, which correspond to winter and summer in the northern hemisphere, respectively (Reverdin et al. 1986; Schott and McCreary 2001). Around the Indian Ocean, there are consequently dry and wet seasons. The rainy season occurs across the northern Indian Ocean continent because of the summer monsoon's substantial moisture transport from the Indian Ocean to land (Clark et al. 2000; Chowdary et al. 2019). Instead, with low pressure in the Indian Ocean and high pressure on the Eurasian continent, the winter monsoon blows from that continent to the Indian Ocean, leaving North Africa and South Asia dry (Dimri et al. 2016). SST variability is primarily linked to solar shortwave radiation and sea surface latent heat release, with the latter being somewhat connected

to wind speed, so SST variability is compatible with monsoon variability (Schott et al. 2009).

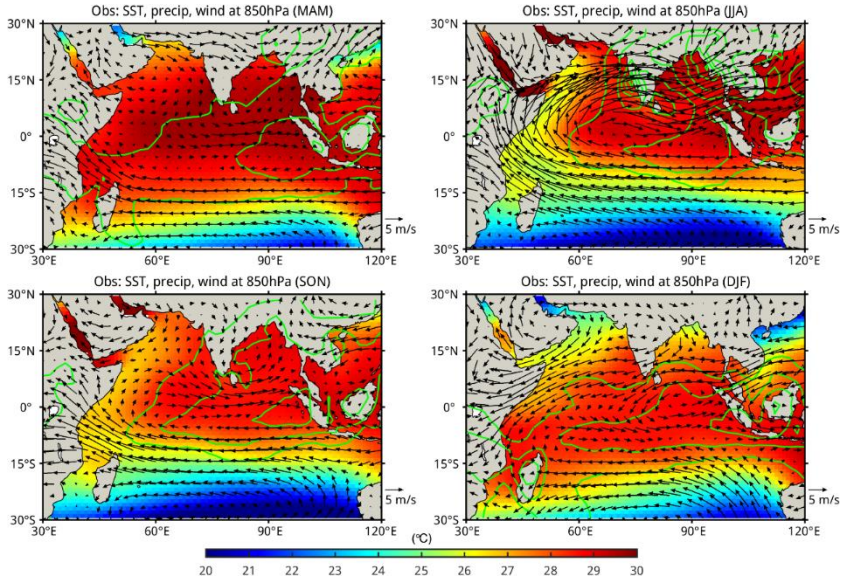


Figure 1.1. Mean-state SST (shading; unit: °C), precipitation (contours in intervals of 3 mm day^{-1}) and 850 hPa wind (vector; unit: m s^{-1}) during March to May (MAM), June to August (JJA), September to November (SON), and December to February (DJF).

The thermocline, which is determined by the depth of 20 °C isotherm (Z20), is deeper in the ETIO than WTIO, which is related to the background westerly winds, in contrast to the Pacific and Atlantic Oceans (Fig. 1.2). In addition, the Sumatra-Java coast, the thermocline dome (Seychelles-Chagos thermocline ridge), and the Somali coast are three major upwelling locations in the Indian Ocean that undergo large SST variations, all modulated by the climatic modes through ocean dynamics and air-sea interactions (Xie et al. 2002; Feng et al. 2003; Hermes and Reason 2008; Izumo et al. 2008; Scott et al. 2009). The thermocline dome in the southern WTIO (SWTIO) is strongest in the boreal summer, which is consistent with the large-scale wind stress curl (Fig. 1.2). Except for the major role of wind stress curl, the local divergence between the southeasterly trade winds and the monsoon westerlies also affects this region, as well as remote forcing through the Rossby waves from the eastern Indian Ocean (Baquero-Bernal and Latif 2005; Doi et al. 2007; Hermes and Reason 2008).

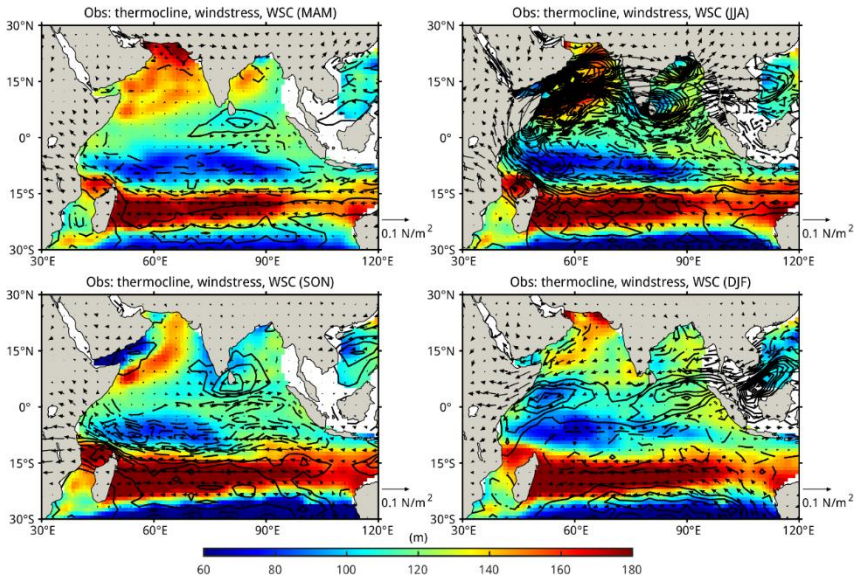


Figure 1.2. Mean-state thermocline (Z20; shading; unit: m), wind stress curl (contour; interval: 2×10^{-8} N m^{-3}) and 850 hPa wind stress (see scale vector in lower right; unit: N m^{-2}) during MAM, JJA, SON, and DJF.

The seasonal changes in the monsoon are accompanied by notable seasonal changes in currents (Fig. 1.3) (Lumpkin and Johnson 2013; Chen et al. 2015; Wu et al. 2020). The surface Indian Ocean currents are mainly wind-driven currents. During the summer monsoon, the southern hemisphere trade winds approach the equator. Under the influence of the south-easterly winds, the offshore upwelling occurs along the eastern coast of the tropical Indian Ocean (TIO), a renewed westerly flow at the equator, and the western boundary current intensifies. During the winter monsoon, westward currents predominate north of the equator. The north-easterly winds transport seawater from the Bay of Bengal to the Arabian Sea via the southern coast of the Indian subcontinent. During the monsoon transition (northern hemisphere spring and autumn), the equatorial jet (Wyrtki Jet) flows at the equatorial Indian Ocean, which transports hot, salty seawater from the western surface layer eastward (Wyrtki 1973; Nagura and McPhaden 2010). In addition, a west-to-east equatorial undercurrent that has its core depth near the 20 °C isotherm also exists in the equatorial subsurface and plays a significant role in zonal exchanges of energy and material (Knauss and Taft 1964; Chen et al. 2016a). The mixed layer, serving as the interface between the atmosphere and the ocean, plays a crucial role in establishing the mean state and variability of the ocean. In the context of air-sea interactions, the mixed layer is a key parameter, regulating the amplitude of SST response. In boreal autumn, the equatorial Wyrtki Jet leads to a west-to-east decline in mixed-layer depth (MLD) (O'Brien and Hurlburt 1974) (Fig. 1.3).

While winter rainfall forms a barrier layer near Sumatra, shallowing the MLD (Masson et al. 2002; Qu and Meyers 2005). Seasonal changes in MLD in the south-western TIO are linked to the wind's annual cycle, due to its effect on stirring and its influence on buoyancy fluxes and the thermocline depth (Foltz et al. 2010).

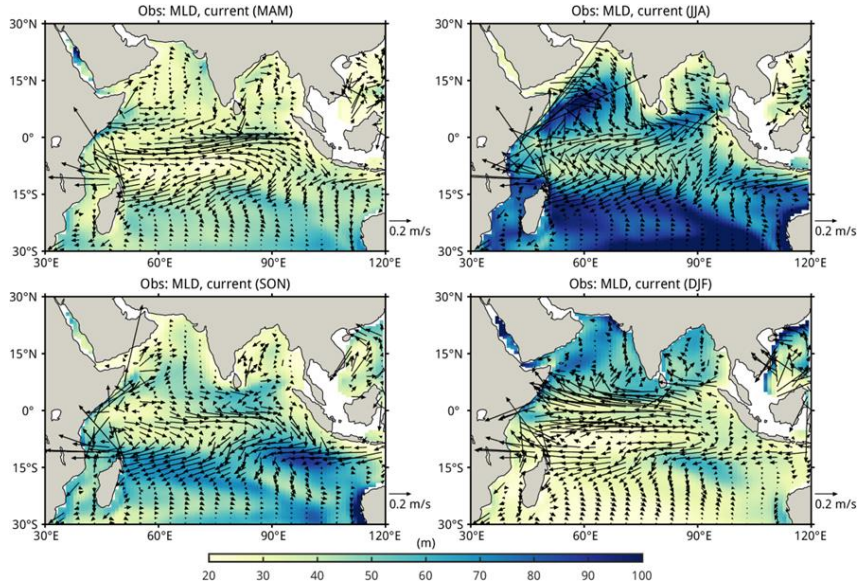


Figure 1.3. Mean-state MLD (shading; unit: m) and surface current (see scale vector in lower right; unit: m s^{-1}) during MAM, JJA, SON, and DJF.

1.2. Physics of IOD

1.2.1. Triggering mechanisms

The TIO is an area of active air-sea interactions, due to the background Indo-Pacific warm pool and the absence of steady equatorial wind and upwelling systems (Li et al. 2003; Cai et al. 2013) (Fig. 1.4). The Indian Ocean Dipole (IOD) is the most remarkable interannual phenomenon in the TIO (Saji et al. 1999; Webster et al. 1999), which causes weather or climate anomalies not only in the nearby Indian Ocean region but also worldwide (Annamalai et al. 2003; Ashok et al. 2003; Behera et al. 2005; Abram et al. 2008; Schott et al. 2009). The IOD's influence extends to the triggering of floods (Zubair et al. 2003; Endo and Tozuka 2016), droughts (Cai et al. 2009; Xu et al. 2020), heat waves (Guan and Yamagata 2003), and other extreme events that impact agricultural productivity, freshwater resources, public health, and economic stability, especially in African and Asian nations. The most severe IOD event recorded in the satellite era transpired in late 2019, inducing Australia's extreme drought in 2019 (Zhang et al. 2021) and historic Yangtze flooding in 2020 (Takaya et al. 2020; Zhou et al. 2021), posing significant challenges to human livelihoods and economic progress.

Beyond terrestrial impacts, the IOD also affects marine ecosystems (Abram et al. 2003) and influences the global carbon cycle (Page et al. 2002). It plays a role in various coupled processes, including North Indian Ocean tropical cyclones (Yuan and Cao 2013), the Indian summer monsoon (Gadgil et al. 2004), and the development of the El Niño-Southern Oscillation (ENSO) (Izumo et al. 2010). Investigating IOD mechanisms can enhance our understanding of physical processes in models, thus improving weather and climate predictions related to the IOD.

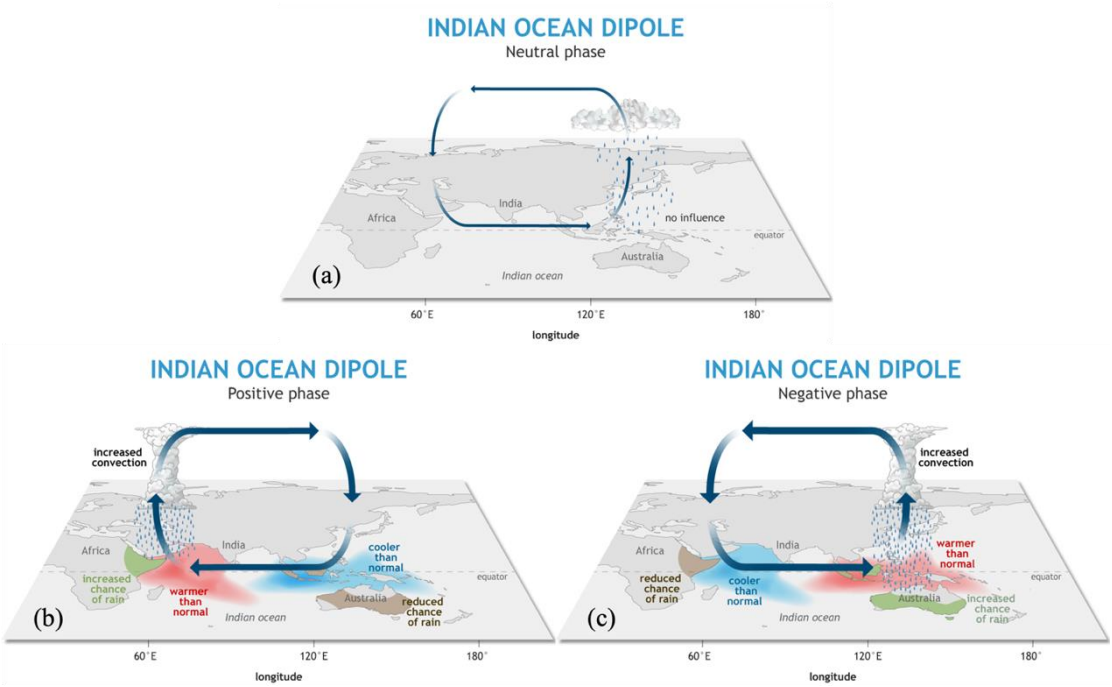


Figure 1.4. (a) Neutral phase, (b) negative phase and (c) positive phase of IOD. Source: https://snowbrains.com/noaa-march-enso-update-meet-ensos-neighbor-the-indian-ocean-dipole/.

The IOD is characterized by a zonal SST anomaly (SSTA) gradient in the TIO (Tozuka et al. 2008). During pIOD, the ETIO becomes anomalously cooler while the WTIO becomes anomalously warmer, constituting a dipole pattern, marked by distinct easterly wind anomalies over the TIO and southeasterly wind anomalies along the Sumatra-Java coast (Saji et al. 1999; Tozuka et al. 2008) (Fig. 1.4b). The negative phase of IOD roughly mirrors its positive phase (Fig. 1.4c). IOD events typically occur in the boreal summer and fall, with the autumn season being regarded as the IOD mature phase (Saji et al. 1999; Du et al. 2013). The phase locking of the IOD is intimately linked to the Indian Ocean summer monsoon variability. In association with the Asian monsoon, the Sumatra-Java coast is occupied by the east-to-southeasterly winds from June to November (JJASON), which lift the thermocline to a shallow depth in a year,

providing a conducive environment for the emergence of a pIOD event (Cai et al. 2013; McPhaden and Nagura 2014). Generally, stronger southeasterly trade winds along the Sumatra-Java coast induce local upwelling, leading to anomalous cooling and supporting the pIOD development (Luo et al. 2008), which is the fundamental development mechanism for IOD (referred to as local Bjerknes feedback, Bjerknes 1969). In December, pIOD events abruptly decay as the winds change to westerlies, marking the onset of the Australian summer monsoon (Jourdain et al. 2013).

In general, the triggers of IOD are usually classified into two main categories, namely, internal forcing in the Indian Ocean as well as external forcing. ENSO is one of the most important external triggers of IOD (Wang and Wang 2014; Fan et al. 2017). Since the concept of IOD was proposed, many people have questioned whether IOD is an accessory product of ENSO, and questions about whether IOD is independent of ENSO and whether it interacts with ENSO have been a hot research topic (Behera et al. 2006; Meyers et al. 2007; Luo et al. 2010). ENSO can trigger IOD events by influencing the Walker circulation system in the Indo-Pacific Region (Yang et al. 2015). In autumn of the same year in which the El Niño event occurred, the original weak westerly winds in the equatorial Indian Ocean became easterly, triggering a pIOD due to the weakening of the Walker circulation upward branch located in the maritime continent as a result of the anomalous warming in the eastern Pacific Ocean (Saji et al. 1999; Meyers et al. 2007; Xie et al. 2016). Similarly, La Niña corresponds to negative IOD (nIOD). For example, in 1997, the strongest El Niño on record was accompanied by an extreme pIOD (Yu and Rienecker 1999; Webster et al. 1999), while the following year also saw a corresponding La Niña and nIOD (Meyers et al. 2007). In addition to the atmospheric channel, Indonesian Throughflow (ITF) can propagate ENSO and even lower-frequency signals into the Indian Ocean by adjusting the thermocline along the Sumatra-Java coast and the Rossby waves in the southern TIO (Tozuka et al. 2007; Shi et al. 2007).

About 1/3–2/3 of IOD events can occur independently of ENSO (Stuecker et al. 2017). Such IODs can be referred to as independent IODs (Fischer et al. 2005), such as the extreme 1994 pIOD event that is not accompanied by ENSO's signals (Vinayachandran et al. 1999; Annamalai et al. 2005). Behera et al. (2006) utilized a coupled general circulation model (CGCM) to demonstrate that the IOD can be accurately simulated in a Pacific decoupled no-ENSO experiment. In the absence of ENSO, the occurrence of an independent IOD depends mainly on the internal variability

of the Indian Ocean, such as wind field anomalies caused by the Madden-Julian Oscillation (MJO; Zhang 2013), changes in upwelling along the eastern coast of the TIO due to equatorial Kelvin waves, or anomalous changes in the monsoon winds, among others (Rao et al. 2009; Tanizaki et al. 2017). For instance, the cross-equatorial monsoon in summer can cause significant zonal momentum from the southern hemisphere to the equator, thereby creating easterly wind along the equator (Ogata and Xie 2011) and leading to notable oceanic responses (Schott and McCreary 2001; Schott et al. 2009). Furthermore, IOD can be triggered by southern annular mode (SAM) (Lau and Nath 2004; Zhang et al. 2020). During positive SAM, cold SSTA commences in the southern Indian Ocean, accompanied by an anomalous subtropical high system and anomalous southeasterly winds. The eastward movement of these anomalies enhances the summer monsoon off Sumatra-Java, leading to an early pIOD onset.

1.2.2. IOD life cycle

IOD originates from ocean-atmosphere interactions and grows through a series of feedback mechanisms, including the wind-evaporation-SST (WES) feedback (Xie and Philander 1994), thermodynamic air-sea feedback (Li et al. 2003), wind-thermocline-SST feedback (referred to as Bjerkens feedback, Bjerknes 1969), cloud-radiation-SST feedback (Fischer et al. 2005), and oceanic Rossby wave response (Webster et al. 1999). The WES feedback varies seasonally and depends on the prevailing wind direction. In a pIOD event, the anomalous cooling in the southern ETIO (SETIO) induces anomalous southeasterly winds, which enhances the climatological southeasterly winds in boreal summer. This results in increased sea surface evaporation, further amplifying the surface cooling in the ETIO (Sun et al. 2022). The IOD activity is seasonally locked, generally evolving in boreal summer, reaching its peak in boreal autumn, and rapidly decaying thereafter (Saji et al. 1999), which can be explained by the seasonally dependent thermodynamic air-sea feedback (Li et al. 2003). Consider a pIOD event, the cold SSTA in the SETIO signifies an atmospheric heat sink which triggers a descending Rossby wave response to its west based on Gill's (1980) solution. The anomalous low-level anticyclonic flow subsequently increases coastal wind in boreal summer and further lowers the SST through enhanced sea surface evaporation (known as WES feedback), vertical mixing and coastal upwelling (Li et al. 2003). The Bjerknes feedback in the Indian Ocean, involving SST response to thermocline modulation, wind response to SSTAs, and thermocline response to wind anomalies, has been extensively

studied (Schott et al. 2009; Zheng et al. 2010). During pIOD, cold SSTAs in the ETIO trigger anomalous easterly winds across the TIO, initiating upwelling in the ETIO, which further cools the SST and reinforces the feedback loop. The cloud-radiation-SST feedback (Fischer et al. 2005) is negative: increased SST can lead to more clouds that reflect solar radiation, lowering SST, and conversely, decreased SST leads to fewer clouds, allowing more solar radiation absorption by the ocean and raising SST.

Regarding the oceanic Rossby wave response (Webster et al. 1999), the anomalous wind stress curl during pIOD triggers oceanic Rossby waves, which carry deeper thermocline westward and increase the SST in the WTIO where the average thermocline is relatively shallow, leading to a positive effect on the development stage of IOD. Subsequently, Rossby waves reflect at the western boundary to form equatorially downwelling Kelvin waves and propagate rapidly eastward, terminating the cold signal at the eastern pole of the IOD (Rao et al. 2009; Yuan and Liu 2009; Zhang et al. 2014). In addition, the background southeasterly winds retreat to the Southern Hemisphere, and the conditions for the pIOD development disappear (Li et al. 2003). However, the warm anomaly caused by the Kelvin wave persists into the following year's IOD window, creating conditions for the occurrence of negative events, and giving rise to an alternation of positive and negative events (Yamagata et al. 2004; Lu et al. 2018). For example, positive and negative events occurred successively in both 1997-98 and 2015-16, reflecting the two-year cycle. Collectively, these mechanisms contribute to the complex genesis and evolution of IOD, indicating that IOD is a complex dynamic phenomenon, and it is important to explore underlying dynamics in the context of climate change.

1.2.3. Asymmetry mechanisms

Positive IOD skewness is the tendency for pIOD events to have a larger amplitude than nIOD events and to be more extreme than nIOD (Cai and Qiu 2013). Interannual anomalies of SST, wind, and precipitation over the SETIO all exhibit negative skewness (Ogata et al. 2013). Extreme pIOD is the main source of positive IOD skewness (Hong et al. 2008b). The 1961, 1994, 1997 and 2019 pIOD events are usually called "extreme pIOD". Although there is no consensus on the definition of such extreme IOD, discernible discrepancies arise when comparing these occurrences to their negative counterparts—the observations have no nIOD event comparable to such extreme pIOD events. The observed extreme IOD events, which happened in 1961, 1994, 1997, and

2019, brought vast hazards to nature and society (Page et al. 2002; Xu et al. 2020) but also created a burst of scientific activity. For example, the 1997 extreme pIOD event directly led to the birth of the IOD concept (Webster et al. 1999; Saji et al. 1999).

The intrinsic to IOD asymmetry is likely related to the nonlinear processes within the coupled ocean-atmosphere system of the TIO, such as the nonlinear Bjerknes feedback processes (Cai and Qiu 2013). An influential oceanic component in this nonlinear Bjerknes feedback is the nonlinear dynamical heating (NDH), including nonlinear zonal, meridional and vertical components (Hong et al. 2008a, b). Hong et al. (2008a) emphasized that IOD amplitude asymmetry is attributed to the asymmetry of the wind stress–ocean advection–SST feedback, which induces negative SSTA tendency over the ETIO regardless of SSTA signs. Thus, this mechanism amplifies pIOD while dampening nIOD. However, Hong and Li (2010) contended that the SSTA asymmetry is primarily steered by the asymmetric atmospheric heating and wind responses to the ETIO SSTAs, rather than nonlinear vertical advection. Another nonlinear oceanic process is related to the thermocline-temperature asymmetry, associated with the mean-state deep thermocline in the ETIO (Cai and Qiu 2013, Ogata et al. 2013). Because of the background deep thermocline, this dynamic gives rise to minimal surface warming in response to the wind-driven deepening thermocline during nIOD, in contrast to the pIOD's shallower thermocline, which induces more pronounced surface cooling across the ETIO (Cai and Qiu 2013). Nevertheless, other studies asserted that the thermocline–temperature feedback is unfavorable for pIOD occurrence and intensity under circumstances where the ETIO thermocline is excessively deep (Zhang et al. 2018). This counterintuitive outcome arises due to relatively shallow thermoclines allowing for the entrainment of colder waters into the mixed layer (Annamalai et al. 2005).

Asymmetric SST–cloud–radiation (SCR) feedback is one of the atmospheric effects that may contribute to the positive IOD skewness (Hong et al. 2008b). This feedback implies that warm SSTAs during nIOD are thermally damped by negative SCR feedback, while cold SSTAs during pIOD are not affected by SCR feedback under clear skies and can intensify faster (Hong et al. 2008b). However, Cai et al. (2012) argued that the SCR feedback increases with the development of cold ETIO SSTAs and the IOD skewness does not occur because of a breakdown in the SCR feedback. In addition, the IOD asymmetry can be enhanced by a nonlinear barrier layer response, which shows a greater barrier layer thinning to colder ETIO and less barrier layer thickening to

warmer ETIO (Masson et al. 2004; Qiu et al. 2012; Cai and Qiu 2013). Nakazato et al. (2021) found that vertical mixing also plays an important role in causing IOD asymmetry in SST using a regional ocean model. Due to the Indo-Pacific interactions (Cai et al. 2019), IOD skewness is also modulated by the El Niño–Southern Oscillation (ENSO) (Schott et al. 2009; Xie et al. 2010b; Abram et al. 2020; An et al. 2023). ENSO's asymmetric influence can contribute to IOD asymmetry through ENSO–IOD interactions and ENSO's nonlinear teleconnection with the IOD (Cai et al. 2012; Le and Bae 2019; An et al. 2023).

1.3. Present-day simulations of IOD in CMIP models

Due to the short-term observing system in the Indian Ocean (Beal et al. 2020), a limited number of IOD events were relatively well observed and documented. The exploration of related climate processes within the Indian Ocean has faced substantial limitations, attributed to the lagging development of the Global Ocean Observing System in the Indian Ocean, in contrast to the strides made in the Pacific and Atlantic domains (Hermes et al. 2019; Beal et al. 2020). Consequently, researchers often rely on models to overcome this shortfall. CGCMs are important tools in deciphering climate variability and predicting future climate shifts in the Indian Ocean (Meehl 1995). Specifically, CGCMs generations involved in the Coupled Model Intercomparison Project (CMIP, Meehl et al. 1997; Meehl et al. 2007; Taylor et al. 2012; Eyring et al. 2016) are widely used to investigate the fundamental physical mechanisms of IOD and their possible responses to increasing greenhouse warming (Cai et al. 2013).

Among CMIP models, there are common mean-state biases that closely mimic the anomaly pattern of pIOD, referred to as mean-state positive IOD-like biases (Li et al. 2015; Long et al. 2020). The mean-state positive IOD-like biases are characterized by excessive precipitation and warm SST biases in the WTIO, deficient precipitation and cold SST biases in the ETIO, and easterly wind biases along the TIO (Long et al. 2020). Climate models that exhibit significant IOD-like biases tend to replicate larger IOD amplitude by modulating the related ocean-atmosphere coupling processes in the present-day simulations (Li et al. 2015). Using CMIP3 and CMIP5 models, Cai and Cowan (2013) pointed out that the larger simulation of the IOD amplitude is associated with the larger strength of the thermocline–SST feedback due to the unrealistic simulation of the climatological west-east slope of the equatorial thermocline.

Evaluating both the Bjerknes dynamic air-sea feedback and thermodynamical feedback, Liu et al. (2014) found that the thermocline response to surface wind forcing is more unrealistic, which contributes to larger IOD amplitude. In CMIP6, there is no substantial improvement in the IOD amplitude simulation, which has even slightly increased compared to the CMIP5 models (McKenna et al. 2020).

Despite the ability of theories and reanalysis datasets to provide insights into IOD extremes (Hong et al. 2008a; Webster et al. 1999), there has been only the 2019 extreme pIOD event that was relatively well observed and documented, supplemented by a limited number of normal IOD events that help to test our understanding. In CMIP5, most models generate too weak IOD skewness in the historical simulations, which is linked with the overly weak present-day westerlies in the contemporary mean state (Ng and Cai 2016). Models with larger mean-state easterly biases (Ng and Cai 2016) and weaker asymmetry of thermocline feedback (Ng et al. 2014) tend to produce smaller IOD asymmetry. In CMIP6, this underestimation remains. As shown by McKenna et al. (2020), a notable absence of systematic skewness across models prevails, with nearly half of CMIP6 models exhibiting negative Dipole Mode Index (DMI) skewness.

1.4. IOD Projections in CMIP models

Global warming, defined as the long-term rise in the average temperature of the Earth's climate system (IPCC 2013), has led to significant changes in climate patterns around the world (Armstrong Mckay et al. 2022). With the continuous emission of increasing greenhouse gases, the Earth's trajectory toward further warming remains inevitable. Despite a transient decline in carbon emissions due to the recent COVID outbreak, the pandemic's long-term impact remains uncertain (Tollefson 2020). Unraveling the possible changes in IOD under greenhouse warming is a critical concern in the field of climate science.

Existing observations and coral proxies show that IOD has been experiencing long-term changes over the past several decades (Abram et al. 2008; Ihara et al. 2008) and is anticipated to continue evolving in the future. However, there is no consensus yet on the future trajectory of IOD in the face of escalating global warming. The IOD's intimate connection with the tropical Indian mean climate upon which it evolves, underscores the necessity to discern potential changes in the Indian Ocean mean climate induced by greenhouse forcing. Over the latter half of the 20th century, the WTIO

warming intensified distinctly, even relative to other tropical ocean regions (Ihara et al. 2008). In parallel, most future projections conducted with coupled general circulation models consistently unveil a non-uniform warming trend spanning the 21st century within the Indian Ocean. This warming pattern manifests as enhanced warming in the northwestern Indian Ocean and relatively milder warming adjacent to the Sumatra-Java coast, forming a positive IOD-like warming pattern (Sharma et al. 2023). This non-uniform Indian Ocean warming pattern is accompanied by a weakening of the Indian Ocean Walker Circulation (Vecchi et al. 2006; Vecchi and Soden 2007; Sharma et al. 2022). Furthermore, the observed enhanced WTIO warming, as demonstrated by Abram et al. (2008), potentially amplifies the frequency and severity of IOD events. Ihara et al. (2008) stated that the faster warming ETIO during 1880–1919 is favorable for nIOD events and more pIOD events have tended to occur under the conditions of faster warming WTIO during 1960–2004. It has been observed that the induced stronger southeasterly winds contribute to the development of the 2019 extreme pIOD event (Wang et al. 2020a). However, a critical inquiry arises: are these patterns indicative of decadal variations or are they attributable to global warming?

Using CMIP5 models, most studies pointed out that the IOD asymmetry is projected to weaken in a warmer climate due to weaker asymmetry in the SST–thermocline relationship (Zheng et al. 2013; Cai et al. 2013; Ng et al. 2014), which is driven by the faster warming in the WTIO than ETIO and the slowdown of the Indian Walker circulation (Vecchi et al. 2006; Vecchi and Soden 2007). However, Cai et al. (2014) indicated that the frequency of extreme pIOD events will increase by almost a factor of three since the weakening equatorial westerly winds facilitate more frequent occurrences of wind and oceanic current reversal. Subsequently, the CMIP6 results showed that strong pIOD is projected to increase due to the faster surface warming in the WTIO, which favors atmospheric convection in the west and then strengthens equatorial nonlinear advection (Cai et al. 2021). In addition, the response of equatorial easterlies to SSTAs is anticipated to weaken due to the increased atmospheric stability (Zheng et al. 2013), which may affect the Ekman pumping (Webster et al. 1999) and reduce moderate pIOD events (Cai et al. 2021). These intricate interactions highlight the multifaceted nature of IOD responses in a changing climate, underscoring the significance of ongoing research to unravel the various layers of this complex puzzle.

In terms of the IOD amplitude, Zheng et al. (2010) stated that the opposite changes in the thermocline and atmospheric feedbacks result in little change of IOD variance in

the ensemble mean of climate model projections. Their subsequent results using CMIP5 models also support that the interannual variance of IOD remains largely unchanged in terms of SST (Zheng et al. 2013). Using CMIP5/6 models, Cai et al. (2021) show that moderate pIOD is projected to decrease due to the reduced Ekman pumping, while extreme pIOD would increase. However, model projections on future climates may be affected by present-day performances (Zhou and Xie 2015; Li et al. 2016; Wang et al. 2017; Wang et al. 2021). For instance, larger IOD amplitude simulation due to the mean-state positive IOD-like biases may generate a stronger IOD-like change pattern and increase extreme pIOD events in the future climate (Li et al. 2015; 2016). In addition, An et al. (2022) suggested that the intensity of IOD tends to increase as the CO_2 concentration increases, but at high CO_2 concentrations, further increases decrease the IOD intensity. Kim et al. (2024) found that IOD variability exhibits various responses to greenhouse warming on a century time scale, influenced by both internal and external factors, with millennial-scale projections indicating IOD weakening due to greenhouse warming. These aforementioned findings indicate that projected changes in IOD amplitude related to the altered background mean state in a warmer climate require further understanding.

1.5. Climatic impacts of IOD

During pIOD events, anomalous cooling in the ETIO leads to a sharp reduction in local evaporation, causing anomalous arid climates on the Maritime Continent and Australian mainland that last for several months and are susceptible to bushfires (Behera et al. 1999; Vinayachandran et al. 2007; Cai et al. 2009). Ummenhofer et al. (2009b) showed that significant droughts in Southeast Australia, including the “Big Dry” since 1995, the Federation Drought (1895-1902), and the World War II drought (1937-1945), are influenced by the Indian Ocean variability. Since 1950, 11 out of 21 severe fires have occurred after a pIOD event, which is because the pIOD has caused decreased precipitation and increased temperature in Southeast Australia, creating the conditions for the fires (Cai et al. 2009). On the other side, the WTIO experiences abnormal warmth during pIOD events, leading to enhanced atmospheric convective activity. This can trigger large-scale rainfall and flooding in Eastern Africa (Latif et al. 1999; Endo and Tozuka 2016; Palmer et al. 2023). In addition, the IOD can induce strong changes in the Indian Ocean troposphere, such as anomalous Walker circulation system,

southwest monsoon adjustment, and anomalous Hadley circulation in the Bay of Bengal (Jourdain et al. 2016; Ashok et al. 2004). For East Asia, Qiu et al. (2014) pointed out that a pIOD event induces an unusual amplification of autumnal southwesterly winds in China, thereby increasing water vapor and large-scale precipitation in South China. Paleoclimate research indicates that the severe drought in northern China from 1876 to 1878 was attributed to a strong El Niño and a strong pIOD (Singh et al. 2018; Yu et al. 2018). Recent observational data demonstrate that the 2019 record-breaking drought in the Mid-to-Lower Reaches of the Yangtze River was caused by both the 2019/2010 El Niño and the 2019 super pIOD (Xu et al. 2020). The 2020 Yangtze flooding was associated with the stronger anomalous anticyclone in the Philippines related to the 2019/2020 El Niño and significant Indian basin warming due to the super 2019 pIOD (Zhou et al. 2021). Moreover, the Indian Summer monsoon variability signals caused by the IOD can influence East Asia through "north" and "south" teleconnections (Liu and Ding 2008). Wave trains within the westerly wind jet stream can also link the IOD and East Asia climate (Enomoto et al. 2003; Ding and Wang 2005; Behera et al. 2013).

1.5.1. Eastern Africa

Eastern Africa primarily experiences two rainy seasons, the "long rains" from March to May and the "short rains" from October to December (OND), mainly due to the movement of the Intertropical Convergence Zone (ITCZ) (Gamoyo et al. 2015; Palmer et al. 2023). The short rains exhibit significant interannual variability related to the IOD and ENSO (Nicholson 2015; Collier et al. 2018). Since the mid-twentieth century, the Indian Ocean has been a crucial factor in Eastern Africa's rainfall variability (Chan et al. 2008; Nicholson 2015). The pIOD events tend to induce anomalously high precipitation during the short-rain season, but only those reversing the zonal SST gradient for several months trigger high rainfall (Black et al. 2003; Clark et al. 2003; Black 2005). The 2019 short rains in Eastern Africa, one of the wettest in recent decades, were attributed to the extreme 2019 pIOD event (Wainwright et al. 2021). The enhanced precipitation resulted from increased moisture convergence due to strong central African westerlies and equatorial TIO easterlies, coupled with increased regional convective activity (Ummenhofer et al. 2009a). Conversely, the 2021 nIOD event led to extremely dry conditions during the short-rain season, comparable to the severe drought events of 1996, 1998, 2005, and 2016 (Doi et al. 2022).

CMIP5 models tend to overestimate short-rain precipitation and underestimate long-rain precipitation in Eastern Africa (Tierney et al. 2015). Yang et al. (2015b) attributed the overestimated short rains to a bias in convective instability, primarily driven by the near-surface moisture static energy (MSE), which traces back to the warm SST bias in the WTIO. The warmer SSTs heat the boundary layer, inducing anomalous ascent that enhances rainfall over this region, which is opposite the climatological subsidence (Palmer et al. 2023). King et al. (2020) suggested that an underestimated Walker Circulation over the TIO is a key contributor to the overestimated short-rain bias in CMIP5. The combination of Walker Circulation bias (King et al. 2020), warm SST bias in the WTIO (Yang et al. 2015a, b), and zonal wind biases (Hirons and Turner 2018) could augment the moisture flux in Eastern Africa and contribute to the short-rain bias. Weller and Cai (2013) also mentioned that an overestimated IOD amplitude could contribute to the overestimated short rains, though this is not consistently shown across all CMIP5 models (Tierney et al. 2015).

Based on an atmospheric general circulation model (AGCM), Ummenhofer et al. (2009a) found that the WTIO SSTAs are the dominant driver for the East African short-rain variabilities, with the eastern pole of the IOD playing a lesser role. Results from regional model simulations also showed that SSTAs in the western Indian Ocean exert a stronger influence on the equatorial East African short rains than central and eastern Indian Ocean SSTAs both in terms of the coverage of significantly-changed precipitation and the magnitude of the precipitation response (Liu et al. 2020). Both the hybrid statistical-dynamical framework (Doi et al. 2022) and ensemble seasonal prediction systems (Lu et al. 2018), like SINTEX-F climate model (Behera et al. 2005), can predict the IOD's influence on East African short rains. However, the IOD simulations are still partial control of the forecast errors of short rains (Kolstad et al. 2021). Additionally, despite potential ENSO influences on short rains, the IOD-short rains relationship remains unchanged in the SINTEX-F model experiment, even with the removal of ENSO influence (Behera et al. 2005).

Contrary to 20th-century drying, CMIP5, CMIP6, and Coordinated Regional Downscaling Experiment (CORDEX) models predict increased precipitation during the short-rain season in the Horn of Africa due to anthropogenic warming (Palmer et al. 2023). However, these models, with parameterized convection, may underestimate extreme rainfall compared to a convection-permitting regional model that captures increased mean and extreme rainfall during short rains (Finney et al. 2020). The

projected rainfall enhancement is attributed to enhanced moisture convergence, associated with a strengthening of the continental low over southern Africa and the subtropical high over the South Indian Ocean, and a weakening of the eastern Sahara subtropical high (Palmer et al. 2023). A large-scale weakening of the TIO Walker circulation due to global warming also supports the projected rainfall increase (Tierney et al. 2015). Under these changing conditions, the IOD is expected to have a stronger correlation with rainfall over the Horn of Africa and a weaker one with rainfall over the southern part of Eastern Africa (Endris et al. 2019). The intensified hydrological cycle under a warmer climate is likely to enhance rainfall in the Horn of Africa, even without an IOD change. Additionally, its future rainfall projection is linked with the IOD amplitude and its present-day climate rainfall teleconnection (Weller and Cai 2013). However, limitations in model representations of key processes and climatology (Lyon 2020; 2021) and an unrealistic dominance of the TIO Walker circulation (King et al. 2020), cast doubts on these rainfall projections.

1.5.2. Australia

Australian weather and climate are significantly influenced by the IOD, ENSO and SAM (Holgate et al. 2022). In terms of the IOD, Ashok et al. (2003) found negative correlations between IOD and rainfall in western and southern Australia from June to September. This is due to anomalous anticyclonic circulation caused by IOD over the eastern Indian Ocean and Australia. IOD events also impact South Australian rainfall by affecting westerlies and storm-track activity (Ashok et al. 2007; Weller et al. 2012). However, England et al. (2006) stated no straightforward relationship between IOD and interannual variability in southwest Western Australia rainfall. As for temperature, IOD events show a stronger correlation with surface air temperature in austral spring, with warmer temperatures during pIOD and colder temperatures during nIOD (Saji and Yamagata 2003; Saji et al. 2005). Observations and atmospheric models indicate that IOD affects the austral subtropics through Rossby-wave propagation (Saji et al. 2005). Additionally, the Indian Ocean serves as a pathway for ENSO's impact on southeast Australia in austral spring, with two wave trains originating from the east and west poles of IOD (Cai et al. 2011). McIntosh and Hendon (2018) noted that the Rossby wave along the subtropical jet is inhibited across the South of Australia, while another Rossby wave along the eddy-driven jet appears to emanate upstream of Australia into the Pacific sector of the Southern Ocean. Nevertheless, during pIOD events, extremely

low minimum temperatures decrease in northern and eastern Australia due to cold advection from an anomalous anticyclone and increased radiative cooling at night-time due to reduced cloud cover (Lim et al. 2021). Early austral spring maximum temperatures are influenced by low-level wind changes which are more related to the SAM, while late spring maximum temperatures are more linked to warming via subsidence which is more related to tropical variability because of the breakdown of the subtropical jet (McKay et al. 2022).

Using MPI-ECHAM5 simulations, Fan et al. (2016) proposed a stronger correlation between Australian precipitation and SSTAs over the Indo-Pacific warm pool. The present-day simulations of the IOD teleconnections in Australia are systematically weaker than the observed and this may stem from the mean state biases in the Indian and western Pacific Oceans (Lim et al. 2021). Compared to CMIP5, the multi-model average of CMIP6 shows improved simulations of IOD teleconnections to Australia, but they still underestimated these IOD teleconnections, despite an overestimation of the IOD amplitude (Chung et al. 2023). This discrepancy underscores the challenges in accurately simulating the complex interactions between the IOD and Australia's climate and suggests that further research is needed to understand and correct these biases.

1.6. Objectives and framework

This study examines IOD asymmetry in observations and CMIP6 models, with a specific focus on historical simulations and projected changes. Section 2 outlines the data and methods used. Section 3 presents the IOD asymmetry in observations and its potential factors. Section 4 demonstrates the historical performance of CMIP5/6 models in simulating IOD asymmetry and related dynamical processes. Understanding the impact of mean-state biases on simulated IOD skewness can enhance climate projections in IOD-affected regions. Although previous studies have pointed out some reasons for the biases in simulated IOD skewness, the exact mechanisms of underestimated IOD skewness remain uncertain. Additionally, previous findings are mostly based on CMIP5 models and the performance of IOD skewness in CMIP6 models needs further research. This study's primary objective is to evaluate whether CMIP6 models demonstrate improvements in replicating IOD skewness compared to CMIP5 models. While McKenna et al. (2020) previously assessed the performance of IOD skewness in CMIP5 and CMIP6 models, our study focuses more on the origins

behind the underestimation of IOD skewness. This study will explore the specific processes influencing IOD skewness simulation in CMIP6 models compared to CMIP5 models, contributing to a comprehensive understanding of this crucial climate variable.

Section 5 is the projected changes of IOD asymmetry under the Shared Socio-economic Pathway 5 (SSP5-8.5) scenario simulations (O'Neill et al. 2016; Riahi et al. 2017). Understanding the future evolution of IOD asymmetry under greenhouse warming relies on key factors such as changes in the Indian Ocean mean state, modifications in nonlinear processes that interplay with the mean Indian Ocean climate, and by extension, the broader global climate landscape. Various simulations of future IOD responses can be explained by the fact that IOD asymmetry essentially arises from an imbalance between positive and negative feedback processes (Hong et al. 2008a). Previous research about future IOD skewness has mainly emphasized the reduced asymmetry of thermocline feedback (Zheng et al. 2013; Ng et al. 2014). This study's primary objective rests upon unveiling the expected shifts in IOD asymmetry and NDH using CMIP6 simulations. Moreover, previous investigations largely concentrated on extreme pIOD events which are projected to be more frequent under global warming (Cai et al. 2014, 2021). The study links the reduced IOD asymmetry with the increased extreme nIOD events. Section 6 investigates the IOD's pattern response to global warming. Previous studies primarily focused on the IOD amplitude in the whole TIO or ETIO region. This study aims to go into detail, exploring changes in the IOD pattern and the driving mechanisms within CMIP6 simulations. Predicted alternations in the IOD pattern could influence atmospheric teleconnections and further regulate its climate impacts on land.

Section 7.1–7.3 focuses on the precipitation and surface air temperature responses to IOD events in Eastern Africa using CMIP6 historical and SSP5-8.5 scenario simulations. Prior research has largely analyzed the effects of IOD events through observational studies with a limited sample size (Guan and Yamagata 2003; Cai et al. 2009). Despite recognition of the profound influence of IOD on East African short rains (Ummenhofer et al. 2009a; Liu et al. 2020), the efficacy of CMIP6 models in capturing these responses, along with the underlying physical processes, remains ambiguous. This study investigates the overestimated simulations of East African short-rain responses to IOD events, linking them to the larger IOD amplitude and the overestimated mean state of short rains. On the other hand, although there is a consensus regarding human influence on Eastern Africa's short rains (Nicholson et al. 2015), the anthropogenic

impact on related physical processes, such as projected IOD changes and their influence on future short rains (Thielke and Mölg 2019; Blau and Ha 2020), is less clear. Additionally, previous research has examined the projected rainfall response changes in Eastern Africa using CMIP5 models, with a focus on extreme pIOD events (Cai et al. 2014). With global warming, extreme nIOD events are projected to increase in frequency, yet their impact on Eastern Africa's short-rain characteristics is yet to be determined. Hence, this section will explore these projected changes and their connection with IOD changes, emphasizing the increased drought risk associated with more frequent extreme nIOD events in a warmer climate.

Additionally, Section 7.4 explores the IOD's climatic impacts on Australia. Besides the modulation of the Walker Circulation, the IOD-induced Rossby wave trains serve as significant conduits between the tropics and higher latitudes (Saji et al. 2005). The IOD's teleconnections to Australia remain a focal point in IOD research. This study re-examines the IOD's influence on Australia in observations and assesses the historical simulations and future projections of these teleconnections utilizing CMIP6 models. Finally, Section 8 concludes this study, highlighting existing knowledge gaps and proposing directions for future research.

2. Data and methods

2.1. Observation/Reanalysis datasets

Monthly precipitation is obtained from the NASA/GSFC Global Precipitation Climatology Project (GPCP) Version 2.3 (Adler et al. 2003, 2018). GPCP combines rainfall data from a variety of satellite, sounding, and terrestrial stations to provide the most complete analysis of global rainfall to date. In addition to rainfall data, the GPCP also provides rainfall uncertainty estimates. It is spatially resolved to 2.5° × 2.5°. The European Center for Medium-Range Weather Forecasts (ECMWF) Reanalysis v5 (ERA5) monthly mean meteorological data is the fifth generation of its Global Climate Atmosphere Reanalysis (Hoffmann et al. 2019). Compared with ERA-Interim, the ERA5 dataset incorporates more satellite observations with improved spatial and temporal resolution. In this study, we select the surface heat flux, 2-meter temperature, vertically integral of mass tendency, vertically integral of water vapor flux, specific humidity and upper-air wind with a resolution of 0.25° × 0.25°. When exploring the IOD identification in Section 2.4, atmospheric wind from NCEP-NCAR Reanalysis 1 is also used (Kalnay et al. 1996). The surface level pressure (SLP) data are also taken from the NCEP-NCAR Reanalysis 1. Additionally, Extended Reconstructed Sea Surface Temperature Version 5 (ERSST V5) is also used (Huang et al. 2017) in Section 2.4. The 3-month standardized precipitation evapotranspiration index (SPEI) is taken from the SPEIbase v.2.9 (Beguería et al. 2023).

Monthly mean ocean reanalysis data including potential temperature, salinity, three-dimensional ocean current and sea surface height are taken from the Global Ocean Data Assimilation System (GODAS) (Behringer et al. 1998). GODAS is based on a quasi-global configuration of the Geophysical Fluid Dynamics Laboratory's Modular Ocean Model version 3. The model domain extends from 75°S to 65°N and has a resolution of 1° by 1° enhanced to 1/3° in the N-S direction. The model has 40 levels with a 10-meter resolution in the upper 200 meters. It is forced by the momentum flux, heat flux and freshwater flux from the NCEP atmospheric Reanalysis 2. GODAS assimilates temperature profiles and synthetic salinity profiles as well. When comparing the GODAS dataset and the historical simulations from CMIP models, the study period spans from 1980 to 2020, with anomalies computed as deviations from the detrended climatology for the same period. Monthly anomalies are also de-trended.

2.2. CMIP datasets

The monthly mean outputs from 34 CMIP5 (Taylor et al. 2012) and 31 CMIP6 (Eyring et al. 2016) are used in this study because the required variables (oceanic and atmospheric) and experiments are available. Then, due to the better simulation of IOD, 24/34 CMIP5 models and 20/31 CMIP6 models are selected for further research. When certain models feature multiple realization members, we only analyzed the first realization member (r1i1p1 for CMIP5 and r1i1p1f1 for CMIP6) run of each model. Numerous parameters are extracted from the CMIP5/6 dataset, spanning SST (tos in the data archives), wind (ua, va), sea surface height (zos), surface air temperature (tas), surface heat fluxes (hfds, hfls, hfss, rsus, rsds, rlus, rlds), precipitation (pr), specific humidity (hus), air temperature (ta), omega (wap), ocean potential temperature (thetao), salinity (so), and three-dimensional ocean currents (uo, vo, wo or wmo). In the historical simulations, 1950–2005 and 1950–2014 are chosen for the CMIP5 and CMIP6 models, respectively. In future change research, 1950–1999 for historical runs and 2050–2099 for the SSP5-8.5 scenario simulations are chosen among the CMIP6 models. The vertical velocity (wo) is not provided in the CMIP5 models, and it thus is computed by dividing the vertical mass transport (wmo) by the horizontal area of a grid cell and reference density (1035 kg m^{-3}) (Griffies et al. 2009). For some CMIP6 models (historical run in the BCC-CSM2-MR model; SSP5-8.5 simulations in the BCC-CSM2-MR, EC-Earth3-CC, EC-Earth3-Veg and EC-Earth3 models), the vertical velocity is not provided but the vertical mass transport is provided, and therefore the vertical velocity is computed through the vertical mass transport. In addition, the vertical velocity in the CIESM, CMCC-CM2-SR5, KIOST-ESM and TaiESM1 models in CMIP6 is calculated using the continuity equation. All the ocean and atmosphere outputs are firstly interpolated onto a uniform spatial grid of 1°×1° horizontal resolution before analysis. The anomalies in the historical (SSP5-8.5 scenario) simulations correspond to the climatological reference period of 1950–1999 (2050–2099). To eliminate the influence of decadal and longer-term climate variability, a high-pass filter is applied to all physical variables, thereby retaining variations characterized by periods of less than 9 years.

CMIP6 Model	Ocean	Atmosphere	Land
ACCESS-ESM1-5	ACCESS-OM2	HadGAM2	CABLE2.4
BCC-CSM2-MR	MOM4	BCC_AGCM3_MR	BCC_AVIM2
CAMS-CSM1-0	MOM4	ECHAM5_CAMS	CoLM 1.0

CAS-ESM2-0	LICOM2.0	IAP AGCM 5.0	CoLM
CESM2-WACCM	POP2	WACCM6	CLM5
CIESM	CIESM-OM	CIESM-AM	CIESM-LM
CMCC-CM2-SR5	NEMO3.6	CAM5.3	CLM4.5
CMCC-ESM2	NEMO3.6	CAM5.3	CLM4.5
E3SM-1-1	MPAS-Ocean	EAM	ELM
EC-Earth3-CC	NEMO3.6	IFS cy36r4	HTESSEL and LPJ-GUESS v4
EC-Earth3-Veg-LR	NEMO3.6	IFS cy36r4	HTESSEL and LPJ-GUESS v4
EC-Earth3-Veg	NEMO3.6	IFS cy36r4	HTESSEL and LPJ-GUESS v4
EC-Earth3	NEMO3.6	IFS cy36r4	HTESSEL
FGOALS-f3-L	LICOM3.0	FAMIL2.2	CLM4.0
FGOALS-g3	LICOM3.0	GAMIL3	CAS-LSM
FIO-ESM-2-0	POP2-W	CAM4	CLM4.0
KIOST-ESM	GFDL-MOM5.0	GFDL-AM2.0	NCAR-CLM4
MRI-ESM2-0	MRI.COM4.4	MRI-AGCM3.5	HAL 1.0
NESM3	NEMO v3.4	ECHAM v6.3	JSBACH v3.1
TaiESM1	POP2	TaiAM1	CLM4.0

Table 2.1. The selected CMIP6 models.

2.3. Methods

(1) Empirical Orthogonal Function

Empirical Orthogonal Function (EOF) decomposition, also known as orthogonal decomposition and natural orthogonal function decomposition, is comparable to Principal Component Analysis in terms of its fundamental ideas and computational approaches. Lorenz (1956) was the first to introduce EOF decomposition to climate studies in the 1950s. The EOF decomposition is widely used to extract the dominant spatial modes and the related time variations. The main idea is to achieve "separation of time and space" by linearly combining orthogonal temporal and spatial functions from a matrix $(m \times n)$, where m is the number of spatial positions and n is the number of observations. The primary information of the elements can be effectively represented by the EOF analysis while keeping the secondary information and removing random interference, which facilitates data processing.

The Season-reliant EOF (S-EOF) analysis is used to describe element variability with emphasis on its seasonal-dependent evolution. The fundamental premise of S-EOF is that the climatological annual cycles may dramatically affect an element's interannual variability. The idea of S-EOF is illustrated in terms of analysis of the year-to-year

variations of the element with special interest in the seasonally evolving pattern from one year to another (Wang and An 2005). Instead of analyzing a single seasonal mean value for each year or all seasons, the S-EOF examines the element in a seasonal sequence $(m \times nm) \times yr$, where nm is the number of selected months and yr is the number of years. The derived spatial pattern for each S-EOF mode will contain sequential patterns representing the seasonal evolution of the element, sharing the same yearly value in their corresponding principal component.

(2) Mixed layer heat budget

Heat budget analysis has been used to identify the contributions of the dynamic and thermodynamic processes to the IOD growth (Cai et al. 2021; Wang et al. 2020a). The upper-ocean heat budget is computed as the balance between the heat storage term, surface heat flux terms, oceanic horizontal advection terms and the oceanic entrainment. This computation is executed within a layer, typically chosen as the mixed layer. Therefore, the mixed-layer temperature (MLT) budget is outlined as follows (de Boyer Montégut et al. 2007):

$$\frac{\partial T'}{\partial t} = Q' - (u\frac{\partial T}{\partial x} + v\frac{\partial T}{\partial y})' - (w\frac{T - T_{-h}}{h})' - [(u\frac{\partial h}{\partial x} + v\frac{\partial h}{\partial y})\frac{T - T_{-h}}{h}]' - (\frac{\partial h}{\partial t}\frac{T - T_{-h}}{h})' + \mathrm{Res} \quad (1),$$

where *T*, *u*, and *v* are the ocean potential temperature, zonal and meridional ocean current velocities averaged over the mixed layer, respectively. *w* is the vertical ocean current velocity at the MLD. Primes indicate anomalies from the climatological state. Subscript (–*h*) represents values below the base of the mixed layer. MLD (*h*) is defined as the depth of a layer with a difference in potential density from the surface value and the potential density calculated by a 0.5 °C decrease in SST (Kara et al. 2000). The budget term on the left-hand side of Eq. (1) is the MLT tendency. Generally, the heating rate within the mixed layer is balanced by the net heat flux, horizontal advection and mixing, and subsurface processes (vertical advection, lateral induction, entrainment due to MLD tendency and subsurface mixing). The mixing is not taken into account due to the difficulty of measuring mixing. On the right-hand side of Eq. (1), there is the net heat flux, horizontal advection, vertical advection, lateral induction, entrainment due to MLD tendency, and residual term (Res). The *Q* term is the sum of latent heat flux, sensible heat flux, shortwave heat flux, and longwave heat flux at the air-sea interface, divided by the product of a reference density of 1026 kg m^{-3}, the specific heat capacity

of seawater (3986 J kg^{-1} K^{-1}) and the MLD. Any unresolved processes and other higher-order perturbations are typically included in the residual term. Estimation errors from different datasets also contribute to the residual term.

The horizontal and vertical advection components can be further decomposed into:

$$-(u\frac{\partial T}{\partial x}+v\frac{\partial T}{\partial y})'=-(\bar{u}\frac{\partial T'}{\partial x}+u'\frac{\partial \bar{T}}{\partial x}+u'\frac{\partial T'}{\partial x})-(\bar{v}\frac{\partial T'}{\partial y}+v'\frac{\partial \bar{T}}{\partial y}+v'\frac{\partial T'}{\partial y}) \quad (2),$$

$$-(w\frac{T-T_{-h}}{h})'=-[\bar{w}(\frac{T-T_{-h}}{h})'+w'\frac{\overline{T-T_{-h}}}{h}+w'(\frac{T-T_{-h}}{h})'] \quad (3),$$

in which the overbar denotes long-term averaged quantities. The NDH includes nonlinear zonal advection $[-u'(\partial T'/\partial x)]$, nonlinear meridional advection $[-v'(\partial T'/\partial y)]$ and nonlinear vertical advection $\{-w'[(T-T_{-h})/h]'\}$, while linear dynamical heating (LDH) is the sum of the remaining terms, excluding the nonlinear part. Abbreviations for the budget terms on the RHS of Eq. 2 from left to right are umta, uatm, uata, vmta, vatm, and vata, and those for RHS of Eq. 3 are referred to as wmta, watm, and wata.

The lateral induction can be decomposed into:

$$-(u\frac{\partial h}{\partial x}\frac{T-T_{-h}}{h})'=-[\overline{u\frac{\partial h}{\partial x}}(\frac{T-T_{-h}}{h})'+(u\frac{\partial h}{\partial x})'\frac{\overline{T-T_{-h}}}{h}+(u\frac{\partial h}{\partial x})'(\frac{T-T_{-h}}{h})'] \quad (4),$$

$$-(v\frac{\partial h}{\partial y}\frac{T-T_{-h}}{h})'=-[\overline{v\frac{\partial h}{\partial y}}(\frac{T-T_{-h}}{h})'+(v\frac{\partial h}{\partial y})'\frac{\overline{T-T_{-h}}}{h}+(v\frac{\partial h}{\partial y})'(\frac{T-T_{-h}}{h})'] \quad (5),$$

with the third term in each equation being nonlinear. RHS of Eq. 4 terms are referred to as lateral-umta, lateral-uatm, and lateral-uata, and those for Eq. 5 are lateral-vmta, lateral-vatm, and lateral-vata.

(3) Convective response

Following Ham (2017), the precipitation response to SST changes is used as a representation of the convective response. Here the climatological precipitation is first binned based on the background SST within 45°E–110°E, 15°S–10°N. Then, the anomalous precipitation response by changing SST is calculated with respect to background SST. For a positive SSTA, the convective response is calculated by $P'_{+}=\mathrm{Pr}(T+0.5℃)-\mathrm{Pr}\,(T)$, where $\mathrm{Pr}\,(T)$ is the binned value of precipitation with respect to SST. Similarly, for a negative SSTA, the convective response is given by $P'_{-}=\mathrm{Pr}(T-0.5℃)-\mathrm{Pr}\,(T)$. The net response is the sum of the convective responses

to positive and negative SSTA ($Pr'_+ + Pr'_-$), which reflects the asymmetry of precipitation changes to SSTAs.

(4) Emergent constraint

The concept of an emergent constraint offers a valuable tool to mitigate the uncertainty inherent in Earth System Models (ESMs) (Cox et al. 2013; Huang and Ying 2015; Lian et al. 2018). The basic concept is that, despite disparities among ESMs, there are various robust one-to-one relationships (emergent constraints) that emerge when the multi-model outputs are analyzed. Typically, the first variable is a quantity of key importance that describes the functioning of the Earth system, but with an unknown true value. In contrast, the second diagnostic variable often might be a quantity for which measurements are available (Lian et al. 2018). From this, it is possible to use measurements of the second variable, via the emergent constraint, to constrain the first quantity. Following Huang and Ying (2015), we first define the historical simulated biases as $P(m)' = P(m) - P_{obs}$, in which $P(m)$, P_{obs} and m are the model value, observational value and model number, respectively. Subsequently, an unknown quantity $C(s,m)$ is introduced, signifying the change due to climate change, where s is location and may not be applicable in all cases. Establish a statistical relationship between P and C: $C(s,m) = a(s) \times P(m) + b(s) + \varepsilon(s,m)$, in which $a(s)$ and $b(s)$ are coefficients, while $\varepsilon(s,m)$ represents an error term. Later, use simulated P biases combined with statistical relationship to estimate the C biases: $C(s,m)' = a(s) \times P(m)'$, and this is a strong assumption. The corrected model values are then computed as $C(s,m)^* = C(s,m) - C(s,m)'$. Since the sum of residual is 0, ε is eliminated so that the corrected multi-model ensemble (MME) value is by $\overline{C(s,m)^*} = \frac{1}{N}\sum_{m=1}^{N} C(s,m)^* = a(s) \times P_{obs} + b(s)$. This method effectively leverages observed data and statistical relationships to enhance the accuracy of ESMs by estimating unknown quantities and refining model-derived outputs.

(5) Skewness

The degree of asymmetry in the anomalous field is measured by the normalized statistical third moment, represented as $E(x-\mu)^3/\sigma^3$, where μ denotes the mean of data x, σ is the standard deviation (STD) of data x, and $E(x-\mu)^3$ represents the expected value of $(x-\mu)^3$ (Mardia 1980). When the skewness is negative, the data

distribution tends to extend further to the left of the mean compared to the right. Conversely, a positive skewness implies a tendency for the data to extend more towards the right. Skewness towards high values indicates that occurrences of high extremes are more likely than low extremes (Burgers and Stephenson 1999). Observed IOD exhibits significant amplitude asymmetry with stronger pIOD events than nIOD events, manifesting positive skewness of the first principal component (PC1) of EOF or DMI. When focusing on the eastern core of IOD, a positively skewed PC1 generally corresponds to negative SSTA skewness across the ETIO.

(6) Ocean stratification calculation

The ocean stratification is defined as the squared buoyancy frequency (Jones 1995):

$$N^2 = g[-(\frac{1}{\rho})(\frac{\partial \rho_p}{\partial z})] \qquad (6),$$

where g, ρ and ρ_p denotes gravity acceleration, seawater density and potential density. The static stability and buoyancy frequency increase proportionally with the stratification of the water column (Li et al. 2020).

(7) Moisture budget

The first widely accepted water vapor budget theory was proposed by Budyko (1974), which quantified the relative contributions of water vapor transport and local evaporation to local precipitation based on the principle of conservation of water vapor mass in the atmosphere. Previous studies (Brubaker et al. 1993; Li et al. 2013) showed that in large-scale studies, local precipitation can be roughly balanced with external water vapor transport and local evaporation. Here, the moisture budget analysis (Trenberth and Guillemot 1995) is notated as

$$P - E = -\frac{\partial \langle q \rangle}{\partial t} - \left\langle \nabla \bullet \left(q\vec{V} \right) \right\rangle = -\frac{\partial \langle q \rangle}{\partial t} - \left\langle \frac{\partial u_2 q}{\partial x} + \frac{\partial v_2 q}{\partial y} \right\rangle \qquad (7),$$

$$\langle q \rangle = \frac{1}{g\rho_w} \int_0^{p_s} q dp \qquad (8),$$

where $\langle q \rangle$ means the total precipitable water. P and E are the precipitation and evaporation. $\vec{V}$ is the atmospheric wind vector. u_2 and v_2 are the zonal and meridional wind velocities. g, ρ_w, p_s and q are the gravitational acceleration, water density, surface pressure and specific humidity, respectively. The left-hand side denotes

the freshwater forcing. The right-hand side terms of Eq. 7 represent the local derivation of the vertically integrated moisture and the convergence of vertically integrated moisture flux (CVIMF).

The anomaly of vertically integrated moisture convergence is defined as follows:

$$-\left\langle \nabla\bullet\left(q\vec{V}\right)\right\rangle' = -\left[\left\langle \nabla\bullet\left(\overline{q}\vec{V}'\right)\right\rangle + \left\langle \nabla\bullet\left(q'\overline{\vec{V}}\right)\right\rangle + \left\langle \nabla\bullet\left(q'\vec{V}'\right)\right\rangle\right] \qquad (9).$$

Terms on the right-hand side of Eq. 9 represent the dynamic effect, the thermodynamic effect and the nonlinear effect, respectively. The nonlinear effect is generally a minimal contributor on the interannual time scale.

The dynamic and thermodynamic effect changes due to greenhouse warming can be divided into (Huang and Xie 2015; Wang et al. 2020b):

$$\begin{aligned}
-\Delta\left\langle \nabla\bullet\left(\overline{q}\vec{V}'\right)\right\rangle &= -\left[\left\langle \nabla\bullet\left(\overline{q}_S\overline{V_S}'\right)\right\rangle - \left\langle \nabla\bullet\left(\overline{q}_H\overline{V_H}'\right)\right\rangle\right] \\
&= -\left[\left\langle \nabla\bullet\left(\overline{q}_S\overline{V_S}'\right)\right\rangle - \left\langle \nabla\bullet\left(\overline{q}_H\overline{V_H}'\right)\right\rangle + \left\langle \nabla\bullet\left(\overline{q}_H\overline{V_S}'\right)\right\rangle - \left\langle \nabla\bullet\left(\overline{q}_H\overline{V_S}'\right)\right\rangle\right] \\
&= -\left\langle \nabla\bullet\left[\overline{q}_H\left(\overline{V_S}'-\overline{V_H}'\right)\right]\right\rangle - \left\langle \nabla\bullet\left[\overline{V_S}'\left(\overline{q}_S-\overline{q}_H\right)\right]\right\rangle \\
&= -\left\langle \nabla\bullet\left(\overline{q}_H\Delta\vec{V}'\right)\right\rangle - \left\langle \nabla\bullet\left(\overline{V_S}'\Delta\overline{q}\right)\right\rangle
\end{aligned} \qquad (10),$$

$$\begin{aligned}
-\Delta\left\langle \nabla\bullet\left(q'\overline{\vec{V}}\right)\right\rangle &= -\left[\left\langle \nabla\bullet\left(q_S'\overline{\overline{V_S}}\right)\right\rangle - \left\langle \nabla\bullet\left(q_H'\overline{\overline{V_H}}\right)\right\rangle\right] \\
&= -\left[\left\langle \nabla\bullet\left(q_S'\overline{\overline{V_S}}\right)\right\rangle - \left\langle \nabla\bullet\left(q_H'\overline{\overline{V_H}}\right)\right\rangle + \left\langle \nabla\bullet\left(q_S'\overline{\overline{V_H}}\right)\right\rangle - \left\langle \nabla\bullet\left(q_S'\overline{\overline{V_H}}\right)\right\rangle\right] \\
&= -\left\langle \nabla\bullet\left[\overline{\overline{V_H}}\left(q_S'-q_H'\right)\right]\right\rangle - \left\langle \nabla\bullet\left[q_S'\left(\overline{\overline{V_S}}-\overline{\overline{V_H}}\right)\right]\right\rangle \\
&= -\left\langle \nabla\bullet\left(\overline{\overline{V_H}}\Delta q'\right)\right\rangle - \left\langle \nabla\bullet\left(q_S'\Delta\overline{\vec{V}}\right)\right\rangle
\end{aligned} \qquad (11),$$

where subscript (*H*) represents historical value and subscript (*S*) represents SSP5-8.5 value. The right-hand side terms of Eq. 10 are changes due to IOD-related wind circulation anomaly changes and mean-state moisture changes. The right-hand side terms of Eq. 11 are changes due to IOD-related moisture anomaly changes and mean-state wind circulation changes. These equations can diagnose historical precipitation anomaly biases compared to the observations by substituting *H* with *O* and *S* with *H*.

(8) Rossby wave

The Rossby wave source (RWS) is given by (Sardeshmukh and Hoskins 1988):

$$F' = -\overline{\zeta}D' - \vec{V}_\chi'\bullet\nabla\overline{\zeta} \qquad (12),$$

where ζ is the absolute vorticity, D is the wind divergence and $\vec{V}_\chi$ is the divergent wind. The first term is the vortex stretching term and the second term is the advection of the mean absolute vorticity by the anomalous divergent wind (McIntosh and Hendon 2018).

(9) Statistical analysis

The proximity of the two elements can be evaluated using correlation analysis, which mostly reflects their linear relationship. In this thesis, the Pearson correlation is calculated. It should be noted that the Pearson correlation analysis will be impacted by the distribution characteristics and extreme values of the data. Secondly, the correlation coefficient can only indicate how much one variable can be explained by another; it cannot demonstrate physically that the change in one variable is caused by the change in the other. The t-statistic is typically used to assess the correlation coefficient's significance.

A bootstrap method (Efron and Gong 1983; Efron 1987) is used to examine whether the frequency change of extreme nIOD is statistically significant. The procedure involves the random resampling of IOD samples derived from the selected CMIP6 models. This resampling process generates a total of 10,000 realizations, enabling a comprehensive evaluation of the underlying statistical characteristics. Importantly, the resampling process allows for the selection of extreme nIOD events to be repeated.

2.4. Model selection

2.4.1. IOD identification in observations

DMI is frequently utilized to identify the IOD cases in observations. DMI is defined by the SST difference between the western Indian Ocean (50°E–70°E, 10°S–10°N) and the eastern Indian Ocean (90°E–110°E, 10°S–0°) (Saji et al. 1999). SST is a core variable for IOD, as it is the main way through which ocean-atmosphere feedbacks are mediated. Other variables are also used to determine IOD, such as the zonal wind index averaged over the central TIO (60°E–90°E, 5°S–5°N) (Gadgil et al. 2004) and the sea level anomaly (SLA) index averaged over the southeastern Indian Ocean (90°E–110°E, 10°S–0°) (Deshpande et al. 2014) (Fig. 2.1a). Generally, DMI can capture the IOD events in observation, although sometimes it is better to both consider zonal wind and SSH indices. Note that DMI may not yield the maximum intensity of IOD, and it may

not include some IOD events with shorter lifetimes (Du et al. 2013), such as the 2007 IOD event. As for EOF analysis, EOF1 of detrended SSTAs (20°S–20°N, 40°E–120°E) shows the Indian Ocean Basin (IOB) mode (Fig. 2.2a) and the EOF2 can represent the IOD in long-term reanalysis data (Fig. 2.1b, 2.2b). Sometimes, EOF can't separate IOB and IOD when using short-term SST data. If just focusing on the developing and mature phases of IOD, the EOF1 of SSTAs during JJASON seems like an IOD pattern, but EOF2 also seems like the eastern part of IOD (not shown), suggesting that this may be not a good way to identify IOD cases. Compared to SST, SLA reflects more ocean dynamics and may have fewer disturbances from the atmosphere. The EOF1 of SLA (10°S–5°N, 45°E–110°E) can represent the IOD with a high contribution rate (Fig. 2.1b, 2.2d) and it can be used to select IOD events.

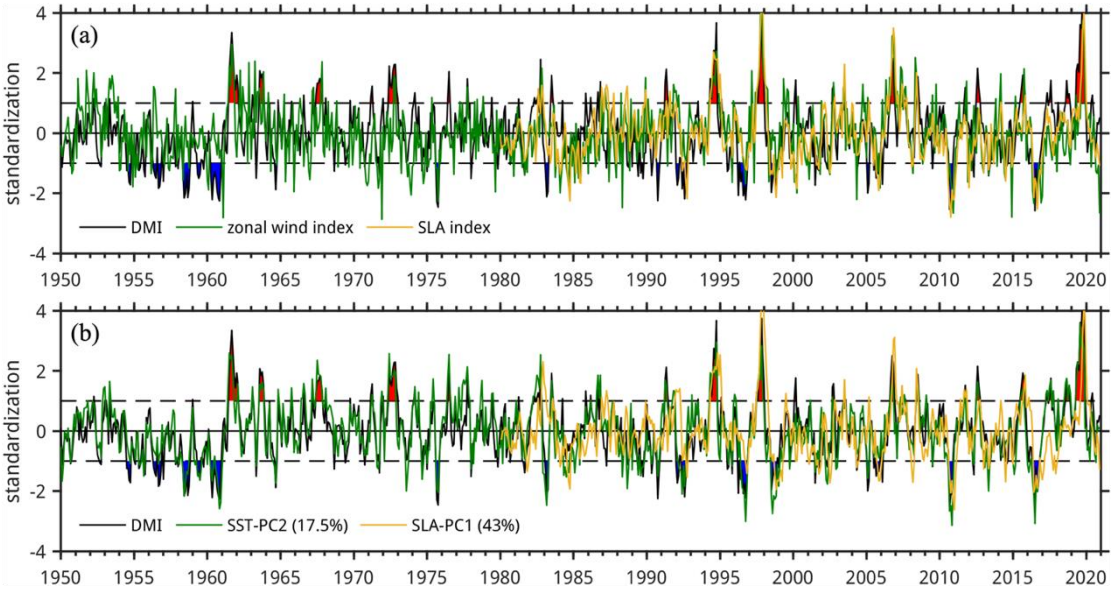


Figure 2.1. Standardized IOD indices. (a) DMI (black line; dataset: ERSST), zonal wind index (green line; dataset: NCEP/NCAR), and SLA index (yellow line; dataset: GODAS). (b) DMI (black line, dataset: ERSST), PC2 of SST (green line, dataset: ERSST), and PC1 of SLA (yellow line, dataset: GODAS). Red (blue) shading is that the DMI is larger (smaller) than 1 (–1) STD.

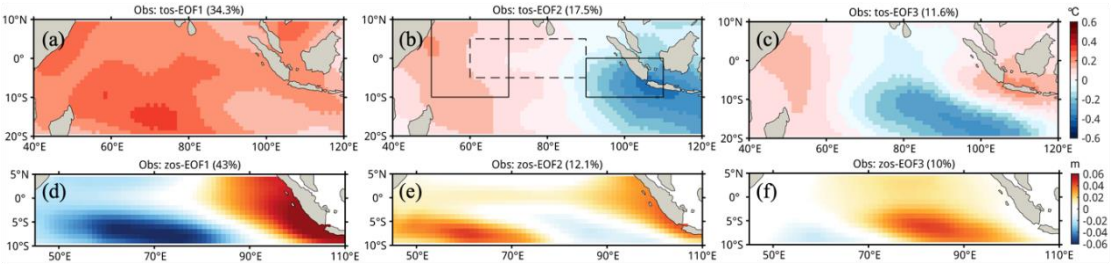


Figure 2.2. EOF1 to EOF3 patterns of (a, b, c) SSTA (ERSST, 1950–2020) and (d, e, f) SLA (dataset: GODAS, 1980–2020). The dashed box is 5°S–5°N, 60°–90°E. The solid

box in the western (eastern) Indian Ocean is 10°S–10°N, 50°–70°E (10°S–0°, 90°–110°E).

S-EOF analysis is suitable for detecting the evolutionary or propagative patterns of a given climate mode that has distinct seasonality by strongly interacting with the annual cycle (Wang and An 2005). IOD is a seasonally dependent mode that is phase-locked to the annual cycle and the Asian monsoon (Saji and Yamagata 2003). To focus on the IOD mode and evaluate the relationship between IOD and ENSO, Yang et al. (2015) applied S-EOF to equatorial (40°E–120°E, 5°S–5°N) thermocline depth anomalies because IOB barely involves ocean dynamics in this region. S-EOF of SLA is also useful to identify the IOD events in observation (not shown). Likewise, the S-EOF of SSTA during JJASON can be used to detect the IOD development and extract the IOD mode. Although S-EOF captures a series of fixed seasonally evolving patterns at the cost of temporal resolution, S-EOF during JJASON reduces the influences from other months and catches the IOD development, which is better than the EOF that assigns the same weight to each month. S-EOF1 in Fig. 2.3a represents the growth of the IOD with a high contribution rate of 31.9% compared to the EOF2 of SST in Fig. 2.2b. The period of the S-EOF1 is about 3–4 years (Fig. 2.3d). This can be partly related to the ENSO forcing, which has multiple cycles, such as quasi 2- and 4-5-year interannual variability (Yang et al. 2015). S-EOF2 and S-EOF3 are not the basic climate modes in the Indian Ocean and their estimates of power spectra all fail the 95% significant test (Figs. 2.3b, c, e, f). Therefore, S-EOF1 of SSTA during JJASON can be used to identify the IOD events in observations, showing similar results in other ways. Using S-EOF during 1980–2020, pIOD events contain 1982, 1983, 1987, 1994, 1997, 2006, 2007, 2015, 2019, and nIOD events are 1984, 1985, 1989, 1992, 1996, 1998, 2001, 2005, 2010, 2013, 2016.

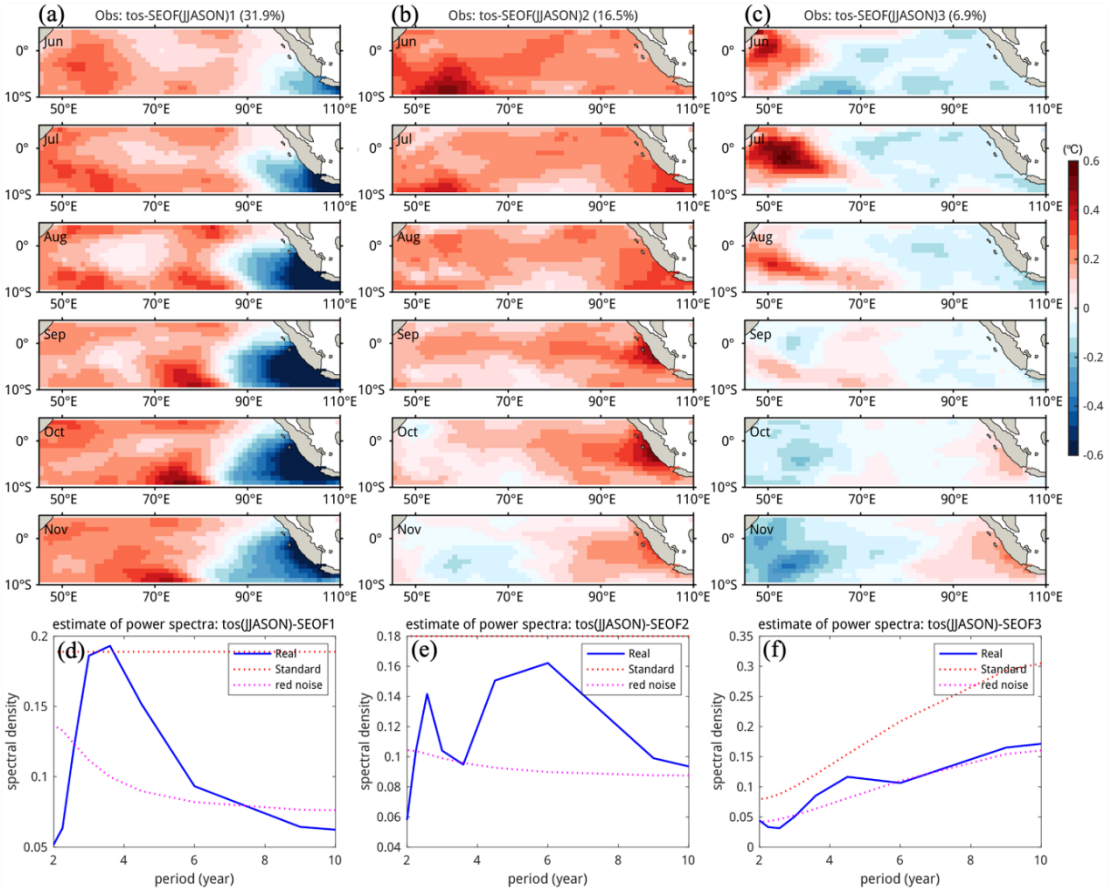


Figure 2.3. (a, b, c) S-EOF1 to 3 patterns of SSTA during JJASON and (d, e, f) their estimates of power spectra (dataset: GODAS, 1980–2020). The dotted red line in the estimate of power spectra is the 95% significant test and the dotted pink line is the red noise.

2.4.2. IOD identification in CMIP models

Previous examinations of this issue focused on SST variability at a fixed location, typically the regions associated with the DMI. This approach assumes that models simulate the IOD SSTA centers that can be represented by the DMI, as is the case in observations. Although the multi-model average position of the anomaly center compares well with the observed position, the anomaly center differs from one model to another (Figs. 2.4, 2.5). Therefore, EOF analysis is a better way to select well-simulated models and identify IOD events in each model rather than indices that focus on a fixed region.

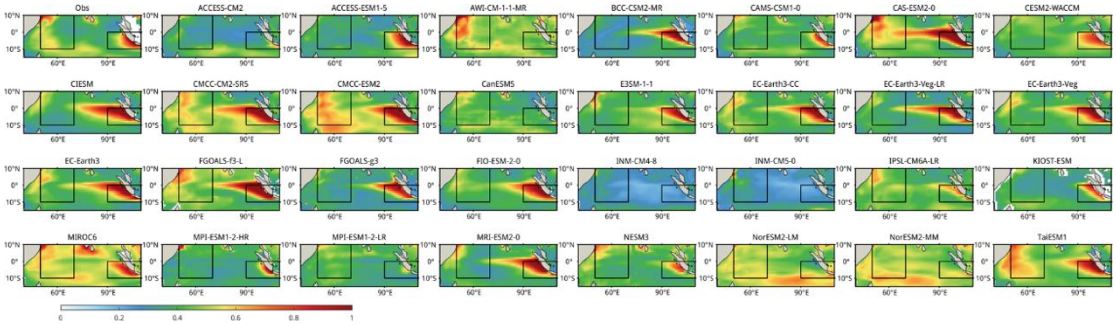


Figure 2.4. SST STD (unit: ℃) in observation (dataset: GODAS, 1980–2020) and 31 CMIP6 models using historical experiments. The solid box in the western (eastern) Indian Ocean is 10°S–10°N, 50°–70°E (10S°–0°, 90°–110°E).

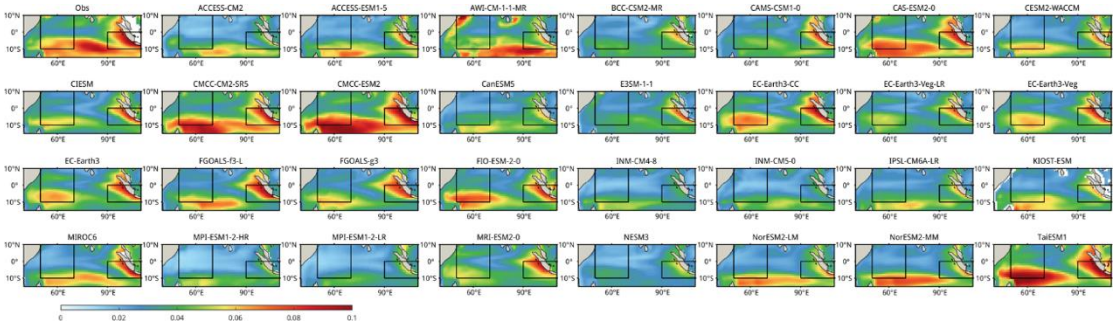


Figure 2.5. The same as Fig. 2.4, but for STD of SLA (unit: m).

Based on the required variables (oceanic and atmospheric) and experiments, 31 CMIP6 and 34 CMIP5 models are selected. The next step is to choose models that can simulate IOD well. In observation, EOF2 of SST can represent the IOD mode (Fig. 2.2b). In CMIP models, the EOF2 of SST is not the best technique for choosing the well-simulated models since IOD mode may appear in the EOF1, EOF2, or both the EOF1 and EOF2 (Fig. 2.6). The EOF of SST during JJASON also shows the same situation as the EOF of SST (not shown). If considering a longer dataset, the EOF of SST from 1900 to 2014 also cannot properly distinguish the IOD signals (not shown).

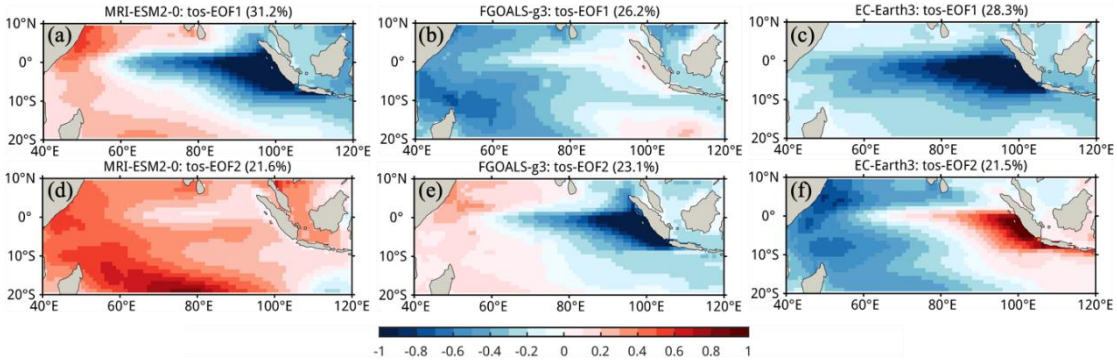


Figure 2.6. (a, b, c) EOF1 and (d, e, f) EOF2 of SST (unit: ℃) in (a, d) MRI-ESM2-0, (b, e) FGOALS-g3 and (c, f) EC-Earth3 models using historical experiments.

Compared to the SST which is deeply influenced by both the thermodynamic and dynamic processes, SLA represents the dynamic part and may contain fewer disruptions. The results reveal a significant contribution rate for all EOF1 SLA in observation and CMIP6 models (Figs. 2.2d, 2.7). This way can capture the dynamic process of IOD and can be used to recognize the IOD events. If focusing on the mature phase of IOD (JJASON), the contribution rates of EOF1 would be higher (Fig. 2.7). However, due to the SLA EOF1 patterns sharing similarities across CMIP models, it is challenging to identify well-simulated models. The patterns of S-EOF of SLA in the TIO are also similar with different variabilities among CMIP models (not shown).

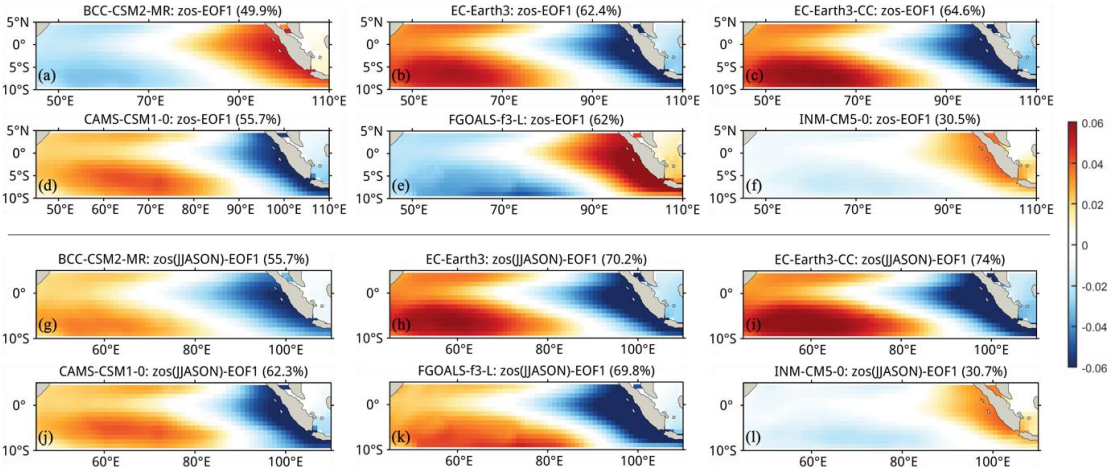


Figure 2.7. EOF1 of SLA (unit: m) in (a) BCC-CSM2-MR, (b) EC-Earth3, (c) EC-Earth-CC, (d) CAMS-CSM1-0, (e) FGOALS-f3-L and (f) INM-CM5-0 models using historical experiment. (g, h, i, j, k, l) EOF1 of SLA during JJASON.

Hence, the S-EOF analysis is applied to identify major modes of year-to-year SST variability during JJASON in the Indian Ocean (45°E–110°E, 10°S–5°N) (Fig. 2.8). The leading mode, namely S-EOF1, performs well in extracting IOD signals with a high contribution rate in both observations and CMIP6 models, as opposed to the EOF of SSTA or SLA. One benefit of using S-EOF is that it is a good approach to present a given climate mode that is strongly interacting with the annual cycle. Another point is that the S-EOF1 growth patterns can be utilized to find well-simulated models. Nearly all the CMIP models show the IOD mode in the first S-EOF pattern. Some models exhibit a poor simulation of IOD by failing to exhibit the IOD-like mode in the S-EOF1 to S-EOF3 pattern. If considering both the SST and SLA during JJASON, their S-EOF1 can also represent the IOD mode (not shown), which is another useful method for choosing models and identifying the IOD cases. Since the results of S-EOF1 of SST

(JJASON) and S-EOF1 of combined SST and SLA (JJASON) are quite similar, we choose the S-EOF of SST (JJASON) for further research.

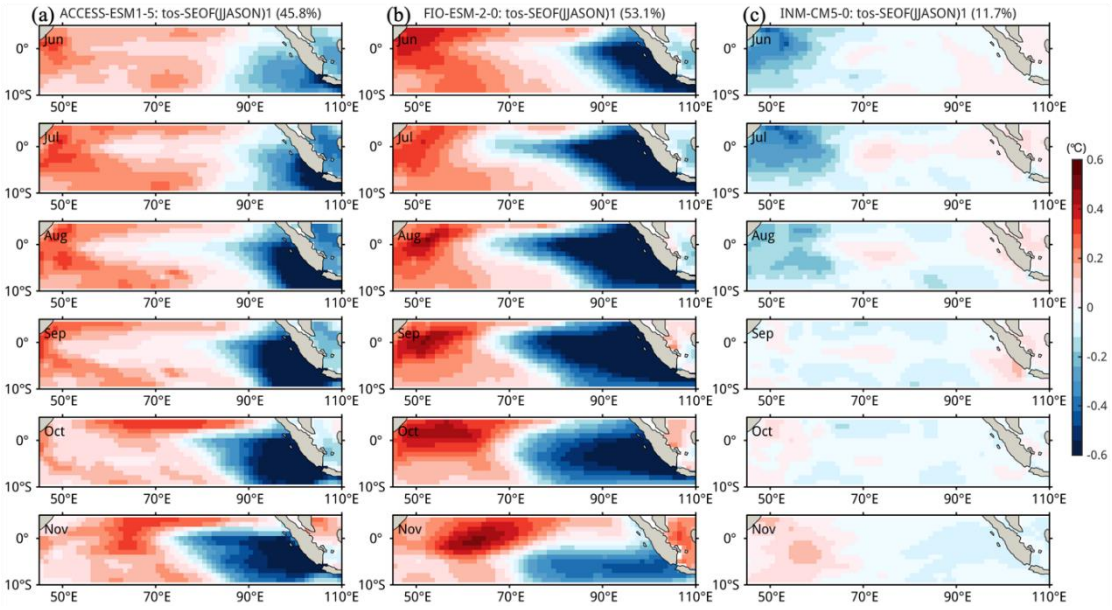


Figure 2.8. S-EOF1 of SST (unit: ℃) during JJASON based on (a) ACCESS-ESM1-5, (b) FIO-ESM-2-0 and (c) INM-CM5-0 models.

24 out of 34 CMIP5 models and 20 out of 31 CMIP6 models are chosen for further study, on the basis of the spatial correlation between S-EOF1 patterns in observations and historical runs (Fig. 2.9). To identify the top models, other methods are also employed (e.g., cluster analysis, dipole index). Due to the varied simulation of IOD, space correlation may be the best and simplest method to connect models and observation, and it truly catches the well-simulated models when checking the EOF1 pattern and composite results. This selection process ensures that the selected models have more ability to reflect the complex dynamics underlying IOD events, lending credibility and robustness to subsequent analyses and conclusions. To categorize events, a positive (negative) IOD event is identified wherever the PC1 is greater (less) than its threshold of +0.8 (–0.8) STD.

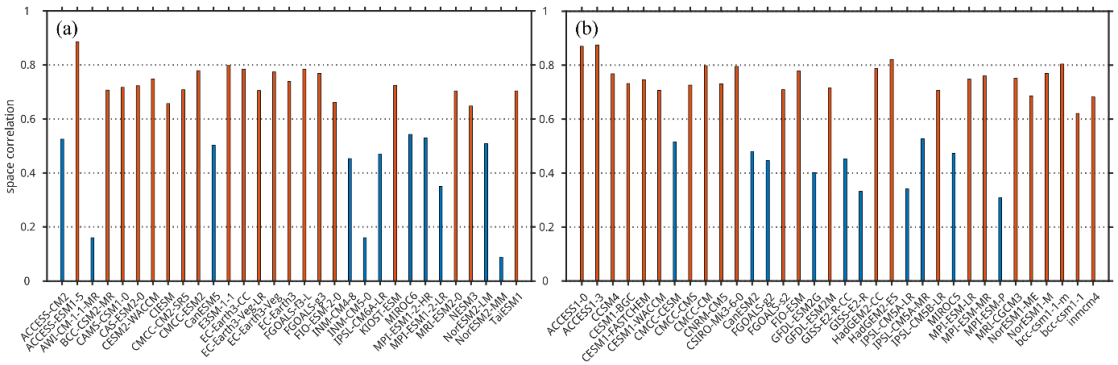


Figure 2.9. Spatial correlation of S-EOF1 pattern between observations (dataset: GODAS) and each (a) CMIP6 or (b) CMIP5 model. Orange (blue) bars denote models with IOD well (poorly) simulated.

Composite patterns of pIOD and nIOD are displayed to evaluate the chosen models. Regarding pIOD, the composite patterns in selected models are more significant and similar to those in observation, showing significant negative SSTAs in the ETIO, considerable rainfall reduction in the ETIO, and strong easterly anomaly in the TIO (Fig. 2.10). In terms of non-selected models, the composite results do not shape the IOD pattern, except for the ACCESS-CM2, MIROC6, and NorESM2-LM models. However, ACCESS-CM2, MIROC6, and NorESM2-LM models simulate significantly stronger variabilities in the western and central TIO than those in the ETIO, which is opposite to the observation. Composites of nIOD events in selected models are comparable to those in observations (Fig. 2.11). ACCESS-CM2, MIROC6, and NorESM2-LM models also simulate greater variations in the western and central TIO during nIOD.

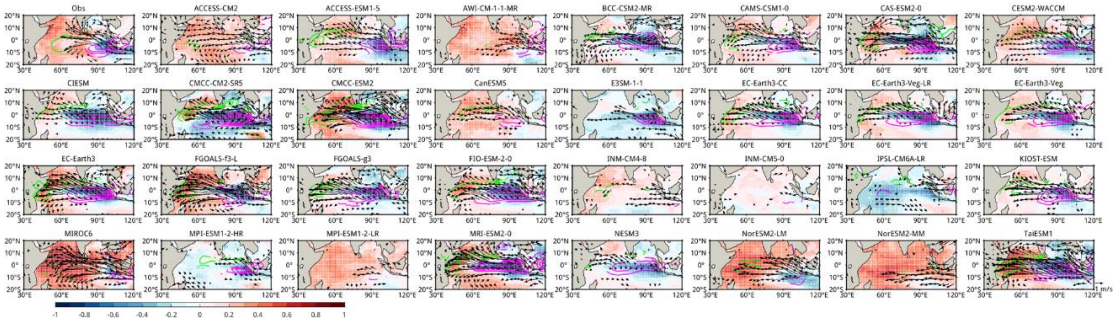


Figure 2.10. Composite pIOD during August to October of SST (shading; unit: °C), precipitation (contours in intervals of 1 mm day^{-1}) and 850 hPa wind (vector; unit: m s^{-1}) anomalies in observations and CMIP6 historical runs. IOD is identified by the PC1 of S-EOF.

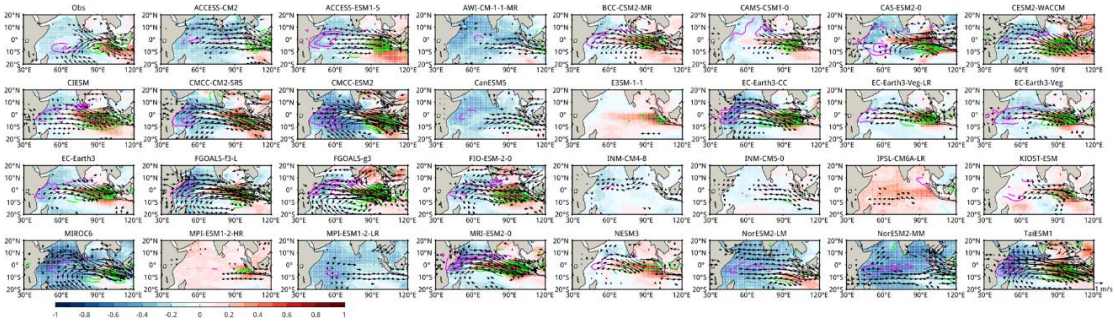


Figure 2.11. The same as Fig. 2.10, but for nIOD.

Additionally, IOD composite patterns determined by the DMI are also calculated (Figs. 2.12, 2.13). Composite patterns of pIOD and nIOD events in selected models

resemble those in the observation. Non-selected models produce more varied results. In NorESM2-LM, IOD cases are diverse with fewer points passing the 95% significant test in wind and precipitation. When compared to the S-EOF, DMI would spot a few odd situations that are different from the IOD and would have an impact on the composite results. S-EOF is a tighter method of IOD identification than DMI.

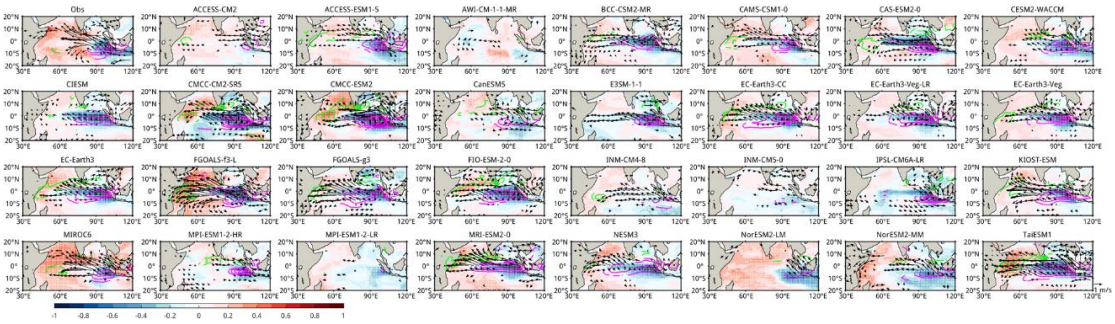


Figure 2.12. The same as Fig. 2.9, but using DMI.

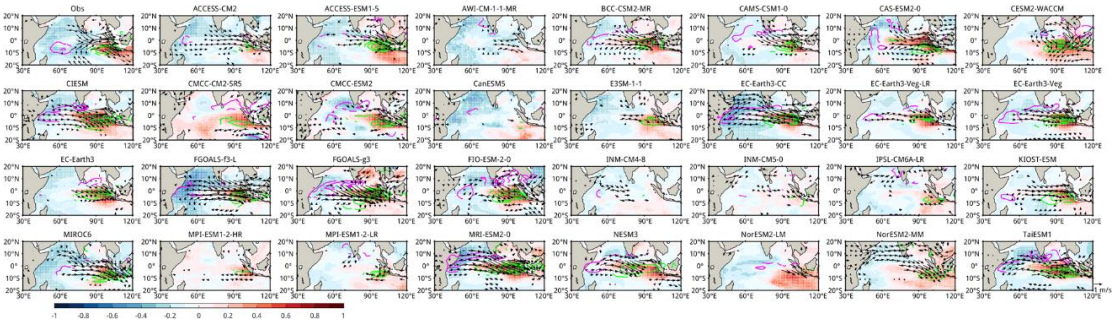


Figure 2.13. The same as Fig. 2.12, but for nIOD.

In CMIP models, there is little correlation between IOD amplitude and IOD skewness, and most of the selected models exhibit slightly higher SST variations in the eastern Indian Ocean than non-selected models (Fig. 2.14). In comparison to the observation, most of the non-selected models in CMIP6 simulate less variability and skewness of IOD. The MME of IOD amplitude and skewness in 31 CMIP6 models is smaller than the MME of the 20 selected models in which 6 out of 20 selected models have skewness that is comparable to observation (Fig. 2.14a). Nearly all CMIP5 models simulate less skewness than observation (Fig. 2.14b). The chosen CMIP5 models simulate a slightly higher STD of SSTA and selected CMIP6 models have a bigger STD than CMIP5 models and observation. Positive, negative, or both positive and negative IOD biases may contribute to STD prejudice. While skewness refers to the contrast between positive and negative IODs. The skewness center hence might not coincide with the STD center. In observation, the centers of STD and skewness may be in the

same region to a certain extent. However, due to the diverse simulation of IOD in CMIP models, the STD center and skewness center exhibit less correlation among CMIP models. Instead of STD and skewness, the crucial distinction between selected and non-selected models is the phase development of SSTA, further supporting that S-EOF1 is a better way to choose the well-simulated CMIP models and identify IOD events.

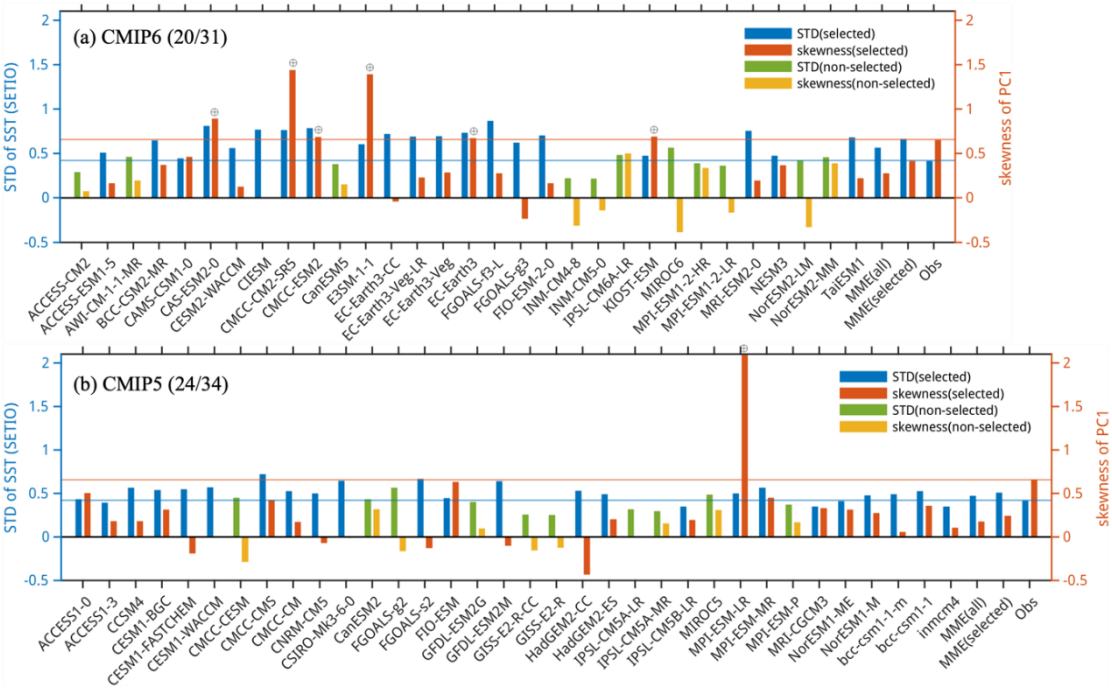


Figure 2.14. Skewness of PC1 for representing IOD skewness (orange and yellow bars) and SSTA STD over ETIO (85°E–100°E, 8°S–2°N) during JJASON (blue and green bars) in (a) CMIP6 and (b) CMIP5 models. Orange and blue (yellow and green) bars denote selected (non-selected) models. Models with PC1 skewness larger than the observed are marked by grey circles above the skewness bars. Orange (blue) line denotes the observed skewness (STD) value (dataset: GODAS).

3. IOD asymmetry in observations

3.1. Performances of IOD asymmetry

In observation, DMI can capture the IOD events. In addition to strong interannual variations, DMI demonstrates positive skewness, while the equatorial zonal wind anomaly and the SLA within SETIO are negatively skewed (Fig. 2.1). The positive skewness of DMI is season-dependent, showing large values from summer to winter (Fig. 3.1a). Since the IOD amplitude asymmetry is primarily attributed to the skewness in the eastern pole of the Indian Ocean, SSTA skewness in the ETIO is also shown in Fig. 3.1a, which is also season-dependent and most noticeable from July to December in recent decades. Fig. 3.1b provides a more detailed view, illustrating the seasonal development of IOD events from 1980 to 2020. In recent decades, the SST amplitude in pIOD is larger than that in nIOD. There have been three extreme IOD events, namely the 1994, 1997 and 2019 pIOD events. The 1994 pIOD events developed earlier than other positive events, with a large DMI value in summer, which caused a severe heatwave in Japan (Guan and Yamagata 2003). A recent study further categorizes summer IOD into two types, coastal IOD and offshore IOD, each with different climatic impacts, particularly in Australia (Fan et al. 2024). The 1997 pIOD event coincided with the super El Niño event, with the largest SSTA amplitude occurring in November 1997. In comparison, nIOD events are more comparable.

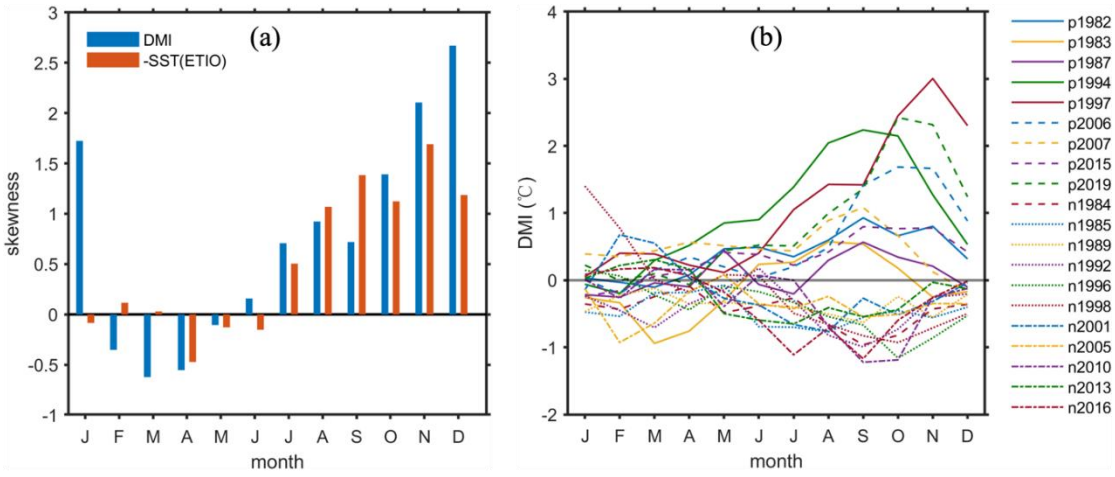


Figure 3.1. (a) Seasonal skewness of DMI and SSTA (multiplied by –1) averaged over the ETIO (8°S–2°N, 85°–100°E). (b) Phase development of DMI during the IOD cases from 1980 to 2020. SST data is from GODAS (1980–2020).

IOD asymmetry can result from the asymmetry of Bjerknes feedback (Cai and Qiu 2013). The Bjerknes feedback is one of the main development mechanisms for IOD,

and it can be partly represented by the three IOD indices (DMI, zonal wind index, and SLA index), showing the SST–zonal wind–SLA feedback loop. The lead-lag correlations suggest that SST, zonal surface wind, and SLA tend to change almost simultaneously (Fig. 3.2a–c). July–October (JASO) is selected as the core phase of IOD based on the observations and CMIP simulations. In Fig. 3.2d, the slope between DMI and zonal wind index during nIOD is a little bit larger than that during pIOD. The slope between DMI and zonal wind index tends to be linear when the extreme positive IOD is excluded, indicating that this relationship may not be the primary cause of the positive IOD skewness. The relationship between the zonal wind index and the SLA index is linear, while the SLA index and DMI show a significant nonlinear relationship with large differences in the slope. This suggests the important role of thermocline, which leads to the asymmetry of the thermocline-temperature feedback (Cai et al. 2013). After the IOD is triggered, SSTA induces anomalies of pressure gradient and convection, subsequently causing wind anomaly and then SSH anomaly, which ultimately contributes to the SSTA development. The anomalous winds stress response and the SST response to thermocline change are both stronger during pIOD, resulting in IOD asymmetry.

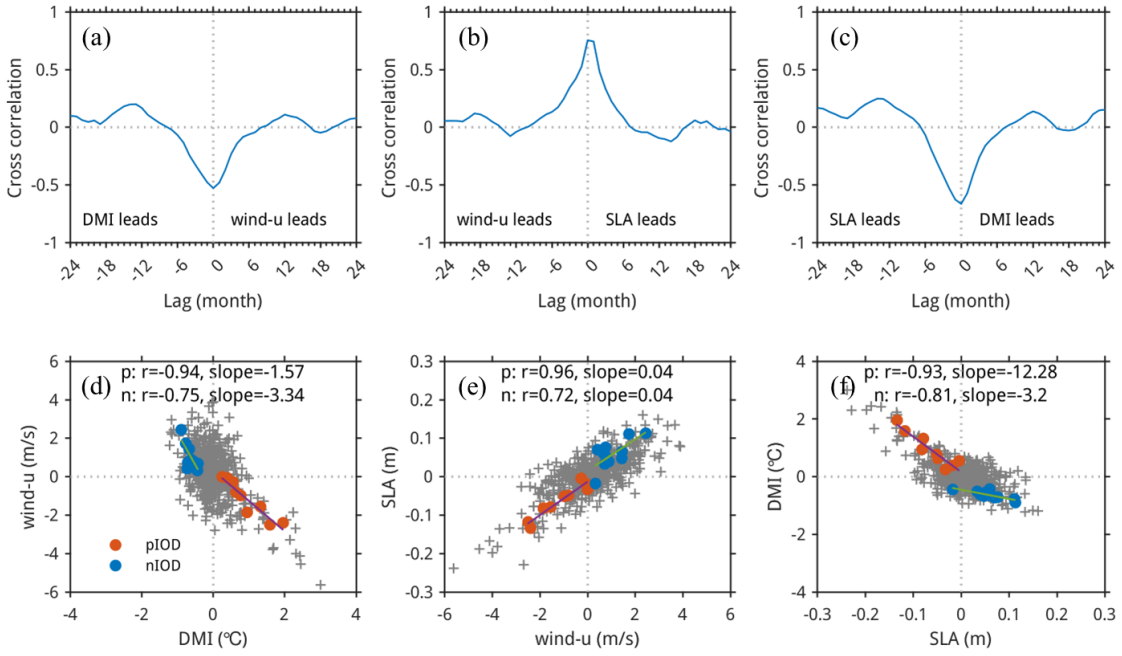


Figure 3.2. Lead-lag correlation between (a) DMI (unit: °C) and zonal wind index (unit: m s^{-1}), (b) zonal wind index and SLA index (unit: m), (c) SLA index and DMI. (d) Monthly DMI vs zonal wind index. (e) Monthly zonal wind index vs SLA index. (f) Monthly SLA index vs DMI. Grey + is the monthly anomaly. Red (Blue) dot is the anomaly during JASO in pIOD (nIOD). Purple (Green) line is the least squares linear fit of pIOD (nIOD). The r and slope values are the correlation coefficient and the slope between the two indices, respectively.

If the anomaly occurs, the SST, wind, current, and SLA would all be amplified by the Bjerknes feedback. One key question is what causes the current anomaly against the surface wind stress anomaly. It is found that the horizontal ocean mixed-layer current anomaly in the ETIO is correlated with the wind stress anomaly in situ (Fig. 3.3). This implies that the ocean current anomaly is directly driven by the wind stress anomaly. Therefore, the current anomaly is mostly the wind-induced Ekman current, different from the ENSO in which the geostrophic current associated with the thermocline depth anomaly is more important (Su et al. 2010). The anomalous local vertical motion is caused by the divergence of the current anomalies to a large extent, resulting in the advection of subsurface water and further strengthening the SSTA. Negative IOD experiences fewer thermocline fluctuations because of the warm background state in the ETIO.

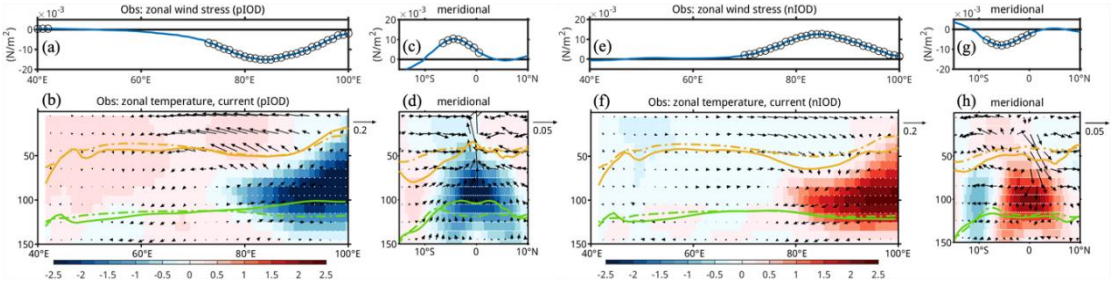


Figure 3.3. Composite (a) zonal wind stress (blue curve; unit: N m^{-2}), (b) zonal temperature (shading; unit: ℃) and current (see scale vector in lower right; unit: u in m s^{-1}, w in 10^{-4} m s^{-1}) anomalies along the equator (2°S–2°N), (c) meridional wind stress, (d) meridional temperature and current (v in m s^{-1}, w in 10^{-4} m s^{-1}) anomalies averaged in the ETIO (85°E–100°E) during JASO in pIOD. (e, f, g, h) is the same as (a, b, c, d) but for nIOD. The black circle means passing the 95% significant test. The yellow (green) line is MLD (20 °C isotherm) (dotted: mean state, solid: IOD). White stippling indicates the 95% significance level based on Student's t-test.

3.2. Nonlinear dynamical heating

To further explore the detailed processes contributing to the IOD skewness, a mixed-layer heat budget is used. Fig. 3.4 shows the distributions of MLT tendency, NDH, LDH, net heat flux, subsurface entrainment (lateral induction, entrainment due to MLD tendency), residual term, nonlinear zonal advection, nonlinear vertical advection, and nonlinear meridional advection in normal pIOD, normal nIOD, and super pIODs (1994, 1997, 2019). In normal IOD cases, each budget term tends to be symmetrical and the LDH is the first contributor followed by the NDH. Notably, the NDH is negative in both the warm and cold episodes. The biggest difference between

normal and super IOD is the comparable role of NDH to LDH during super IOD. According to Yang et al. (2020), nonlinear zonal and vertical advection plays a crucial part in creating the nonlinearity of pIOD. Relative to NDH and LDH, net heat flux and subsurface entrainment have a smaller impact. The mixed-layer heat budget analysis indicates that positive IOD skewness is mainly induced by anomalous nonlinear horizontal and vertical ocean temperature advection. The nonlinear zonal and vertical advections have much higher values than the nonlinear meridional advection which is the damping term across the entire ETIO. The linear ocean advection terms contribute to the growth of both the positive and negative SSTAs, having a symmetric effect. Some asymmetric LDH terms {e.g., $-\overline{w}[(T-T_{-h})/h]'$} are the manifestation of the nonlinear nature of the problem. However, analyzing high-order (quadratic) terms will shed light on how the placement of various anomalous circulation elements itself can lead to asymmetric IOD. Additionally, in contrast to the earlier super IOD events in 1994 and 1997, the latest 2019 super IOD is favored by the net heat flux anomaly. The net heat flux anomaly is linked with the latent heat flux anomaly associated with the enhanced coastal wind in recent decades (Wang et al. 2020a).

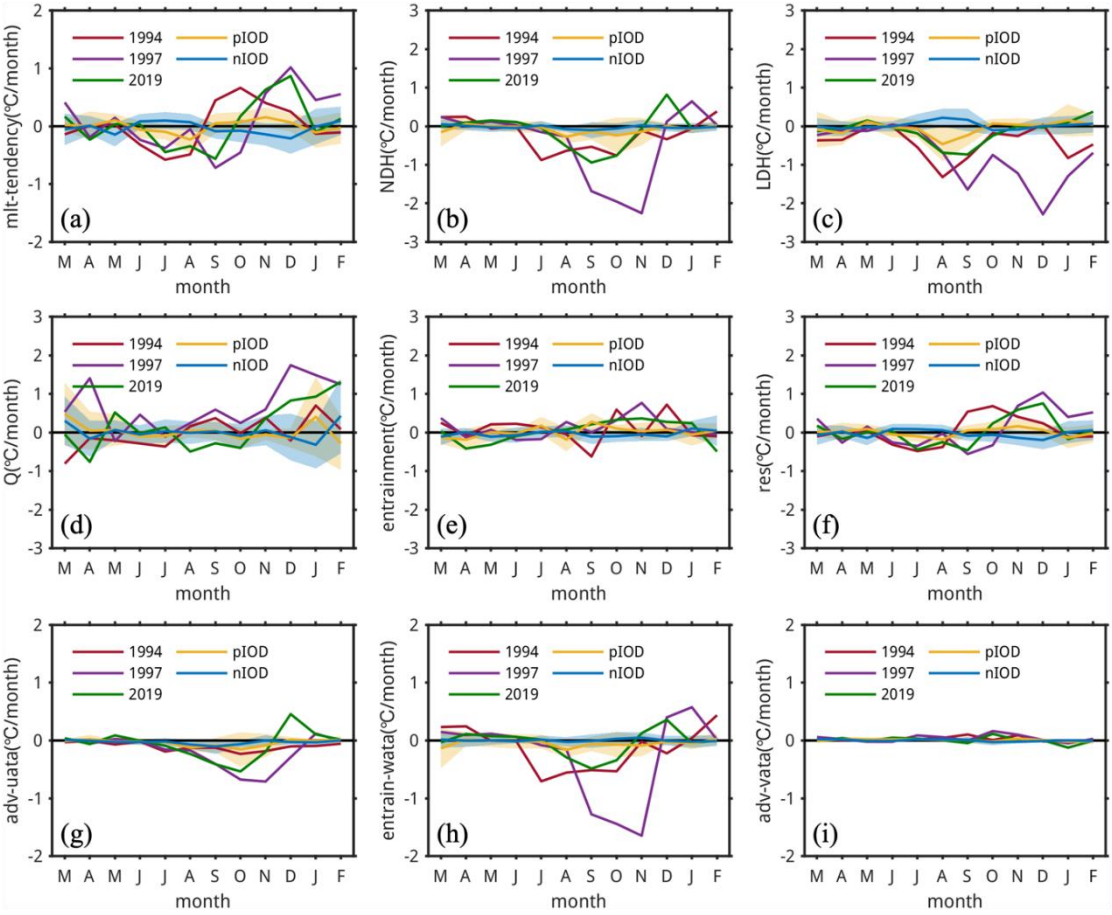


Figure 3.4. Seasonal changes of (a) MLT tendency (unit: ℃ month^{-1}), (b) NDH, (c) LDH, (d) net heat flux, (e) subsurface entrainment, (f) residual term, (g) nonlinear zonal advection, (h) nonlinear vertical advection and (i) nonlinear meridional advection in super pIODs (1994, 1997, 2019), normal pIOD, and normal nIOD averaged over the ETIO (8°S–2°N, 85°–100°E).

The time series analysis reveals a negative correlation between NDH and DMI from 1980 to 2020 (Fig. 3.5). The nonlinear advection terms have an asymmetric effect, contributing to ocean cooling in both positive and negative phases, thereby amplifying cold events while weakening the warm events. Consequently, large DMI values align with large NDH anomalies, notably in 1994, 1997, 2006 and 2019 (Fig. 3.5). These significant NDH anomalies primarily stem from nonlinear vertical advection, followed by nonlinear zonal advection.

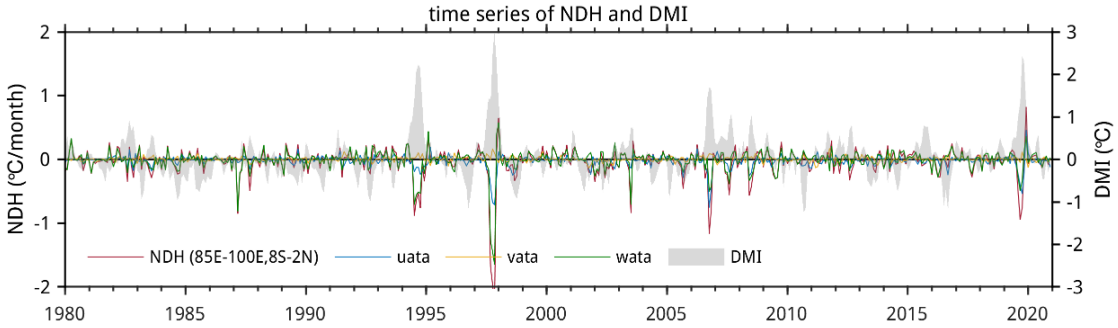


Figure 3.5. Time series of NDH (red line; unit: ℃ month^{-1}), nonlinear zonal advection (blue line), nonlinear meridional advection (yellow line), nonlinear vertical advection (green line), and DMI (grey shading; unit: ℃) from 1980 to 2020.

Fig. 3.6 illustrates the relationship between the surface zonal wind anomaly and the nonlinear zonal advection, influencing the IOD asymmetry. The surface zonal wind anomaly causes the zonal ocean mixed-layer current anomaly (Fig. 3.6b) and the zonal MLT gradient anomaly (Fig. 3.6c) upon IOD initiation. Assuming an initial negative SSTA in the ETIO, anomalous easterly winds generate Ekman transport, moving cold anomalies from east to west. On the contrary, anomalous eastward current and positive anomalous zonal MLT gradient develop in nIOD. The relationships between surface zonal wind anomaly and zonal mixed-layer current or zonal MLT gradient anomalies during IOD events appear nonlinear. However, these relationships denote the displacement of IOD asymmetry rather than the cause. The slopes between zonal mixed-layer current anomaly and nonlinear zonal advection during pIOD are comparable to those during nIOD, as are the slopes between zonal MLT gradient

anomaly and nonlinear zonal advection (Figs. 3.6d, e). Both scenarios result in zonal cold advection during pIOD and nIOD, contributing to ETIO cooling (Fig. 3.6f).

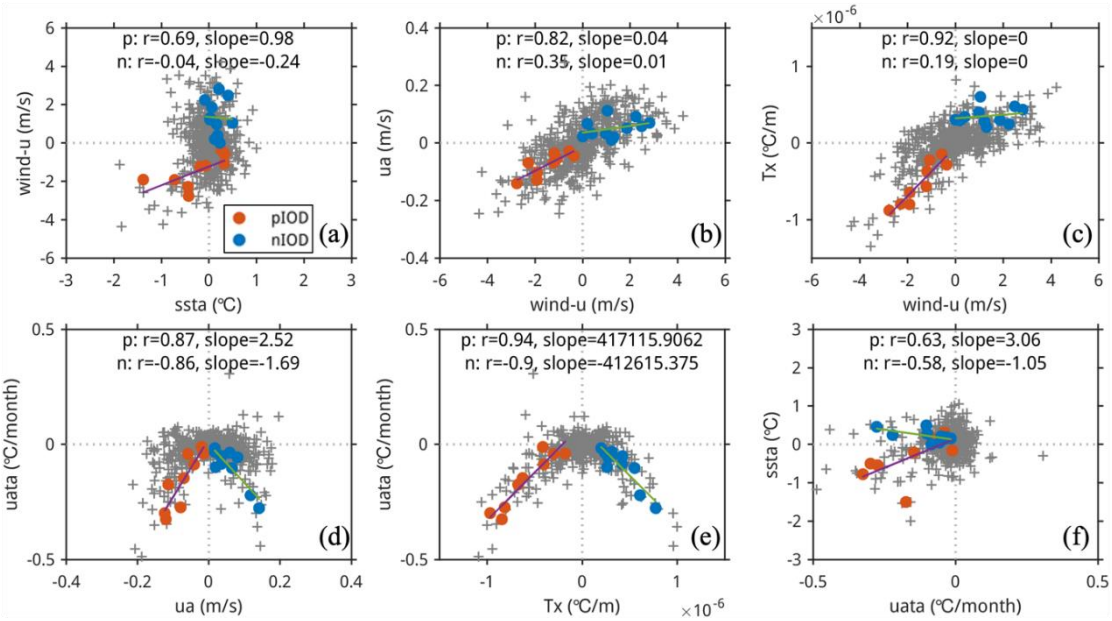


Figure 3.6. (a) SSTA (unit: °C) vs surface zonal wind anomaly (unit: m s^{-1}) averaged over the ETIO (8°S–2°N, 85°–100°E). (b) Surface zonal wind anomaly vs zonal mixed-layer current anomaly (unit: m s^{-1}). (c) Surface zonal wind anomaly vs zonal MLT gradient anomaly (unit: °C m^{-1}). (d) Zonal current anomaly vs nonlinear zonal advection (unit: °C $month^{-1}$) within MLD. (e) Zonal MLT gradient anomaly vs nonlinear zonal advection within MLD. (f) Nonlinear zonal advection vs SSTA.

The loop in Fig. 3.2 shows a nonlinear SST response to thermocline fluctuation, pointing to the important roles of nonlinear vertical advection. Figure 3.7 illustrates how the surface wind anomalies affect the nonlinear vertical advection and finally contribute to the IOD asymmetry. Both surface zonal and meridional wind variations account for the changes in oceanic vertical motion and vertical temperature gradient at the base of the mixed layer (Fig. 3.7a–d). In pIOD, both anomalous easterly and northerly induce anomalous upwelling at the equator and near the Sumatra coast and positive vertical temperature gradient near the Sumatra coast, leading to cold vertical advection. Note that the maximum amplitude of the temperature anomaly is located at the subsurface layer so that the MLT anomaly is smaller than that below the MLD, forming the positive anomalous vertical temperature gradient in pIOD. The vertical motion response to wind anomaly tends to be linear, while the response of vertical temperature gradient to wind anomaly is nonlinear, which enlarges the nonlinear vertical advection in pIOD and finally the IOD asymmetry. The thermocline-temperature feedback asymmetry can be represented by the vertical temperature

gradient anomalies (Fig. 3.6f). The negative nonlinear zonal advection is similar during positive and negative IOD events, while the nonlinear vertical advection enhances significantly during super pIOD (Fig. 3.7g), meaning that nonlinear vertical advection can be the first contributor, followed by the nonlinear zonal advection.

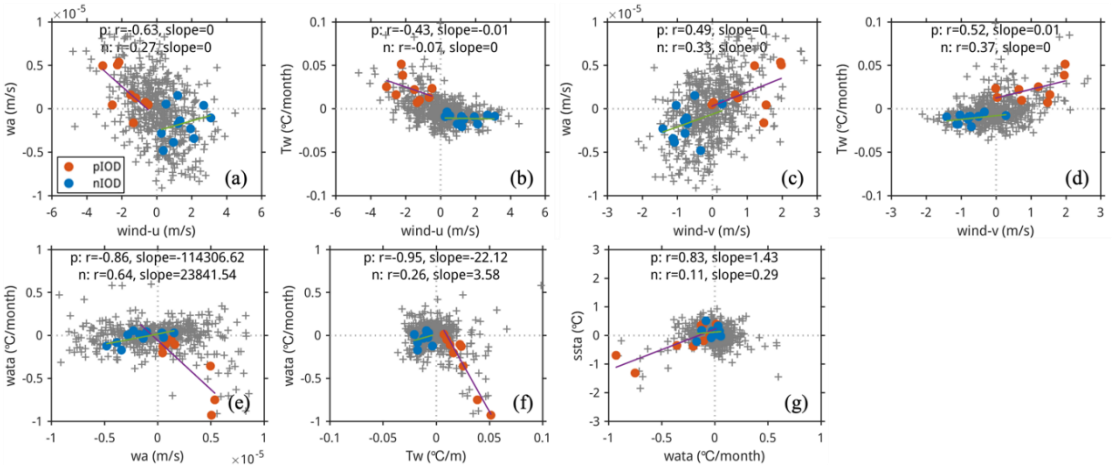


Figure 3.7. (a) Surface zonal wind anomaly (unit: m s^{-1}) vs vertical velocity anomaly (unit: m s^{-1}) at the base of mixed layer averaged over the ETIO (8°S–2°N, 85°–100°E). (b) Surface zonal wind anomaly vs vertical temperature gradient anomaly (unit: °C m^{-1}) at the base of mixed layer. (c, d) are the same as (a, b), but for surface meridional wind anomaly (unit: m s^{-1}). (e) Vertical velocity anomaly vs nonlinear vertical advection (unit: °C $month^{-1}$). (f) Vertical temperature gradient anomaly vs nonlinear vertical advection. (g) Nonlinear vertical advection vs SSTA (unit: °C).

The third component in NDH is nonlinear meridional advection. Fig. 3.8 depicts the formation of nonlinear meridional advection. Compared to the other two terms, the nonlinear meridional advection during IOD is small (less than 0.2 °C $month^{-1}$) (Fig. 3.8f). Although the anomalous meridional temperature gradient is comparable to, or even larger than, the anomalous zonal temperature gradient within the MLD (Figs. 3.6e, 3.8e), the zonal mixed-layer current anomaly is roughly four times greater than the meridional current anomaly (Figs. 3.6d, 3.8d). Consequently, the nonlinear meridional advection can be easily canceled by the other two terms. All in all, the observed asymmetry in IOD is related to the NDH, where the nonlinear vertical advection comes first, followed by the nonlinear zonal advection, and the nonlinear meridional advection shows a small damping effect.

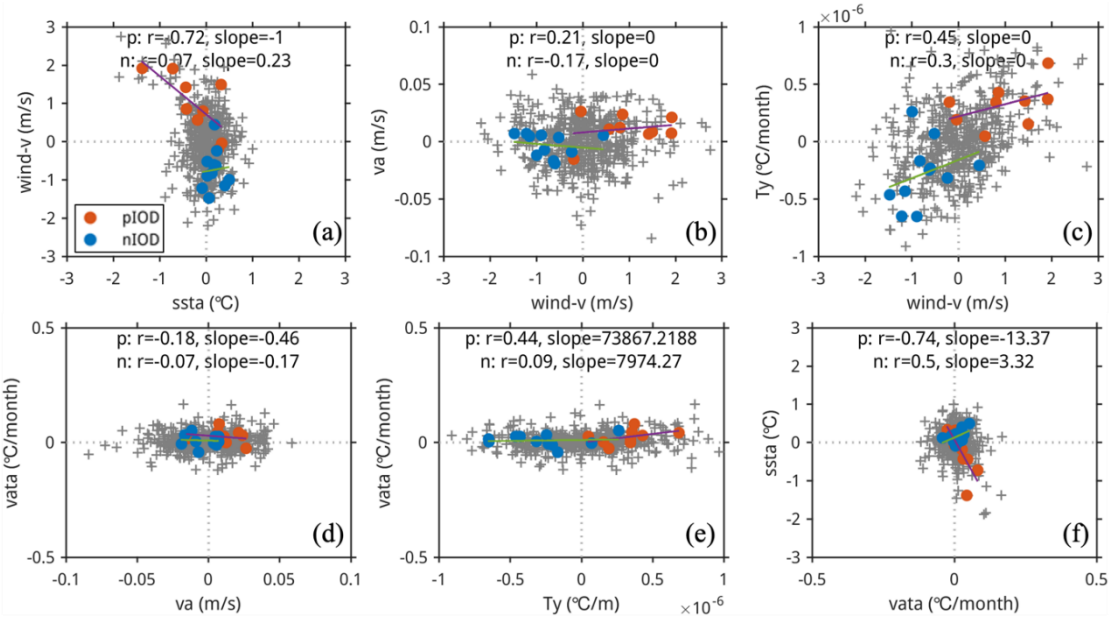


Figure 3.8. (a) SSTA (unit: °C) vs surface meridional wind anomaly (unit: m s^{-1}) averaged over the ETIO (8°S–2°N, 85°–100°E). (b) Surface meridional wind anomaly vs meridional mixed-layer current anomaly (unit: m s^{-1}). (c) Surface meridional wind anomaly vs meridional MLT gradient anomaly (unit: °C m^{-1}). (d) Meridional current anomaly vs nonlinear meridional advection (unit: °C $month^{-1}$) within MLD. (e) Meridional MLT gradient anomaly vs nonlinear meridional advection within MLD. (f) Nonlinear meridional advection vs SSTA.

3.3. Barrier Layer Thickness

Beyond the thermocline-temperature asymmetry in the ETIO, this region is occupied by the Indo-Pacific warm pool, giving rise to the barrier layer—a substantial structure that isolates the mixed layer and subsurface entrainment. Different from the MLD, an isothermal layer depth (ILD) can be defined using only temperature, representing the depth at which the temperature deviates by 0.5°C from its 10-meter value. Subsequently, the barrier layer thickness (BLT) is determined as the difference between ILD and MLD. Within the ETIO, ILD tends to be deeper than the MLD, leading to positive BLT (Figs. 3.9a–c). This positive BLT acts as a barrier, hindering the turbulent entrainment of cold thermocline water into the mixed layer (Lukas and Lindstrom 1991). During pIOD, intensified coastal winds induce a slightly shallower MLD and significantly shallower ILD, causing a thinning of the BLT (Figs. 3.9d–f). Conversely, nIOD events witness a deepening of both MLD and ILD, contributing to an enhanced BLT in the ETIO (Figs. 3.9g–i). However, the deepened MLD anomaly during nIOD is more pronounced than the shallower MLD anomaly during pIOD, while the deepened ILD anomaly during nIOD is smaller than the shallower ILD anomaly

during pIOD. These dynamics lead to more substantial changes in BLT during pIOD (Figs. 3.9d, g), favoring the subsurface entrainment flowing into the mixed layer. Scatter plots among SSTA, BLT, ILD and MLD are also shown in Fig. 3.10. SSTA exhibits a high correlation with BLT in the ETIO during pIOD, boasting a correlation coefficient of 0.85, whereas a less linear relationship is apparent during nIOD (Fig. 3.10a). Similar nonlinearity is observed between ILD and SSTA in the ETIO (Fig. 3.10b). The connection between MLD and SSTA is weaker compared to the relationship between ILD and SSTA, signifying that ILD generally plays a more pivotal role in shaping BLT changes. As discussed by Cai et al. (2013), this effect, which is considered purely the thermal effect without the salinity effect, reinforces the asymmetry of the Bjerknes feedback.

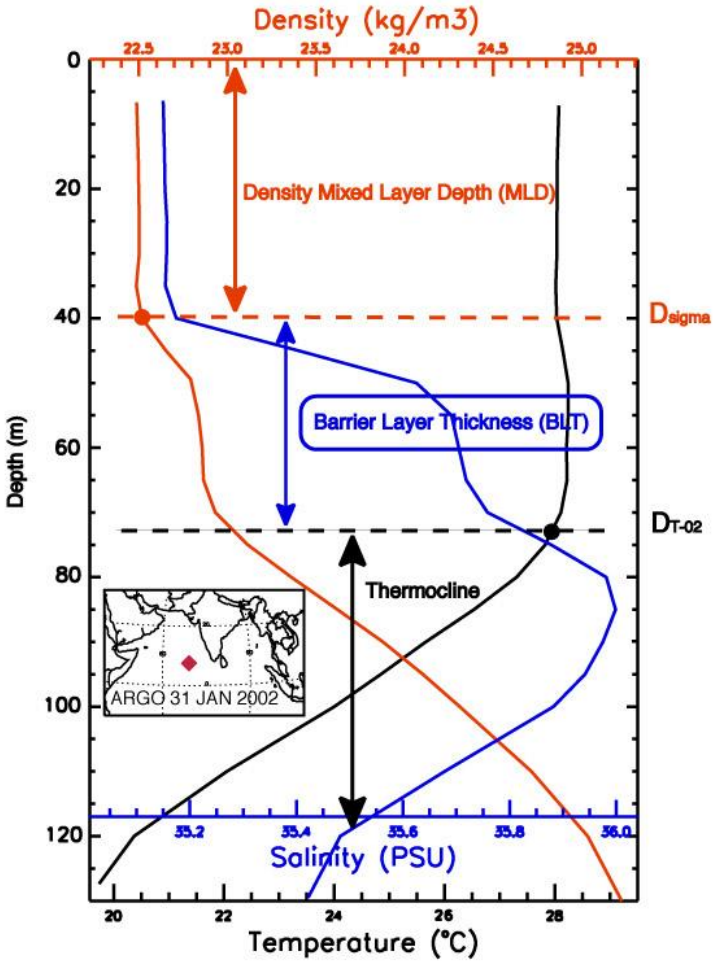


Figure 3.9. The definition of BLT. Source: https://cerweb.ifremer.fr/deboyer/mld/Subsurface_Barrier_Layer_Thickness.php.

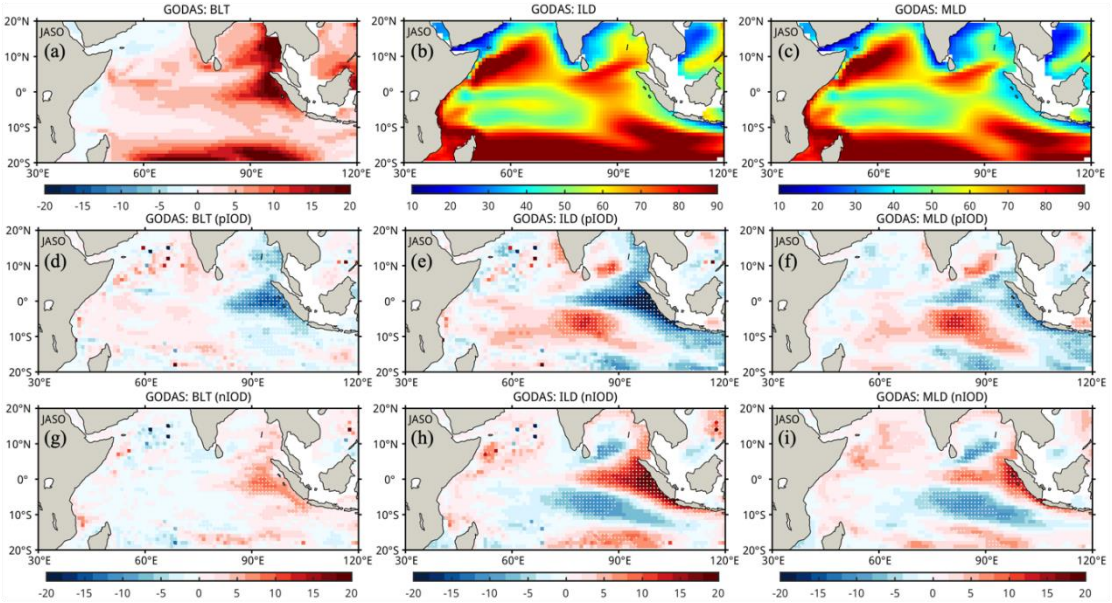


Figure 3.10. (a, b, c) Mean state, (d, e, f) composite pIOD and (g, h, i) composite nIOD of (a, d, g) BLT (unit: m), (b, e, h) ILD and (c, f, i) MLD anomalies.

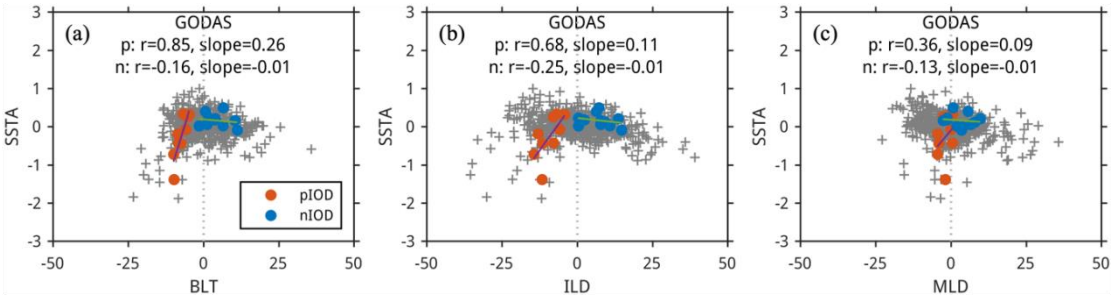


Figure 3.11. (a) BLT anomaly (unit: m) vs SSTA (unit: °C) averaged over the ETIO (85°E–100°E, 8°S–2°N). (b) ILD anomaly vs SSTA. (c) MLD anomaly vs SSTA.

3.4. Thermodynamic process

In addition to the ocean dynamic, the air-sea coupling processes are also crucial for the IOD development, such as the cloud-radiation-SST feedback (Hong et al. 2008a) and the WES feedback (Xie and Philander 1999). Hong et al. (2008a) pointed out that thermal damping caused by the cloud-radiation-SST feedback is another important mechanism for generating amplitude asymmetry. With increased positive SSTAs, more convection clouds would develop, and less shortwave radiation would reach the sea surface in the ETIO, while negative SSTAs in the ETIO do not react in the same way. When reaching the cloud-free condition, the thermal damping weakens significantly, demonstrating less damping effect in strong pIOD. In ETIO, there is a linear relationship between precipitation and shortwave radiation anomalies, and the shortwave radiation response to SSTA is larger during pIOD (Figs. 3.9a, b). This

suggests that it may be easier to weaken the mean state convection than strengthen the convection above the ETIO warm pool. The shortwave radiation in the ETIO divided by the SSTA during super pIOD is less negative than that during normal IOD, suggesting less damping effect during super pIOD (Figs. 3.9 c, d). However, the mixed-layer heat budget analysis in Fig. 4.3 shows that the asymmetry of the shortwave radiation forcing is small and the shortwave radiation response during IOD is diversified (fails 95% significant test). Hence, the contribution of NDH to IOD skewness is more important. Additionally, the WES feedback is not the cause of IOD skewness, but it may efficiently amplify the SSTA asymmetry (Figs. 3.9 e, f). Surface cooling (warming) accompanies greater (weaker) coastal surface wind and enhanced (weaker) evaporation, which enlarges the SSTAs.

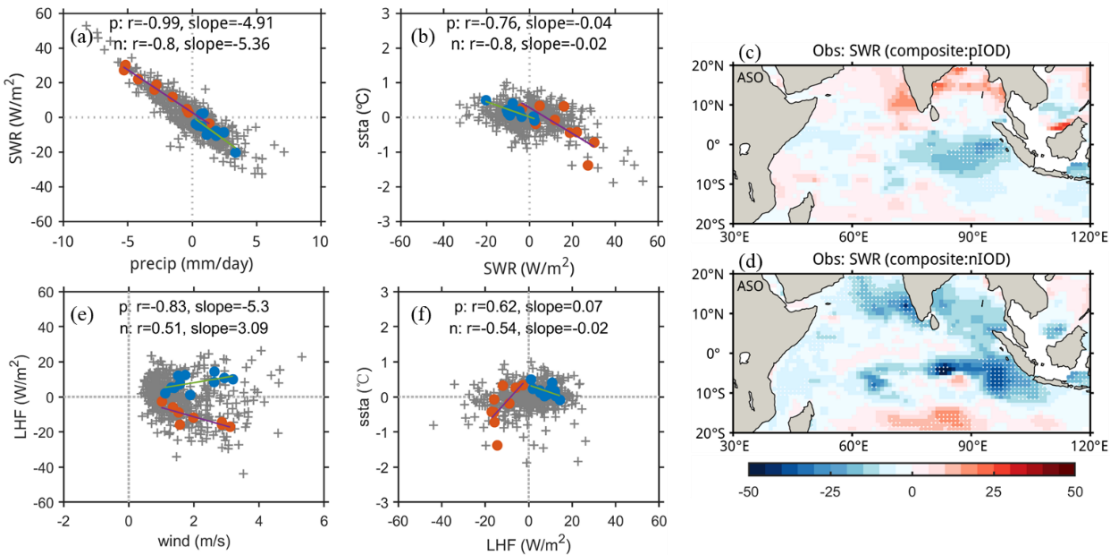


Figure 3.12. (a) Precipitation anomaly (unit: mm day^{-1}) vs shortwave radiation anomaly (unit: W m^{-2}) during JASO averaged over the ETIO (8°S–2°N, 85°–100°E). (b) Shortwave radiation anomaly vs SSTA (unit: °C). (c) and (d) are shortwave radiation anomalies per SSTA (unit: W m^{-2} °C^{-1}) in pIOD and nIOD, respectively. (e) Surface wind speed anomaly (unit: m s^{-1}) vs latent heat flux anomaly (unit: W m^{-2}). (f) Latent heat flux anomaly vs SSTA.

3.5. Summary

The IOD is an asymmetrical system in the TIO, with pIOD exhibiting a larger amplitude than nIOD. Multiple factors contribute to IOD asymmetry, including the significant role of Bjerknes feedback. This feedback mechanism involves the interplay between SST, surface zonal wind, and SLA. The relationship between the zonal wind index and SLA index is linear, while the relationship between SLA index and DMI is nonlinear, highlighting the importance of the thermocline-temperature feedback. To

gain a comprehensive understanding of the processes driving IOD skewness, a mixed-layer heat budget analysis is employed. The analysis reveals that positive IOD skewness primarily arises from anomalous nonlinear horizontal and vertical ocean temperature advection. Furthermore, differences in the BLT response during positive and negative IOD events contribute to IOD asymmetry. The study also emphasizes the significance of the cloud-radiation-SST feedback in generating IOD amplitude asymmetry through thermal damping. Other ocean reanalysis datasets, such as Simple Ocean Data Assimilation (SODA; Carton and Giese 2008) and ECMWF Ocean Reanalysis System 5 (ORAS5; Zuo et al. 2017, 2019), are utilized and generally capture similar characteristics, although they exhibit discrepancies in vertical motion anomalies during IOD events.

4. Historical simulations of IOD in CMIP5/6 models

4.1. IOD asymmetry

4.1.1. Simulated IOD asymmetry

Fig. 4.1 depicts the IOD skewness and amplitude in CMIP5/6 models. Notably, 6 (CAS-ESM2-0, CMCC-CM2-SR5, CMCC-ESM2, E3SM-1-1, EC-Earth3, KIOST-ESM) out of 20 selected CMIP6 models capture a comparable IOD skewness to observations using PC1 (Fig. 4.1a). It's worth mentioning that these six models were not covered in a prior study (McKenna et al. 2020). However, all CMIP5 models simulate a smaller skewness than observations with the exception of the MPI-ESM-LR model (Fig. 4.1b), indicating that CMIP6 outperforms CMIP5 in terms of IOD skewness. For the STD of SSTA, most selected models exhibit slightly higher SST variations in the ETIO in contrast to observations, and the CMIP6 MME mean of SST STD is higher than the counterpart in the CMIP5 ensemble (Fig. 4.1). Instead of skewness, i.e. the discrepancy between pIOD and nIOD, both enhanced pIOD and nIOD events would contribute to a positive bias in the STD of SSTA. However, due to the diversity of IOD characteristics in CMIP5/6 models, IOD amplitude and skewness show only a weak inter-model correlation. To explore the origins of IOD skewness biases, 20 selected CMIP6 models are categorized into two groups: the more-skewed CMIP6 model group (CAS-ESM2-0, CMCC-CM2-SR5, CMCC-ESM2, E3SM-1-1, EC-Earth3, KIOST-ESM) and the less-skewed CMIP6 model group (remaining selected CMIP6 models). CMIP5 models are also used for comparison.

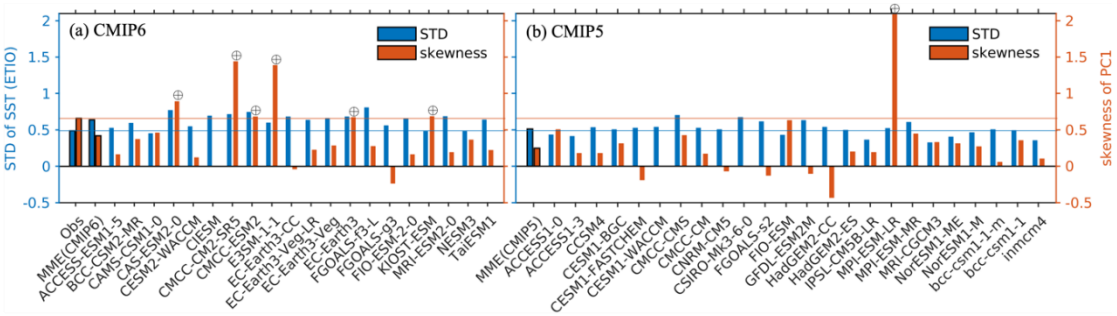


Figure 4.1. Skewness of PC1 for representing IOD skewness (orange bars) and SSTA STD over ETIO (8°S–2°N, 85°–100°E) during JJASON (blue bars) in (a) CMIP6 and (b) CMIP5 models. Orange (blue) line denotes the observed skewness (STD) value. Models with PC1 skewness larger than the observed are marked by grey circles above the skewness bars.

In the observed surface horizontal skewness pattern during JJASON, there is a pronounced negative SST skewness over the ETIO and the area associated with the

thermocline dome (Fig. 4.2a). Regarding the ocean vertical pattern, the negative ocean temperature skewness is mainly observed above 100 m in the ETIO (Figs. 4.2b, c). Hence, the IOD amplitude asymmetry is predominantly attributed to the ETIO asymmetry, which is seasonally dependent and most noticeable during the mature phase of the IOD. Moreover, the SST skewness center in surface horizontal patterns generally corresponds to the SST STD center, whereas in ocean vertical patterns, the most negative ocean temperature skewness signals are always positioned above the strongest signals of the ocean temperature STD. This is because even a small fluctuation of thermocline would lead to significant temperature changes and produce the strongest STD near the thermocline. However, the IOD skewness is a result of air-sea coupling processes, exhibiting its highest values within the MLD, which is typically shallower than the thermocline. Both CMIP5 and CMIP6 models can reproduce similar SST skewness patterns, characterized by negative signals in the ETIO, but all of the models perform poorly in terms of their ocean vertical skewness (Figs. 4.2d–l). The more-skewed CMIP6 model group demonstrates the closest resemblance to the observed skewness (Figs. 4.2g–i), while the other two groups show much smaller skewness values than those in observations and the more-skewed CMIP6 model group. In addition, the negative temperature skewness simulated by CMIP models is shallower than those in observations, which might be associated with the simulated shallower thermocline (Ng and Cai 2016).

Figure 4.2 illustrates distinct IOD patterns observed in both observations and CMIP models. In observations, the IOD pattern is primarily located near the Sumatra-Java coast (Fig. 4.2a). Conversely, nearly all CMIP5/6 models exhibit larger SSTA standard deviations along the equatorial ETIO, indicating a greater simulation of IOD amplitude. The less-skewed CMIP6 model group and CMIP5 model group demonstrate a further enhancement of SSTA fluctuation along the equator compared to the more-skewed CMIP6 model. Notably, the more-skewed CMIP6 model group excels not only in capturing IOD asymmetry but also in replicating the IOD pattern accurately.

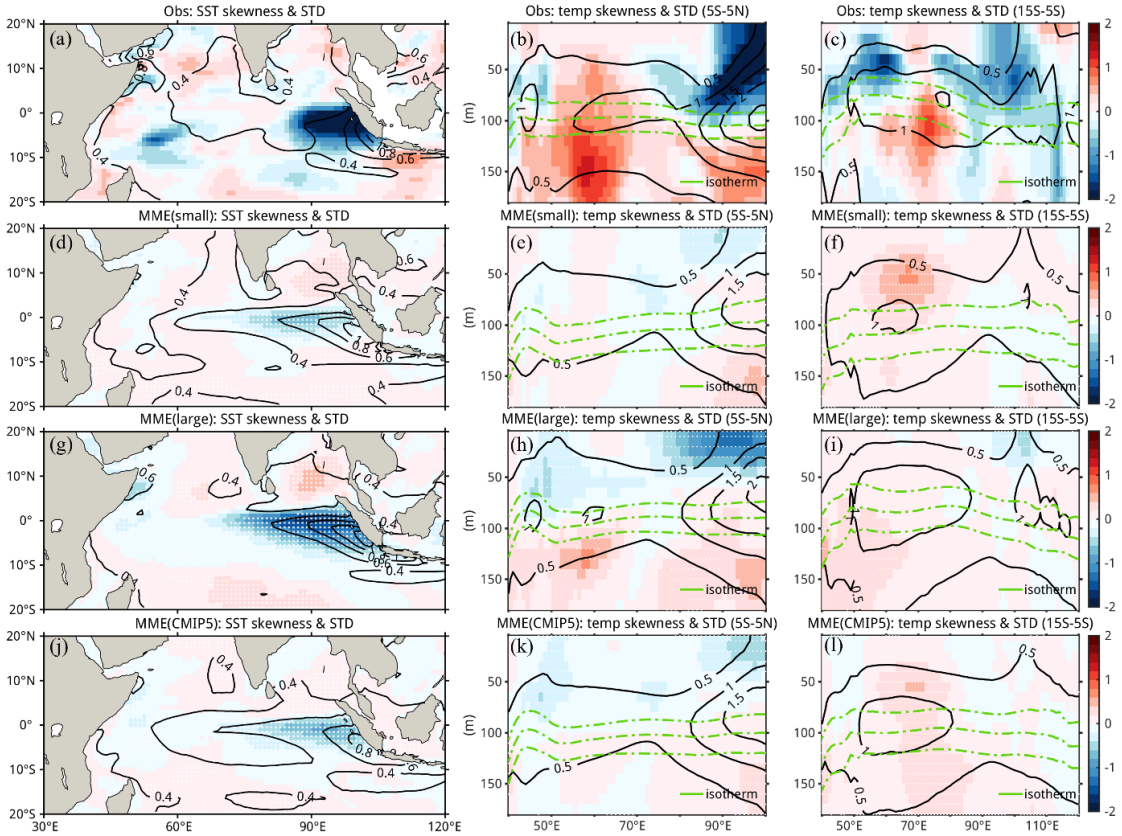


Figure 4.2. JJASON skewness (shading) and STD (contour) of (a, d, g, f) SSTA, anomalous ocean temperature averaged over (b. e. h. k) 5°S to 5°N and (c, f, i, l) 15°S to 5°S, based on (a, b, c) observations, (d, e, f) less-skewed CMIP6 model group, (g, h, i) more-skewed CMIP6 model group and (j, k, l) CMIP5 models. The observed and model-simulated 24, 22 and 20 ℃ isotherms (dash-dot contours) are also shown in the ocean vertical cross sections. White stippling indicates the 95% significance level based on Student's t-test.

Composite patterns of pIOD and nIOD during JASO are also shown in Fig. 4.3. In observations, stronger SSTAs occur near the Sumatra-Java coast during pIOD than nIOD, accompanied by easterly wind anomalies in the TIO and negative precipitation anomalies in the ETIO during pIOD (Figs. 4.3a, e). In the historical simulations, the amplitudes of SST, precipitation, and 850 hPa wind tend to be larger in CMIP6 than in CMIP5 models, which is consistent with the DMI results in McKenna et al. (2020). These indicate that CMIP6 models continue to simulate an overestimated IOD amplitude compared to observations, which is associated with the larger simulation of the Bjerknes feedback (Cai and Cowan 2013). However, when considering IOD asymmetry, some CMIP6 models perform better than the CMIP5 models. The more skewed CMIP6 model group displays larger coastal wind anomalies, larger SSTAs, and more precipitation anomalies in pIOD compared to nIOD, particularly in the SETIO (Figs. 4.3c, g). Conversely, in the less-skewed CMIP6 model group (Figs. 4.3b, f) and

the CMIP5 models (Figs. 4.3d, h), the composites of pIOD and nIOD are comparable. Notably, nIOD in the less-skewed CMIP6 model group even captures stronger precipitation anomalies than that in pIOD.

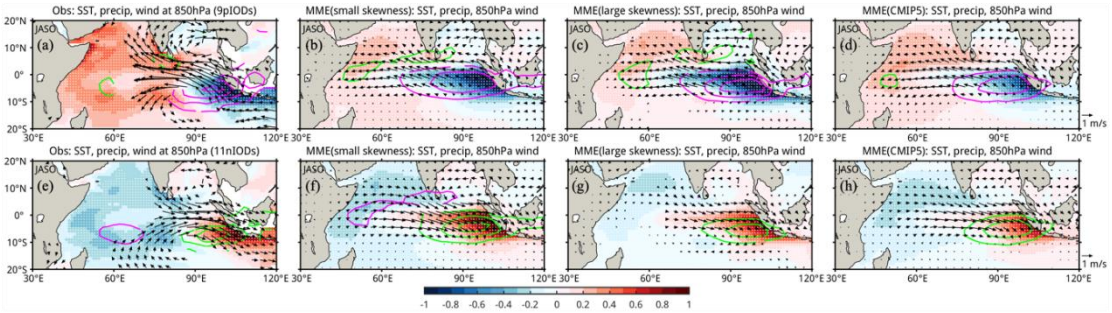


Figure 4.3. Composite (a, b, c, d) positive and (e, f, g, h) negative IOD for SST (shading; unit: ℃), precipitation (contour, in intervals of 1 mm day^{-1}) and 850 hPa wind anomalies (see scale vector in lower right; unit: m s^{-1}) during JASO, based on (a, e) observations, (b, f) less-skewed CMIP6 model group, (c, g) more-skewed CMIP6 model group and (d, h) CMIP5 models. Anomalies of SST (white stippling), precipitation and wind are shown when exceeding the 95% significance level based on Student's t-test.

4.1.2. Simulated dynamics of IOD asymmetry

Previous studies revealed that observed IOD asymmetry is mainly caused by the nonlinear zonal $[-u'(\partial T'/\partial x)]$ and vertical $\{-w'[(T-T_{-h})/h]'\}$ advection (Hong et al. 2008b; Cai et al. 2014). Thus, a mixed-layer heat budget analysis is used to investigate the relative contributions of the thermodynamic and dynamic processes to the IOD skewness biases in observations and CMIP5/6 models (Fig. 4.4). Here we focus on the core phase (JASO) of the IOD. In observations, vertical advection and nonlinear zonal advection are the key dynamical processes for the MLT tendency during JASO (Fig. 4.4a). Nonlinear zonal and vertical advection are observed to be negative during both pIOD and nIOD, but nonlinear meridional advection $[-v'(\partial T'/\partial y)]$ is slightly positive, with much lower values than the formers. As a result, negative NDH tends to cool the upper ETIO, strengthening pIOD but weakening nIOD. Regarding the LDH component, linear zonal advection terms $[-\bar{u}(\partial T'/\partial x)\ \&\ -u'(\partial \bar{T}/\partial x)]$ tend to offset each other, similar to the linear meridional advection terms $[-\bar{v}(\partial T'/\partial y)\ \&\ -v'(\partial \bar{T}/\partial y)]$, while linear vertical advection terms $\{-\bar{w}[(T-T_{-h})/h]'\ \&\ -w'\overline{(T-T_{-h})/h}\}$ both contribute to an enhanced MLT tendency. The positive (negative) anomalous vertical temperature gradient cools (warms) the surface ETIO through the $-\bar{w}[(T-T_{-h})/h]'$ term in pIOD (nIOD) events. The $-w'\overline{(T-T_{-h})/h}$ term is slightly asymmetric, associated with thermocline-temperature asymmetry (Cai

and Qiu 2013; Ogata et al. 2013). Because of the background deep thermocline, this term gives rise to minimal surface warming in response to the wind-driven deepening thermocline during nIOD. In contrast, during pIOD, the shallower thermocline induces more pronounced surface cooling in the ETIO (Cai and Qiu 2013). The $-\overline{w}[(T - T_{-h})/h]'$ term is linear, and because the temperature anomaly is asymmetric, it follows that the $-\overline{w}[(T - T_{-h})/h]'$ term is also asymmetric. The enhanced (weakened) upwelling also cools (warms) the surface ETIO through the $-w'\overline{(T - T_{-h})/h}$ term during pIOD (nIOD). Thus, the sum of LDH terms promotes the growth of IOD. In addition, the asymmetries in the shortwave radiation and latent heat flux terms are small despite their large fluctuations (Fig. 4.4a), indicating linear WES feedback (Xie and Philander 1994) during IOD. These indicate that the simulation of NDH is essential for properly simulating IOD skewness. As for CMIP models, only the more-skewed CMIP6 model group can reasonably simulate NDH in the ETIO during IOD (Figs. 4.4a, d). The less-skewed CMIP6 model group and CMIP5 models simulate much smaller nonlinear zonal and vertical advection in the ETIO compared to observations (Figs. 4.4a–c).

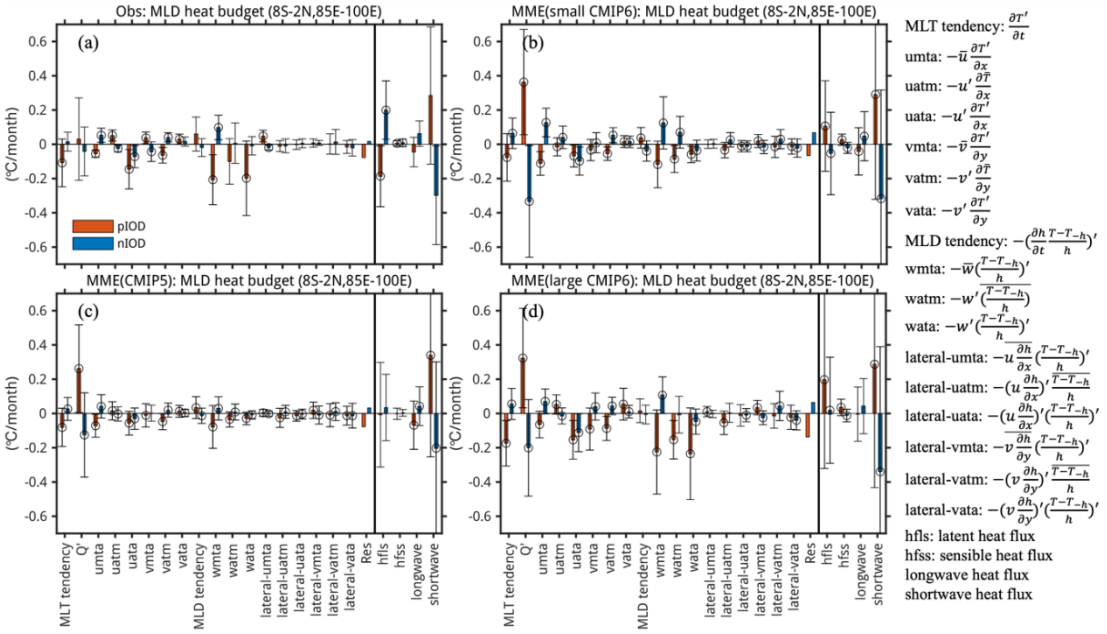


Figure 4.4. Composite mixed-layer heat budget during positive and negative IODs during JASO within the ETIO (8°S–2°N, 85°–100°E) in (a) observations, (b) less-skewed CMIP6 model group, (c) CMIP5 models and (d) more-skewed CMIP6 model group. Error bar is based on one STD. Circle over the bar indicates signals passing the 95% significance level.

To a large extent, lower simulated ETIO NDH leads to a smaller positive IOD skewness. In addition, the composite results of the net heat flux term in CMIP5/6 models differ significantly from observations, which is related to the unrealistic simulation of the latent heat flux feedback (Fig. 4.4). In observations, latent heat flux forcing promotes the development of SSTA in the ETIO (Fig. 4.4a). However, this term behaves diversely in CMIP models and it appears to dampen the development of ETIO SSTA (Figs. 4.4b, d). This is related to the opposite simulation of latent heat flux forcing in the southern ETIO during IOD (Figs. A1f–h, j–l). Typically, latent heat flux is mainly influenced by the wind speed and the air-sea humidity difference (Kumar et al. 2017). In CMIP, the surface wind anomalies enhance (weaken) the coastal wind in pIOD (nIOD), which aligns with the observed (Fig. A1). Hence, the unrealistic simulation of latent heat flux forcing may be related to the biases in simulating the air-sea humidity difference. Unfortunately, the humidity above the sea surface is not provided by CMIP models. What's more, the SCR feedback acts as negative feedback in IOD development, reflected by the shortwave radiation term (Fig. 4.4). This term varies across CMIP5/6 models and exhibits a comparable role with the observed. The term's influence may extend to the IOD skewness bias, given that the more-skewed CMIP6 model group captures a stronger negative effect than the less-skewed CMIP6 model group during nIOD.

The results of the long-term mean NDH within the mixed layer (Fig. 4.5) are consistent with the composite budget results shown in Fig. 4.4. The observed NDH exhibits noticeably negative signals in the ETIO (Fig. 4.5a). The negative long-term mean nonlinear zonal advection is found in the ETIO and southern WTIO (Fig. 4.5e), and the negative long-term mean nonlinear vertical advection is also observed near the equator and along the Sumatra-Java coast (Fig. 4.5i). In contrast, the long-term mean nonlinear meridional advection is slightly positive in the southern TIO (Fig. 4.5m), contributing less to NDH. Both CMIP5 and CMIP6 models are capable of simulating negative NDH in the ETIO, with the largest NDH occurring in the more-skewed CMIP6 model group, followed by the less-skewed CMIP6 model group, and the smallest NDH occurring in the CMIP5 models (Figs. 4.5b–d). The more-skewed CMIP6 model group simulates comparable nonlinear zonal and vertical advection to observations, while the other two groups reproduce much smaller values, especially the CMIP5 models, indicating improved NDH simulation from CMIP5 to CMIP6 (Figs. 4.5e–h, i–l). These results suggest that both the mean and variability of the mixed-layer NDH are too weak

in the less-skewed CMIP6 model group and CMIP5 models, which contributes to a simulated small skewness of the IOD.

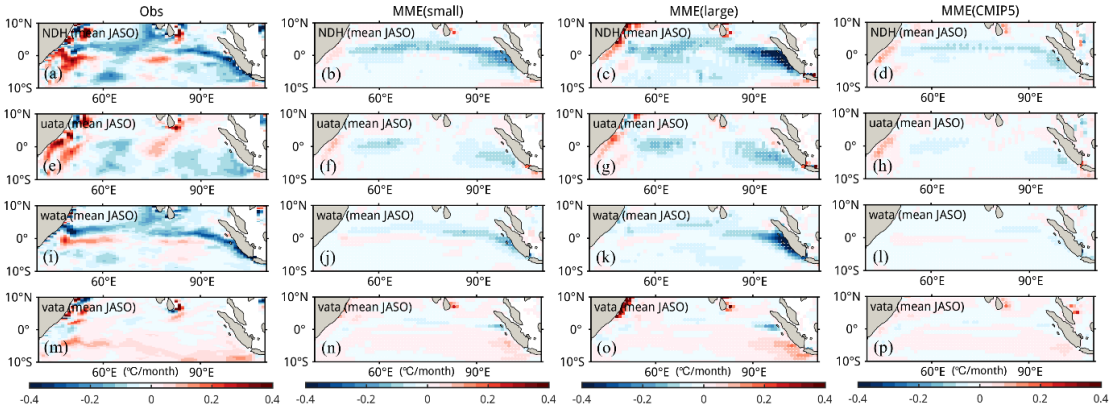


Figure 4.5. Long-term mean (a, b, c, d) NDH (unit: °C month^{-1}), (e, f, g, h) nonlinear zonal advection, (i, j, k, l) nonlinear vertical advection and (m, n, o, p) nonlinear meridional advection within the mixed layer during JASO based on (a, e, i, m) observations, (b, f, j, n) less-skewed CMIP6 model group, (c, g, k, o) more-skewed CMIP6 model group and (d, h, l, p) CMIP5 models. White stippling indicates the 95% significance level based on Student's t-test.

4.2. Model biases in nonlinear zonal advection

Figs. 4.6 and 4.7 show the composite JASO nonlinear zonal advection during pIOD and nIOD, respectively. Consider an initial occurrence of negative SSTA in the ETIO at the beginning of a pIOD event. In response to this anomaly, the generated easterly anomalies trigger Ekman transport that moves the anomalously cold temperature from the east to the west (Figs. 4.6e, i), resulting in anomalous zonal cold advection and favoring cooling in the ETIO (Fig. 4.6a). On the contrary, nIOD induces anomalous eastward current and positive anomalous zonal temperature gradient (Figs. 4.7e, i), as well as causing anomalous zonal cold advection and inhibiting warming in the ETIO (Fig. 4.7a). The nonlinear zonal advection patterns during pIOD are similar across all CMIP groups, but only the more-skewed CMIP6 group matches the observed variability (Figs. 4.6a–d). This depends on how well the models simulate the zonal current and temperature gradient anomalies in the mixed layer, especially the zonal current anomalies (Figs. 4.6f–h, j–l). The more-skewed CMIP6 model group produces larger anomalies in zonal current and zonal temperature gradient due to stronger easterly wind anomalies (Fig. 4.6o). The less-skewed CMIP6 group and the CMIP5 models, on the other hand, have weaker atmospheric responses than the more-skewed CMIP6 model group and observations (Figs. 4.6m–p). For nIOD, the nonlinear zonal advection and the westerly wind anomalies in CMIP6 are consistent with observations

(Figs. 4.7a–c, m–o). The CMIP5 models show the smallest nonlinear zonal advection, which is related to their weak surface wind anomalies (Figs. 4.7d, p). In conclusion, nonlinear zonal advection biases are larger during pIOD than nIOD, and the simulation of nonlinear zonal advection is improved from CMIP5 to CMIP6.

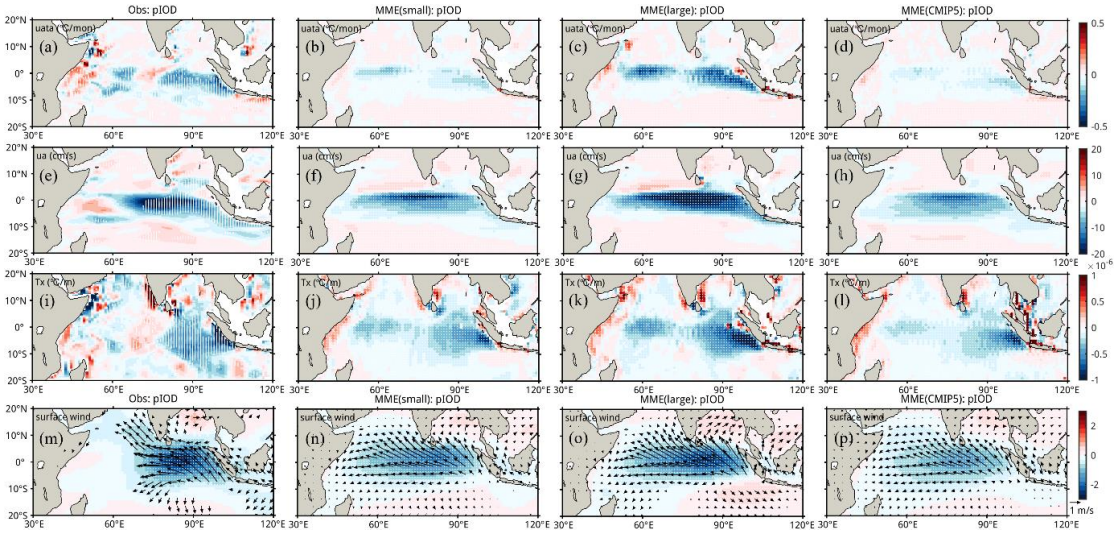


Figure 4.6. Positive IOD composites during JASO for (a, b, c, d) nonlinear zonal advection (unit: °C month^{-1}), (e, f, g, h) zonal mixed-layer current anomalies (unit: cm s^{-1}), (i, j, k, l) zonal temperature gradient anomalies within the mixed layer (unit: 10^{-6} °C m^{-1}) and (m, n, o, p) surface wind anomalies (see scale vector in lower right; unit: m s^{-1}; shading is surface zonal wind anomaly), based on (a, e, i, m) observations, (b, f, j, n) less-skewed CMIP6 model group, (c, g, k, o) more-skewed CMIP6 model group and (d, h, l, p) CMIP5 models. White stippling indicates the 95% significance level based on Student's t-test. Wind vectors in m, n, o, and p are shown when exceeding the 95% significance level based on Student's t-test.

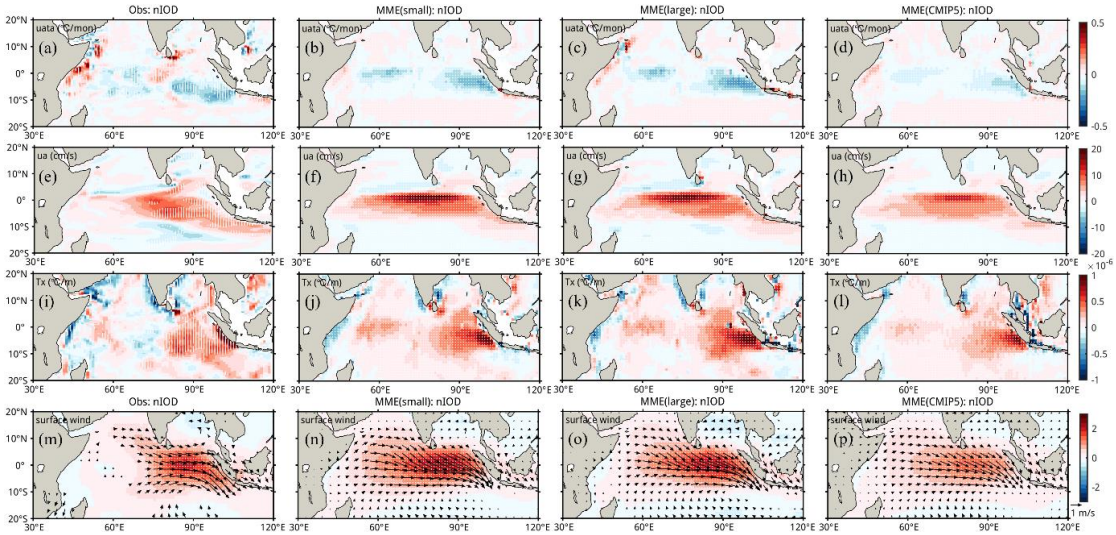


Figure 4.7. Same as Fig. 4.6, but for negative IOD.

The simulations of atmospheric response to SST changes during IOD events are reflected in the simulated surface zonal wind anomalies. The asymmetric atmospheric response has been attributed to the nonlinear relationship between SST and precipitation by previous studies (Hoerling et al. 1997; Ohba and Ueda 2009). In observations, increasing SST typically causes an increase in precipitation if SSTs are lower than around 29 °C (Fig. 4.8a), implying that the convective response to SST forcing is strongly dependent on the background SST. The observed SST for maximum precipitation sensitivity to positive SSTA is around 27 ℃ and to negative SSTA is around 27.5 ℃ (Fig. 4.8e). Most of the CMIP models can reproduce similar precipitation responses to SSTA as observations, with positive (negative) net convective response lower (greater) than 27.5 ℃ (Figs. 4.8e–h).

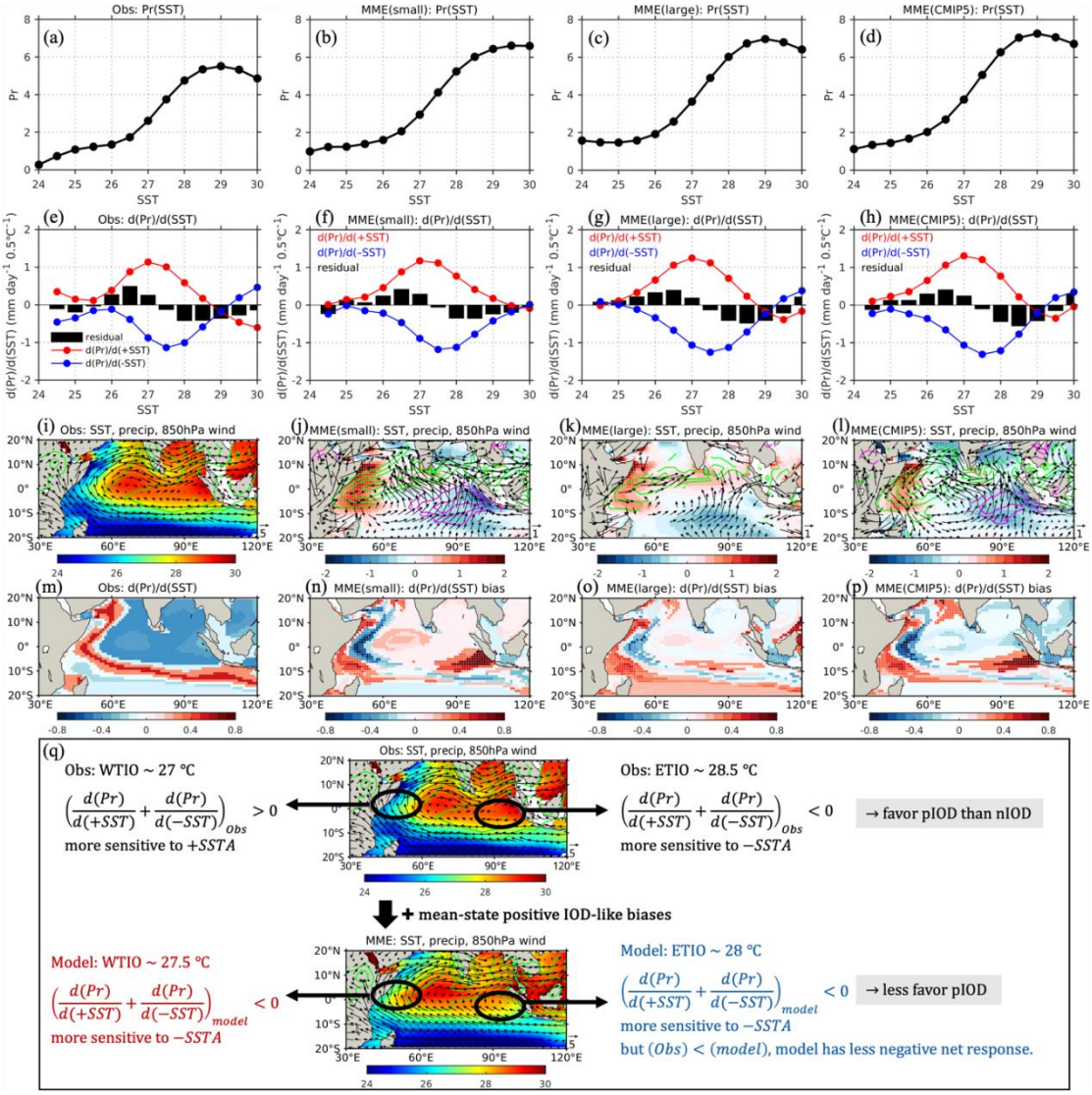


Figure 4.8. (a, b, c, d) Average precipitation (unit: mm day^{-1}) with respect to SST (unit: ℃) and (e, f, g, h) precipitation responses to SST changes (unit: mm day^{-1} 0.5℃$^{-1}$), based on (a, e) observations, (b, f) less-skewed CMIP6 model group, (c, g) more-

skewed CMIP6 model group and (d, h) CMIP5 models. Red (blue) line gives precipitation change due to a 0.5°C increase (decrease) in SST and black bar is net precipitation response. (i) Mean-state SST (shading; unit: ℃), precipitation (contour, in intervals of 3 mm day^{-1}) and 850 hPa wind (see scale vector in lower right; unit: m s^{-1}) and (m) net precipitation response (unit: mm day^{-1} $0.5℃^{-1}$) during JASO in observations. (j, k, l) Mean state biases of SST, precipitation and 850 hPa wind and (n, o, p) net precipitation response, based on (j, n) less-skewed CMIP6 model group, (k, o) more-skewed CMIP6 model group and (l, p) CMIP5 models. White stippling indicates the 95% significance level based on Student's t-test. (q) Schematic diagram illustrating how mean-state positive IOD-like biases affect atmospheric response to SSTA. In observation, WTIO (ETIO) captures larger precipitation response to positive (negative) SSTA than to negative (positive) SSTA, favoring the pIOD with stronger atmospheric response. In models with mean-state positive IOD-like biases, warmer WTIO results in less (more) precipitation response to positive (negative) SSTA and colder ETIO causes less negative net precipitation response, leading to weaker atmospheric response during pIOD, less favor of pIOD and less IOD asymmetry.

To understand how asymmetric precipitation changes with SSTA, we can compute the net convective response from a given mean-state SST. Fig. 4.8i shows the observed mean-state SST during JASO, and Fig. 4.8m shows its corresponding net convective response. The observations reveal that the WTIO has a mean-state SST of about 27 ℃ during JASO, which means that positive SSTAs trigger stronger convection than negative SSTAs, resulting in a positive net convective response. On the other hand, the ETIO has a mean-state SST of about 28.5 ℃, which means that negative SSTAs induce more precipitation anomalies than positive SSTAs, resulting in a negative net convective response. In the models with significantly mean-state positive IOD-like biases, the WTIO becomes warmer and less sensitive to positive SSTAs, leading to less positive net convective response. While the ETIO becomes colder and induces less negative net convective response. For more-skewed CMIP6 models, there are weaker warm WTIO bias and minor ETIO bias, accompanied by less convective response biases except the slightly negative net convective response bias in the WTIO. Thus, these models can simulate comparable atmospheric response and nonlinear zonal advection during pIOD. In contrast, mean-state positive IOD-like biases are evident in both the less-skewed CMIP6 model group and CMIP5 models (Figs. 4.8j, l), resulting in less positive (negative) net convective response in the WTIO (SETIO) (Figs. 4.8n, p). These results imply that WTIO (SETIO) in these less-skewed models is less sensitive to positive (negative) SSTA than observations, leading to less atmospheric response to SSTA and weaker efficiency in the Bjerknes feedback during pIOD. In

conclusion, mean-state positive IOD-like biases contribute to less convective response and less negative nonlinear zonal advection during pIOD.

Inter-model statistics of CMIP6 also support that the simulated less IOD skewness is associated with the mean-state positive IOD-like biases. Among the CMIP6 models, models with larger mean-state SST gradient during JASO in the TIO tend to have a less positive IOD skewness, with a correlation coefficient of –0.70 (passes the 95% significance level) (Fig. 4.9a). Similarly, the models with a weaker mean-state westerly wind in the TIO during JASO, which also implies stronger positive IOD-like biases, tend to have a less positive IOD skewness, with a correlation coefficient of 0.67 (significant at the 95% level) (Fig. 4.9b). As mentioned above, mean-state biases would affect nonlinear zonal advection by modulating the sensitivity of atmospheric response to SST changes. Weaker mean-state westerly in the TIO during JASO, that is, stronger mean-state positive IOD-like biases, reduces the mean-state negative nonlinear zonal advection by decreasing the west-east net convective response gradient. Notably, the west-east net convective response gradient is highly correlated with the IOD skewness, with a correlation of 0.68 (passes the 95% significance level) (Fig. 4.9c).

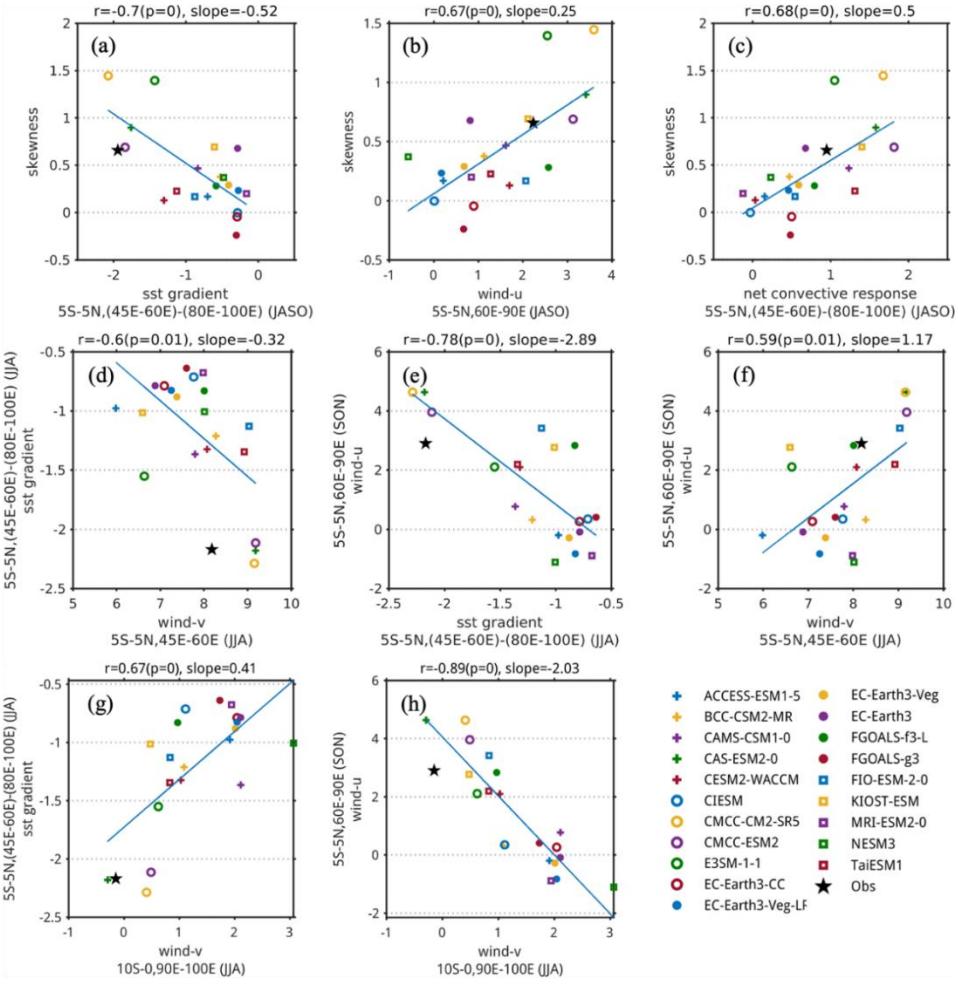


Figure 4.9. Mean state in observations and CMIP6 models. (a) SST gradient (unit: ℃; 45°–60°E minus 80°–100°E, 5°S–5°N; JASO) vs IOD skewness. (b) Surface zonal wind (unit: m s^{-1}; 5°S–5°N, 60°–90°E; JASO) vs IOD skewness. (c) Net convective response gradient (unit: mm day^{-1} 0.5℃$^{-1}$; 45°–60°E minus 80°–100°E, 5°S–5°N; JASO) vs IOD skewness. (d) Surface meridional wind (unit: m s^{-1}; 5°S–5°N, 45°–60°E; JJA) vs SST gradient (unit: ℃; 45°–60°E minus 80°–100°E, 5°S–5°N; JJA). (e) SST gradient (unit: ℃; 45°–60°E minus 80°–100°E, 5°S–5°N; JJA) vs surface zonal wind (unit: m s^{-1}; 5°S–5°N, 60°–90°E; SON). (f) Surface meridional wind (unit: m s^{-1}; 5°S–5°N, 45°–60°E; JJA) vs surface zonal wind (unit: m s^{-1}; 5°S–5°N, 60°–90°E; SON). (g) Surface meridional wind (unit: m s^{-1}; 10°S–0°, 90°–100°E; JJA) vs SST gradient (unit: ℃; 45°–60°E minus 80°–100°E, 5°S–5°N; JJA). (h) Surface meridional wind (unit: m s^{-1}; 10°S–0°, 90°–100°E; JJA) vs surface zonal wind (unit: m s^{-1}; 5°S–5°N, 60°–90°E; SON). Blue line is the least square linear fit. The r value is the correlation coefficient.

Previous studies have mentioned that CMIP models frequently exhibit positive IOD-like biases in the mean state, which is associated with the weaker simulation of Indian summer monsoon (Li et al. 2015; Long et al. 2020). Our results also support the hypothesis that the surface meridional wind bias in the WTIO is responsible for the seasonally dependent IOD-like biases. Models with a weaker summer monsoon in JJA tend to develop larger TIO SST gradient bias in JJA, with a correlation coefficient of –0.60 (Fig. 4.9d). The mean-state TIO SST gradient in JJA and the mean-state TIO surface zonal wind in SON are correlated at 0.78, suggesting that JJA SST gradient bias drives the SON easterly bias in the TIO (Fig. 4.9e). Weaker simulated Indian summer monsoon leads to warmer mean conditions of WTIO in JJA; at the same time, Bjerknes feedback amplifies the TIO SST gradient and easterly biases in SON (Fig. 4.9f). On the other hand, the simulation of surface meridional wind near the Sumatra-Java coast likewise promotes the growth of positive IOD-like biases. The presence of stronger mean-state southeasterly wind in JJA leads to the cooling of ETIO through the wind-forced Ekman transport, thus facilitating the formation of a more pronounced easterly bias in SON (Figs. 4.9g, h).

Figure 4.10 depicts the MME patterns of SST, precipitation, and 850 hPa wind biases. These patterns provide additional insight into the development of IOD-like biases from June to October. The less-skewed CMIP6 model group and CMIP5 models show stronger positive IOD-like biases than the more-skewed CMIP6 model group, with much warmer WTIO, cooler ETIO, and stronger TIO easterly bias (Figs. 4.10f–t). In June, weaker WTIO southerly wind generates warmer WTIO in the less-skewed models (Figs. 4.10f, p). Through the Bjerknes feedback, this WTIO warm bias grows

and peaks during July–September (JAS), leading to significant ETIO cold bias and stronger TIO easterly bias during August–October (ASO) (Figs. 4.10g–j, q–t). In addition, the southeasterly wind bias near the Sumatra-Java coast in summer also helps the development of the ETIO cold bias and the TIO easterly bias (Figs. 4.10f–g, p–q). The southeasterly wind bias may be related to the stronger simulated Mascarene High. In summary, weaker Indian summer monsoon and stronger Sumatra-Java coastal wind cause mean-state positive IOD-like biases that reduce the positive (negative) net convective response in the WTIO (ETIO), leading to weaker easterly anomalies during pIOD, less negative mixed-layer nonlinear zonal advection, and ultimately less simulated IOD skewness in models.

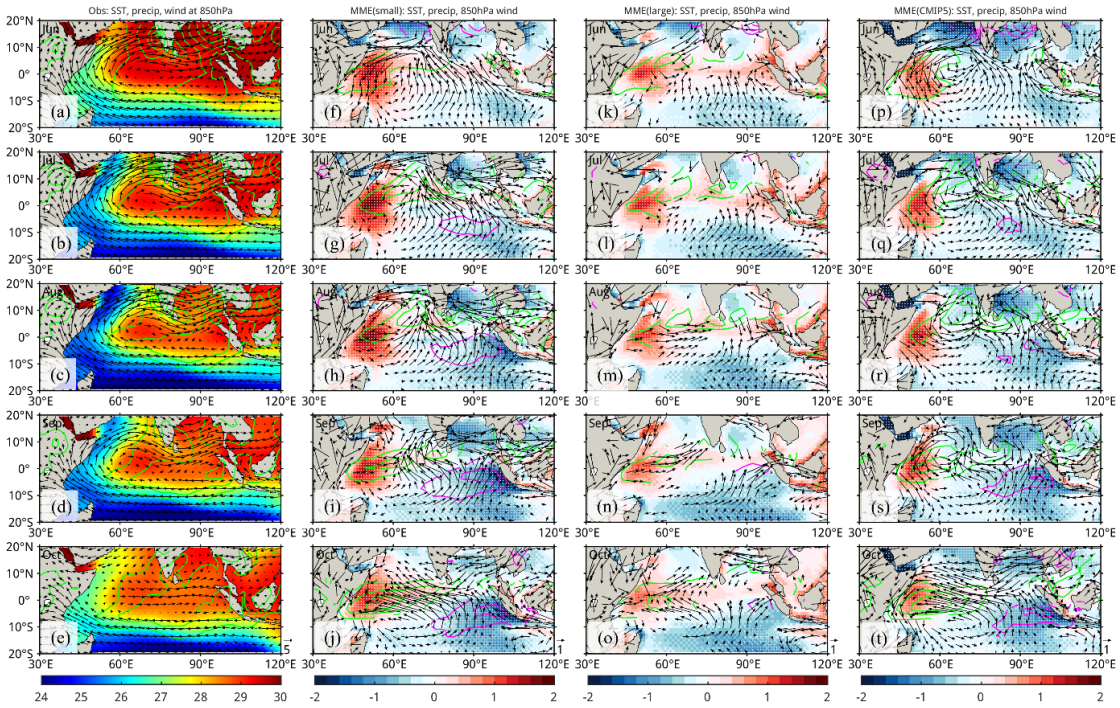


Figure 4.10. (a, b, c, d, e) Mean-state SST (shading; unit: ℃), precipitation (contours in intervals of 3 mm day^{-1}) and 850 hPa wind (see scale vector in lower right; unit: m s^{-1}) from June to October in observations. Mean-state biases of SST, precipitation, 850 hPa wind based on (f, g, h, i, j) less-skewed CMIP6 model group, (k, l, m, n, o) more-skewed CMIP6 model group and (p, q, r, s, t) CMIP5 models. Biases of SST (white stippling), precipitation and wind are shown when exceeding the 95% significance level based on Student's t-test.

4.3. Model biases in nonlinear vertical advection

Nonlinear vertical advection is another important factor in IOD. Figs. 4.11 and 4.12 show the composite patterns of nonlinear vertical advection, vertical velocity anomalies, and vertical temperature gradient anomalies at the base of the mixed layer during pIOD and nIOD, respectively. In observations, both anomalous easterly and

southerly winds play a role in contributing to anomalous upwelling at the equator and near the Sumatra-Java coast during pIOD (Fig. 4.11e), leading to positive anomalous vertical temperature gradient and cold nonlinear vertical advection (Figs. 4.11a, i). Note that the maximum temperature amplitude is located at the subsurface layer so that the MLT anomalies are smaller than those below the mixed layer, forming a positive anomalous vertical temperature gradient in pIOD. Negative nonlinear vertical advection emerges in nIOD as well (Fig. 4.12a). The response of vertical motion to wind anomaly tends to be linear (Figs. 4.11e, 4.12e), while the response of vertical temperature gradient is nonlinear (Figs. 4.11i, 4.12i) and it enlarges the negative nonlinear vertical advection during pIOD, favoring the IOD asymmetry.

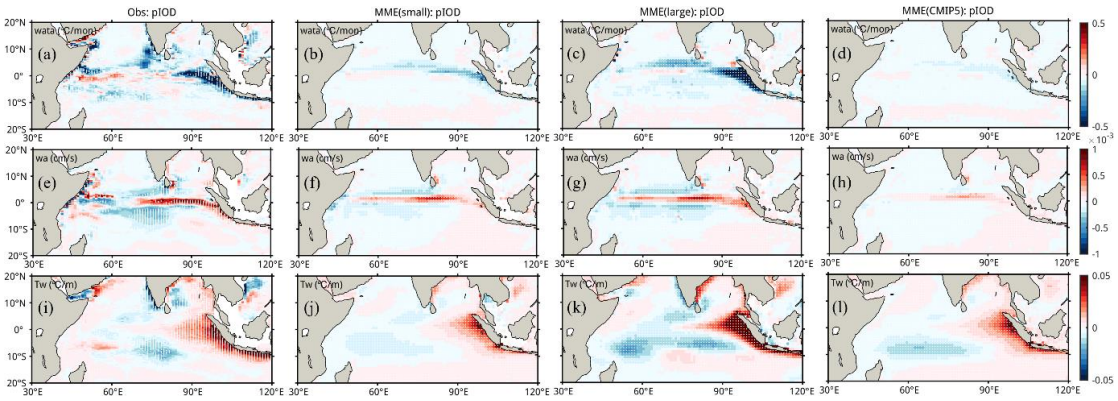


Figure 4.11. Positive IOD composites during JASO for (a, b, c, d) nonlinear vertical advection (unit: °C month^{-1}), (e, f, g, h) vertical velocity anomalies (unit: 10^{-3} cm s^{-1}) and (i, j, k, l) vertical temperature gradient anomalies at the base of mixed layer (unit: °C m^{-1}), based on (a, e, i) observations, (b, f, j) less-skewed CMIP6 model group, (c, g, k) more-skewed CMIP6 model group and (d, h, l) CMIP5 models. White stippling indicates the 95% significance level based on Student's t-test.

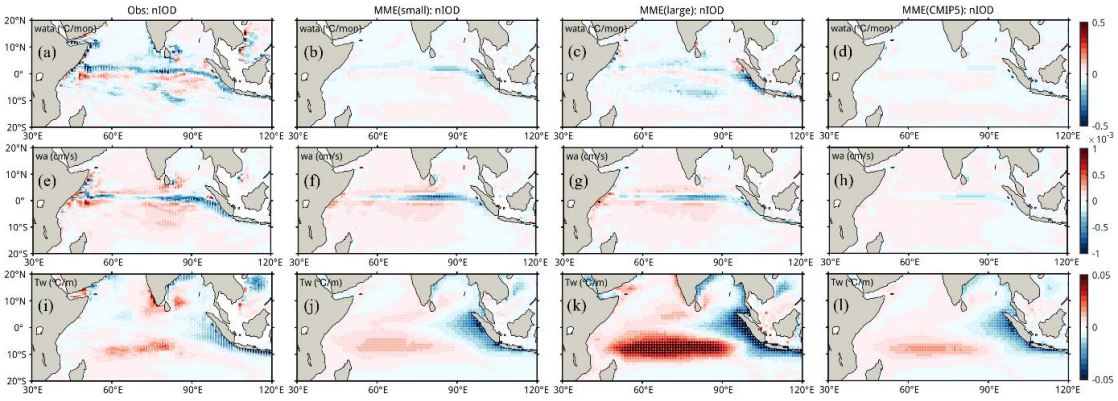


Figure 4.12. Same as Fig.4.11, but for negative IOD.

Observations and CMIP5/6 models share similar composite patterns of nonlinear vertical advection and its associated variables. During pIOD, the ETIO nonlinear

vertical advection in the more-skewed CMIP6 model group is comparable to observations and notably larger than that in the less-skewed CMIP6 model group (Figs. 4.11a–c). This is mainly due to the larger simulations of anomalous vertical temperature gradient (Figs. 4.11i–k). In terms of nIOD, both CMIP6 groups can capture variations in nonlinear vertical advection as in observations, with slightly higher values in the more-skewed CMIP6 model group (Figs. 4.12a–c). The CMIP5 models have the weakest MME nonlinear vertical advection (Figs. 4.11d, 4.12d), which is related to the small variations in vertical motion (Figs. 4.11h, 4.12h). Since there is no vertical velocity (wo) variable output in CMIP5 models, vertical motion is derived from vertical mass transport (wmo), which may introduce biases in the derived vertical motion.

The nonlinear response of SST to thermocline changes is important in developing positive IOD skewness in observations. SLA versus SSTA in the ETIO (Fig. 4.13a) illustrates this nonlinear relationship (α = –0.15, α is the nonlinear coefficient of a quadratic function), indicating that ETIO SST is more sensitive to a shallower thermocline. In comparison to observations, most of the CMIP5/6 models exhibit reduced nonlinear SST response to the thermocline changes. Only the more-skewed CMIP6 model group can capture the nonlinear relationship between SLA and SSTA (α = –0.13) (Fig. 4.13c), indicating improved simulation of this nonlinear relationship in these CMIP6 models. In the other two groups, the relationship between SLA and SSTA remains linear (Figs. 4.13b, d), implying a smaller SST response to a shallower thermocline.

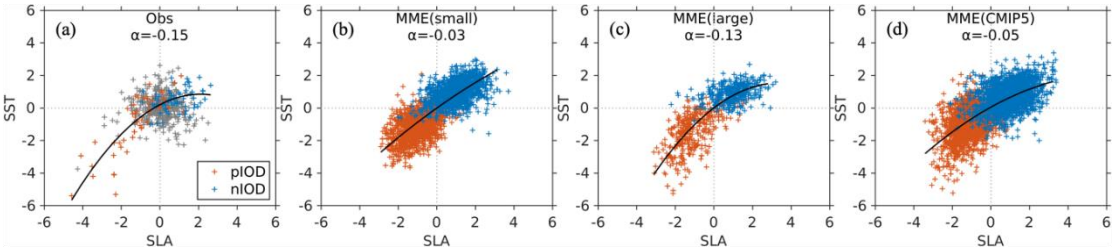


Figure 4.13. Standardized monthly SLA (8°S–2°N, 85°–110°E) vs SSTA (8°S–2°N, 85°–110°E) based on (a) observations, (b) less-skewed CMIP6 model group, (c) more-skewed CMIP6 model group and (d) CMIP5 models. Red (blue) crosses refer to positive (negative) IOD during JJASON. (b) to (d) consist of data during IOD events only. Black curve gives a quadratic fit of SLA and SST, and α is the nonlinear coefficient.

The nonlinear SST response to thermocline changes is tightly related to the background upper-ocean temperature. Previous research using CMIP5 models showed that IOD skewness is caused by asymmetric thermocline feedback, which is associated

with the mean-state simulation of thermocline (Ng et al. 2014; Ng and Cai 2016). Here, we find that ocean stratification in the ETIO accounts for simulated IOD skewness by affecting the MLT response to thermocline changes. In fact, ocean stratification in the ETIO is positively correlated with simulated IOD skewness (r = 0.70) (Fig. 4.14a), whereas thermocline (Z20) is negatively correlated with the simulated IOD skewness (r = –0.53) (Fig. 4.14b) among selected CMIP6 models. An enhanced ocean stratification contributes to a stronger anomalous vertical temperature gradient. Although a shallower thermocline may sometimes weaken the asymmetry of thermocline-SST feedback (Cai et al. 2013), a stronger MLT response to thermocline changes would enlarge the anomalous vertical temperature gradient during both pIOD and nIOD, all leading to more negative nonlinear vertical advection and positive IOD skewness.

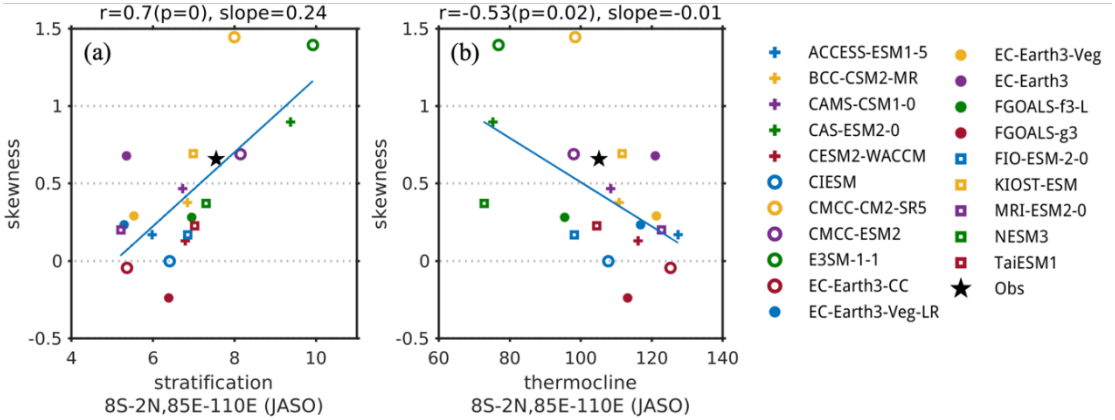


Figure 4.14. Mean ocean state in observations and CMIP6 models. (a) Ocean stratification (unit: °C; 8°S–2°N, 85°–110°E; JASO) vs IOD skewness. (b) Thermocline (Z20; unit: m; 8°S–2°N, 85°–110°E; JASO) vs IOD skewness. Blue line is the least square linear fit. The r value is the correlation coefficient. The ocean stratification is calculated as the difference between the mean temperature over the upper 60 m and the temperature averaged from 90 m to 120 m.

Fig. 4.15 depicts the vertical patterns of MLD and temperature from June to October. The less-skewed CMIP6 model group and CMIP5 models have similar vertical temperature patterns, with a deeper MLD in the TIO, deeper thermocline in the WTIO, significant warm bias in the WTIO, and slightly cold bias in the ETIO between 60 m and 150 m depth (Figs. 4.15f–j, p–t). These biases are consistent with the strong positive IOD-like biases in the mean state. Through the Bjerknes feedback loop, an easterly wind bias develops along the equator, causing unrealistic thermocline tilting and significantly warmer (colder) mean temperatures over the upper WTIO (ETIO) in SON. On the other hand, the more-skewed CMIP6 model group has more realistic

thermocline depths in most regions, except for a slightly shallower thermocline in the ETIO (Figs. 4.15k–o). Despite having larger cold temperature biases within the ETIO, the more-skewed CMIP6 model group can simulate more realistic nonlinear vertical advection with the help of stronger ocean stratification. Increased mean-state ocean stratification promotes larger anomalous vertical temperature gradients during IOD, resulting in more negative nonlinear vertical advection and larger IOD skewness. Therefore, better simulations of upper-ocean temperature and oceanic responses in the ETIO are important to reproduce a realistic IOD skewness.

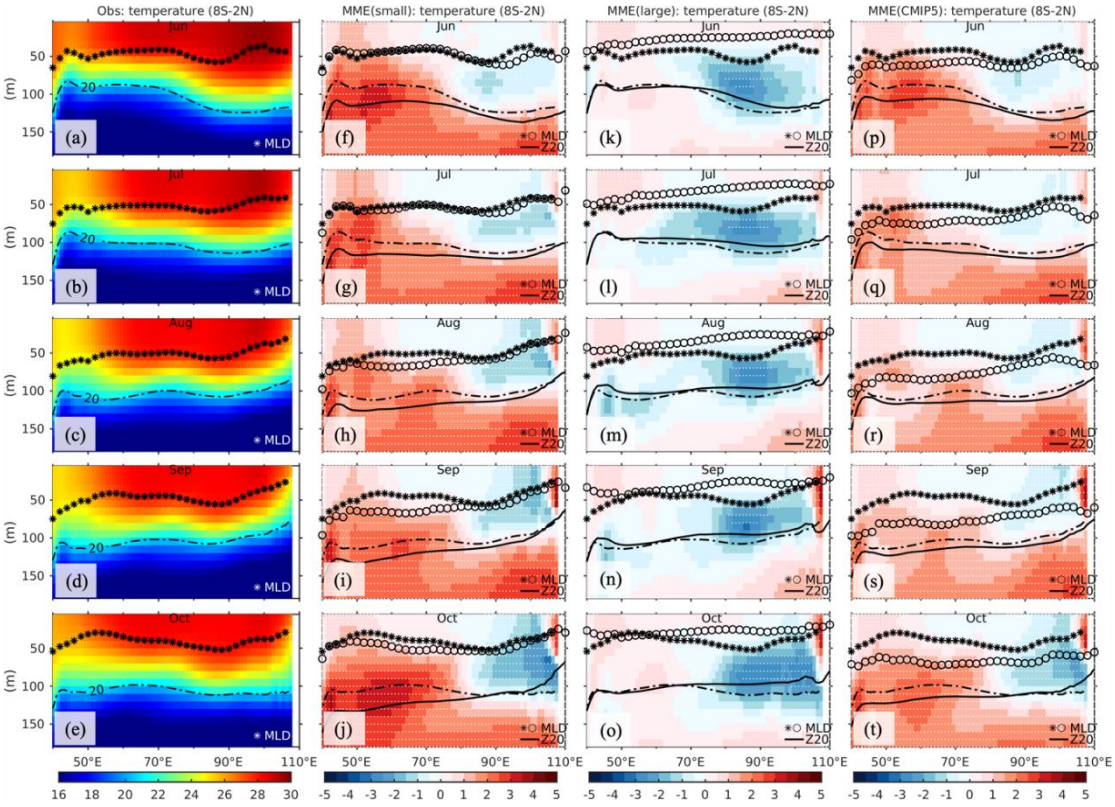


Figure 4.15. (a, b, c, d, e) Mean-state vertical cross sections of temperature (unit: ℃) averaged over 8°S–2°N from June to October in observations. Temperature biases based on (f, g, h, i, j) less-skewed CMIP6 model group, (k, l, m, n, o) more-skewed CMIP6 model group and (p, q, r, s, t) CMIP5 models. Asterisk (circle) denotes observed (simulated) MLD. Black dash-dot (solid) contour is observed (simulated) Z20. White stippling indicates the 95% significance level based on Student's t-test.

4.4. Nonlinear meridional advection

Nonlinear meridional advection acts as the damping term in the negative NDH. Figs. 4.16 and 4.17 show composite patterns of nonlinear meridional advection during pIOD and nIOD, respectively. The observed nonlinear meridional advection during IOD is small (less than 0.2 ℃ month^{-1}), with positive values in the SETIO and somewhat negative values near the equator (Figs. 4.16a, 4.17a). In CMIP5/6 models,

nonlinear meridional advection is also a minor contributor to NDH (Figs. 4.16b–d, 4.17b–d). During pIOD (nIOD), CMIP models simulate significant positive (negative) anomalous meridional temperature gradient in the northern ETIO (NETIO) and negative (positive) gradient in the SETIO (Figs. 4.16j–l, 4.17j–l). These meridional temperature gradient anomalies are comparable to or slightly larger than the anomalous zonal temperature gradient. However, since the anomalous zonal current is greatly boosted by the Bjerknes feedback, it is nearly four times larger than the anomalous meridional current. Hence, nonlinear meridional advection can be easily offset by the other two NDH terms. Additionally, even though the nonlinear meridional advection during pIOD in the more-skewed CMIP6 model group is greater than observations (Figs. 4.16a, c), the negative anomaly in the NETIO and positive anomaly in the SETIO tend to neutralize each other, reducing their net impact on NDH.

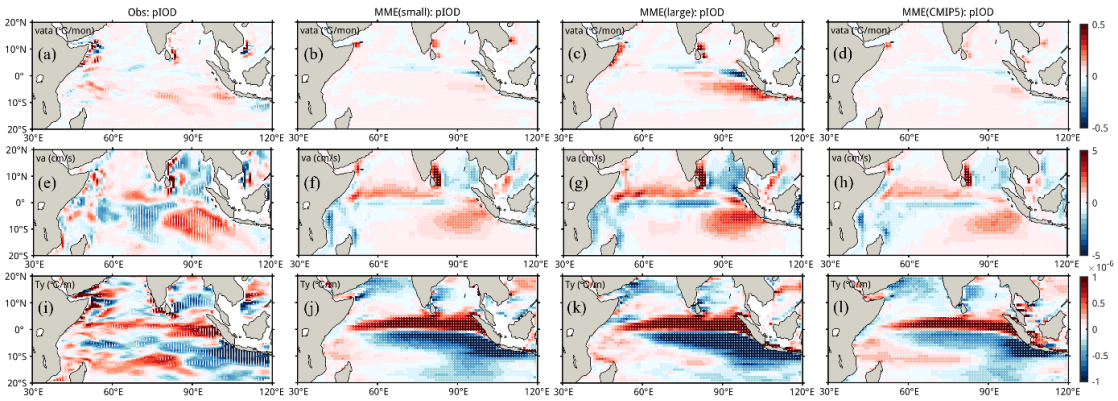


Figure 4.16. Positive IOD composites during JASO for (a, b, c, d) nonlinear meridional advection (unit: °C month^{-1}), (e, f, g, h) meridional mixed-layer current anomalies (unit: cm s^{-1}) and (i, j, k, l) meridional temperature gradient anomalies within the mixed layer (unit: 10^{-6} °C m^{-1}), based on (a, e, i) observations, (b, f, j) less-skewed CMIP6 model group, (c, g, k) more-skewed CMIP6 model group and (d, h, l) CMIP5 models.

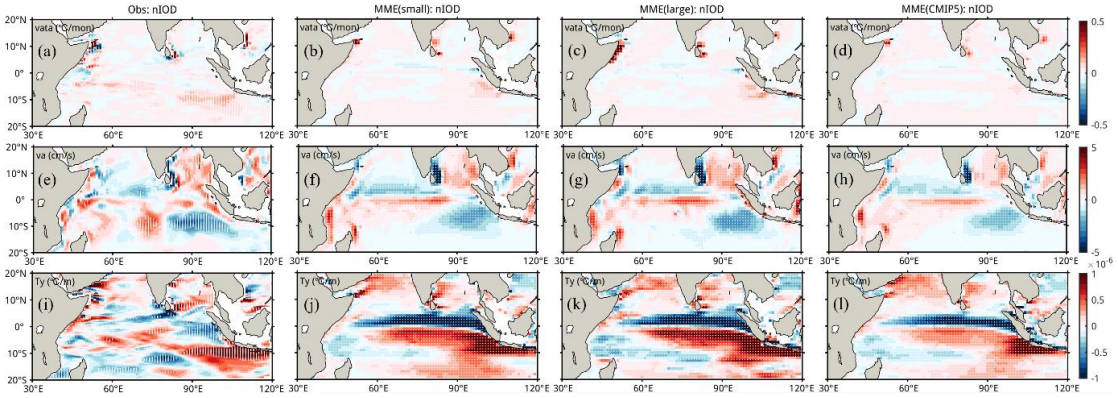


Figure 4.17. Same as Fig. 4.16, but for negative IOD.

5. Projections of IOD asymmetry by CMIP6 models

5.1. Reduction of IOD asymmetry due to global warming

Figure 5.1 depicts the multi-model averaged SSTA skewness for the summer and autumn seasons (JJASON). The historical SSTA skewness pattern shows strong negative signals over the ETIO (Fig. 5.1a), even though it is still underestimated compared to observations (Ng and Cai 2016; McKenna et al. 2020; Zheng et al. 2024). Notably, greenhouse warming brings a reduction in the intensity of negative SSTA skewness over the ETIO, with only the equatorial ETIO exhibiting negative values (Figs. 5.1b, c). The CMIP6 MME of ETIO SSTA skewness during JJASON is about –0.32 in the historical simulation. This value escalates to around –0.07 under the SSP5-8.5 scenario, reflecting a remarkable 78% increase in the ETIO SST skewness due to global warming. Boxplots are also used to depict statistical characteristics of the seasonal variations in ETIO SSTA skewness among 20 selected CMIP6 models. In the historical simulation, most models capture the seasonal fluctuations of ETIO SSTA skewness, albeit with underestimations in over half of the models compared to observations (Fig. 5.1d). It's noteworthy that significant skewness values mainly appear during the core phase of IOD, spanning from July to October. In observation, except for the JASO, November skewness is another peak value, not replicated by the selected CMIP6 models. Under the SSP5-8.5 scenario, the temporal shifts in ETIO SSTA skewness become imperceptible, with monthly skewness values nearing zero (Fig. 5.1e). The key finding is that the MME skewness change is statistically distinct from zero, indicating meaningful shifts in IOD asymmetry due to changing climate conditions.

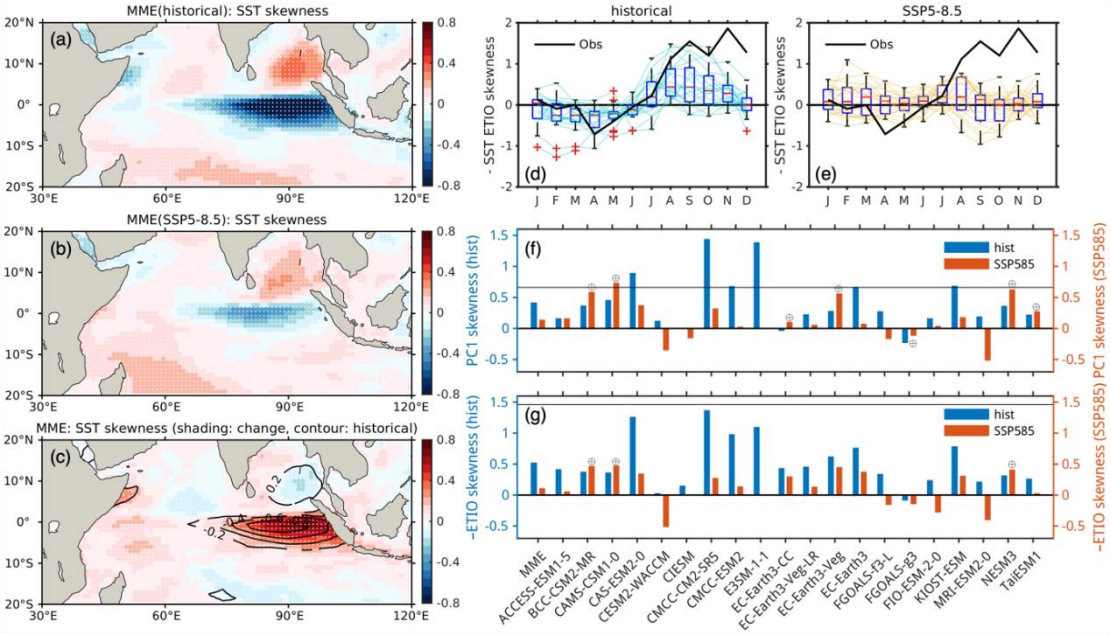


Figure 5.1. Multi-model averaged SSTA skewness during JJASON in the (a) historical and (b) SSP5-8.5 scenario simulations. Shading in (c) donates its greenhouse-warming-induced change with historical results shown by contours. White stippling indicates the 95% significance level based on Student's t-test. Seasonal fluctuations of SSTA skewness (multiplied by –1) within the ETIO (8°S–2°N, 85°–100°E) in the (d) historical and (e) SSP5-8.5 scenario simulations. Boxplot shows their median (red dash), interquartile range (blue box), lower and upper 1.5 times the interquartile range (black dash), and outlier (red + sign). The bold black solid line is the observed skewness. Skewness of (f) PC1 and (g) ETIO SSTA (multiplied by –1) during JJASON in the historical (blue bars) and SSP5-8.5 scenario (orange bars) simulations, with the black line denoting the observed skewness. Models with larger skewness in the SSP5-8.5 than the historical run are marked by a grey circle above the bar.

Out of 20 selected Earth System Models, 13 models indicate reduced IOD asymmetry, while 7 models show a slight increase based on the PC1 index (Fig. 5.1f). In the historical simulation, 6 out of 20 CMIP6 models (CAS-ESM2-0, CMCC-CM2-SR5, CMCC-ESM2, E3SM-1-1, EC-Earth3, KIOST-ESM) match or exceed observed IOD asymmetry. Under simulated greenhouse warming, only the CAMS-CSM1-0 model has a PC1 skewness reaching the observed PC1 skewness (0.66). Focusing on the IOD's eastern part, 17 CMIP6 models yield less negative SSTA skewness (Fig. 5.1g), with only BCC-CSM2-MR, CAMS-CSM1-0 and NESM3 models showing a minor tendency towards more negative SSTA skewness in the ETIO. These skewness changes are reinforced by each model's spatial SSTA skewness pattern (Fig. 5.2). It is worth noting that increased SSTA skewness in the WTIO could slightly raise IOD asymmetry in certain models, such as FGOALS-g3 and TaiESM1 models, explaining some differences between results using these two IOD indices. Given the inter-model

discrepancy and significant IOD asymmetry changes, it's essential to explore the mechanisms driving potential IOD asymmetry shifts due to global warming.

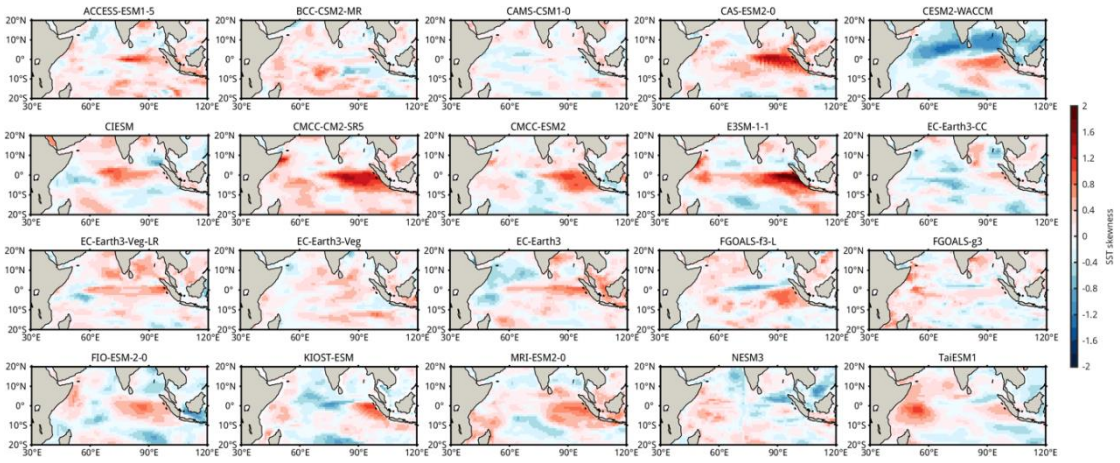


Figure 5.2. Changes in SSTA skewness during JJASON in 20 CMIP6 models.

5.2. Oceanic contribution to reduced IOD asymmetry

A heat budget analysis within the ocean mixed layer has been generally used to examine the fundamental mechanisms behind IOD (Hone et al. 2008a; Wang et al. 2020a; Cai et al. 2021). Hong et al. (2008a, b) pointed out that the nonlinear terms can be key in giving rise to the IOD amplitude asymmetry. By comparing moderate and extreme pIOD events, Yang et al. (2020) offered further validation of the significance of nonlinear zonal and vertical advection terms. Across both observations and historical simulations, the NDH significantly shapes IOD asymmetry (Zheng et al. 2024). Figure 5.3 presents the composite mixed-layer heat budget analysis for pIOD and nIOD events in historical and SSP5-8.5 scenario simulations. The JASO period is chosen so as to capture the peak phase of the heating rate during IOD. The heat budget mainly focuses on the eastern part of IOD, given its propensity to produce unusually large cooling anomalies that underscore IOD as a nonlinear system. In the historical simulation, the MLT tendency during pIOD is nearly double that of nIOD (Fig. 5.3a). Even though the net heat flux has a large amplitude, it exhibits minimal asymmetry. Nonlinear zonal and vertical advection terms are negative during both pIOD and nIOD events, with nonlinear meridional advection having small positive values which are much lower than the formers. As a result, NDH is generally negative during IOD and tends to amplify cold SSTAs but damp warm anomalies in the ETIO, strengthening pIOD but weakening nIOD. Additionally, the influence of lateral induction on IOD development and asymmetry proves relatively minor. In future projections, the MLT tendency during

nIOD surges to roughly twice as much as that during pIOD (Fig. 5.3b), which is a reversal from historical simulations. The future net heat flux still varies greatly but shows little asymmetry. In terms of NDH, the nonlinear zonal advection becomes less negative relative to the historical run, especially during pIOD (Fig. 5.3c). While the overall composite of nonlinear vertical advection remains similar, showing marginally less negative during pIOD and slightly more negative during nIOD. There is still little contribution from the oceanic subsurface entrainment to the MLT tendency changes.

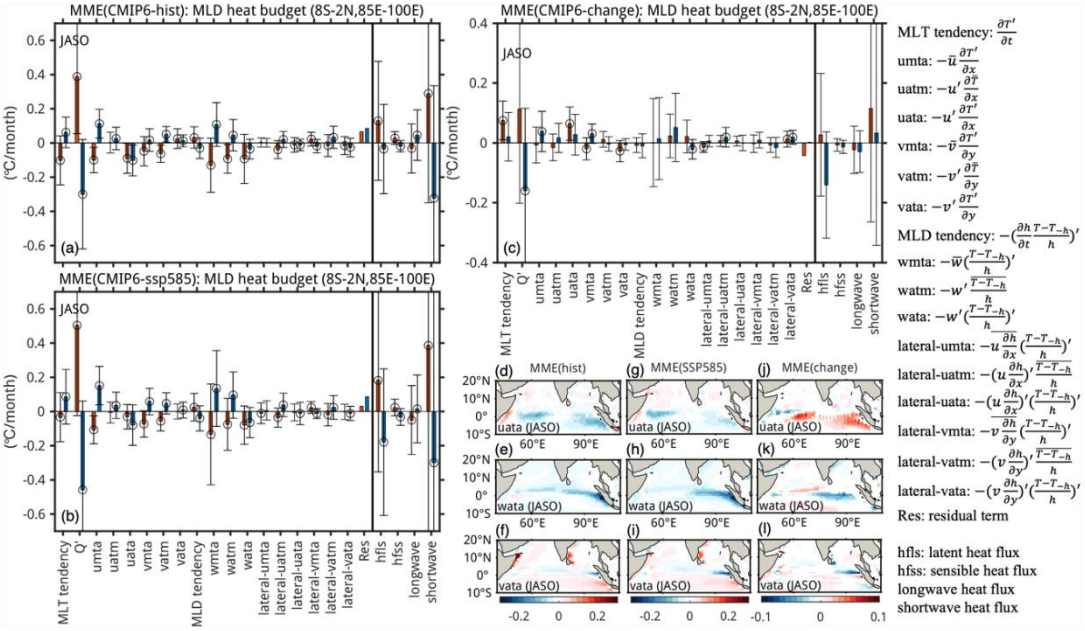


Figure 5.3. IOD composite during JASO for mixed-layer heat budget within the ETIO (8°S–2°N, 85°–100°E) in the (a) historical, (b) SSP5-8.5 scenario simulations and (c) their greenhouse-warming-induced changes. The error bar is based on one STD. A circle over the bar indicates signals that are statistically significant at the 95% significance level. Long-term mean (d) nonlinear zonal advection (units: °C month^{-1}), (e) nonlinear vertical advection and (f) nonlinear meridional advection during JASO based on historical simulations. (g, h, i) are the same as (d, e, f), but for the SSP5-8.5 scenario simulations. (j, k, l) are the same as (d, e, f), but for changes. Shading values are shown when exceeding the 95% significance level based on the Student's t-test.

To provide a clearer understanding, detailed values of ocean advection terms are shown in Table 5.1. During pIOD, the amplitude of nonlinear zonal advection experiences a significant reduction from –0.090 °C month^{-1} to –0.031 °C month^{-1}, resulting in a difference up to 0.059 °C month^{-1}. Similarly, nIOD composite exhibits less negative nonlinear zonal advection, with a difference of 0.022 °C month^{-1}. On the other hand, the nonlinear vertical advection is slightly less negative during pIOD (a difference of 0.015 °C month^{-1}) but turns more negative during nIOD (a difference of –0.032 °C month^{-1}). The nonlinear meridional advection becomes less positive (with a

difference of –0.026 °C month^{-1}) during pIOD but nearly no change during nIOD. The nonlinear zonal advection change dominates NDH changes, less favoring pIOD and less damping nIOD. As for the amplitude development, the $-\bar{u}(\partial T'/\partial x)$ term becomes a larger contributor to the nIOD development mainly due to the enhanced westward mixed-layer zonal current under greenhouse warming. Furthermore, the thermocline feedback (associated with the $-\bar{w}[(T-T_{-h})/h]'$ term) and Ekman pumping feedback (associated with the $-w'\overline{(T-T_{-h})/h}$ term) are the other two important processes for IOD development. The thermocline feedback remains nearly unchanged during pIOD but undergoes a slight increase during nIOD. The Ekman pumping feedback is significantly conducive to the development of nIOD, with a value of 0.106 °C month^{-1} compared to the historical value of 0.050 °C month^{-1}. The outcomes of the long-term mean nonlinear zonal, vertical and meridional advection within the mixed layer (Figs. 5.3d–l) are consistent with the composite budget findings (Figs. 5.3a–c). The historical nonlinear zonal advection exhibits noticeably negative signals in the ETIO (Fig. 5.3d), but the SSP5-8.5 nonlinear zonal advection becomes less negative in the ETIO (Figs. 5.3g, j). On the contrary, the nonlinear vertical and meridional advection terms have little change under greenhouse warming (Figs. 5.3e–l). Both the long-term mean and variability of the nonlinear zonal advection become less negative under the SSP5-8.5 scenario, contributing to the reduction of IOD asymmetry.

budget term	pIOD			nIOD		
	historical	SSP5-8.5	change	historical	SSP5-8.5	change
$-\bar{u}\frac{\partial T'}{\partial x}$	–0.101	–0.108	–0.007	0.112	0.151	0.039
$-u'\frac{\partial \bar{T}}{\partial x}$	0.002	–0.007	–0.009	0.026	0.035	0.010
$-u'\frac{\partial T'}{\partial x}$	–0.090	–0.031	0.059	–0.102	–0.080	0.022
$-\bar{v}\frac{\partial T'}{\partial y}$	–0.049	–0.073	–0.025	0.016	0.057	0.041
$-v'\frac{\partial \bar{T}}{\partial y}$	–0.064	–0.057	0.006	0.050	0.047	–0.004
$-v'\frac{\partial T'}{\partial y}$	0.025	–0.001	–0.026	0.013	0.008	–0.004
$-\bar{w}(\frac{T-T_{-h}}{h})'$	–0.145	–0.150	–0.005	0.120	0.149	0.029
$-w'\overline{\frac{T-T_{-h}}{h}}$	–0.104	–0.084	0.020	0.050	0.106	0.056

$-w'(\frac{T-T_{-h}}{h})'$	–0.104	–0.090	0.015	–0.040	–0.072	–0.032

Table 5.1. Composite mixed-layer advection terms (unit: ℃ month^{-1}) in pIOD and nIOD during JASO within 8°S–2°N, 85°–100°E, including their historical values, SSP5-8.5 scenario values and greenhouse-warming-induced changes.

Figure 5.4 is the composite JASO nonlinear zonal advection during pIOD and nIOD in the historical and SSP5-8.5 simulations. During pIOD, the generated easterly wind anomalies induce westward zonal current anomalies and shift the anomalously cold temperature from east to west, forming negative zonal temperature gradient anomalies and negative nonlinear zonal advection (Figs. 5.4a, d, g). Conversely, nIOD produces westerly anomalies, eastward current anomalies and positive zonal temperature gradient anomalies, also resulting in negative nonlinear zonal advection (Figs. 5.4j, m, p). Both pIOD and nIOD cause anomalous zonal cold advection, prompting cooling in the affected region. Due to greenhouse warming, the surface wind anomalies become weaker compared to the historical results (Fig. 5.5). Specifically, the composite surface zonal wind anomalies are notably smaller (Figs. 5.5c, f), causing weaker zonal current anomalies (Figs. 5.4f, o) and zonal MLT gradient anomalies (Figs. 5.4i, r). This overall weakening reduces the magnitude of the negative nonlinear zonal advection in the ETIO. Moreover, under the SSP5-8.5 scenario, the coastal wind anomaly near the Sumatra-Java coast in pIOD is weaker than that in nIOD, further decreasing the zonal MLT gradient anomalies near the Sumatra-Java coast and the magnitude of the negative nonlinear zonal advection during pIOD.

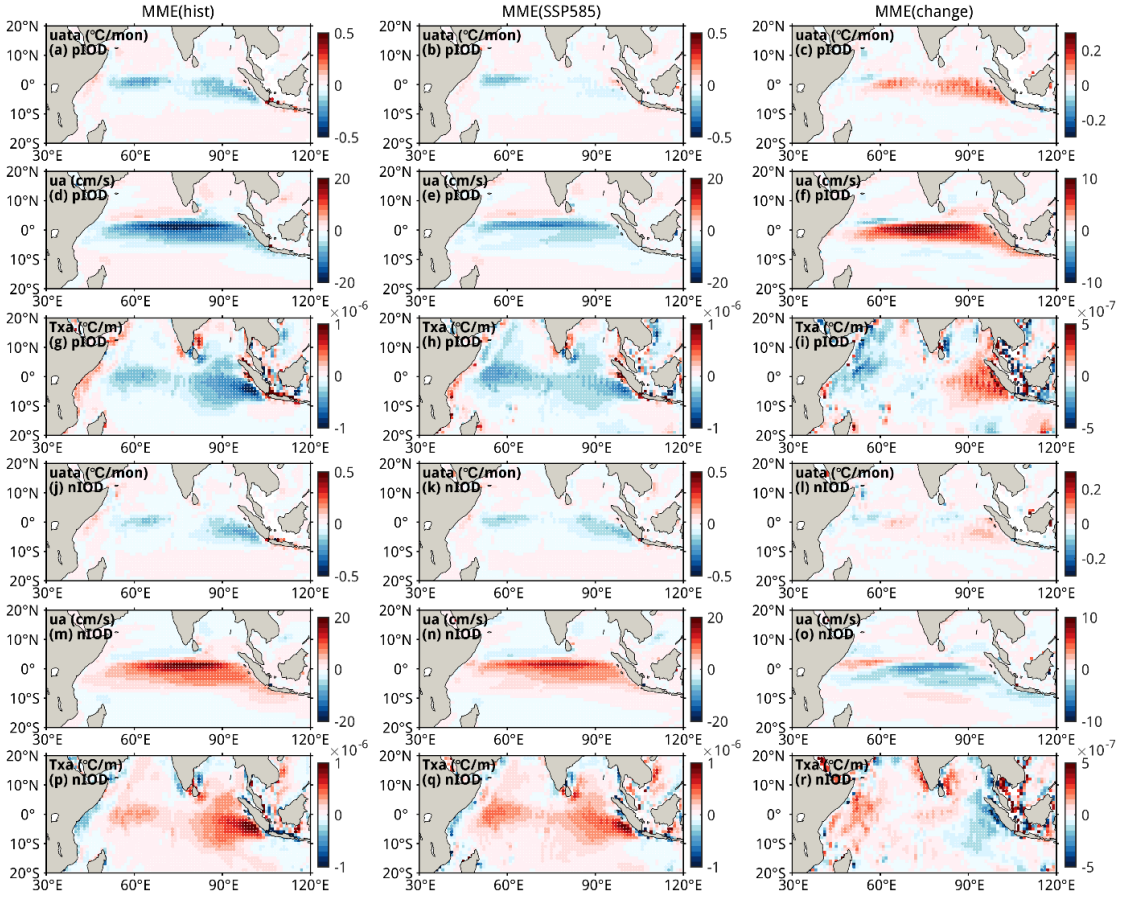


Figure 5.4. IOD composites during JASO for (a, b, c, j, k, l) nonlinear zonal advection (units: °C month^{-1}), (d, e, f, m, n, o) zonal current anomalies (units: cm s^{-1}) and (g, h, i, p, q, r) zonal MLT gradient anomalies (units: °C m^{-1}) based on (a, d, g) historical pIOD, (b, e, h) SSP5-8.5 pIOD, (c, f, i) pIOD changes, (j, m, p) historical nIOD, (k, n, q) SSP5-8.5 nIOD and (l, o, r) nIOD changes. White stippling is shown when exceeding the 95% significance level based on Student's t-test.

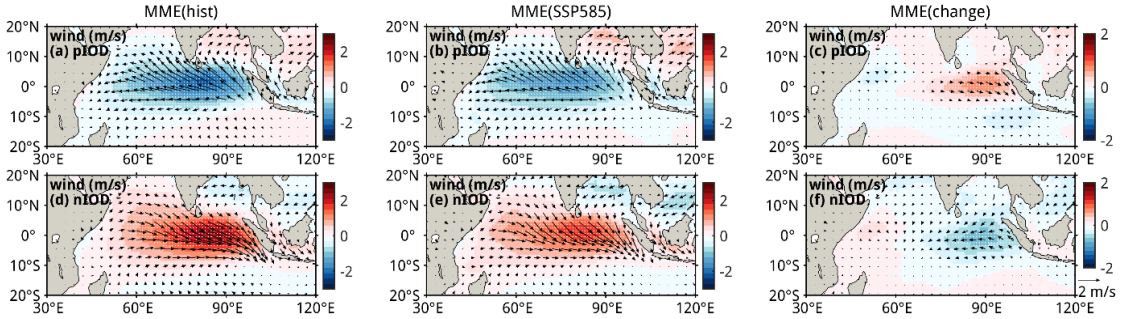


Figure 5.5. IOD composites during JASO for surface wind anomalies (see scale vector in lower right; units: m s^{-1}; shading is surface zonal wind anomaly) based on (a) historical pIOD, (b) SSP5-8.5 pIOD, (c) pIOD changes, (d) historical nIOD, (e) SSP5-8.5 nIOD and (f) nIOD changes. White stippling and vectors are shown when exceeding the 95% significance level based on Student's t-test.

Inter-model statistics of selected CMIP6 models also support that the nonlinear zonal advection becomes weaker due to greenhouse warming. The ensemble mean as

well as the majority of individual models exhibit a decrease in the variance of nonlinear zonal advection (Fig. 5.6a). Specifically, the MME variance of nonlinear zonal advection reduces from 0.19 °C month^{-1} in the historical simulation to 0.16 °C month^{-1} in the SSP5-8.5 scenario simulation, indicating a 16% decrease. This decline in variance is associated with the weaker surface wind response to SSTAs in the TIO (Fig. 5.6c). The atmospheric convective response to SSTAs and the zonal wind response to atmospheric convective anomalies are both projected to weaken slightly in the TIO under the SSP5-8.5 scenario. Consequently, the surface zonal wind variance over the central TIO is reduced in both the ensemble mean and most individual models (Fig. 5.6b). The MME value of surface zonal wind variance, which is 1.8 m s^{-1} during 1950–1999, experiences a reduction to 1.5 m s^{-1} during 2050–2099, marking a decrease of approximately 17%. The weakened surface zonal wind variabilities indicate a decline in the efficiency of the atmospheric component of Bjerknes feedback during IOD development, which is consistent with the findings of Zheng et al. (2013) under the representative concentration pathway (RCP) 8.5 scenario. Weaker atmospheric modulation to SSTAs at the basin scale contributes to decreased variance of nonlinear zonal advection in a warmer climate. Under greenhouse warming, the lower troposphere warms faster than the surface (Figs. 5.6h–j), increasing the atmospheric static stability and weakening the response of TIO surface zonal wind to SSTAs. Inter-model statistics from CMIP6 corroborate the robust relationship between the mean-state changes in the vertical average lapse rate and the IOD skewness changes (Figs. 5.6d, e). Models with a larger lapse rate change, indicative of more increased atmospheric static stability, produce a larger decrease in IOD asymmetry. Furthermore, due to air-sea coupling, the increased atmospheric static stability is also reflected by the mean-state changes of surface zonal wind, showing weaker mean-state westerly winds in the TIO. Models demonstrating a larger reduction in mean-state westerly winds generally exhibit a larger decrease in IOD asymmetry (Figs. 5.6f, g). It should be noted that other factors, such as ENSO influences, may also contribute to the IOD asymmetry changes under global warming (Cai et al. 2019; Le and Bae 2019). In summary, the Indian Ocean is projected to experience increased atmospheric stability, leading to a reduction in large-scale atmospheric modulation to SSTAs, less negative mixed-layer nonlinear zonal advection, and ultimately less IOD asymmetry in the future.

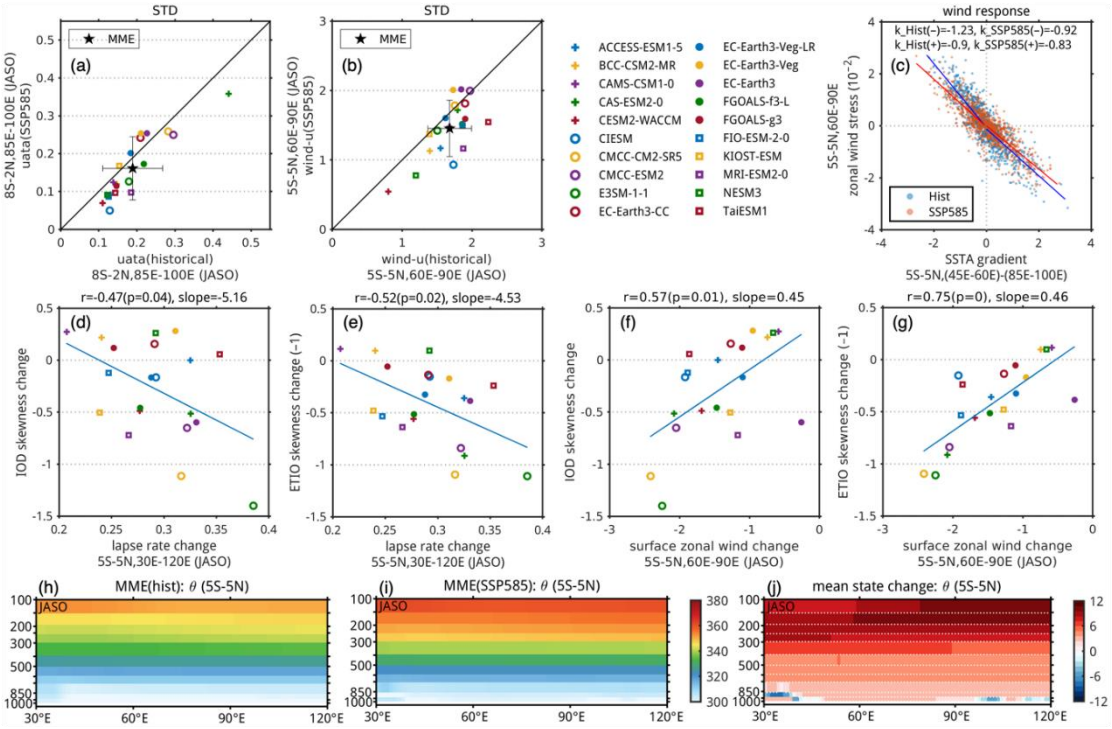


Figure 5.6. STD of (a) nonlinear zonal advection (units: °C month^{-1}; 8°S–2°N, 85°–100°E; JASO) and (b) surface zonal wind anomaly (units: m s^{-1}; 5°S–5°N, 60°–90°E; JASO) during 1950–1999 vs 2050–2099. The black star and error bar denote the ensemble mean and one STD of inter-model variability, respectively. (c) SSTA gradient (units: °C; 5°S–5°N, 45°–60°E minus 85°–100°E; JASO) vs surface zonal wind stress anomalies (units: 10^{-2} N m^{-2}; 5°S–5°N, 60°–90°E; JASO). The blue (red) line is the least squares linear fit of historical (SSP5-8.5 scenario) simulations. The k(–) [k(+)] values are the slope between two indices when SSTA gradients are smaller (larger) than zero. (d) Vertical average mean-state lapse rate change (units: °C km^{-1}; 30°E–120°E, 5°S–5°N; JASO) vs PC1 skewness change. (e) Vertical average mean-state lapse rate change vs SSTA skewness change (multiplied by –1) within ETIO (8°S–2°N, 85°–100°E; JASO). (f, g) are the same as (d, e), but for mean-state surface zonal wind change (units: m s^{-1}; 5°S–5°N, 60°–90°E; JASO). The blue line is the least squares linear fit and the r value is the correlation coefficient. (h) Historical mean state, (i) SSP5-8.5 mean state and (j) mean-state change of atmospheric potential temperature (units: K) averaged over 5°S–5°N during JASO. White stippling indicates the 95% significance level based on Student's t-test.

Observations and climate models have emphasized the role of nonlinear vertical advection in the IOD asymmetry (Hong et al. 2008a; Cai et al. 2021). Given its pivotal role, detailed research is necessary to reveal why the nonlinear vertical advection remains comparable in future simulations. Figure 5.7 provides the composite patterns involving nonlinear vertical advection, vertical velocity anomalies, and vertical temperature gradient anomalies at the base of the mixed layer during pIOD and nIOD in the historical and SSP5-8.5 simulations. Although the nonlinear vertical advection in the historical simulation displays somewhat less negative values compared to observed

results, the CMIP6 historical runs manage to capture patterns similar to those observed (Zheng et al. 2024). During pIOD, the maximum temperature amplitude appears in the subsurface layer, leading to positive vertical temperature gradient anomalies in the ETIO (Fig. 5.7g). These vertical temperature gradient anomalies, combined with wind-driven upwelling anomalies at the equatorial and Sumatra-Java coast regions (Fig. 5.7d), contribute to the negative nonlinear vertical temperature advection (Fig. 5.7a). During nIOD, the anomalous downwelling and the anomalous vertical temperature gradient are somewhat milder than those during pIOD (Figs. 5.7d, g, m, p), attributed to smaller surface wind anomalies and weaker temperature–thermocline feedback during nIOD (Cai and Qiu 2013; Ogata et al. 2013). The nonlinear vertical advection is thereby less negative during nIOD than pIOD in the historical runs. Under a warmer climate, both the upwelling during pIOD and the downwelling during nIOD become weaker in contrast to the historical runs, particularly noticeable in the equatorial regions (Figs. 5.7d–f, m–o). The anomalous vertical temperature gradient decreases slightly in pIOD but is enhanced in nIOD along the Sumatra-Java coast (Figs. 5.7g–i, p–r). Consequently, in the context of a warmer climate scenario, the nonlinear vertical advection is slightly weakened during pIOD while intensified during nIOD. These changes suggest that the reduced variance of vertical motion can be compensated by the increased vertical temperature gradient variation under the SSP5-8.5 scenario.

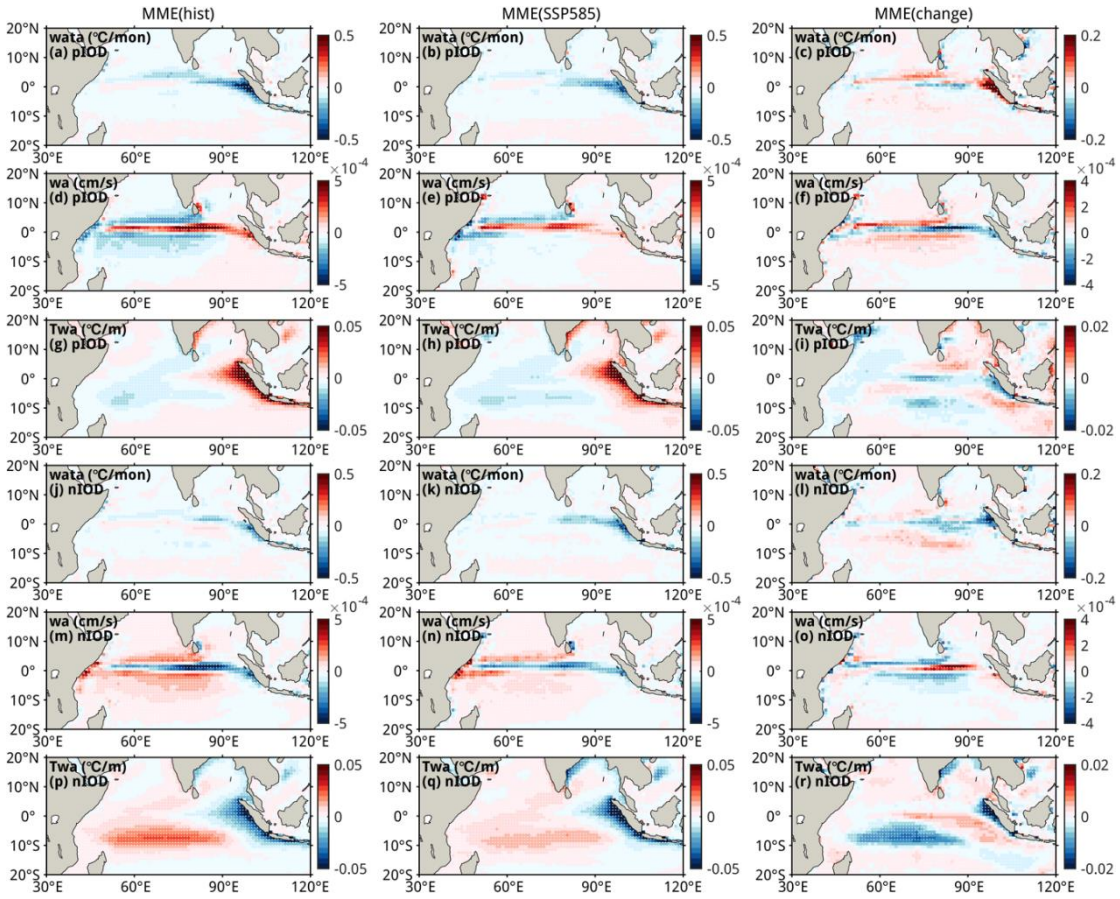


Figure 5.7. IOD composites during JASO for (a, b, c, j, k, l) nonlinear vertical advection (units: °C month^{-1}), (d, e, f, m, n, o) vertical velocity anomalies (units: cm s^{-1}) and (g, h, i, p, q, r) vertical temperature gradient anomalies at the base of mixed layer (units: °C m^{-1}), based on (a, d, g) historical pIOD, (b, e, h) SSP5-8.5 pIOD, (c, f, i) pIOD changes, (j, m, p) historical nIOD, (k, n, q) SSP5-8.5 nIOD and (l, o, r) nIOD changes. White stippling indicates the 95% significance level based on Student's t-test.

The decline in vertical motion variance during IOD is a result of diminished surface wind variance, attributed to the increased atmospheric static stability. Conversely, the amplified vertical temperature gradient anomaly stems from the enhanced upper-ocean stratification. The upper Indian Ocean experiences significant warming under the SSP5-8.5 scenario (Figs. 5.8a, b), with stronger warming within the mixed layer than the subsurface layer in the ETIO (Fig. 5.8c). In addition, the upper Indian Ocean also becomes fresher, with significant deepening of the 35 PSU isohaline between 50°E and 80°E and the westward extension of the ETIO freshwater pool (Figs. 5.8d–f). Hence, surface-intensified warming and freshening, mainly the warming component, cause enhanced upper-ocean stratification, which strengthens the response of the mixed layer to a given wind forcing (Timmermann et al. 1999; Thual et al. 2013) and promotes larger vertical temperature gradient anomalies during IOD. Thus, despite the decreased

efficiency of the atmospheric component of Bjerknes feedback due to greenhouse warming, the SSP5-8.5 yields nearly comparable nonlinear vertical advection relative to the historical simulation with the help of enhanced upper-ocean stratification in the ETIO. Therefore, changes in nonlinear vertical advection contribute minimally to the simulated changes of IOD asymmetry.

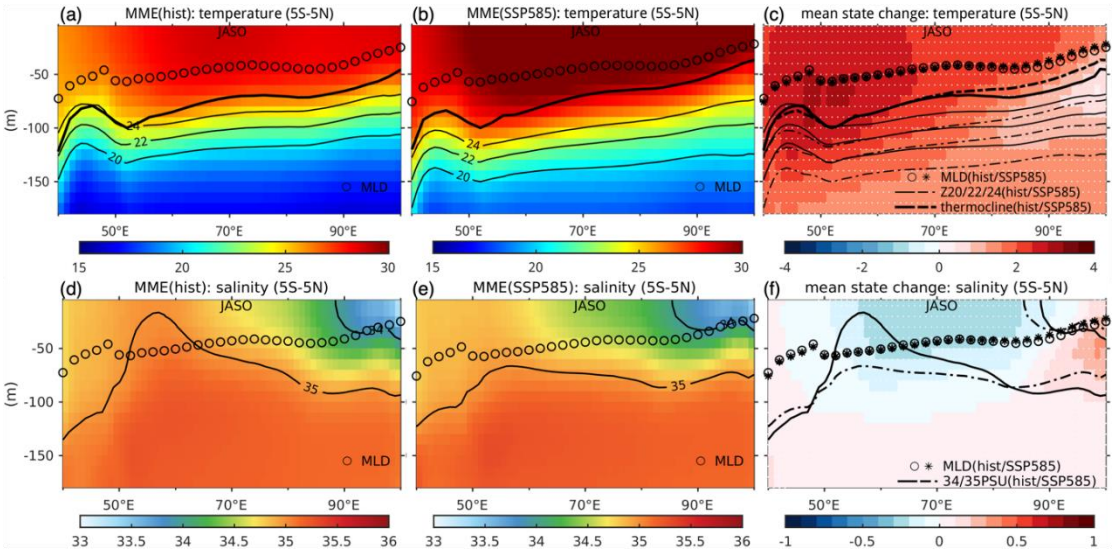


Figure 5.8. Mean-state temperature (shading, units: ℃) averaged over 5°S–5°N during JASO in the (a) historical and (b) SSP5-8.5 scenario simulations. The circle (black solid contours) denotes climatological MLD (20℃, 22℃ and 24℃ isotherms). The bold solid line is the thermocline defined as the depth of the maximum vertical temperature gradient. (c) is the mean-state temperature change (shading). The circle (asterisk) denotes historical (SSP5-8.5) MLD. The black solid (dash-dot) contours are 20℃, 22℃ and 24℃ isotherms in historical (SSP5-8.5) simulation. The bold solid (dash-dot) line represents the historical (SSP5-8.5) thermocline. (d, e, f) are the same as (a, b, c), but for salinity (shading, units: PSU; contour, 34-35 PSU isohalines). White stippling indicates exceeding the 95% significance level based on Student's t-test.

5.3. Increased extreme nIOD events

Under a warmer climate, IOD asymmetry is projected to weaken, indicating a smaller difference in amplitude between pIOD and nIOD compared to historical conditions. The analysis of the mixed-layer heat budget in Fig. 2 shows that the MLT tendency during pIOD is smaller than that during nIOD under the SSP5-8.5 scenario and this nIOD MLT tendency is notably larger than that in the historical run. A possibility is that the reduced IOD asymmetry under greenhouse warming links with more frequent extreme nIOD events. Figure 5.9 depicts the multi-model ensemble histograms of standardized PC1, ETIO SSTA (multiplied by –1) index and DMI for both the historical and climate change (SSP5-8.5) periods. These distributions support

the above finding that IOD amplitude becomes more symmetric under global warming. The standardized PC1 in the historical simulation shows peak occurrence when the PC1 is about –0.4, and the occurrence is clearly and systematically higher during pIOD than nIOD (Fig. 5.9a). For example, there are several pIOD cases greater than 2, while nIOD lower than –2 is only 3 cases in the historical simulation. In contrast, under the SSP5-8.5 scenario, the occurrence of standardized PC1 lower than –2 increases to 8 cases (Fig. 5.9d). Similarly, when focusing on the core region of IOD, the symmetric distribution of ETIO SSTA (multiplied by –1) index is more notable than the standardized PC1 under the SSP5-8.5 scenario. The ETIO SSTA (multiplied by –1) index shows peak occurrence when the index is about –0.4 ℃, and there are more extremely negative SSTAs appearing in the ETIO during the historical period (Fig. 5.9b). However, the peak occurrence of the ETIO SSTA (multiplied by –1) index moves to zero under greenhouse warming. Moreover, under the SSP5-8.5 scenario, the ETIO is projected to experience extremely positive value more frequently, which is nearly comparable to that extremely negative value. DMI analysis aligns closely with the findings of the above two indices and its peak occurrence even moves to the positive range, displaying significantly increased extreme nIOD events under a warmer climate (Figs. 5.9c, f). The reduction in IOD asymmetry suggests an intensification of nIOD. Both the nIOD amplitude and the extreme nIOD amplitude are projected to increase (Figs. 5.9d–f). According to the ETIO SSTA index, the future amplitude of nIOD events is projected to match the historical amplitude of extreme nIOD events (Fig. 5.9e). The composite patterns of extreme nIOD events indicate a significant enhancement of positive SSTAs in the central and eastern TIO under the SSP5-8.5 scenario, accompanied by increased positive precipitation anomalies along the equator (Figs. 5.9g–i). During extreme nIOD events, the positive SSTAs are projected to be less confined near the Sumatra-Java coast and are likely to extend westwards.

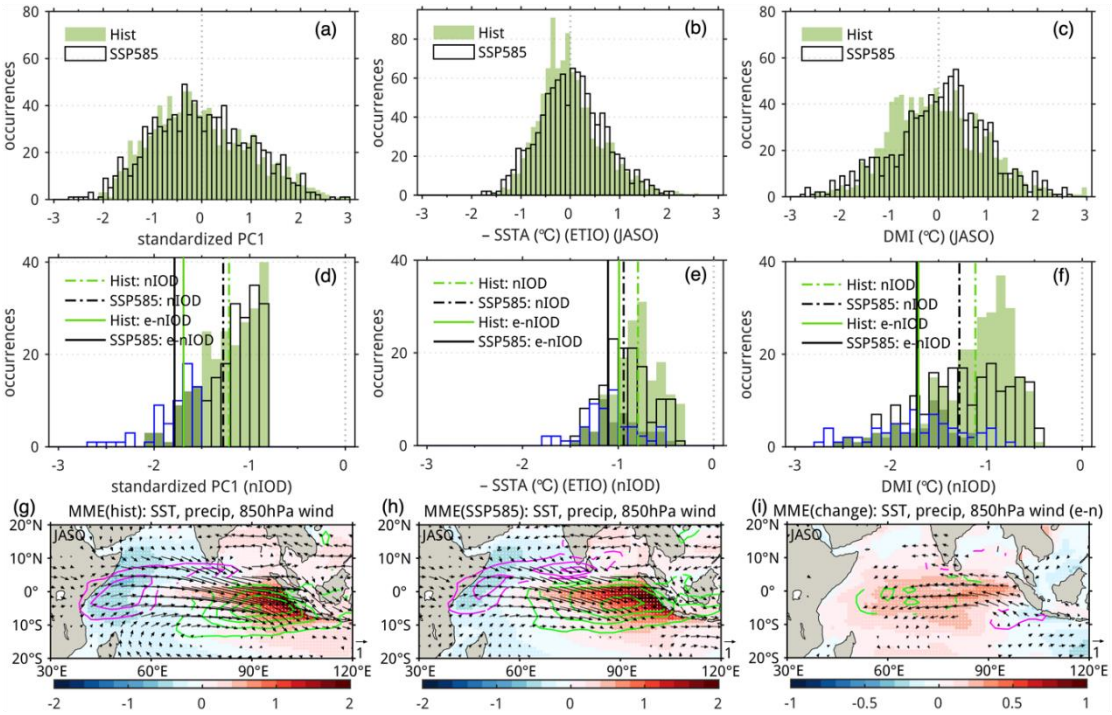


Figure 5.9. (a) Multi-model ensemble histograms of standardized PC1 during the historical (1950–1999; green shading bar) and climate change (2050–2099; black bar) periods. (b) is the same as (a), but for SSTA (multiplied by –1) in the ETIO (units: ℃; 8°S–2°N, 85°–100°E) during JASO. (c) is the same as (a), but for DMI (units: ℃) during JASO. (d, e, f) are the same as (a, g, c), but for nIOD events only. The darker green shading bar (blue bar) denotes the extreme nIOD events in the historical (SSP5-8.5) simulations. The green (black) dash-dot and solid lines indicate the nIOD mean and the extreme nIOD mean in historical (SSP5-8.5) simulations, respectively. Composite extreme nIOD of SST (shading; unit: ℃), precipitation (contours in intervals of 1 mm day^{-1}; green: positive; pink: negative) and 850 hPa wind (see scale vector in lower right; unit: m s^{-1}) anomalies during JASO in the (g) historical and (h) SSP5-8.5 simulations. (i) is their greenhouse-warming-induced changes. Anomalies of SST (white stippling), precipitation and 850 hPa wind are shown when exceeding the 95% significance level based on Student's t-test.

Using a threshold value of 1.5 STD, the PC1 result yields a 53.6% increase in the frequency of extreme nIOD events (Table 5.2). In the historical simulation, nearly 17.9% of nIOD is identified as extreme nIOD, while under greenhouse warming, 27.3% of nIOD events will evolve to be extreme cases, representing an increase of 9%. This suggests an increased frequency of extreme nIOD events, from one event every 24.4 years to one event every 15.9 years. Similarly, when utilizing the ETIO SSTA during JASO, there is a 20% increase in the frequency of extreme nIOD events. This corresponds to about 37% of nIOD cases evolving into extreme nIOD events under greenhouse warming, also representing an increase of 9% compared to historical conditions (Table 5.2). With the ETIO SSTA index, the frequency of the extreme nIOD

events changes from one per 22.2 years to one per 18.5 years. DMI is also used to test this result, in which 30.6% of nIOD cases (compared to 19.9% in the historical run) qualify as extreme nIOD events (Table 5.2). Using DMI, the frequency of the extreme nIOD events shifts from one event per 19.2 years to one event per 15.2 years. This rise in the occurrences of extreme nIOD events between the historical and climate change periods has been established as statistically significant through bootstrap testing. The robustness of this result is underpinned by a strong inter-model consensus, with only 3 out of 20 models producing a reduction of extreme nIOD events using the PC1 and 5 out of 20 models using the ETIO SSTA index. Among selected CMIP6 models, 6 out of 20 models capture realistic IOD skewness compared to the observed, and these well-skewed model names are shown in italics and bold in Table 5.2. Based on PC1, all well-skewed models predict more extreme nIOD events under the SSP5-8.5 scenario than in the historical runs except the CMCC-ESM2 model. While the CMCC-ESM2 model does predict more extreme nIOD events using the DMI. These results consistently suggest an increase in extreme nIOD events due to greenhouse warming across various models. However, accurately quantifying future IOD changes remains challenging and relies on realistic simulation of current IOD processes. Nevertheless, for well-skewed CMIP6 models, an increase in extreme nIOD due to greenhouse warming is confirmed. To further confirm the statistical significance of this finding, a comparative analysis between the periods 1900–1949 and 2050–2099 is also conducted (Table A1), which also shows a significant increase in extreme nIOD events.

Model (Hist/SSP585)	PC1		ETIO SSTA		DMI	
	nIOD	extreme nIOD	nIOD	extreme nIOD	nIOD	extreme nIOD
ACCESS-ESM1-5	12/13	*3/3*	9/6	**2/3**	13/10	*2/2*
BCC-CSM2-MR	9/10	4/2	8/7	4/2	15/10	5/4
CAMS-CSM1-0	8/10	3/1	10/5	2/1	10/6	*0/0*
CAS-ESM2-0	10/14	*1/1*	3/10	**1/2**	13/11	**1/4**
CESM2-WACCM	10/11	**3/5**	11/7	*5/5*	12/9	*6/6*
CIESM	15/10	**2/4**	12/8	**3/4**	13/6	4/2
CMCC-CM2-SR5	8/12	**0/2**	3/8	**0/1**	9/19	*0/0*
CMCC-ESM2	9/11	3/2	5/9	*2/2*	15/14	**0/4**
E3SM-1-1	12/12	**0/2**	4/4	**0/2**	11/9	**0/2**
EC-Earth3-CC	14/10	**1/2**	10/8	*2/2*	16/14	**2/5**
EC-Earth3-Veg-LR	11/14	**1/3**	7/10	2/1	17/12	**1/5**
EC-Earth3-Veg	12/13	*1/1*	7/4	3/0	15/14	4/2
EC-Earth3	14/14	**0/3**	7/5	**0/1**	14/13	*3/3*
FGOALS-f3-L	15/11	**1/6**	8/7	**3/4**	14/10	**3/4**

FGOALS-g3	12/10	**5/7**	11/8	**3/6**	16/10	**3/5**
FIO-ESM-2-0	12/7	**2/4**	10/6	**2/4**	14/7	6/5
KIOST-ESM	12/14	**1/3**	5/8	3/2	8/12	**0/2**
MRI-ESM2-0	11/13	**5/6**	9/8	**5/6**	13/11	**4/5**
NESM3	11/10	*3/3*	11/7	*2/2*	12/8	2/1
TaiESM1	12/12	**2/3**	9/11	**1/4**	11/11	**6/5**
total	229/231	41/63	159/146	45/54	261/216	52/66
extreme/all (%)		17.9/27.3		28.3/37.0		19.9/30.6

Table 5.2. Frequency of nIOD using different indices. A normal (extreme) nIOD event is defined as when the PC1 of each model is negative and greater than 0.8 (1.5) STD in amplitude. As for the ETIO SSTA, a normal (extreme) nIOD event is defined as when the ETIO SSTA during JASO of each model is positive and greater than 1 (1.5) STD. In terms of DMI, a normal (extreme) nIOD event is defined as when the DMI of each model is negative and greater than 1 (2) STD. Model names in italics and bold indicate well-skewed models that capture comparable IOD skewness to observations in the historical run. Bold numbers indicate an increase in extreme nIOD events, and numbers in italics indicate no change from the historical (1950–1999) to climate change (2050–2099) periods.

Under the SSP5-8.5 scenario, the frequency of extreme pIOD events is projected to decrease. In the historical simulation, approximately 40.2% of pIOD events are classified as extreme nIOD. However, under greenhouse warming, this percentage decreases to 34.4%, representing a 6% reduction (Table 5.3). Similarly, when using the ETIO SSTA during JASO, the percentage of extreme pIOD events is observed to decrease from 50.0% to 43.8%, indicating a 6% difference. The DMI is also utilized to validate these findings, with 15.9% of pIOD cases qualifying as extreme nIOD events (compared to 25.1% in the historical run). This finding contrasts with the studies conducted by Cai et al. (2014, 2021). In their research, they employed historical climatology to assess the future simulations of IOD variability. However, considering the anticipated IOD-like warming pattern in the mean state, this approach incorporates the mean-state change signals as part of the pIOD change signals. Given that the IOD represents interannual variability, we recommend referencing the future mean state when extracting the IOD signals.

Model (Hist/SSP585)	PC1		ETIO SSTA		DMI	
	pIOD	extreme pIOD	pIOD	extreme pIOD	pIOD	extreme pIOD
ACCESS-ESM1-5	11/12	*4/4*	8/7	*4/4*	13/14	1/2
BCC-CSM2-MR	8/9	**5/3**	8/3	**5/3**	10/11	2/3
CAMS-CSM1-0	9/12	3/7	4/9	3/6	9/8	4/6
CAS-ESM2-0	10/13	*6/6*	8/10	5/5	11/8	**6/0**
CESM2-WACCM	14/9	**4/2**	11/5	**3/1**	12/11	**2/1**

CIESM	10/12	**5/2**	8/7	*4/4*	16/10	**2/0**
CMCC-CM2-SR5	9/12	**5/3**	9/11	**6/5**	10/23	**6/1**
CMCC-ESM2	9/12	**7/3**	9/11	**7/4**	11/19	**7/5**
E3SM-1-1	7/11	4/5	4/8	*4/4*	11/14	**4/1**
EC-Earth3-CC	14/12	4/5	10/8	*5/5*	14/16	2/3
EC-Earth3-Veg-LR	12/12	**5/4**	8/9	**5/3**	12/12	*2/2*
EC-Earth3-Veg	13/12	4/5	8/12	3/6	12/17	1/5
EC-Earth3	8/16	**5/2**	8/14	5/7	13/17	*4/4*
FGOALS-f3-L	13/11	**4/3**	10/10	**4/3**	11/11	**2/1**
FGOALS-g3	12/12	3/4	9/8	1/4	7/13	**3/0**
FIO-ESM-2-0	14/10	4/5	8/10	**3/1**	13/12	**2/0**
KIOST-ESM	10/12	**5/4**	7/11	**5/4**	10/13	3/4
MRI-ESM2-0	12/9	**4/1**	11/7	**2/1**	15/12	**4/2**
NESM3	12/8	*4/4*	7/7	4/5	8/7	*1/1*
TaiESM1	12/11	3/6	11/9	**5/2**	13/16	0/1
total	219/227	88/78	166/176	83/77	231/264	58/42
extreme/all (%)		40.2/34.4		50.0/43.8		25.1/15.9

Table 5.3. The same as Table 5.2, but for pIOD.

The IOD is tightly connected to the mean climate of the Indian Ocean. An increased frequency of extreme nIOD can be comprehended since the Indian Ocean mean-state patterns increasingly resemble the background conditions found in the Pacific Ocean. These changes in the mean state are interconnected and collectively impact the IOD asymmetry through various atmospheric feedback and ocean dynamic processes, including wind stress–ocean advection–SST feedback. Due to the increased atmospheric static stability, less inhibition of negative nonlinear zonal advection is conducive to the nIOD development. The more symmetric IOD suggests that future NDH may not hold the same significance as those during the historical period. Additionally, the thermocline–temperature asymmetry is projected to diminish under global warming (Fig. 5.10). The sea level anomaly (SLA) versus SSTA in the ETIO shows a slightly nonlinear relationship ($\alpha = -0.07$, α is the nonlinear coefficient of a quadratic function) in the historical runs, suggesting that the MLT in the ETIO is more sensitive to a shallower thermocline. However, under the SSP5-8.5 scenario, this relationship becomes nearly linear ($\alpha = -0.02$), resulting in more symmetrical thermocline feedback and nonlinear vertical advection during pIOD and nIOD events (Fig. 5.3). The SST response to deepening thermocline increases during nIOD events, exhibiting a slope of 0.45 in the historical runs and 0.58 in the SSP5-8.5 scenario simulations (Fig. 5.10). In summary, the greenhouse-warming-induced background

change in the Indian Ocean may increase the frequency of extreme nIOD events, implying more frequent extreme climate and weather events in nIOD-affected regions.

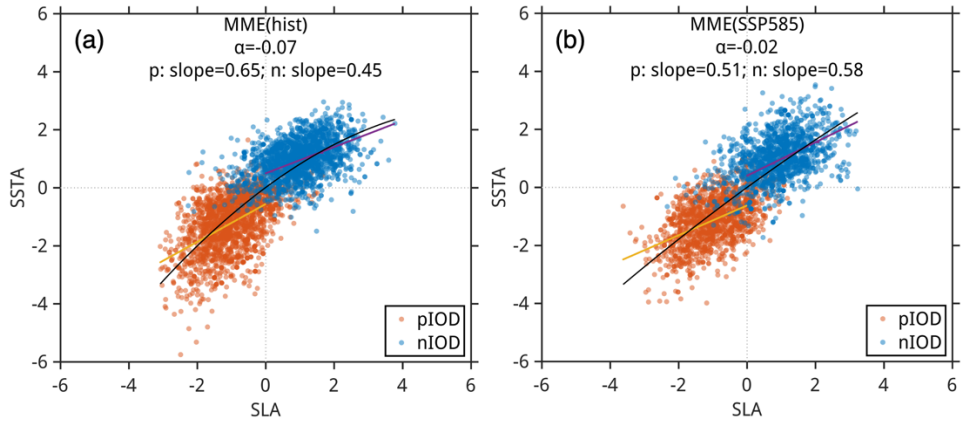


Figure 5.10. Standardized monthly SLA vs SSTA (8°S–2°N, 85°–100°E) during IOD based on (a) historical and (b) SSP5-8.5 scenario simulations. The black curve gives a quadratic fit, and α is the nonlinear coefficient. The yellow (purple) line is the least squares linear fit of pIOD with negative SLA (nIOD with positive SLA).

Based on the mixed-layer heat budget, the main contributor to the enhancement of extreme nIOD events is the reduced inhibition of nonlinear zonal advection, with a difference of 0.054 ℃ month^{-1} (Table 5.4). Note that the nonlinear zonal advection acts as a large damping term in nIOD and this term exhibits a significant enhancement during extreme nIOD (Table 5.4) compared to normal nIOD (Table 5.1). The second factor is the amplified linear zonal advection, specifically the $-\bar{u}(\partial T'/\partial x)$. The third contributor is the Ekman pumping term $[-w'\overline{(T-T_{-h})/h}]$, which will be further discussed in Section 6.

budget term	Extreme nIOD		
	historical	SSP5-8.5	change
$-\bar{u}\frac{\partial T'}{\partial x}$	0.143	0.182	0.039
$-u'\frac{\partial \bar{T}}{\partial x}$	0.046	0.054	0.008
$-u'\frac{\partial T'}{\partial x}$	-0.153	-0.099	0.054
$-\bar{v}\frac{\partial T'}{\partial y}$	0.023	0.049	0.026
$-v'\frac{\partial \bar{T}}{\partial y}$	0.057	0.042	-0.016
$-v'\frac{\partial T'}{\partial y}$	0.021	0.02	-0.001
$-\bar{w}(\frac{T-T_{-h}}{h})'$	0.177	0.17	-0.007

$-w'\overline{\frac{T-T_{-h}}{h}}$	0.088	0.135	0.047
$-w'(\frac{T-T_{-h}}{h})'$	-0.071	-0.08	-0.009

Table 5.4. The same as Table 5.1, but for extreme nIOD only.

5.4. Constrained IOD asymmetry changes

To build the usefulness of CMIP6 estimates of IOD asymmetry, we made use of related variable measurements through an emergent constraint approach (Cox et al. 2013; Huang and Ying 2015; Lian et al. 2018). This approach can lever additional information from a multi-model ensemble to reduce the uncertainty in characterizing Earth system features. The concept relies on the fact that, although ESMs may have many large inter-model structural and parameter differences, there may exist a tight regression across them between a quantity of interest and a second variable for which observational data are readily available (Lian et al. 2018). Although no direct linear relationship exists between current-day IOD asymmetry and future IOD asymmetry (not shown), the present-day IOD skewness is highly correlated with the change in IOD skewness due to greenhouse warming, with a correlation coefficient of –0.74 (significant at the 95% level) (Fig. 5.11a). A similar relationship is also shown between the SSTA skewness in the ETIO and the corresponding change in SSTA skewness due to climate change (Fig. 5.11d). Previous studies highlighted that the historical simulation of IOD skewness is associated with positive IOD-like biases in the mean state (Li et al. 2015; Long et al. 2020). Given this mechanism, to better understand the projection uncertainty, we focus on the role of positive IOD-like biases in the present-day simulation. It is clear from Fig. 5.11b that models with a weaker westerly in present-day climatology tend to exhibit smaller IOD skewness changes in the future. Similarly, there is also a significant relationship between the change in ETIO SSTA skewness and present-day westerly (Fig. 5.11e). This strong linear relationship between individual model simulations of positive IOD-like biases for the contemporary period and the estimated changes of IOD skewness in the future provides an emergent constraint on the actual westerly value—that is, by using the regression to map from surface zonal wind measurements (Figs. 5.11b, e). As the Walker circulation weakens in a warmer climate, models with a stronger present-day mean westerly are able to simulate a greater IOD-like warming pattern (Sharma et al. 2022, 2023) under the SSP5-8.5 scenario (Fig. 5.11c). In contrast, if the present-day surface equatorial wind is already close to zero,

the impact on skewness under greenhouse warming is restricted as the skewness is already weak. Therefore, the reduction in IOD asymmetry tends to be larger for models with stronger mean-state westerly winds, that is, less positive IOD-like biases in the mean state.

The change in MME IOD skewness is about –0.28 from its historical value of 0.42 based on PC1 (Fig. 5.11b), that is, the future MME IOD skewness is about 0.144. The corrected result predicts a greater decrease (–0.48) in IOD asymmetry in a warmer climate, implying an even higher frequency of extreme nIOD events and their impacts. Regarding the MME ETIO SSTA skewness (multiplied by –1), its corrected change is about –0.67 (raw change: –0.46) from a historical value of 0.56 (Fig. 5.11e), that is, the future MME ETIO SSTA skewness is about 0.098. The corrected result shows that there will be a larger reduction in IOD asymmetry under a warmer climate, implying even more frequency of extreme nIOD events. The impact of present-day simulation biases of IOD skewness on future IOD changes remains uncertain. Previous research emphasized the significance of thermocline and its associated feedback mechanisms (Ng and Cai 2016; Wang et al. 2021). However, other processes, including NDH and thermodynamic air-sea feedback, which primarily arise from atmospheric responses, are closely linked to mean-state changes. These processes also play a crucial role in shaping and simulating IOD asymmetry. Exploring how these processes can be utilized to constrain projected IOD changes is a valuable consideration.

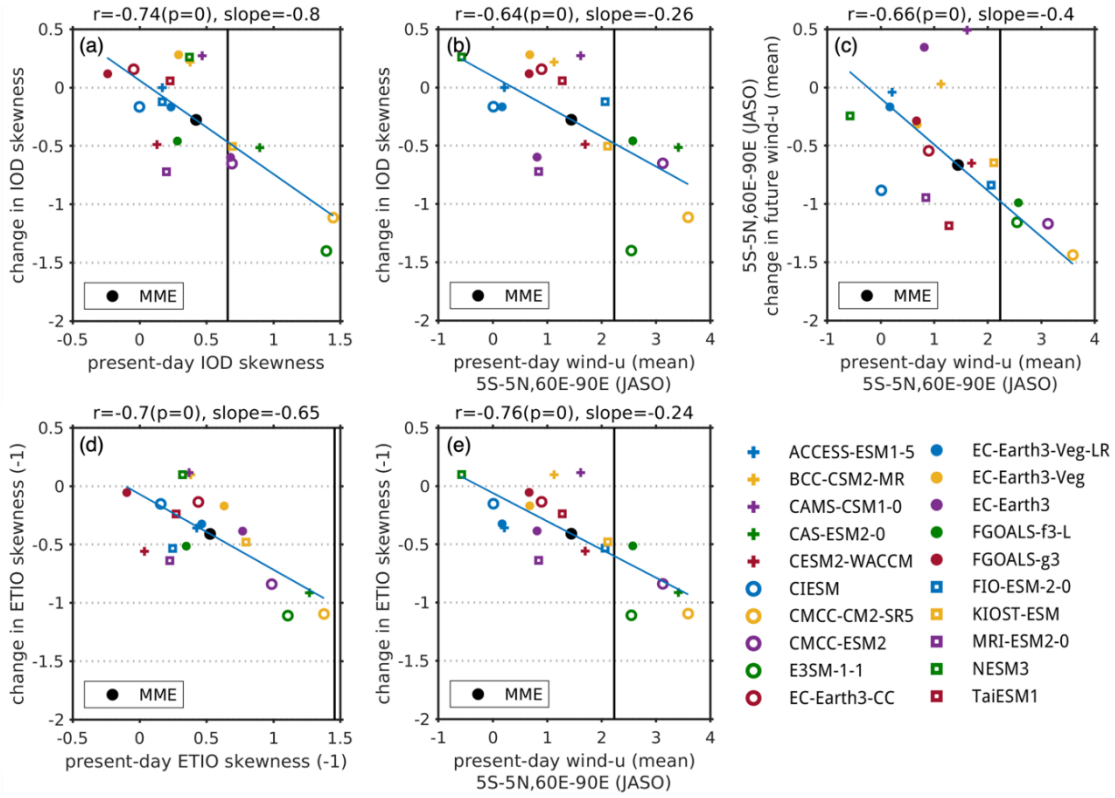


Figure 5.11. Emergent constraint on the IOD skewness. (a) Present-day PC1 skewness vs its change. (b) Present-day surface zonal wind (unit: m s^{-1}; 5°S–5°N, 60°–90°E; JASO) in the mean state vs PC1 skewness change. (c) Present-day surface zonal wind (unit: m s^{-1}; 5°S–5°N, 60°–90°E; JASO) in the mean state vs its change. (d) Present-day SSTA skewness (multiplied by –1) within ETIO (8°S–2°N, 85°–100°E; JASO) vs its change. (e) Present-day surface zonal wind (unit: m s^{-1}; 5°S–5°N, 60°–90°E; JASO) in the mean state vs change in ETIO SSTA skewness (multiplied by –1). The blue line indicates the best-fit regression line across the models. The black line represents the observation value. The intersection of the blue and black lines is the constrained value.

6. Projections of IOD pattern by CMIP6 models

6.1. Alterations in IOD pattern due to global warming

Figure 6.1 depicts the multi-model averaged STD of SSTA for the summer and autumn seasons (JJASON). Notably, the historical simulation reveals considerable SST fluctuations in the ETIO, particularly near the Sumatra-Java coast (Fig. 6.1a). The MME mean outcome under the SSP5-8.5 scenario also simulates significant SSTA variance in the ETIO (Fig. 6.1b). The MME STD of SSTA in the ETIO during JJASON is approximately 0.65 ℃ in the historical simulation and 0.68 ℃ under the SSP5-8.5 scenario (Fig. 6.1f), indicating little change in IOD amplitude across the entire ETIO due to global warming. The relatively unchanged IOD amplitude in the ETIO aligns with findings from the DMI of CMIP5 models (Cai et al. 2013; Zheng et al. 2013), attributable to the offsetting changes in weakened atmospheric feedback and strengthened thermocline feedback (Zheng et al. 2010). However, a more detailed analysis reveals approximately a 10% decrease in SSTA amplitude near the Sumatra coast and a 10% increase along the equatorial ETIO, signifying meaningful alterations in the IOD pattern due to climate change (Fig. 6.1c). This suggests that the eastern part of IOD will exhibit enhanced equatorial symmetry in the projected future.

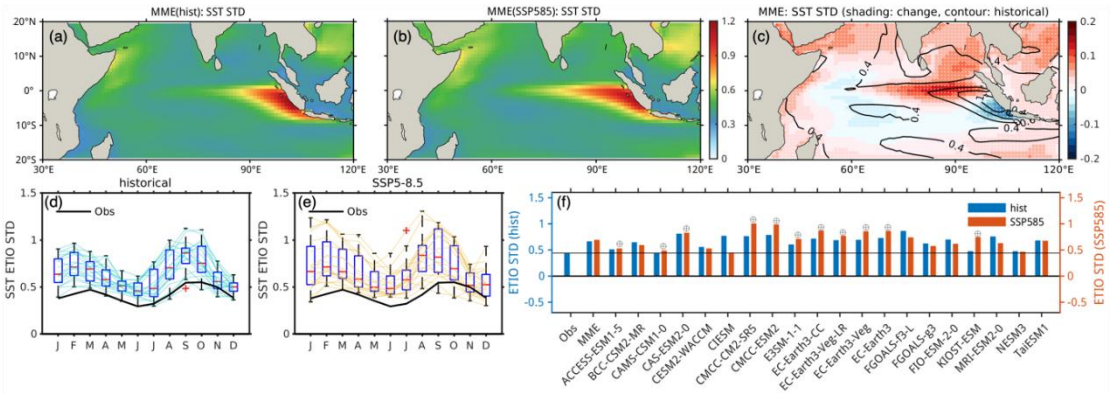


Figure 6.1. Multi-model averaged STD of SSTA (unit: ℃) during JJASON in the (a) historical and (b) SSP5-8.5 scenario simulations. Shading in (c) donates the greenhouse-warming-induced changes with historical simulation shown by contours. White stippling indicates the 95% significance level based on the Student's t-test. Seasonal fluctuations of SSTA STD within the ETIO (8°S–2°N, 85°–100°E) in the (d) historical and (e) SSP5-8.5 scenario simulations. Boxplot shows their median (red dash), interquartile range (blue box), lower and upper 1.5 times the interquartile range (black dash), and outlier (red + sign). The bold black solid line is the observed result. (f) SSTA STD over the ETIO during JJASON in the historical (blue bars) and SSP5-8.5 scenario (orange bars) simulations. The black line denotes the observed value. Models with larger STD under the SSP5-8.5 than the historical simulation are marked by grey circles above the bars.

Boxplots are also used to depict crucial statistical features of the seasonal variations in SSTA STD over the ETIO, based on 20 selected CMIP6 models. In the historical simulation, nearly all models manifest a higher ETIO SST amplitude compared to observations, yet they still accurately capture seasonal fluctuations (Fig. 6.1d). Prior research indicates that this increased simulated IOD amplitude is linked to the mean-state simulation of the west-east thermocline slope, which triggers more robust thermocline-SST feedback in CMIP models (Cai and Cowan 2013; Liu et al. 2014). Moreover, most CMIP6 models successfully capture the IOD peak phase in September or October, aligning with the observed (Fig. 6.1d). Under the SSP5-8.5 scenario, the ETIO SST amplitude remains comparable to historical runs during the IOD developmental and mature phases, with some models displaying larger seasonal variations due to global warming (Fig. 6.1e). Additionally, SST variations within the ETIO become more diverse among the selected CMIP6 models from July to September, and the simulated future IOD seems to peak earlier. McKenna et al. (2020) suggested that there is a slight shift in the IOD's seasonality toward an earlier peak in September among CMIP6 models. This seasonal advancement of IOD development in future projections may be related to the shallower thermocline in the ETIO and the IOD-like warming pattern (Zheng et al. 2021).

In more detail, only the CAMS-CSM1-0, KIOST-ESM and NESM3 models capture an ETIO amplitude comparable to the observed, while the remaining models simulate a larger amplitude in the historical simulation (Fig. 6.1f). Under simulated greenhouse warming, three CMIP6 models (CAMS-CSM1-0, CIESM, NESM3 models) have a comparable SSTA STD in the ETIO to the observed (Fig. 6.1f). Among the 20 selected Earth System Models, 11 models show a slightly increased IOD amplitude in the ETIO and 9 models depict a slight decrease, implying that the future simulated STD of SSTA in the ETIO under SSP5-8.5 scenario is close to the historical simulation on average (Fig. 6.1f). Given the inter-model discrepancy in the CMIP6 archives, it may not be sufficient to consider the entire ETIO. Instead, a key finding emerges in terms of the IOD pattern changes in SSTA, with a decrease in SSTA amplitude near the Sumatra coast and an increase along the equatorial ETIO. This highlights the need to explore the mechanisms driving potential shifts in the IOD pattern due to global warming. Alterations in IOD patterns could influence the anomalous convection center, consequently modifying the IOD teleconnections.

Figure 6.2 illustrates the individual variances of pIOD and nIOD events. In the ETIO, pIOD typically exhibits a smaller amplitude, whereas nIOD is anticipated to display a larger amplitude under the SSP5-8.5 scenario (Figs. 6.2a, b, d, e), which is consistent with the projected decrease of IOD symmetry in the future (Ng and Cai 2016). The overall reduction in SSTA STD near the Sumatra-Java coast in Fig. 6.1c mainly results from the pIOD changes (Fig. 6.2c). In contrast, alterations in nIOD make a minor contribution to the decreased SSTA amplitude near the Java coast (Fig. 6.2f). With respect to the increased SSTA STD in the equatorial ETIO, both pIOD and nIOD generate larger amplitudes in this region, especially the nIOD. This suggests that despite the projected weakening of pIOD amplitude under global warming, it is likely to induce larger SST amplitudes along the equatorial ETIO. As for nIOD, its SSTA STD is predicted to be less confined near the Sumatra-Java coast and will likely extend northwards and westwards.

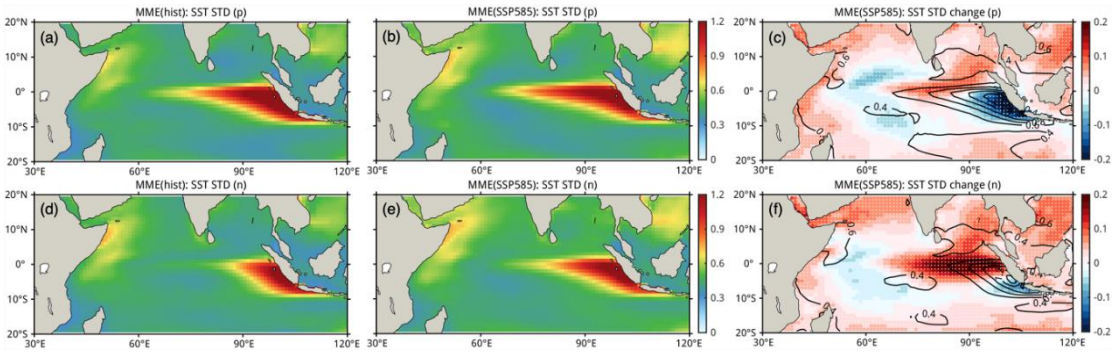


Figure 6.2. (a, b, c) are the same as Fig. 6.1 (a, b, c), but for pIOD only. (d, e, f) are for nIOD only. The SSTA STD for pIOD is calculated by $\sqrt{\sum_1^N (SSTA_P)^2/N}$, where $SSTA_P$ is the SSTA during pIOD and N is the number of pIOD. The same goes for nIOD.

6.2. Reduced SSTA amplitude near the Sumatra coast

Composite IOD results also demonstrate that SSTAs decrease near the Sumatra coast and increase in the equatorial ETIO under the SSP5-8.5 scenario compared to the historical runs (Fig. 6.3). Typically, the JJASON period encapsulates all IOD phases, including triggering, developing and mature phases. Due to the earlier IOD peak under the SSP5-8.5 scenario, July to October is used henceforth to capture the main variations of IOD. During pIOD, historical runs simulate notable negative SSTAs in the ETIO, especially near the Sumatra coast, accompanied by a negative precipitation anomaly center in the SETIO (Fig. 6.3a). Under the SSP5-8.5 scenario, the projected pIOD also displays strong negative SSTA and precipitation variations in the ETIO (Fig. 6.3b).

However, surface cooling near the Sumatra coast weakens noticeably and intensifies in the equatorial ETIO (Fig. 6.3c). These are consistent with the reduced negative precipitation anomalies near the Sumatra coast and the northward extension of these anomalies. As for nIOD events, the positive SSTAs mainly increase in the equatorial ETIO, with increased positive precipitation anomalies along the equator (Fig. 6.3f). The nIOD composite also indicates a westward extension of the eastern precipitation anomalies. Additionally, 850 hPa wind anomalies in the TIO decrease during both pIOD and nIOD on a basin-wide scale (Figs. 6.3c, f), aligning with the weaker atmospheric response to SSTAs due to more stable mean-state atmosphere in a warmer climate (Zheng et al. 2010). For further clarity, the composite vertical pressure velocity (omega) at 500 hPa level exhibits weaker atmospheric convection modulations during both pIOD and nIOD under the SSP5-8.5 scenario on a basin-wide scale (Fig. 6.4). Note that the projected change of omega anomaly in the SETIO during pIOD is significantly larger than that during nIOD. These suggest that the weakened atmospheric response cannot solely account for the reduced SSTA variance near the Sumatra coast. The changes in pIOD appear to precede the projected variance decrease due to the weakened atmospheric response in a warmer climate. The pIOD development near the Sumatra coast may be more suppressed than nIOD from atmospheric contributions under the SSP5-8.5 scenario.

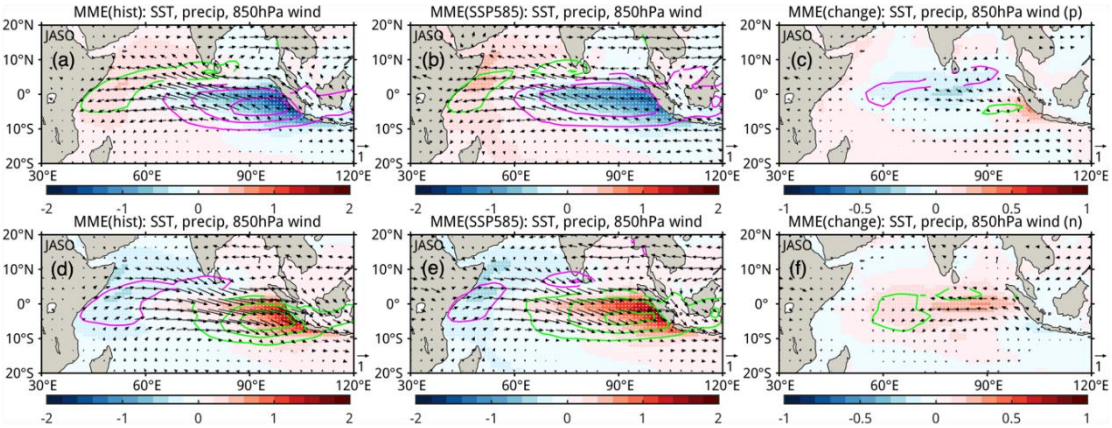


Figure 6.3. Composite pIOD of SST (shading; unit: ℃), precipitation (contours in intervals of 1 mm day^{-1}; green: positive; pink: negative) and 850 hPa wind (see scale vector in lower right; unit: m s^{-1}) anomalies during JASO in (a) historical and (b) SSP5-8.5 scenario simulations. (c) is their greenhouse-warming-induced changes. (d, e, f) are the same as (a, b, c), but for nIOD. Anomalies of SST (white stippling), precipitation and 850 hPa wind are shown when exceeding the 95% significance level based on Student's t-test.

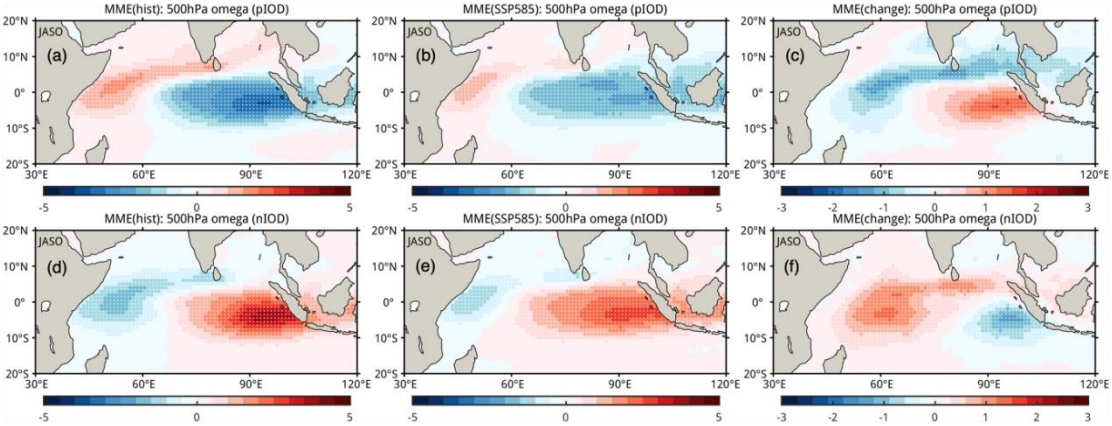


Figure 6.4. Composite pIOD of 500 hPa omega anomalies (unit: –0.01 Pa s^{-1}) during JASO in (a) historical and (b) SSP5-8.5 scenario simulations. (c) is its greenhouse-warming-induced change. (d, e, f) is the same as (a, b, c), but for nIOD. White stippling indicates the 95% significance level based on Student's t-test.

The more significant reduction of SSTAs near the Sumatra coast during pIOD corresponds to the lower efficiency of thermodynamic air-sea feedback (Li et al. 2003). The SETIO region, known for its intense convection due to the Indo-Pacific warm pool, is a site of this feedback mechanism, exhibiting a positive loop between anomalous atmospheric anticyclones and cold SSTAs during the boreal summer in pIOD (Li et al. 2003). When colder SSTs occur in the SETIO, atmospheric convective heating decreases, forming an atmospheric heat sink. According to Gill's solution (Gill 1980), this heat sink triggers a descending Rossby wave response to the west, resulting in an anomalous low-level anticyclonic flow above the SETIO. During the boreal summer, a southeasterly flow prevails near the Sumatra-Java coast so that this anomalous anticyclone would amplify the existing coastal wind. This amplified coastal wind, in turn, intensifies sea surface evaporation through the WES feedback and promotes Ekman transport and coastal upwelling, contributing to surface cooling and significantly influencing the development of pIOD. The lower efficiency of thermodynamic air-sea feedback is evident in the composite surface wind stress curl anomalies, particularly during pIOD under the SSP5-8.5 scenario simulation, which exhibits weaker anomalies (Fig. 6.5). The reduction during both pIOD and nIOD events is attributed to the weakened atmospheric response due to global warming. While the more significant decrease in anomalous surface wind stress curl during pIOD is associated with the lower feedback efficiency in the SETIO. Under the SSP5-8.5 scenario, weaker surface wind stress curl anomalies in the SETIO result in fewer southeasterly wind anomalies near the Sumatra coast during pIOD, leading to weaker

WES feedback and Ekman-induced upwelling compared to historical simulation. This will also result in less negative nonlinear dynamic heating, a crucial factor in pIOD development.

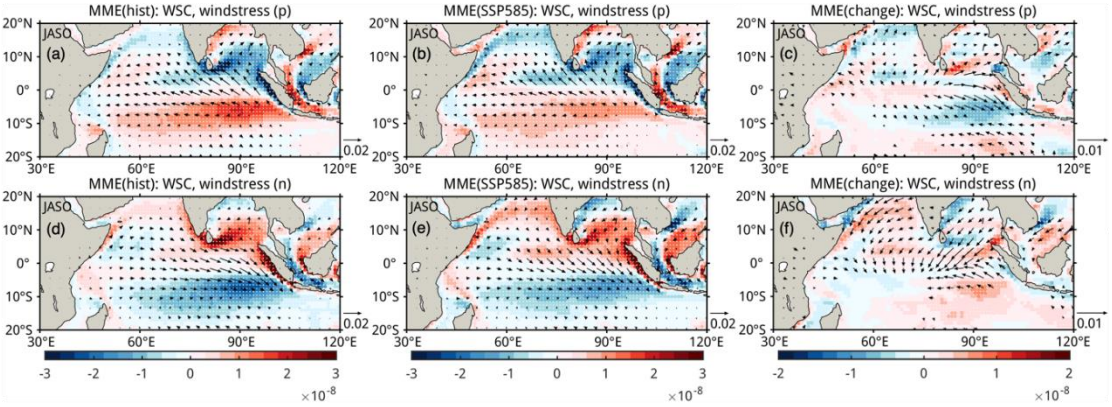


Figure 6.5. Composite pIOD of surface wind stress curl (shading, unit: N m^{-3}) and surface wind stress (vector, unit: N m^{-2}) anomalies during JASO in (a) historical and (b) SSP5-8.5 scenario simulations. (c) is their greenhouse-warming-induced changes. (d, e, f) is the same as (a, b, c), but for nIOD. White stippling and vector are shown when exceeding the 95% significance level based on Student's t-test.

The lower efficiency of thermodynamic air-sea feedback is linked to background changes. Historically, the STD of precipitation anomaly is mainly located in the SETIO, with the core near the Sumatra coast (Fig. 6.6a). However, under the SSP5-8.5 scenario, there is a noteworthy reduction in rainfall variance near the Sumatra coast and an increase in the northern TIO (Figs. 6.6b, c). Notably, the SETIO precipitation variance center disappears under the SSP5-8.5 scenario. This reduction aligns with the decreased precipitation anomaly during pIOD. It can be attributed to the decreased mean-state precipitation in the SETIO or the northward shift of the Indian Ocean rain belt (Figs. 6.6d–f). The projected decrease in the mean-state precipitation center corresponds with the disappearance of the precipitation variance center (Figs. 6.6c, f). Under the SSP5-8.5 scenario, the mean-state precipitation near the Sumatra coast is about 3 mm day^{-1}, restricting the potential reduction during pIOD. This leads to less decrease in atmospheric convective heating, less descending Rossby wave response, and weaker anomalous low-level anticyclonic flow above the SETIO during pIOD. Previous studies have pointed out that the mean-state precipitation changes in the TIO are associated with the weakened Walker Circulation in response to global warming (Vecchi and Soden 2007; Sharma et al. 2022). At present, the eastern Indian basin is occupied by a warm pool with vigorous deep convection (Roxy et al. 2019). Under the high greenhouse gas emission scenario, the mean-state SST in TIO is projected to rise by

over 2 ℃, with the WTIO experiencing more pronounced warming relative to the ETIO (Figs. 6.6h, i), especially during the summer monsoon season. Previous studies have mentioned that most climate models predict such positive IOD-like warming patterns under both low and high greenhouse gas emission scenarios (Vecchi and Soden 2007; Xie et al. 2010a; Cai et al. 2013; Cai et al. 2014; Sharma et al. 2022). This positive IOD-like warming pattern contributes to the weakened Indian Ocean Walker Circulation, a widely accepted projection of mean-state change in response to global warming (Sharma et al. 2022). The weakened Walker circulation, in turn, reduces the west-east SST gradient by a mechanism known as the Bjerknes feedback (Bjerknes 1969). Additionally, the "ocean dynamical thermostat" theory suggests that warming in the eastern Indian Ocean could be balanced by cold upwelling near the Sumatra-Java coast, further reducing the SST gradient and weakening the Indian Ocean Walker Circulation (Clement et al. 1996).

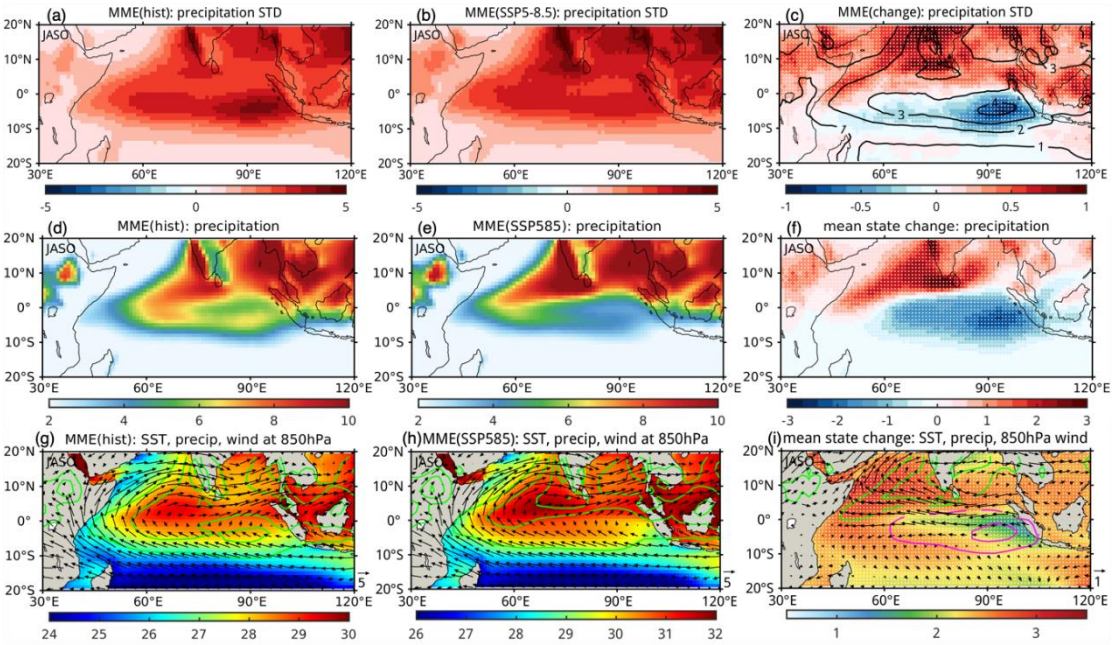


Figure 6.6. Multi-model averaged JASO precipitation STD (unit: mm day^{-1}) in (a) historical and (b) SSP5-8.5 scenario simulations. Shading in (c) donates its changes with historical results shown by contours. (d, e, f) are the same as (a, b, c), but for mean-state precipitation. (g, h, i) are the same as (a, b, c), but for mean-state SST (shading; unit: ℃), precipitation [contours in intervals of 3 mm day^{-1} in (g, h) and 1 mm day^{-1} in (i)] and 850 hPa wind (see scale vector in lower right; unit: m s^{-1}). White stippling indicates the 95% significance level based on the Student's t-test.

Inter-model statistics of CMIP6 also support that the projected decrease in SSTA variance near the Sumatra coast results from the reduction in mean-state precipitation in the SETIO. Among the selected CMIP6 models, those with a greater decrease in

mean-state precipitation tend to have a greater reduction in precipitation variance, a correlation with a high coefficient of 0.72 that passes the 95% significance level (Fig. 6.7a). This indicates that in this region, the projected changes in precipitation anomalies during pIOD are highly correlated with the projected changes in the mean-state precipitation. Furthermore, a more substantial decrease in mean-state precipitation corresponds to a decreased SST variance near the Sumatra-Java coast, calculated from pIOD only (Fig. 6.7b). This robust relationship, with a correlation coefficient of 0.68, retains significance at the 95% level. Therefore, smaller negative SSTAs during pIOD near the Sumatra coast are mainly related to the drier background in this region. This weaker SSTA during pIOD near the Sumatra coast may form an anomalous local meridional circulation in the ETIO and partly contribute to the increased SSTA along the equatorial ETIO (Fig. 6.3c). In summary, the reduced SSTA amplitude near the Sumatra coast can be explained by the weaker atmospheric response due to increased atmospheric static stability and the lower efficiency of thermodynamic air-sea feedback in the SETIO because of a drier future background. The weaker atmospheric response leads to smaller SST variances near the Sumatra-Java coast during both pIOD and nIOD. While the lower efficiency of thermodynamic air-sea feedback further decreases the SSTA amplitude during pIOD.

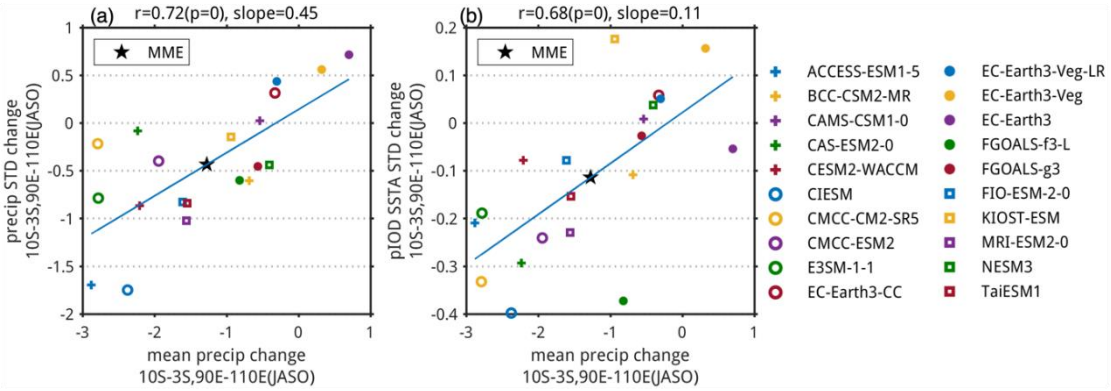


Figure 6.7. (a) Mean-state precipitation changes (unit: mm day^{-1}) vs its STD changes during JASO within 10°S–3°S, 90°–110°E. (b) Mean-state precipitation changes vs SSTA STD for pIOD only (unit: ℃). The SSTA STD for pIOD is calculated by $\sqrt{\sum_1^N (SSTA_P)^2/N}$. The blue line is the least square linear fit. The r value is the correlation coefficient.

6.3. Increased SSTA amplitude along the equatorial ETIO

Apart from the reduced SSTA amplitude near the Sumatra coast, there is an increased SSTA amplitude along the equatorial ETIO (Fig. 6.1c). As previously

discussed, the atmospheric response is expected to weaken under global warming due to the intensified atmospheric static stability, seemingly conflicting with the larger SSTA STD in the equatorial ETIO. Composite IOD results suggest that projected surface wind anomaly changes do not correspond with the amplified SSTA variance in the equatorial ETIO under the SSP5-8.5 scenario (Fig. 6.3), implying that enhanced oceanic modulation may be the primary factor over atmospheric response. To investigate the relative contributions of oceanic dynamic processes, a mixed-layer heat budget analysis is undertaken in the equatorial ETIO. Three key feedback processes are crucial to IOD development: thermocline feedback {associated with the $-\overline{w}[(T - T_{-h})/h]'$ term}, Ekman pumping feedback [associated with the $-w'\overline{(T - T_{-h})/h}$ term], and the linear advection of mean-state zonal current by the anomalous zonal MLT gradient $[-\bar{u}(\partial T'/\partial x)]$. Unlike ENSO, where the zonal advection feedback [associated with the $-u'(\partial \bar{T}/\partial x)$ term] is significant due to the strong mean zonal temperature gradient at the warm pool edge (Picaut et al. 1997), the contribution of zonal advection feedback to IOD dynamics is relatively small due to the limited mean zonal temperature gradient in the TIO.

In the historical simulation, zonal and vertical advection terms are the key dynamical processes influencing the MLT tendency during JASO, with vertical advection playing an important role (Fig. 6.8a). Under the SSP5-8.5 scenario, the most significant increase in oceanic advection is the $-\bar{u}(\partial T'/\partial x)$ term, occurring in both pIOD and nIOD events (Figs. 6.8b, c). In the historical run, this term's composite values are –0.053 ℃ month^{-1} and 0.048 ℃ month^{-1} in the equatorial ETIO during pIOD and nIOD, respectively (Table. 6.1). However, under the SSP5-8.5 scenario, this composite more than doubles to –0.127 ℃ month^{-1} during pIOD and 0.132 ℃ month^{-1} during nIOD (Table. 6.1). Another increase is the vertical advection, including $-\overline{w}[(T - T_{-h})/h]'$, $-w'\overline{(T - T_{-h})/h}$ and $-w'[(T - T_{-h})/h]'$ terms, notably in nIOD composites. Linear vertical advection contributes to the MLT tendency, while nonlinear vertical advection hinders nIOD development and does not support the increased SST variance. Despite a larger amplitude, the net heat flux term suppresses the MLT tendency development. Regarding the lateral induction, certain components may enhance the SSTA amplitude, however, their cumulative effect reveals minimal change, specifically, 0.0057 ℃ month^{-1} in pIOD and 0.0040 ℃ month^{-1} in nIOD. Therefore, the increased SSTA variance in the equatorial ETIO is mainly related to the

$-\bar{u}(\partial T'/\partial x)$ terms. Besides, a slight increase in linear vertical advection may contribute secondarily to the larger SSTA amplitude in the equatorial ETIO during nIOD events.

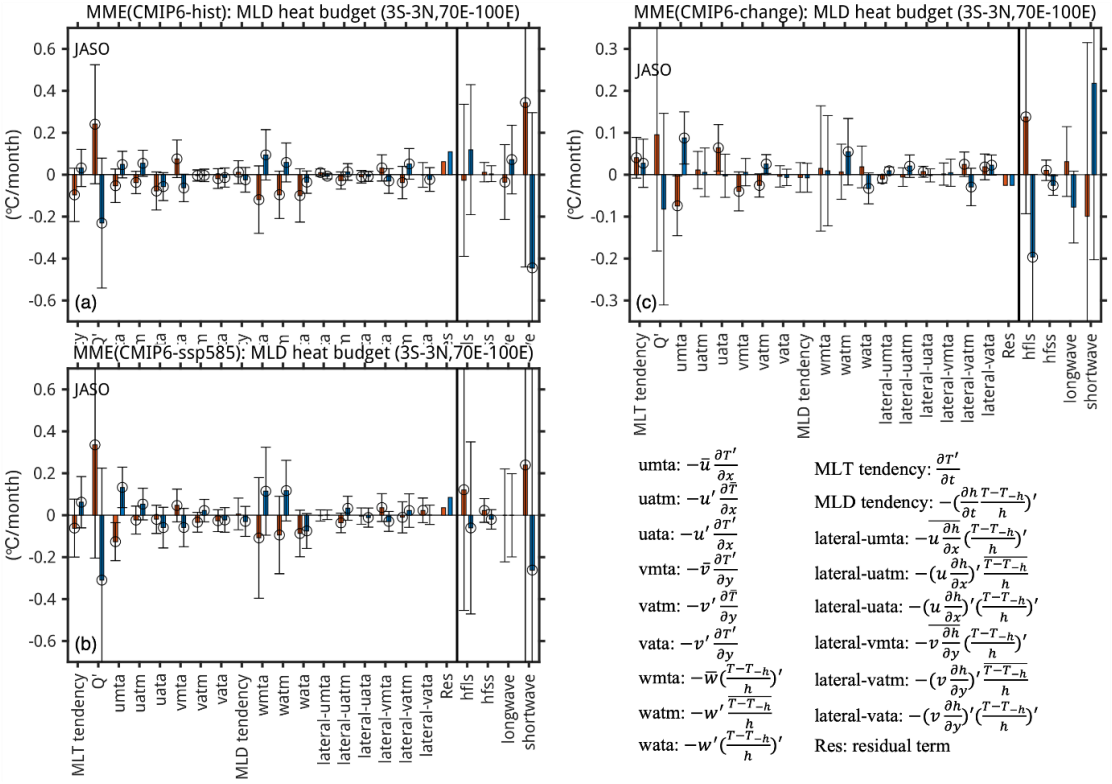


Figure 6.8. IOD composite during JASO for mixed-layer heat budget within 3°S–3°N, 70°–100°E in (a) historical, (b) SSP5-8.5 scenario simulations and (c) their greenhouse-warming-induced changes. The error bar is based on one STD. Circle over the bar indicates signals that are statistically significant at the 95% significance level.

budget	pIOD			nIOD		
term	historical	SSP5-8.5	change	historical	SSP5-8.5	change
$-\bar{u}\frac{\partial T'}{\partial x}$	–0.053	–0.127	–0.073	0.048	0.132	0.085
$-u'\frac{\partial \bar{T}}{\partial x}$	–0.038	–0.024	0.014	0.054	0.053	–0.001
$-u'\frac{\partial T'}{\partial x}$	–0.078	–0.020	0.058	–0.057	–0.060	–0.003
$-\bar{v}\frac{\partial T'}{\partial y}$	0.075	0.046	–0.029	–0.064	–0.059	0.004
$-v'\frac{\partial \bar{T}}{\partial y}$	–0.004	–0.034	–0.030	–0.004	0.022	0.025
$-v'\frac{\partial T'}{\partial y}$	–0.019	–0.027	–0.008	–0.014	–0.023	–0.009
$-\bar{w}(\frac{T-T_{-h}}{h})'$	–0.133	–0.121	0.012	0.105	0.127	0.022

$-w'\overline{\frac{T-T_{-h}}{h}}$	–0.107	–0.106	0.001	0.064	0.130	0.065
$-w'(\frac{T-T_{-h}}{h})'$	–0.111	–0.098	0.013	–0.040	–0.084	–0.044

Table 6.1. Composite mixed-layer advection terms (unit: ℃ month^{-1}) in pIOD and nIOD during JASO within 3°S–3°N, 70°–100°E, including their historical values, SSP5-8.5 scenario values and greenhouse-warming-induced changes.

Fig. 6.9 illustrates the composite $-\bar{u}(\partial T'/\partial x)$ during JASO for pIOD and nIOD in the historical and SSP5-8.5 simulations. In the boreal summer, the mixed-layer zonal current primarily flows westward at the equator, especially in the central Indian Ocean (Fig. 6.9m). During pIOD, more negative SSTAs in the eastern Indian Ocean generate negative anomalies of zonal MLT gradient (Fig. 6.9d). The combination of the westward zonal current in the mean state and the negative anomalies of zonal MLT gradient contributes to a negative $-\bar{u}(\partial T'/\partial x)$ term in the ETIO, fostering pIOD development (Fig. 6.9a). During nIOD, the positive anomalies of zonal MLT gradient (Fig. 6.9j), along with the westward zonal current in the mean state, result in a positive $-\bar{u}(\partial T'/\partial x)$ term in the ETIO (Fig. 6.9g), which favors nIOD development. Under the SSP5-8.5 scenario, the westward mean-state zonal current significantly increases along the equator, especially in the central TIO (Figs. 6.9n, o). This implies enhanced east-to-west temperature anomaly transportation under the SSP5-8.5 scenario, which helps the equatorial SSTA development. Despite a slight decrease in the anomalies of the zonal MLT gradient due to weaker atmospheric response in a warmer climate, the significant enhancement of mean-state zonal mixed-layer current leads to stronger $-\bar{u}(\partial T'/\partial x)$ term along the equator during IOD events (Figs. 6.9a–c, g–i). The amplification of the westward zonal current in the mean state results from background alterations in the surface zonal wind, associated with the IOD-like warming pattern (Fig. 6.6i). Projected greenhouse warming intensifies the southeasterly wind in the southern off-equatorial region and attenuates the westerly wind in the northern off-equatorial region. These modifications induce significant surface easterly wind changes in the TIO (Figs. 6.9p–r), promoting the westward zonal current in the mean state (Figs. 6.9m–o).

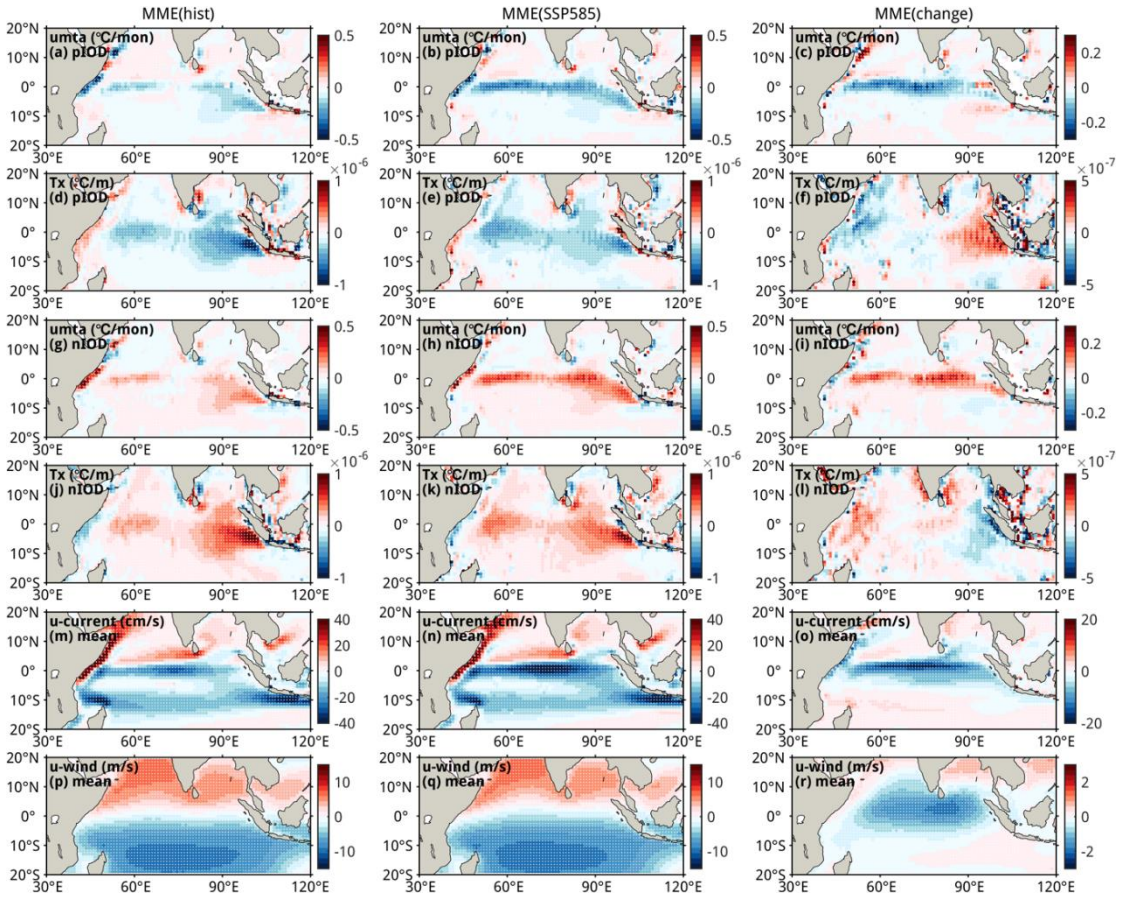


Figure 6.9. Composite (a) pIOD $-\bar{u}(\partial T'/\partial x)$ (unit: °C month^{-1}), (d) pIOD $\partial T'/\partial x$ (unit: °C m^{-1}), (g) nIOD $-\bar{u}(\partial T'/\partial x)$, (j) nIOD $\partial T'/\partial x$, (m) $\bar{u}$ (unit: cm s^{-1}), and (p) mean-state surface zonal wind (unit: m s^{-1}) during JASO in the historical simulations. (b, e, h, k, n, q) are the same as (a, d, g, j, m, p), but for SSP5-8.5 scenario. (c, f, i, l, o, r) are the same as (a, d, g, j, m, p), but for greenhouse-warming-induced changes. White stippling indicates the 95% significance level based on Student's t-test.

Among the selected CMIP6 models, the mean-state change in the mixed-layer zonal current is highly correlated with the $-\bar{u}(\partial T'/\partial x)$ variance change, standing at a coefficient of –0.75 (passes the 95% significance level) (Fig. 6.10a). Models predicting a larger westward zonal current at the equator tend to produce a stronger variance of the $-\bar{u}(\partial T'/\partial x)$ term. Furthermore, there is a pronounced correlation between the $-\bar{u}(\partial T'/\partial x)$ variance change and the SSTA STD change in the equatorial ETIO. This correlation is quite strong, standing at a coefficient of 0.77, and is statistically significant at the 95% level (Fig. 6.10b). In conclusion, under a warmer climate, the weakened Walker Circulation in the TIO, characterized by the weakened westerly winds in the northern off-equatorial TIO and the intensified easterly winds in the southern off-equatorial TIO, would notably enhance the background westward zonal current at the equator during JASO. This enhanced current leads to increased amplitude

of the $-\bar{u}(\partial T'/\partial x)$ term, which in turn contributes to a larger SSTA amplitude in the equatorial ETIO during IOD events, manifesting a northward extension of the IOD pattern compared to the historical simulations.

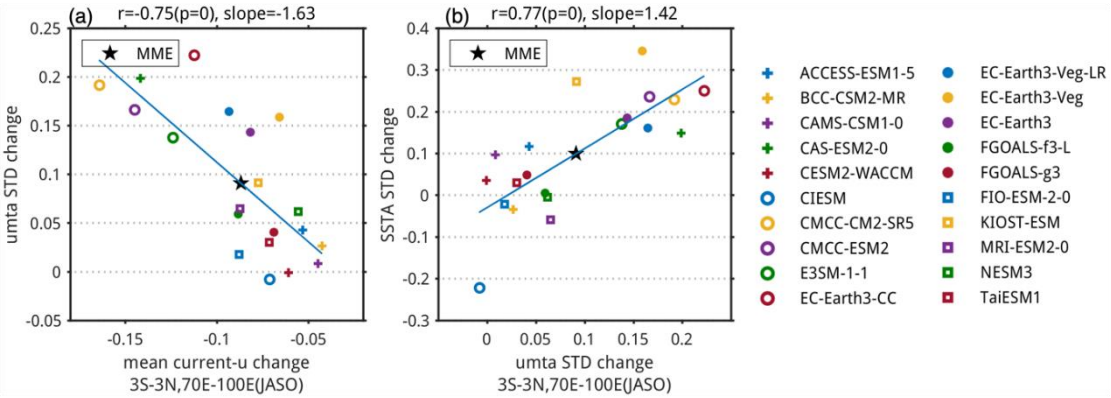


Figure 6.10. (a) $\bar{u}$ changes (unit: m s^{-1}) vs $-\bar{u}(\partial T'/\partial x)$ STD changes (unit: °C $month^{-1}$) during JASO within 3°S–3°N, 70°–100°E. (b) $-\bar{u}(\partial T'/\partial x)$ STD changes vs SSTA STD changes (unit: °C). The blue line is the least square linear fit. The r value is the correlation coefficient.

The ocean stratification has increased globally in recent decades (Li et al. 2020). As for the TIO, model simulations reveal a marked increase in upper-ocean stratification under the SSP5-8.5 scenario, relative to the historical simulations (Fig. 6.11). The squared buoyancy frequency exhibits notable values beneath the MLD in the historical simulations (Fig. 6.11a) and it increases significantly under global warming, especially from 80°E to 100°E (Figs. 6.11b, c). Projections suggest that the ETIO is increasingly susceptible to ocean entrainment, mainly associated with the $-w'\overline{(T-T_{-h})/h}$, $-\bar{w}[(T-T_{-h})/h]'$ and $-w'[(T-T_{-h})/h]'$ terms in the mixed-layer heat budget. However, vertical advection is influenced by both atmospheric and oceanic responses. The large-scale atmospheric response is projected to weaken during IOD due to the increased atmospheric static stability, while the wind-driven oceanic response is expected to intensify during IOD due to the increased upper-ocean stratification. Additionally, a reduction in the efficiency of thermodynamic air-sea feedback will likely further suppress the atmospheric and oceanic responses during pIOD. The combined effects of these responses vary between pIOD and nIOD.

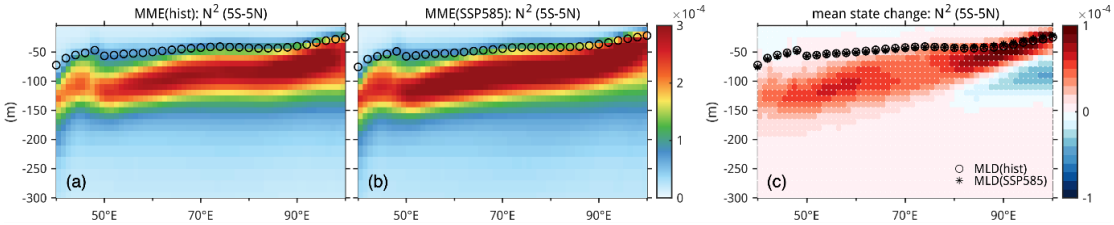


Figure 6.11. Mean-state squared buoyancy frequency (shading; unit: s^{-2}) and MLD (circle) during JASO in the (a) historical and (b) SSP5-8.5 scenario simulations. (c) is the mean-state change. The circle (asterisk) denotes historical (SSP5-8.5) MLD.

The Ekman pumping term, $-w'\overline{(T-T_{-h})/h}$, increases during nIOD and slightly declines during pIOD in the equatorial ETIO (Figs. 6.12a–c, g–i). In the historical simulation, significant values of the mean-state vertical temperature gradient $[\overline{(T-T_{-h})/h}]$ are mainly found in the southern TIO and near the Sumatra-Java coast (Fig. 6.12m). Under global warming, the mean-state $\overline{(T-T_{-h})/h}$ is projected to enhance near the Sumatra-Java coast and in the equatorial ETIO (Figs. 6.12n, o). The ocean vertical velocity variance at the MLD is projected to decrease during IOD due to a weaker atmospheric response and the reduced efficiency of the thermodynamic air-sea feedback will further decrease the vertical motion anomalies near the Sumatra-Java coast during pIOD (Figs. 6.12d–f, j–l). Consequently, the reduced ocean vertical velocity anomalies overwhelm the increased mean-state vertical temperature gradient at the base of the mixed layer, leading to a minor decrease in the Ekman pumping term in the equatorial ETIO during pIOD. This situation only occurs at the equator from 70°E to 100°E during nIOD. The ocean vertical motion anomalies near the Sumatra coast show less decrease during nIOD, producing increased Ekman pumping term in this region and favoring the nIOD development. The $-w'\overline{(T-T_{-h})/h}$ also acts as a damping term in the off-equatorial region. The decreased vertical motion variance will mitigate this damping effect, partially accounting for the increased SSTA STD in the ETIO during nIOD (Fig. 6.2f). Although the off-equatorial $-w'\overline{(T-T_{-h})/h}$ may somewhat favor pIOD development, this influence is likely to be offset by the less negative nonlinear zonal advective (Fig. 6.8), a consequence of a weaker atmospheric response and reduced efficiency of the thermodynamic air-sea feedback.

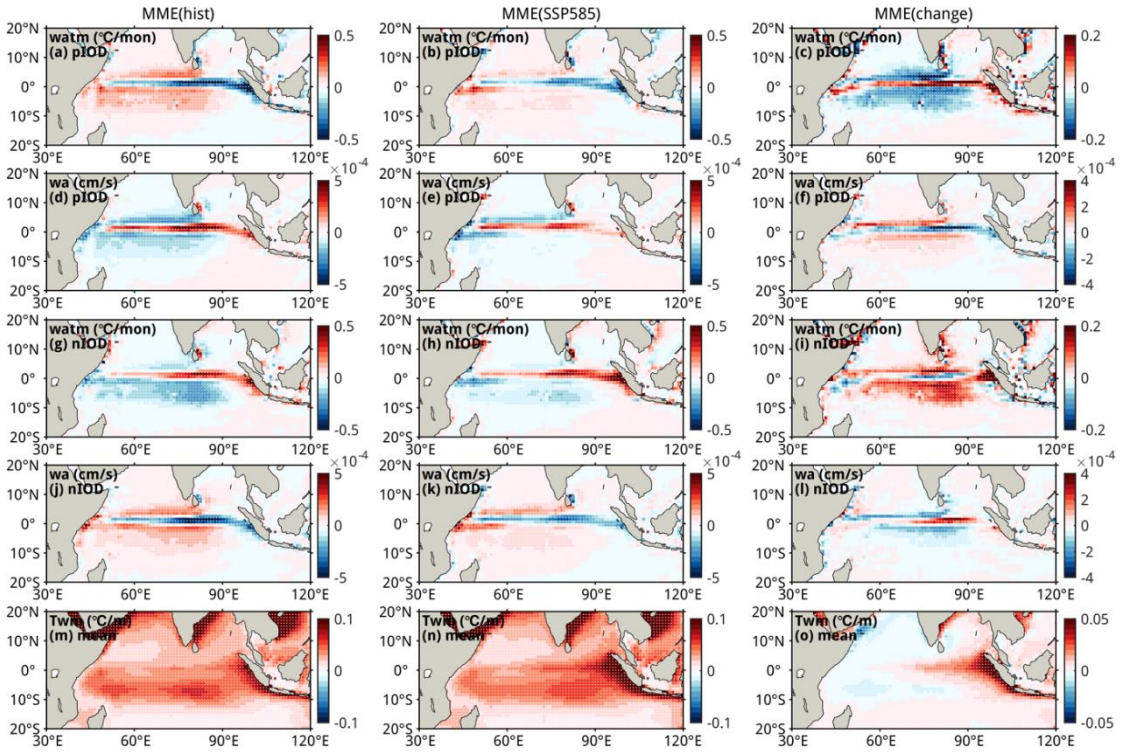


Figure 6.12. Composite (a) pIOD $-w'\overline{(T-T_{-h})/h}$ (unit: °C month^{-1}), (d) pIOD w' (unit: cm s^{-1}), (g) nIOD $-w'\overline{(T-T_{-h})/h}$, (j) nIOD w', and (m) $\overline{(T-T_{-h})/h}$ (unit: °C m^{-1}) during JASO. (b, e, h, k, n) are the same as (a, d, g, j, m), but for SSP5-8.5 scenario. (c, f, i, l, o) are the same as (a, d, g, j, m), but for greenhouse-warming-induced changes. White stippling indicates the 95% significance level based on Student's t-test.

The influence of the $-\overline{w}[(T-T_{-h})/h]'$ term is relatively restricted due to the mean-state upwelling region, mainly located at the equator and near the Sumatra-Java coast (Figs. 6.13m–o). Although previous studies indicate that thermocline feedback tends to intensify due to global warming (Zheng et al. 2010; Ng and Cai 2016), the mixed-layer heat budget reveals that the $-\overline{w}[(T-T_{-h})/h]'$ term has minimal impact on MLT tendency changes (Fig. 6.13a–c, g–i). The weaker atmospheric response will reduce the vertical temperature gradient anomaly $\{[(T-T_{-h})/h]'\}$, while enhanced oceanic stratification could amplify the $[(T-T_{-h})/h]'$. Consequently, the $-\overline{w}[(T-T_{-h})/h]'$ remains comparable under the SSP5-8.5 scenario. Regarding the nonlinear vertical advection $\{-w'[(T-T_{-h})/h]'\}$, it becomes slightly less negative during pIOD and more negative during nIOD (Fig. 6.8). This suggests that the nonlinear vertical advection contributes minimally to the IOD changes, as it does not correspond with the weaker pIOD amplitude and the stronger nIOD amplitude. Overall, the $-\overline{w}[(T-T_{-h})/h]'$ term tends to remain comparable during IOD due to the combined effects of weaker wind response to SSTAs and enhanced wind-driven ocean coupling. Instead,

the $-w'\overline{(T-T_{-h})/h}$ term significantly contributes to the increased nIOD amplitude, showing a more favorable effect near the Sumatra coast and a reduced damping effect in the off-equatorial region. However, a further decrease in ocean vertical velocity anomalies during pIOD causes the decreased w' to overweigh the increased $\overline{(T-T_{-h})/h}$, leading to a slight decrease in the Ekman pumping term.

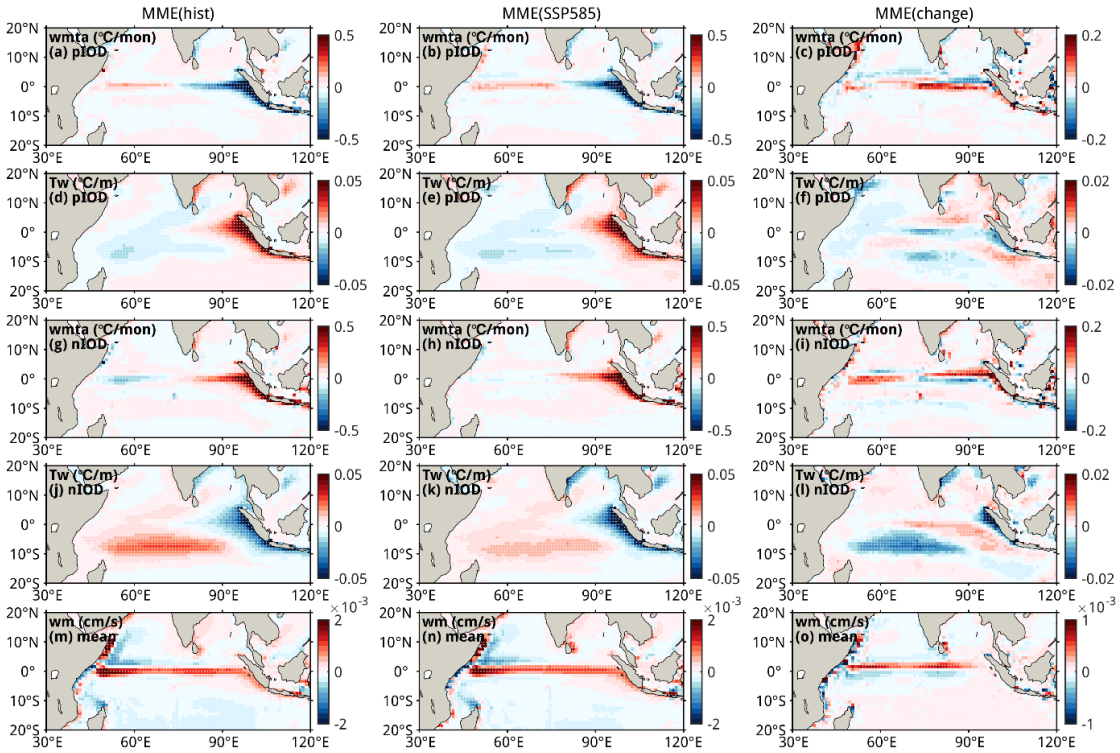


Figure 6.13. Composite (a) pIOD $-\overline{w}[(T-T_{-h})/h]'$ (unit: ℃ month^{-1}), (d) pIOD $[(T-T_{-h})/h]'$ (unit: ℃ m^{-1}), (g) nIOD $-\overline{w}[(T-T_{-h})/h]'$, (j) nIOD $[(T-T_{-h})/h]'$, and (m) $\overline{w}$ (unit: cm s^{-1}) during JASO. (b, e, h, k, n) are the same as (a, d, g, j, m), but for SSP5-8.5 scenario. (c, f, i, l, o) are the same as (a, d, g, j, m), but for greenhouse-warming-induced changes. White stippling indicates the 95% significance level based on Student's t-test.

7. IOD impacts on Eastern Africa and Australia

7.1. Observed IOD climatic impacts

Figures 7.1a–e illustrate the partial least squares regression pattern of the 3-month SPEI onto the DMI, with influences of the Niño 3.4 index removed during JJA, JAS, ASO, SON and OND in observations. The 3-month SPEI, an advanced version of the Standardized Precipitation Index (SPI), considers both precipitation and potential evapotranspiration to assess drought. From July to December, the 3-month SPEI positively correlates with the DMI in Eastern Africa, as well as India and Sri Lanka during the ASO and SON, suggesting wetter conditions during pIOD and drier conditions during nIOD. Conversely, the SPEI indicates a significant negative regression in Sumatra, Java, and Australia during boreal summer and autumn, pointing to a higher drought likelihood during pIOD and increased rainfall during nIOD. This SPEI pattern aligns with the rainfall regression pattern observed in Eastern Africa, South India, Sri Lanka, Sumatra, and Java (Figs. 7.1f–j). Increased rainfall in Eastern Africa, South India, and Sri Lanka during pIOD implies an elevated flood risk, while Sumatra and Java may face drought due to weakened Walker Circulation, potentially increasing regional wildlife. In particular, the IOD significantly influences Eastern Africa's rainfall during OND, this region's short-rain season (Fig. 7.1j). The IOD-induced surface air temperature anomalies in Eastern Africa result from the precipitation anomalies by modulating the cloud and shortwave radiation (Fig. 7.1o). Consequently, precipitation anomalies largely determine Eastern Africa's drought conditions during IOD. For Australia, the most significant 3-month SPEI response to IOD occurs during ASO, primarily due to surface air temperature anomalies in Southwestern Australia (Fig. 7.1m) and precipitation anomalies in Southeastern Australia (Fig. 7.1h). Given the significant impacts on Eastern Africa and Australia and the simulated biases of IOD-related convection (Fig. 7.6), our focus mainly lies on the precipitation and surface air temperature responses to IOD events in these two regions.

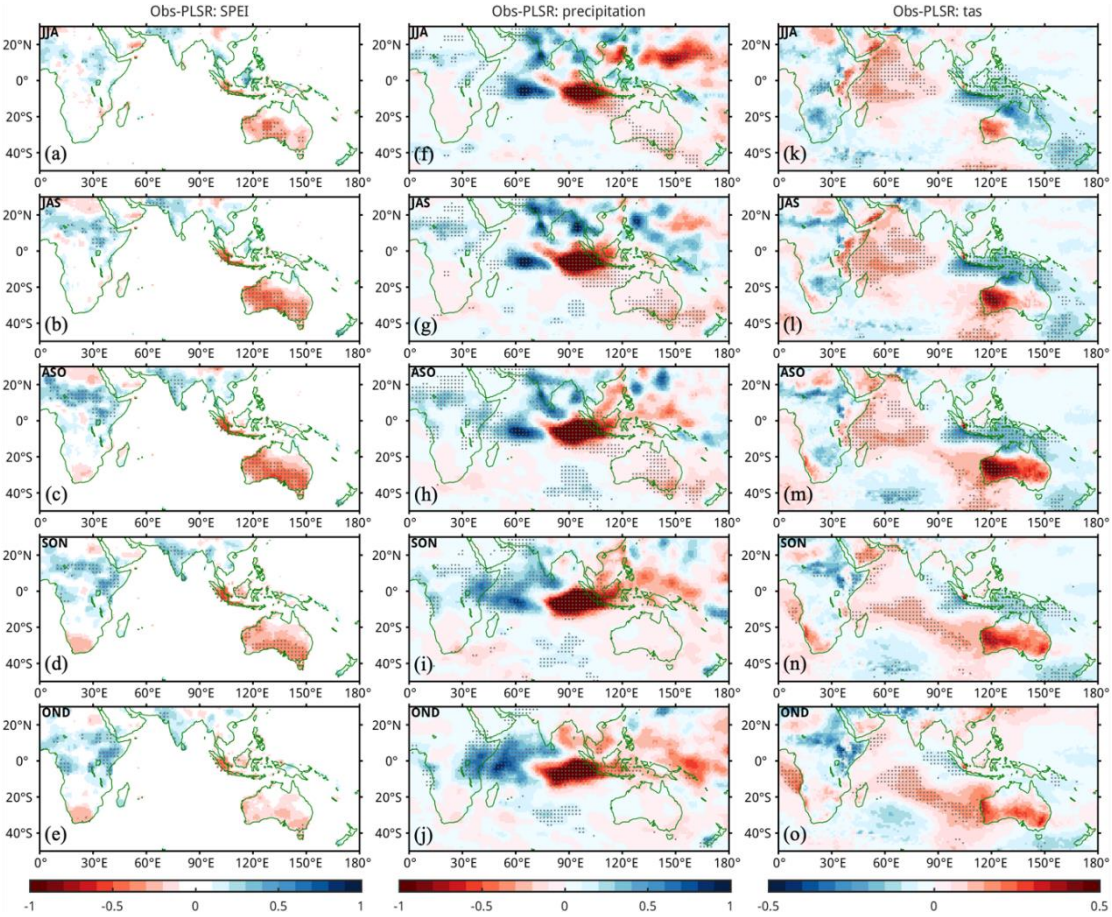


Figure 7.1. Partial least squares regression of (a, b, c, d, e) 3-month SPEI, (f, g, h, i, j) precipitation anomalies (unit: mm day^{-1}) and (k, l, m, n, o) surface air temperature anomalies (unit: K) onto DMI with the influences of Niño 3.4 index removed during (a, f, k) JJA, (b, g, l) JAS, (c, h, m) ASO, (d, i, n) SON and (e, j, o) OND in observations. Stippling indicates the 95% significance level based on Student's t-test.

7.2. Historical rainfall responses in Eastern Africa

7.2.1. Model selection

Eastern Africa experiences bimodal rainfall, comprising long (MAM) and short (OND) rains, which significantly impact socioeconomics and the environment (Palmer et al. 2023). Given that most CMIP5 models tend to overestimate short rains and underestimate long rains in Eastern Africa (Tierney et al. 2015), it's crucial to select models that capture monthly precipitation climatology more accurately. Based on the partial DMI regression pattern (Fig. 7.1), the 10°S–12°N, 30°–52°E region, significantly influenced by the IOD, is chosen to represent Eastern Africa. Figure 7.2a depicts the monthly climatological precipitation pattern in observations, with peak mean-state precipitation in April. Similar to CMIP5, most CMIP6 models underestimate long-rain precipitation and overestimate short-rain precipitation (Fig.

7.2b). The mean-state biases are more pronounced during the short-rain season, with all CMIP6 models, except the FGOALS-f3-L model, simulating larger short-rain precipitation. However, the FGOALS-f3-L model underestimates all monthly climatological precipitation. Considering the spatial correlation and Root Mean Square Error (RMSE) of monthly climatological precipitation over Eastern Africa between observations and CMIP6 models, 16 out of 20 CMIP6 models are selected to study IOD impacts on Eastern Africa precipitation. These include BCC-CSM2-MR, CAMS-CSM1-0, CESM2-WACCM, CIESM, CMCC-CM2-SR5, CMCC-ESM2, E3SM-1-1, EC-Earth3-CC, EC-Earth3-Veg-LR, EC-Earth3-Veg, EC-Earth3, FIO-ESM-2-0, KIOST-ESM, MRI-ESM2-0, NESM3, and TaiESM1 (Fig. 7.2c).

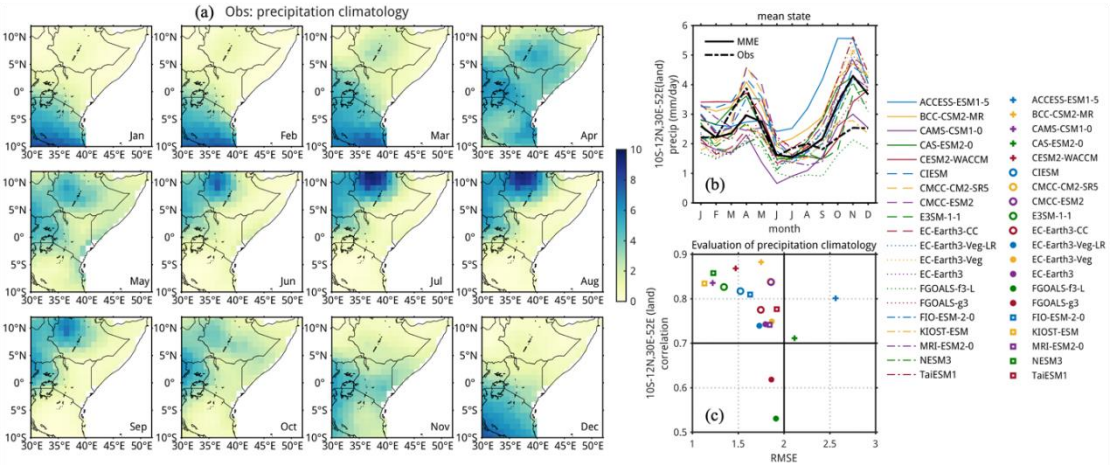


Figure 7.2. (a) Monthly climatological precipitation (unit: mm day^{-1}) pattern in observations. (b) Monthly climatological precipitation averaged over Eastern Africa (10°S–12°N, 30°–52°E) in observations and CMIP6 models. (c) RMSE vs spatial correlation of monthly climatological precipitation over Eastern Africa between observation and CMIP6 models.

7.2.2. Overestimated rainfall responses in Eastern Africa

In pIOD events, Eastern Africa would experience more rainfall, which intensifies from the developing phase and peaks in OND (Figs. 7.3a–c). All extreme pIOD events, such as those in 1994, 1997 and 2019, led to a significant precipitation increase, notably the 1997 pIOD event, which caused more than 3 mm day^{-1} rainfall anomaly during the short-rain season (not shown). This increased precipitation presents severe challenges for developing countries in this region. Contrastingly, the nIOD impact is much smaller than pIOD in observations, with a precipitation amplitude of less than 1 mm day^{-1} (Figs. 7.3g–i). The precipitation anomalies during IOD mainly result from the modulation of Walker Circulation by influencing the vertical motion and associated horizontal flow.

CMIP6 models simulate slightly larger precipitation responses during pIOD (Figs. 7.3d–f) and significantly larger responses during nIOD (Figs. 7.3j–l) compared to the observations. The biases in precipitation responses to IOD are associated with enhanced moisture transport in the eastern boundary of the selected region from the Indian Ocean, resulting from the enhanced zonal wind anomalies during IOD. These anomalies can be traced back to the simulations of IOD amplitude and locations of the IOD SSTA cores.

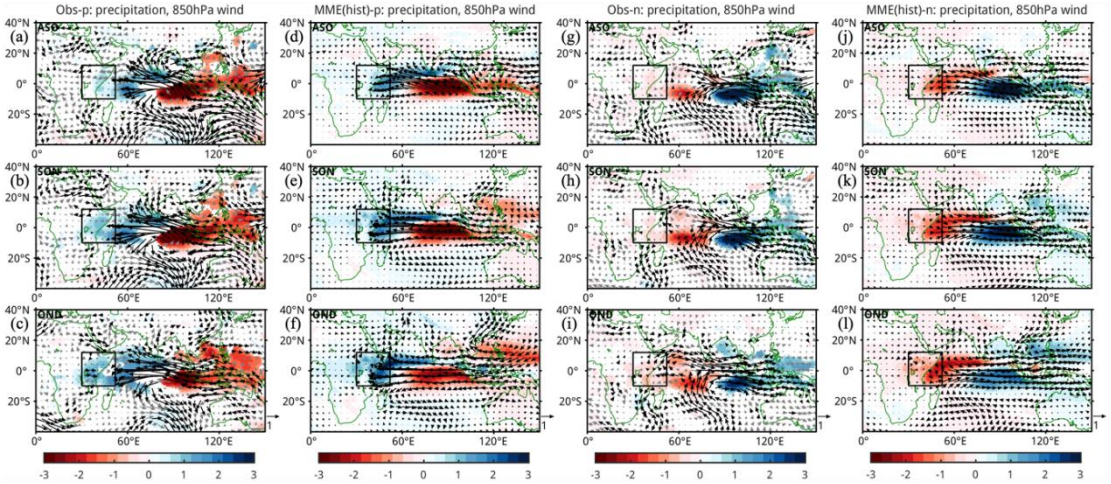


Figure 7.3. Composite precipitation (unit: mm day^{-1}) and 850 hPa wind anomalies (see scale vector in lower right; unit: m s^{-1}) during (a, d, g, j) ASO, (b, e, h, k) SON and (c, f, i, l) OND based on (a, b, c) observed pIOD, (b, e, f) historical pIOD, (g, h, i) observed nIOD and (j, k, l) historical nIOD. The black box is 10°S–12°N, 30°–52°E. Shading values and black vectors are displayed upon surpassing the 95% significance level (Student's t-test).

Precipitation sources are typically determined through a water vapor budget. Evaporation, due to its negligible contribution, is excluded from consideration. Over seasonal and extended time scales, local water vapor propensity is typically negligible, making the convergence and divergence of water vapor transport crucial in determining precipitation (Trenberth and Guillemot 1995). To examine the origins of these precipitation response biases, a water vapor budget is utilized, with emphasis on CVIMF biases (Fig. 7.4). The CVIMF biases are mainly categorized into four components: IOD-related wind circulation anomaly biases $[-\langle\nabla\cdot(\bar{q}_O\Delta\vec{V}')\rangle]$, mean-state moisture biases $[-\langle\nabla\cdot(\overrightarrow{V_H}'\Delta\bar{q})\rangle]$, IOD-related moisture anomaly biases $[-\langle\nabla\cdot(\overrightarrow{\bar{V}_O}\Delta q')\rangle]$, and mean-state wind circulation biases $[-\langle\nabla\cdot(q_H'\Delta\vec{\bar{V}})\rangle]$. Each component can be further divided into the zonal and meridional parts. The larger precipitation responses to IOD are mainly related to the enhanced term due to IOD-related zonal wind anomaly biases $[-\langle\nabla\cdot(\bar{q}_O\Delta u')\rangle]$, followed by the enhanced term

due to mean-state moisture biases in the zonal direction $[-\langle\nabla\cdot(u_H{}'\Delta\bar{q})\rangle]$ (Fig. 7.4). Because the interannual variability of moisture relative to its climatology is much smaller than the ratio of circulation variability to circulation (Huang and Xie 2015), the term due to the IOD-related moisture anomaly biases and the term due to the mean-state wind circulation biases are negligible relative to the terms due to IOD-related wind circulation anomaly biases and mean-state moisture biases.

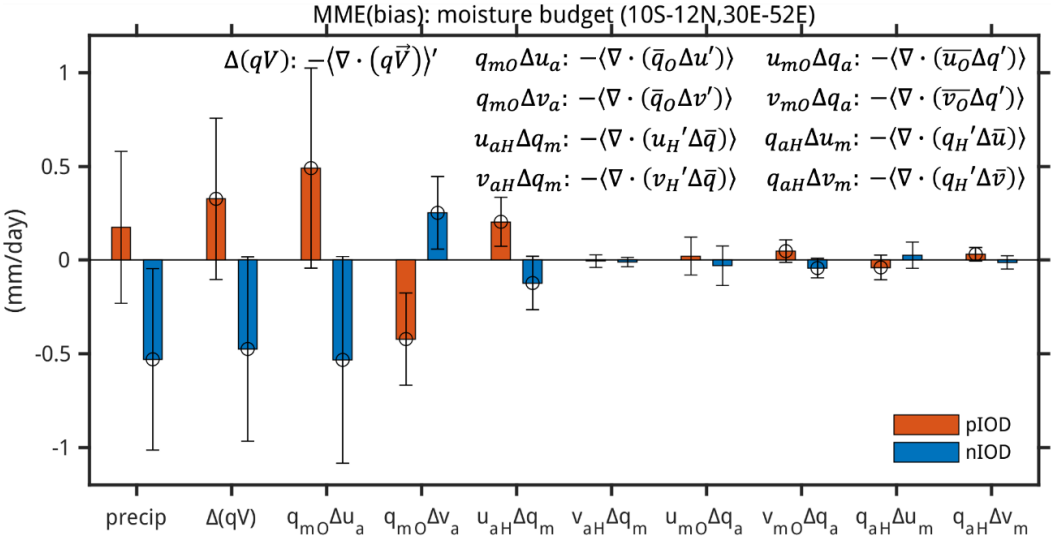


Figure 7.4. Biases of IOD composite biases for precipitation anomalies and water vapor budget terms (unit: mm day^{-1}) averaged over Eastern Africa (10°S–12°N, 30°–52°E) during OND. Error bar is based on one STD. Circle over the bar indicates signals passing the 95% significance level.

7.2.3. Contributions from simulated IOD biases

The overestimated precipitation responses to IOD in Eastern Africa can be linked to the amplified CVIMF simulation, initially traceable to the simulated IOD (Fig. 7.5). In observations, the eastern SSTA core of IOD is mainly situated near the Sumatra-Java coast, not exceeding 80°E in composite patterns. However, CMIP6 models not only simulate the stronger IOD amplitude, specifically a stronger eastern SSTA core, but also an expanded westward shift of the eastern core, surpassing 70°E. Both factors contribute to increased zonal wind anomalies in the WTIO and amplified zonal moisture transport anomalies in Eastern Africa. These SSTA simulation biases lead to simulation biases in convection centers (Fig. 7.6). In observations, the eastern convection center is located on the Maritime Continent, maturing during ASO and decaying subsequently. While the western convection center, on the other hand, develops from summer and peaks in OND. CMIP6 models predict a slight westward shift of the western convection center and a more significant westward shift of the eastern convection center,

irrespective of pIOD or nIOD. Besides, the convection responses to IOD in Eastern Africa during OND are both larger than the observed, especially during nIOD. This is consistent with the weaker IOD amplitude asymmetry in CMIP6 models, implying stronger nIOD simulation (McKenna et al. 2020; Zheng et al. 2024).

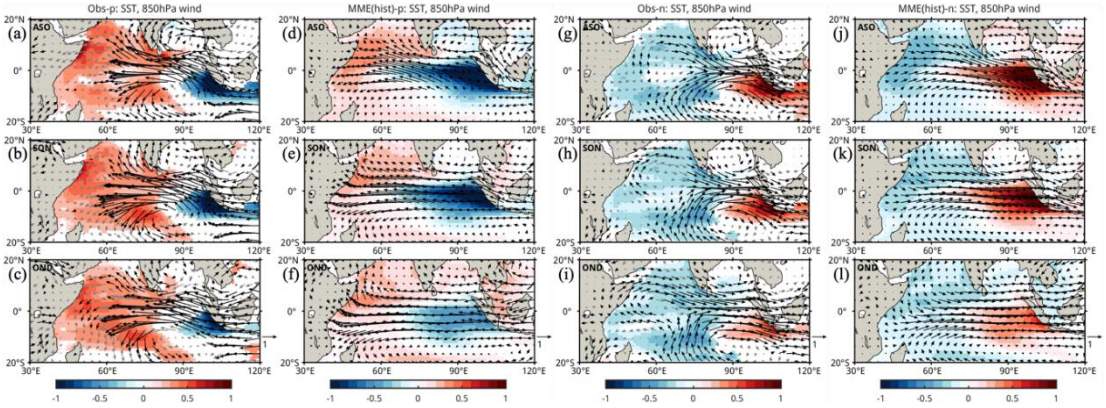


Figure 7.5. The same as Fig. 7.3, but for SSTA (unit: ℃) and 850 hPa wind anomalies (see scale vector in lower right; unit: m s^{-1}).

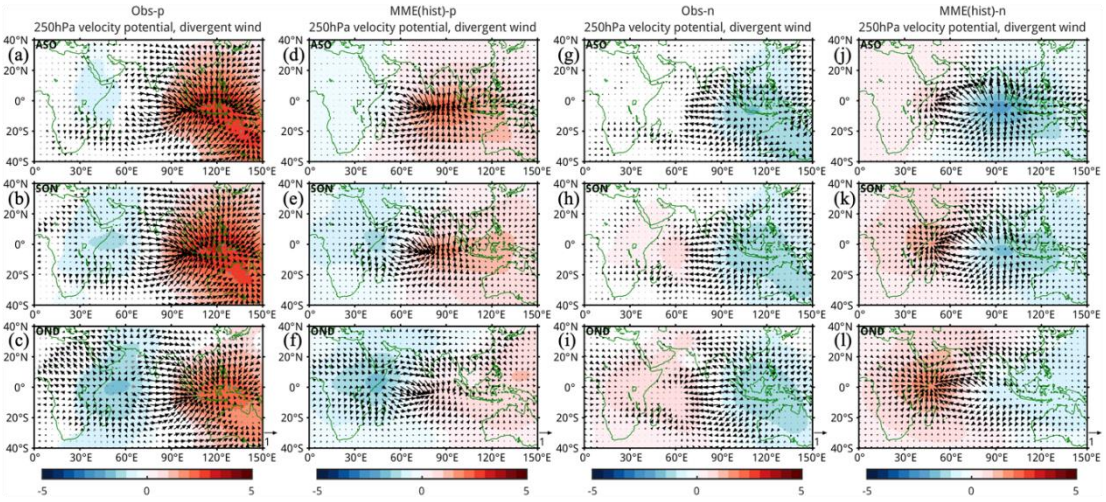


Figure 7.6. The same as Fig. 7.3, but for 250 hPa velocity potential (unit: 10^6 m^2 s^{-1}) and divergent wind anomalies (see scale vector in lower right; unit: m s^{-1}).

Inter-model statistics from CMIP6 corroborate the strong correlation between the amplified precipitation anomalies in Eastern Africa and the IOD SSTA during OND (Fig. 7.7). Models with a larger composite pIOD for the SSTA gradient in the TIO tend to simulate a larger composite pIOD for the precipitation anomalies in Eastern Africa during OND, exhibiting a robust correlation coefficient of 0.80 that surpasses the 95% significance level (Fig. 7.7a). The composite nIOD results mirror those of the composite pIOD (r = 0.77; Fig. 7.7b). It is noteworthy that the precipitation response during nIOD is overestimated in almost all models. In summary, the primary factor driving the

enhanced precipitation response to IOD in Eastern Africa is the amplification of the zonal moisture transport anomaly, stemming from the westward shift of eastern SSTA signals and the larger simulated IOD amplitude. Cai and Cowan (2013), using CMIP3 and CMIP5 models, identified the larger simulated IOD amplitude as being linked to the increased strength of the thermocline-SST feedback, attributable to the unrealistic simulation of the climatological west-east slope of the equatorial thermocline. Liu et al. (2014) discovered that the thermocline response to surface wind forcing is more unrealistic, contributing to a larger IOD amplitude. Among the selected CMIP6 models, the larger simulated IOD amplitude primarily arises from the enhanced thermocline-SST feedback (not shown).

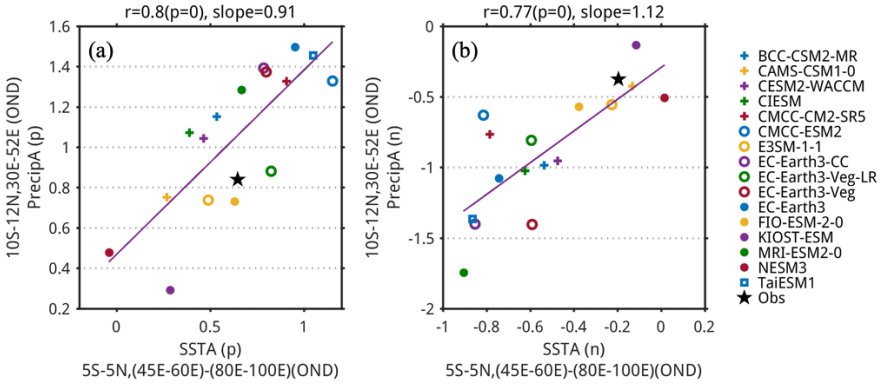


Figure 7.7. (a) Composite pIOD for SSTA gradient in the TIO (unit: °C; 5°S–5°N, 45°–60°E minus 80°–100°E; OND) vs precipitation anomalies in Eastern Africa (unit: mm day^{-1}; 10°S–12°N, 30°–52°E). (b) is the same as (a), but for nIOD. The purple line is the least square linear fit. The r value is the correlation coefficient.

7.2.4. Contributions from mean state biases

Followed by the simulation biases of the IOD, the mean-state precipitation bias also contributes to the enhanced precipitation variabilities during IOD in Eastern Africa. In observations, Eastern Africa is a subsidence region in terms of the mean precipitation during OND, with a value of more than 2 mm day^{-1}, which is smaller than that in Western Africa and the TIO (Fig. 7.8a, d). Nevertheless, the overestimated short-rain precipitation in Eastern Africa is a common mean-state bias in CMIP3/5/6 models (Tierney et al. 2015; Lyon 2021). In the CMIP6 MME pattern, the mean precipitation during OND appears to intensify over Africa and the TIO (Fig. 7.8b). In the historical simulation, Eastern Africa's average precipitation during OND is approximately 4 mm day^{-1}, contrasting with the observed value of roughly 2 mm day^{-1}. The WTIO displays a more significant discrepancy of about 6 mm day^{-1} (Fig. 7.8c), suggesting a correlation between the overestimation of short-rain precipitation and the WTIO simulation. All

selected CMIP6 models simulate larger mean state and variability of precipitation during OND, and models with larger mean-state precipitation tend to generate stronger precipitation variation, with a robust correlation coefficient of 0.75 (Fig. 7.8g). Previous studies pointed out that this overestimation is particularly sensitive to the warmer WTIO (Yang et al. 2015a, b) and the underestimated Walker Circulation (King et al. 2020). In CMIP6 models, the simulated subsidence region is significantly narrower than the observed, mainly occurring within 35°–45°E (Figs. 7.8d, e). The biases of ascending motion are most significant within 40°–75°E, suggesting a weaker simulation of mean-state Walker Circulation in the TIO, mainly the WTIO (Fig. 7.8c). The close relationship between simulated short-rain precipitation and simulated Walker Circulation is also supported by the inter-model statistics of selected CMIP6 models. Models that capture larger 500 hPa omega correspond to larger short-rain precipitation, with a correlation coefficient of 0.87 (Fig. 7.8h). Note that all selected CMIP6 models capture weaker mean-state 500 hPa omega in the WTIO. Furthermore, the weaker Walker Circulation can be traced back to the positive IOD-like biases in the mean state, with mean-state surface zonal wind highly correlated with the mean-state 500 hPa omega in the WTIO (r = 0.73; Fig. 7.8i). All in all, the overestimated short-rain responses to IOD in Eastern Africa are partially attributed to the enhanced precipitation climatology, which is associated with the weaker simulation of Walker Circulation and mean-state positive IOD-like biases.

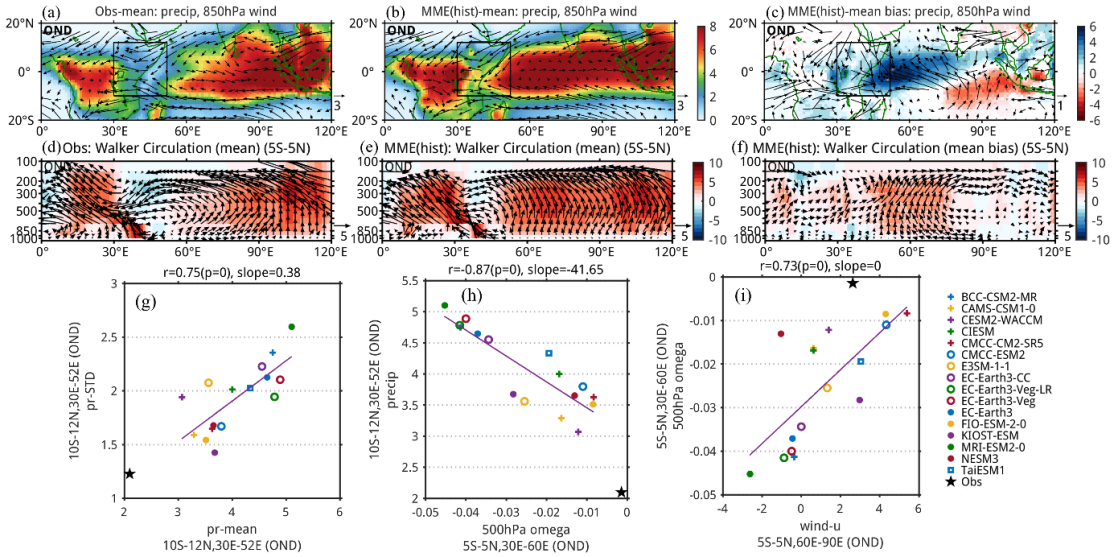


Figure 7.8. (a, b) Mean-state precipitation (shading; unit: mm day^{-1}) and 850 hPa wind (see scale vector in lower right; unit: m s^{-1}), and (d, e) mean-state omega (shading; 0.01 Pa s^{-1}; multiplied by –1), and atmospheric zonal (m s^{-1})–vertical (–0.01 Pa s^{-1}) vectors averaged in 5°S–5°N during OND in (a, d) observations and (b, e) historical simulations.

Mean-state biases of (e) precipitation and 850 hPa wind, and (f) Walker Circulation. Biases of omega (white stippling), precipitation and wind are shown when exceeding the 95% significance level based on Student's t-test. (g) Mean-state precipitation (unit: mm day^{-1}; 10°S–12°N, 30°–52°E; OND) vs its STD. (h) Mean-state 500 hPa omega (unit: Pa s^{-1}; 5°S–5°N, 30°–60°E; OND) vs mean-state precipitation. (i) Mean-state surface zonal wind (unit: m s^{-1}; 5°S–5°N, 60°–90°E; OND) vs mean-state 500 hPa omega. The purple line is the least square linear fit. The r value is the correlation coefficient.

7.3. Projected rainfall responses in Eastern Africa

7.3.1. Enhancement in Somali Peninsula and reduction in Southeastern Africa

The Somali Peninsula, also known as the Horn of Africa, has long endured the dual calamities of flooding and drought. The IOD significantly influences the Peninsula, regardless of ENSO's presence. The observed connection between the IOD and the Eastern Africa short rains, together with the recent drought years in Eastern Africa (Mölg et al. 2006), prompts a crucial question: how does the IOD affect regional precipitation characteristics under global warming? In historical simulations, pIOD would induce increased precipitation in Eastern Africa (Fig. 7.9a). Under the SSP5-8.5 scenario, there will be a greater increase in precipitation in the Somali Peninsula and a lesser increase in Southeastern Africa (Figs. 7.9b, c). This suggests that pIOD is projected to have a larger climatic influence on the Somali Peninsula and a smaller climatic influence on Southeastern Africa under global warming. Regarding the nIOD events, there will be a greater decrease in precipitation in the Somali Peninsula and a lesser decrease in Southeastern Africa (Figs. 7.9e, f). Note that the precipitation anomaly changes during nIOD are significantly larger than those during pIOD, indicating enhanced climatic impacts from nIOD in this region. Endris et al. (2019) also pointed out a stronger IOD-related rainfall anomaly over the Somali Peninsula but a weaker signal in southern Africa during the short rains using CMIP5 models. They suggested that the projected increase in OND rainfall over the Somali Peninsula might be associated with the mean-state changes in SST over Indian and Pacific Ocean basins and their Walker Circulations (Endris et al. 2019). In this study, we focus on the Somali Peninsula and Southeastern Africa, suggesting that both moister atmosphere and IOD circulation changes contribute to these precipitation response changes. The composite precipitation pattern divided by the IOD amplitude mirrors the changes seen in the raw composite (not shown).

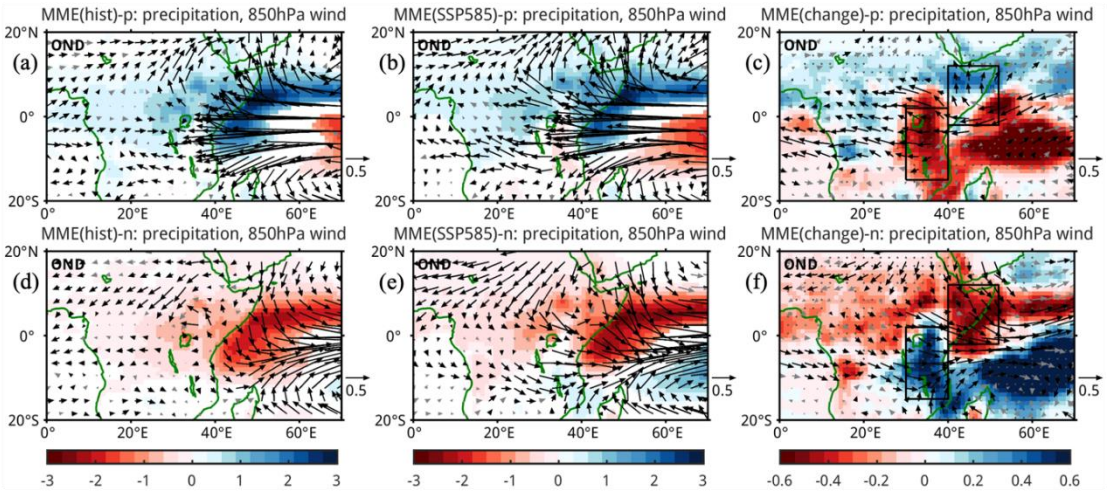


Figure 7.9. Composite precipitation (unit: mm day^{-1}) and 850 hPa wind anomalies (see scale vector in lower right; unit: m s^{-1}) during OND in (a, b) pIOD and (d, e) nIOD based on (a, d) historical and (b, e) SSP5-8.5 simulations. Values exceeding the 95% significance level (Student's t-test) are shown. Their greenhouse-warming-induced changes during (c) pIOD and (f) nIOD with stippling and black vector for statistical significance.

Under the SSP5-8.5 scenario, the Somali Peninsula's short rain is expected to have a larger amplitude during IOD events. The MME CMIP6 pattern indicates a more pronounced negative precipitation response during nIOD, significantly exceeding changes during pIOD. To investigate the origins of these precipitation response alterations, we utilize a water vapor budget, focusing on changes in the CVIMF (Fig. 7.10). CVIMF alterations can be broadly categorized into four factors: IOD-related wind circulation changes ($-\langle\nabla\cdot(\bar{q}_H\Delta\vec{V}')\rangle$), mean-state moisture changes ($-\langle\nabla\cdot(\overrightarrow{V_S}'\Delta\bar{q})\rangle$), IOD-related moisture changes ($-\left\langle\nabla\cdot\left(\overrightarrow{\vec{V}_H}\Delta q'\right)\right\rangle$), and mean-state wind circulation changes ($-\left\langle\nabla\cdot\left(q_S'\Delta\vec{\vec{V}}\right)\right\rangle$). Each factor comprises both zonal and meridional components. Future rainfall changes are the combination of thermodynamic component due to moisture increase and dynamic component due to circulation change (Xie et al. 2015). The "wet-gets-wetter" hypothesis suggests that wet (dry) regions will become wetter (drier) in conjunction with increased moisture content (Held and Soden 2006). This generally corresponds to the thermodynamic component. On the other hand, the "warmer-gets-wetter" mechanism suggests that SST and its changes play a pivotal role in shaping future tropical circulation and precipitation, corresponding to the dynamic effect (Xie et al. 2010a). The primary cause of IOD-related precipitation changes in the Somali Peninsula during OND stems from the zonal component of CVIMF changes due

to mean-state moisture changes (Fig. 7.10a). A more humid atmosphere over the Horn of Africa, resulting from global warming, consistently amplifies rainfall variations, regardless of the intensification or weakening of IOD-related circulation anomalies. The zonal component of CVIMF changes due to IOD-related wind circulation changes, also contributes to the enhanced precipitation response during nIOD, leading to larger anomalous precipitation changes compared to the pIOD. This is consistent with the projected larger nIOD amplitude under global warming. On the other hand, precipitation response changes in Southeastern Africa are generally opposite to those in the Somali Peninsula (Fig. 7.10b). The water vapor budget results suggest that IOD-related precipitation changes in Southeastern Africa are associated with CVIMF changes due to IOD-related wind circulation changes. These circulation anomaly changes show a divergence signal in Southeastern Africa during pIOD and a convergence signal during nIOD (Figs. 7.9c, f), primarily attributed to changes in the IOD-related meridional wind anomaly changes. These findings suggest that both "wet-gets-wetter" and "warmer-gets-wetter" mechanisms should be jointly considered when investigating future precipitation changes.

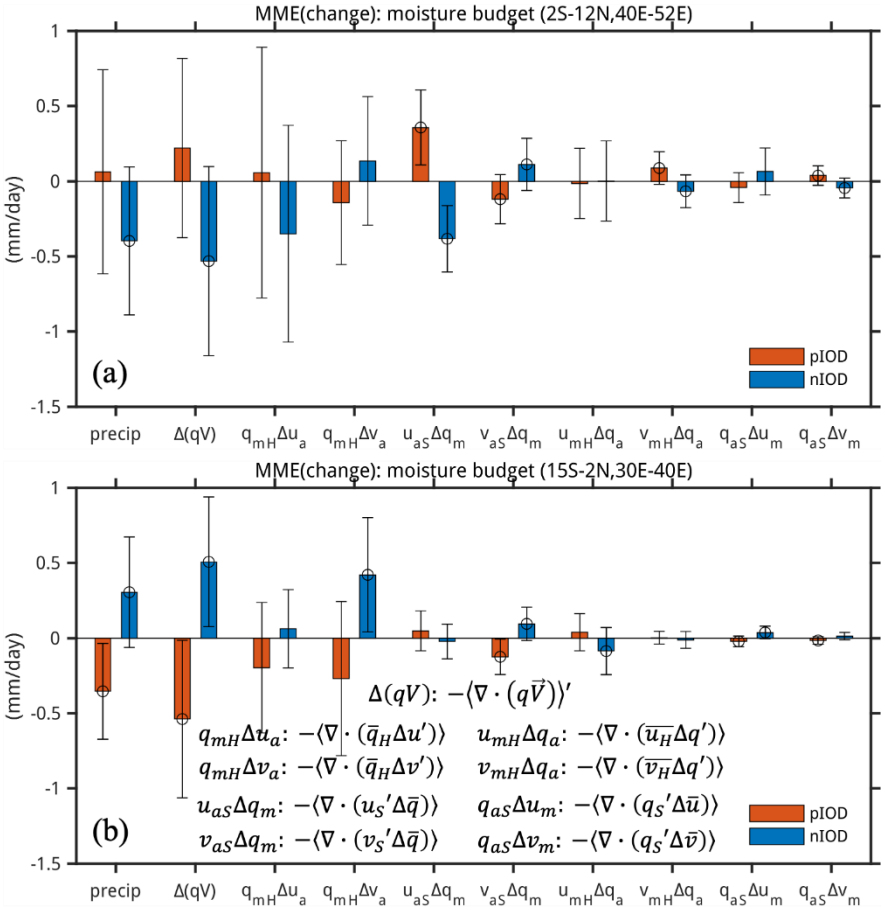


Figure 7.10. Changes of IOD composite for precipitation anomalies and water vapor budget terms (unit: mm day^{-1}) averaged over (a) Somali Peninsula (2°S–12°N, 40°–52°E) and (b) Southeastern Africa (15°S–2°N, 30°–40°E) during OND. Error bar is based on one STD. Circle over the bar indicates signals passing the 95% significance level.

7.3.2. Contributions from IOD circulation changes

The variations in short rains during IOD events in Eastern Africa are closely tied to IOD-related wind circulation changes. In the historical simulations, the increased short rains during pIOD correlate with easterly wind anomalies and the increased moisture content caused by more evaporation due to warmer WTIO (Fig. 7.11a). Conversely, drier conditions during nIOD are attributed to enhanced westerly winds and reduced evaporation due to cooler WTIO (Fig. 7.11d). The SSTA pattern and its circulation anomaly during pIOD are slightly stronger than during nIOD. However, under the SSP5-8.5 scenario, both pIOD and nIOD generate stronger wind anomalies in the WTIO and Eastern Africa, with more significant changes during nIOD (Figs. 7.11b, e). These findings suggest a westward shift in IOD-related circulation in response to projected greenhouse warming, aligning with changes in the IOD pattern. Notably, both pIOD and nIOD display larger SSTAs near the 70°E (Figs. 7.11c, f). Note that stronger nIOD amplitude under global warming may also contribute to the larger circulation anomaly changes during nIOD. To examine the inter-model diversity of IOD-related circulation changes, an inter-model EOF is performed for 850 hPa wind anomaly changes during pIOD (Fig. 7.12a) and nIOD (Fig. 7.12b), respectively. Both EOF1 of pIOD and nIOD have a high variance contribution rate, accounting for more than 50%. EOF1 of pIOD reveals divergence in the lower level of Southeastern Africa, while EOF1 of nIOD captures convergence in the same region, mirroring the MME composite pattern. Figure 7.12c exhibits the inter-model relationship between the PC1 of pIOD-related circulation change and the pIOD-related short-rain change in the Somali Peninsula, with a correlation coefficient of 0.90 (passes the 95% significance level). Models with larger nIOD-related circulation change, produce drier conditions in the Somali Peninsula (Fig. 7.12d; r = –0.68; passes the 95% significance level). In terms of Southeastern Africa, PC1 of IOD-related circulation change also correlates with the precipitation anomaly changes (Figs. 7.12e, f). In conclusion, the changes in IOD-related wind circulation exert a great impact on the Somali Peninsula and Southeastern Africa. The IOD-related precipitation changes in Southeastern Africa are mainly related

to the westward movement of the IOD-related circulation, which can be traced back to changes in the IOD SSTA pattern. This westward shift of the IOD-related circulation also amplifies the precipitation responses to the IOD in the Somali Peninsula, with nearly all CMIP6 models capturing a more severe drought during nIOD events under the SSP5-8.5 scenario.

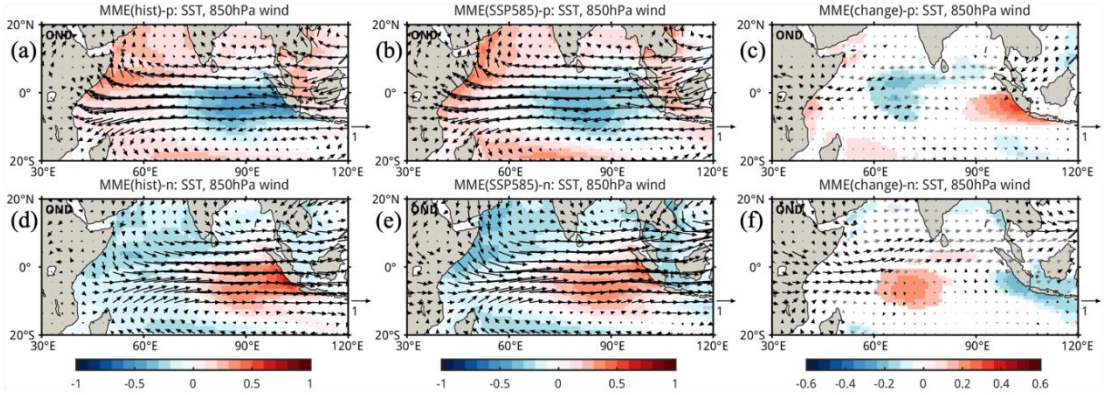


Figure 7.11. The same as Fig. 7.10, but for SSTA (unit: ℃) and 850 hPa wind anomalies (see scale vector in lower right; unit: m s^{-1}).

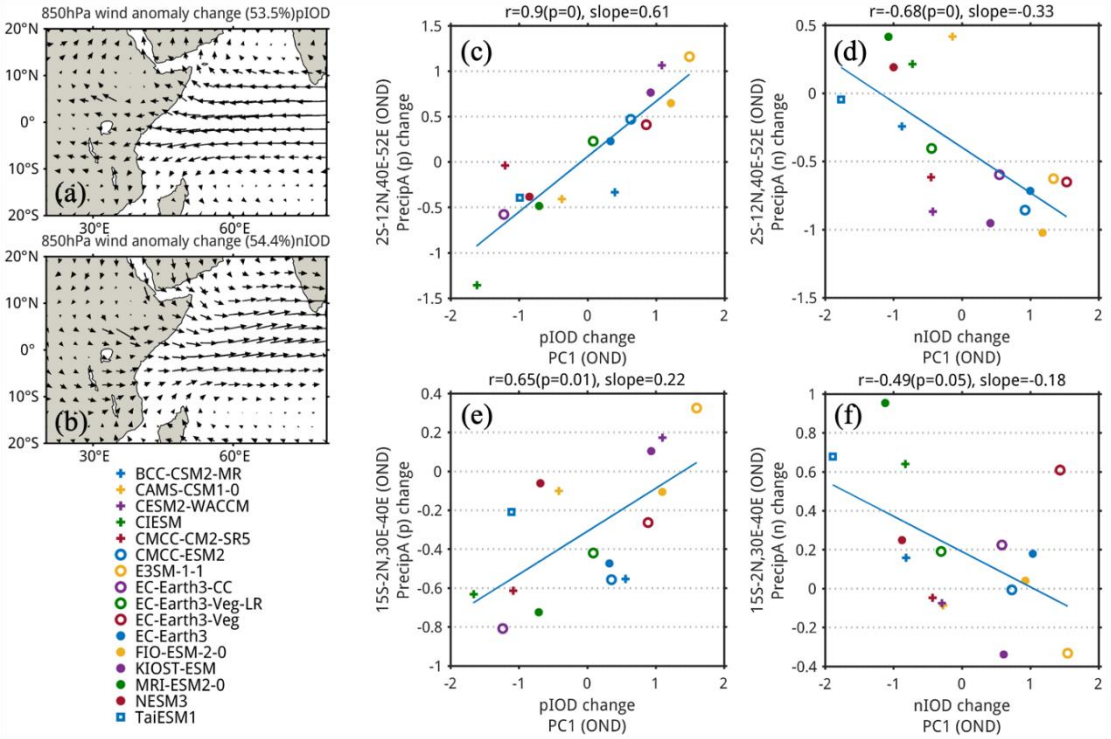


Figure 7.12. Inter-model EOF1 of 850 hPa wind anomaly changes during OND in (a) pIOD and (b) nIOD. (c) Inter-model PC1 of pIOD vs precipitation anomaly changes in Somali Peninsula (unit: mm day^{-1}; 2°S–12°N, 40°–52°E; OND). (d) is the same as (c), but for nIOD. (e, f) are the same as (c, d), but for Southeastern Africa (unit: mm day^{-1}; 15°S–2°N, 30°–40°E; OND). The blue line is the least square linear fit. The r value is the correlation coefficient.

7.3.3. Contributions from mean-state changes

In the Horn of Africa, background changes also play a significant role in short-rain changes during IOD, beyond the IOD-related circulation changes. The overestimated mean-state precipitation in the Somali Peninsula is projected to rise due to global warming, coupled with a weaker winter monsoon (Figs. 7.13a–c). These changes are associated with the future warming pattern of the Indian Ocean, featuring warming hotspots in the Arabian Sea and cooling in the Southeastern Indian Ocean (Sharma et al. 2023). Furthermore, the already weaker Walker Circulation in historical simulations is projected to further diminish under the SSP5-8.5 scenario (Figs. 7.13d–f). The narrow subsidence between 35°E and 45°E, associated with the short rains in the Somali Peninsula, is expected to significantly weaken. Greenhouse warming will lead to increased moisture content at the equator, reflected by the rise in specific humidity at the lower level (Fig. 7.13f). Africa holds more increased specific humidity due to the IOD-like warming pattern (Sharma et al. 2022, 2023). Both thermodynamic and dynamic processes contribute to the increased mean-state precipitation in the Horn of Africa. Models predicting more significant increases in mean-state precipitation tend to project larger short-rain variance in the Somali Peninsula in the future (Fig. 7.14a). An inter-model analysis of selected CMIP6 models also reveals a high correlation between mean-state precipitation changes and mean-state Walker Circulation changes (r = –0.94; Fig. 7.14b), associated with the IOD-like warming pattern (r = 0.75; Fig. 7.14c). In conclusion, a more humid background under global warming contributes to increased precipitation responses to the IOD in the Somali Peninsula, which is associated with projections of weaker Walker Circulation and IOD-like warming pattern.

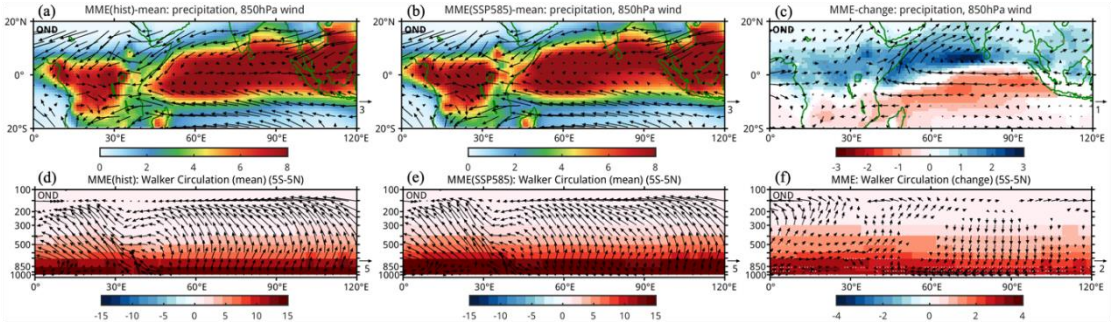


Figure 7.13. Mean-state precipitation (unit: mm day^{-1}) and 850 hPa wind (see scale vector in lower right; unit: m s^{-1}) during OND in the (a) historical and (b) SSP5-8.5 scenario simulations. (c) donates its greenhouse-warming-induced changes. (d, e, f) are the same as (a, b, c), but for specific humidity (shading) and atmospheric zonal (m s^{-1})–vertical (–0.01 Pa s^{-1}) vectors averaged in 5°S–5°N during OND. Changes in specific

humidity (white stippling), precipitation and wind are shown when exceeding the 95% significance level based on Student's t-test.

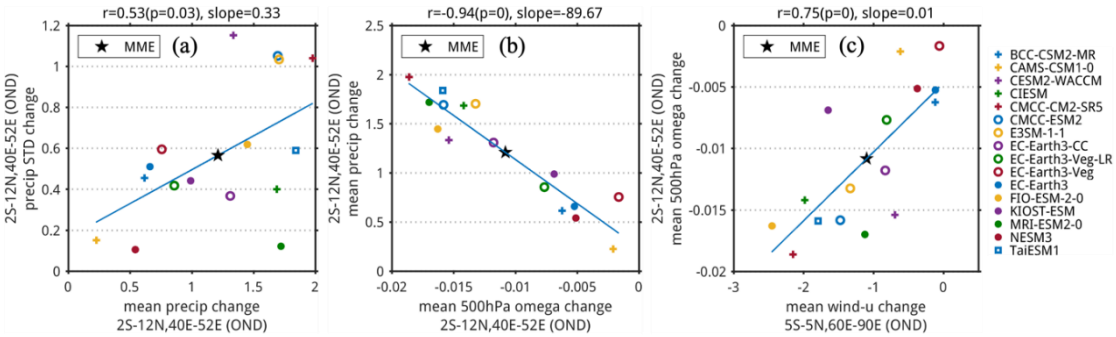


Figure 7.14. (a) Mean-state precipitation changes (unit: mm day^{-1}; 2°S–12°N, 40°–52°E; OND) vs its STD changes. (b) Mean-state 500 hPa omega changes (unit: Pa s^{-1}; 2°S–12°N, 40°–52°E; OND) vs mean-state precipitation changes. (c) Mean-state surface zonal wind changes (unit: m s^{-1}; 5°S–5°N, 60°–90°E; OND) vs mean-state 500 hPa omega changes. The blue line is the least square linear fit. The r value is the correlation coefficient.

To improve the accuracy and reliability of climate model predictions, an emergent constraint is generally used to narrow down the range of uncertainty in climate projections by comparing them with observable present-day measurements (Cox et al. 2013). An emergent constraint refers to a relationship or correlation between inter-model differences in the present-day observable climate and inter-model differences in future climate predictions (Lian et al. 2018). The mean-state precipitation in the Somali Peninsula is overestimated in the historical simulations due to the warm bias in the WTIO and the weaker Walker Circulation. Models with larger mean-state precipitation in the Somali Peninsula in the historical simulation may have less room to increase under global warming. This is because models with fewer positive IOD-like biases in the mean state are able to simulate a greater IOD-like warming pattern under the SSP5-8.5 scenario. Hence, this linear relationship between individual model simulations of contemporary mean-state precipitation in the Somali Peninsula and the estimated changes in future precipitation STD provides an emergent constraint on the observed mean-state precipitation (Fig. 7.15). The simulated historical precipitation STD is 2.43 mm day^{-1}. Under global warming, the raw MME precipitation STD change is 0.57 mm day^{-1}, yielding a corrected precipitation STD change of 1.00 mm day^{-1}. The corrected result predicts a greater change in short-rain variability in the Somali Peninsula under a warmer climate. Besides, Eastern Africa precipitation variability is intimately tied to the simulation of IOD amplitude, with projected changes in IOD amplitude also

strongly connected to mean-state alterations. However, there is a debate about historical IOD amplitude and future IOD amplitude. From the perspective of thermocline, larger historical IOD amplitude corresponds to smaller future IOD amplitude (Wang et al. 2017). Conversely, from an IOD-like warming pattern perspective, larger historical IOD amplitude usually corresponds to a stronger IOD-like warming pattern and stronger IOD amplitude (Li et al. 2016). Exploring how IOD simulations can be utilized to constrain projected short-rain changes is a valuable consideration. It is critical to recognize that employing emergent constraints to constrain future values could introduce additional uncertainties, as it hinges on the premise that the model's efficacy in replicating historical values will persist into the future. Nevertheless, with careful consideration of the limitations and uncertainties inherent in this approach, it can still offer valuable insights into the reliability of model projections for absolute future values.

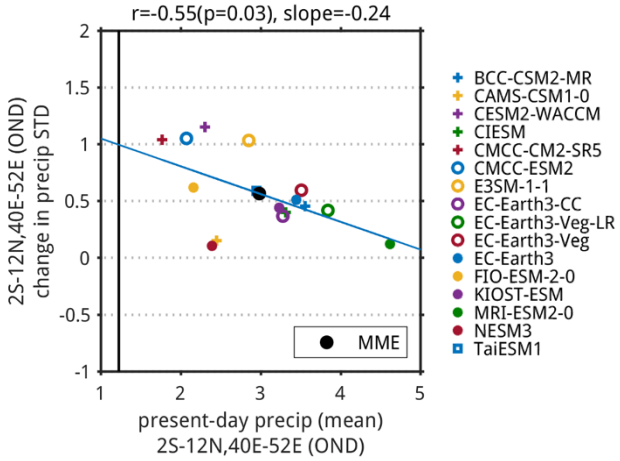


Figure 7.15. Emergent constraint on the precipitation STD changes in the Somali Peninsula. Present-day mean-state precipitation (unit: mm day^{-1}; 2°S–12°N, 40°–52°E; OND) vs its STD changes. The blue line indicates the best-fit regression line across the models. The black line represents the observation value. The intersection of the blue and black lines is the constrained value.

7.3.4. Future rainfall response to extreme nIOD

Under global warming, the frequency of extreme nIOD is projected to increase, suggesting intensified climatic impacts on the Horn of Africa. The historical MME composite pattern of extreme nIOD events exhibits significant dryness in Eastern Africa, extending to Central Africa due to an amplified Walker circulation (Fig. 7.16a). Under global warming, the Somali Peninsula is anticipated to experience worse dryness during extreme nIOD events (Figs. 7.16b, c). Conversely, while the extreme nIOD-related precipitation changes in Southeastern Africa are comparable to those in the Somali

Peninsula, the rise in precipitation anomalies in Southeastern Africa indicates fewer total precipitation anomalies during extreme nIOD. Thus, the Horn of Africa warrants increased attention due to its heightened susceptibility to nIOD events. Figures 7.16d and e depict the multi-model ensemble histograms of precipitation anomalies in the Somali Peninsula during OND for both historical and future climate periods. The nIOD-sample histogram reveals a significant skew towards negative values in precipitation anomalies during the historical simulation. Under the SSP 5-8.5 scenario, predictions lean further towards negative values, showing a substantial increase in dryness exceeding an amplitude of 3 mm day^{-1}. The amplitude of dryness during nIOD is projected to rise by approximately 0.4 mm day^{-1}. Global warming will drive an increase in normal negative precipitation anomalies evolving into extreme values. Regarding the histograms of extreme nIOD cases, the multi-model mean value significantly increases in the future and the difference of multi-model mean based on extreme nIOD is larger than that using all nIOD samples, implying a higher risk of severe droughts in the Somali Peninsula (Fig. 7.16e). Moreover, the constrained result indicates a further decrease in IOD asymmetry, implying the increased occurrence of extreme nIOD events and enhanced climatic impacts from nIOD in the Somali Peninsula. Furthermore, the surface air temperature anomalies during extreme nIOD events are projected to increase (Fig. 7.16g), further increasing the risk of heatwaves and droughts in this region. Africa, as one of the most drought-prone continents, often experiences human migration toward rivers or cities in response to drought occurrences (Ceola et al. 2023). An increase in extreme nIOD events is projected to amplify both the amplitude and frequency of dryness in the Somali Peninsula, potentially triggering increased human migration. This shift toward rivers during droughts could result in substantial human losses should future flood events occur (Ceola et al. 2023).

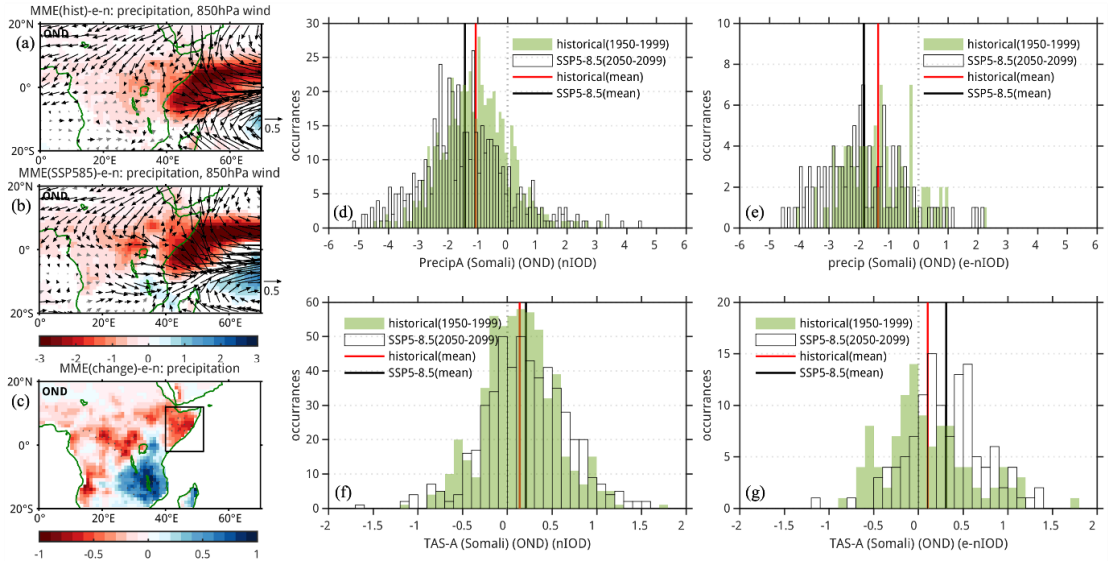


Figure 7.16. Composite extreme nIOD for precipitation (unit: mm day^{-1}) and 850 hPa wind anomalies (see scale vector in lower right; unit: m s^{-1}) during OND in the (a) historical and (b) SSP5-8.5 scenario simulations. Values exceeding the 95% significance level (Student's t-test) are shown. (c) is the precipitation anomaly change with stippling for statistical significance. Multi-model ensemble histograms of precipitation anomalies averaged over the Somali Peninsula (unit: mm day^{-1}; 2°S–12°N, 40°–52°E; OND) during the historical (1950–1999; green shading bar) and climate change (2050–2099; black bar) periods for (d) nIOD samples and (e) extreme nIOD samples, respectively. (f, g) is the same as (d, e), but for surface air temperature anomalies (unit: K). The multi-model mean for the historical (climate change) period is indicated by the red (black) line.

7.4. IOD impacts on Australia

7.4.1. Underestimated IOD impacts on Australia

The IOD plays a pivotal role in shaping Australia's weather and climate (Holgate et al. 2022). The surface air temperature in Australia is positively correlated with the DMI$|_{\text{Niño 3.4}}$ (Fig. 7.1). In observations, based on existing IOD samples, Australia's surface air temperature exhibits notable anomalies, with cooler conditions in Northern Australia and warmer conditions in Southern Australia during pIOD events, especially in Southwestern Australia (Fig. 7.17a). Conversely, nIOD events are associated with warmer conditions in Northern Australia and cooler conditions in Southern Australia (Fig. 7.17b). However, in CMIP6 models, the IOD-induced surface air temperature anomalies are weaker, showing approximately half the magnitude of those observed (Figs. 7.17c, d). CMIP6 models fail to simulate the anomalous temperature center in Southwestern Australia, locating it in Southeastern Australia during pIOD events. CMIP6 models also fail to capture the surface air temperature responses to IOD in Northern Australia. Among the selected CMIP6 models, only the nIOD from the

CMCC-CM2-SR5 model and the pIOD from the CMCC-ESM2 model capture strong surface air temperature anomaly in Southwestern Australia compared to the observations (Fig. 7.17 i). Some models, such as CAMS-CSM1-0, FGOALS-g3, and NESM3 models, fail to simulate this critical IOD teleconnection in Australia.

In addition to surface air temperature, rainfall is another crucial element influenced by the IOD. Observations reveal that pIOD typically triggers reduced precipitation anomalies in Southeastern Australia during ASO (Fig. 7.17c), while nIOD correlates with increased precipitation (Fig. 7.17d). Like the climatic responses of surface air temperature, CMIP6 models underestimate the Australian rainfall responses to the IOD despite their overestimation of the IOD amplitude (Figs. 7.17g, h), which is consistent with Chung et al. (2023). Chung et al. (2023) also pointed out that the CMIP6 models demonstrate improved overall strength of the IOD teleconnections to Australian rainfall compared to CMIP5 models. Nonetheless, the MME results in Southeastern Australia depict less than half of the observed rainfall anomalies, especially during pIOD events. All selected CMIP6 models fail to replicate the comparable rainfall anomalies in Southeastern Australia (Fig. 7.17j), underscoring the need for further improvements in climate modeling.

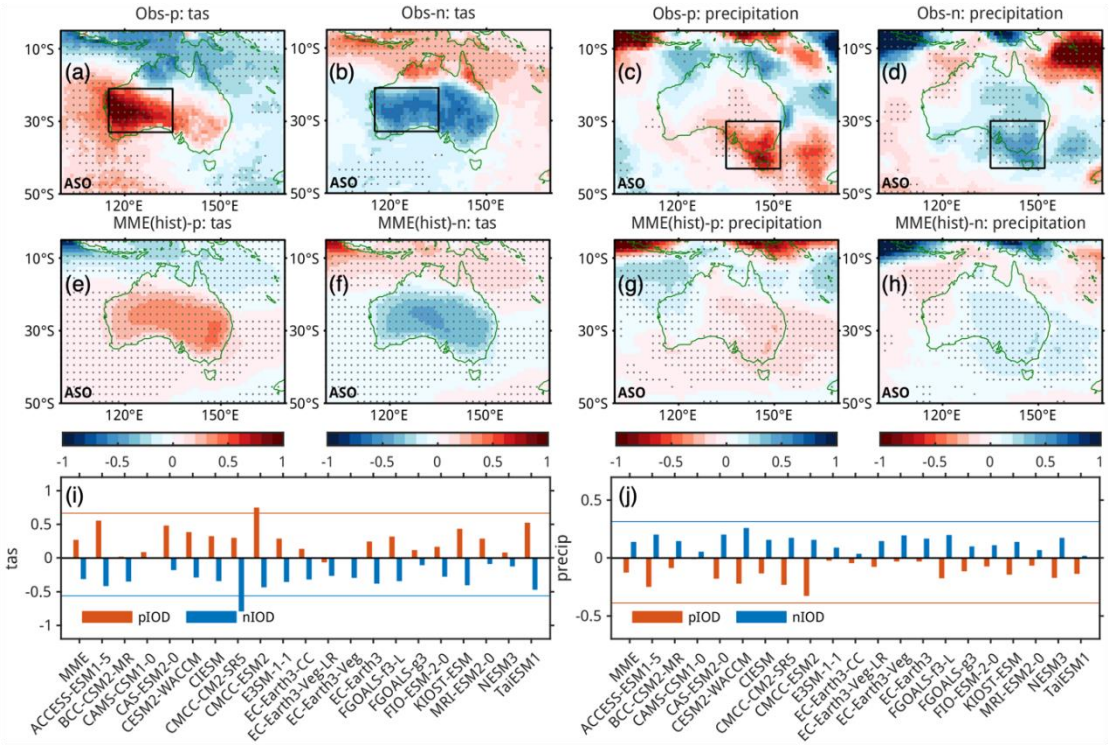


Figure 7.17. Composite surface air temperature anomalies (unit: K) in (a) observed pIOD, (b) observed nIOD, (e) historical pIOD and (f) historical nIOD during ASO. (i) Inter-model composite of surface air temperature anomalies in Southwestern Australia (33°–21°S, 115°–135°E; ASO). The red (blue) line denotes observed pIOD (nIOD)

composite. Stippling indicates the 95% significance level based on Student's t-test. (c, d, g, h, j) are the same as (a, b, e, f, i), but for precipitation (unit: mm day^{-1}). (j) is for Southeastern Australia (43°–30°S, 135°–152°E). Anomalies have been adjusted to exclude the effects of the Niño 3.4 index.

7.4.2. Weaker simulated Rossby waves

The IOD teleconnections to Australia are mainly facilitated through IOD-induced Rossby wave (Saji et al. 2005). The partial least squares regression of SLP and 850 hPa wind anomalies onto DMI$|_{\text{Niño 3.4}}$ exhibits anomalous increased SLP south of Australia during JAS and SON, accompanied by significantly anomalous anticyclone (Fig. 7.18a). The pattern exhibits a west-to-east progression of negative, positive, and negative SLP anomalies. Corresponding upper-level circulation changes mirror these SLP anomalies (Fig. 7.19a), indicative of barotropic Rossby wave trains. These Rossby wave trains are triggered by the IOD-induced vorticity source. With the mid-latitude westerly serving as a Rossby waveguide (Hoskins and Ambrizzi 1993), wave energy propagates eastward along the westerly to Australia. During pIOD, the Rossby wave leads to an anomalous anti-cyclonic circulation from the upper troposphere to the low level in Southern Australia, causing a significant increase in surface air temperature in Southwestern Australia and enhanced precipitation in Southeastern Australia. There are generally two Rossby wave trains. The first extends from the tropics to higher latitudes, but this wave train does not reach southern Australia due to the strong convergence of wave activity flux into the region where $K_s^2 < 0$ (K_s is Rossby wavenumber) (McIntosh et al. 2018). The second wave train originates further upstream of Australia and propagates westward and poleward into the Southern Ocean along the eddy-driven jet (McIntosh et al. 2018). This second Rossby wave train mainly results from the feedback of transient eddies onto the mean flow. Climatic signal locations vary across different variables, with one identified in the Southwest (surface air temperature) and another in the Southeast (precipitation), despite both sharing the same anomalous anticyclone. Surface air temperature anomalies in Southwestern Australia are tied to meridional temperature advection, specifically a decrease in cold air from the Southern Ocean due to the IOD-induced anomalous anticyclone during pIOD (Fig. 7.18b). Conversely, precipitation anomalies in Southeastern Australia are more directly linked to storm anomalies, with winter to spring rainfall in Australia governed by storm activity. Ashok et al. (2009) demonstrated a negative partial correlation between the IOD and the storm track index over Southeastern Australia. The anomalous barotropic

anticyclone inhibits storm activity and reduces Australian rainfall during pIOD. Moreover, IOD-induced Rossby waves during pIOD are stronger than during nIOD (Figs. 7.18b, d, 7.19b, d), aligning with IOD asymmetry. In CMIP6 models, they simulate weaker surface air temperature responses to IOD in Southwestern Australia and weaker precipitation responses in Southeastern Australia. These anomalous biases are believed to be influenced by the simulations of the IOD-induced Rossby wave. Both the streamfunction and SLP anomalies are considerably smaller than those observed, the same as the upper- and low-level wind anomalies (Figs. 7.18, 7.19).

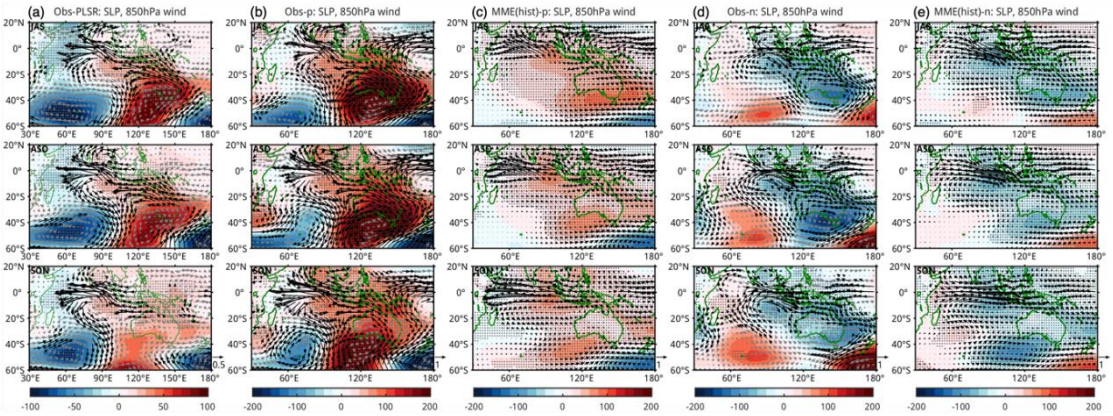


Figure 7.18. Partial least squares regression of (a) SLP (unit: hPa) and 850 hPa wind (see scale vector in lower right; unit: m s^{-1}) anomalies onto DMI with the influences of Niño 3.4 index removed during JAS, ASO and SON in observations. Composite SLP and 850 hPa wind anomalies in (b) observed pIOD, (c) historical pIOD, (d) observed nIOD and (e) historical nIOD. Stippling and vector are shown when exceeding the 95% significance level based on Student's t-test.

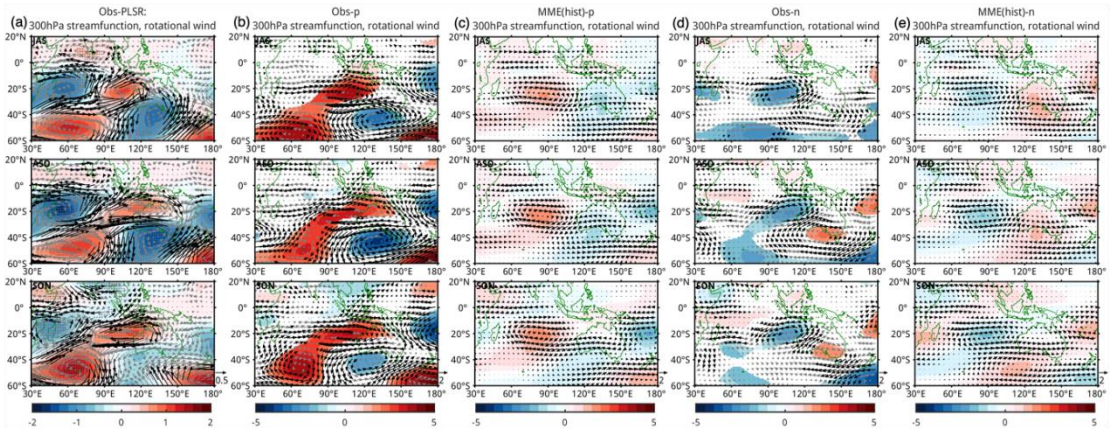


Figure 7.19. The same as Fig. 7.18, but for 300 hPa streamfunction (unit: 10^6 m^2 s^{-1}) and rotational wind anomalies (see scale vector in lower right; unit: m s^{-1}).

The weaker IOD-induced Rossby wave trains in climate simulations are most likely linked to the poor representation of RWS. The RWS can be traced back to the

southeastern TIO in observations (Figs. 7.20a, b, d). However, in CMIP6 models, they not only simulate weaker RWS, but also show different RWS patterns compared to the observed (Figs. 7.20b, e). The RWS simulations are sensitive to the location of the upper-level divergence. From the composites of velocity potential and divergent wind, the simulated velocity potential centers tend to shift westwards during IOD compared to the observed (Fig. 7.21). This westward extension of the IOD eastern center results in the displacement of the IOD-induced diabatic heating anomaly, moving it far west into the central TIO. This displacement subsequently leads to RWS biases, which directly impact the generation of Rossby waves in simulated environments. A recent study also suggested that the coastal IOD, sharing the same eastern pole as the conventional IOD, significantly influences Australian precipitation, unlike the offshore IOD located in the central southern TIO (Fan et al. 2024), implying the important role of the SSTA and convection center's location. The simulations of IOD-induced convective anomalies are challenging (Zhao and Hendon 2009; Shi et al. 2012). Further investigation into these convection and Rossby wave simulations is essential for an accurate depiction of IOD-related climatic processes.

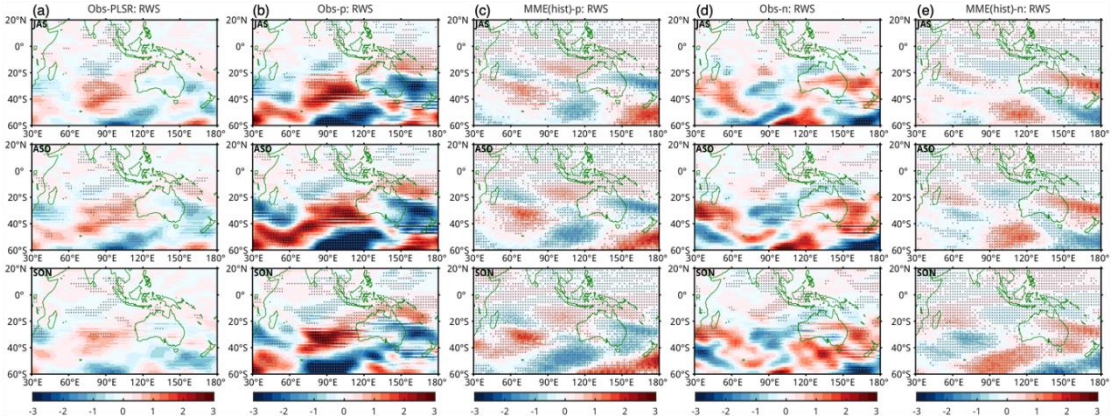


Figure 7.20. The same as Fig. 7.18, but for Rossby wave source (unit: 10^{-10} s^{-1}).

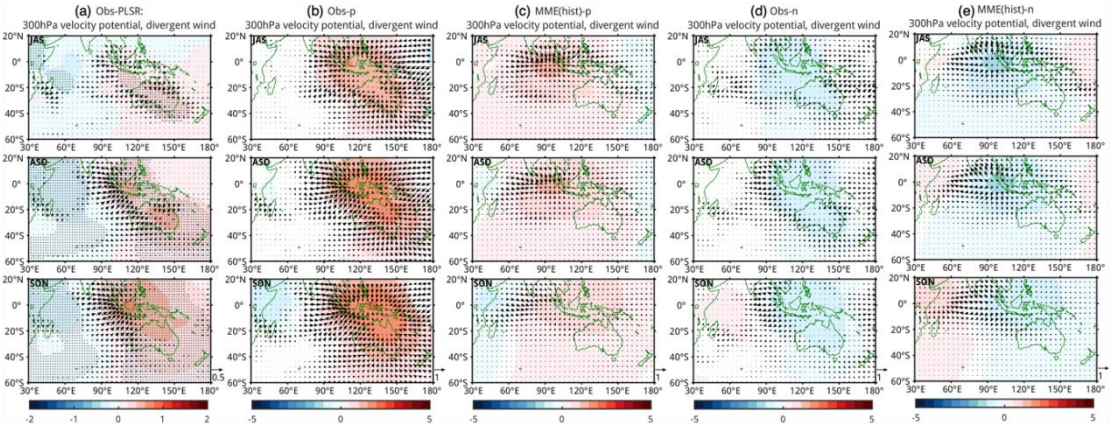


Figure 7.21. The same as Fig. 7.18, but for 300 hPa velocity potential (unit: 10^6 m^2 s^{-1}) and divergent wind anomalies (see scale vector in lower right; unit: m s^{-1}).

7.4.3. Projected changes in IOD impacts on Australia

Historical simulations reveal warmer conditions in Southern Australia during pIOD and cooler conditions during nIOD, with anomalous centers located in Southeastern and Central Australia respectively (Fig. 7.22a, b). Surface air temperature responses to IOD events are projected to intensify under the SSP5-8.5 scenario, particularly in Southeastern Australia (Figs. 7.22e, f). Notably, the increase in surface air temperature anomalies during nIOD surpasses that during pIOD in Southeastern Australia (Figs. 7.22i, j). Regarding precipitation, the IOD induces negative precipitation anomalies in Southeastern Australia during its positive phase and positive precipitation anomalies during its negative phase (Figs. 7.22c, d). Under global warming, rainfall anomalies in this region show minimal change, but rainfall responses to the IOD are anticipated to increase in Northern Australia (Figs. 7.22g, h, k, l). The amplified climatic impacts of the IOD suggest that changes in IOD amplitude may not be the sole factor; this could be linked to the enhancement of IOD-related Rossby wave trains (Fig. 7.23). In a warmer climate, the eddy-driven jet is projected to intensify, especially south of Australia (Fig. 7.24), facilitating the propagation of Rossby waves. The mechanisms driving the Australian climate's response to the IOD merit further research.

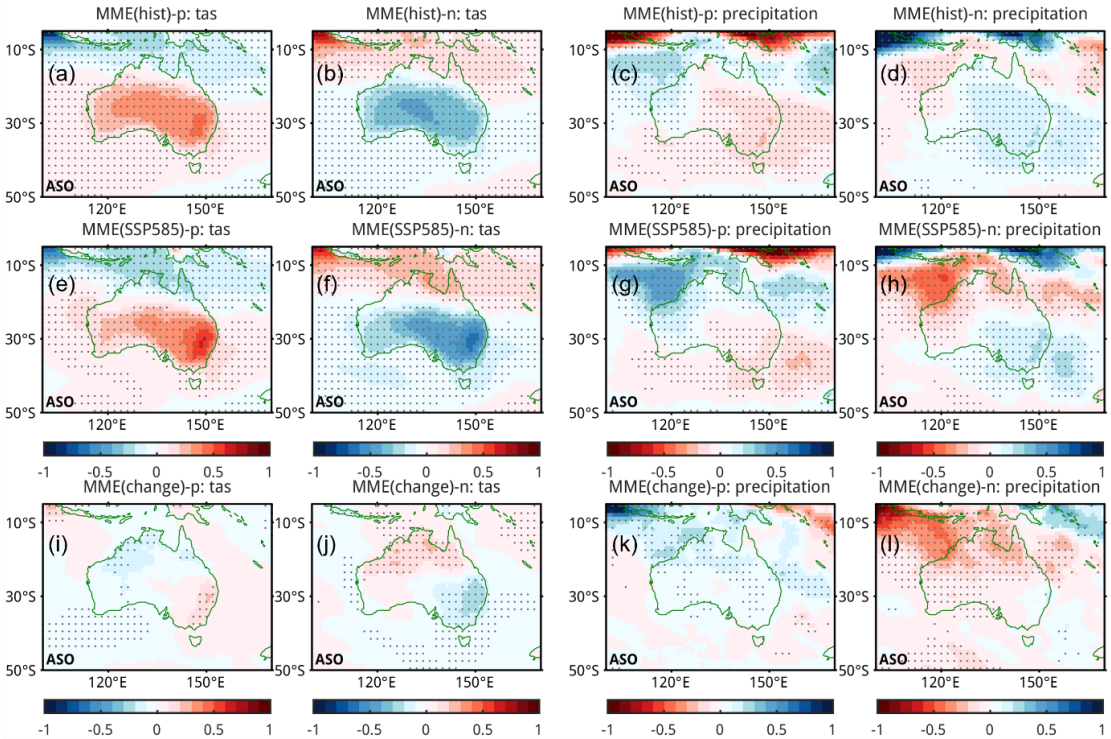


Figure 7.22. Composite surface air temperature anomalies (unit: K) of (a) historical pIOD, (b) historical nIOD, (e) SSP5-8.5 pIOD, (f) SSP5-8.5 nIOD, (i) pIOD change and (j) nIOD change during ASO. (c, d, g, h, k, l) are the same as (a, b, e, f, i, j), but for precipitation anomalies (unit: mm day^{-1}). Stippling indicates the 95% significance level based on Student's t-test. Anomalies have been adjusted to exclude the effects of the Niño 3.4 index.

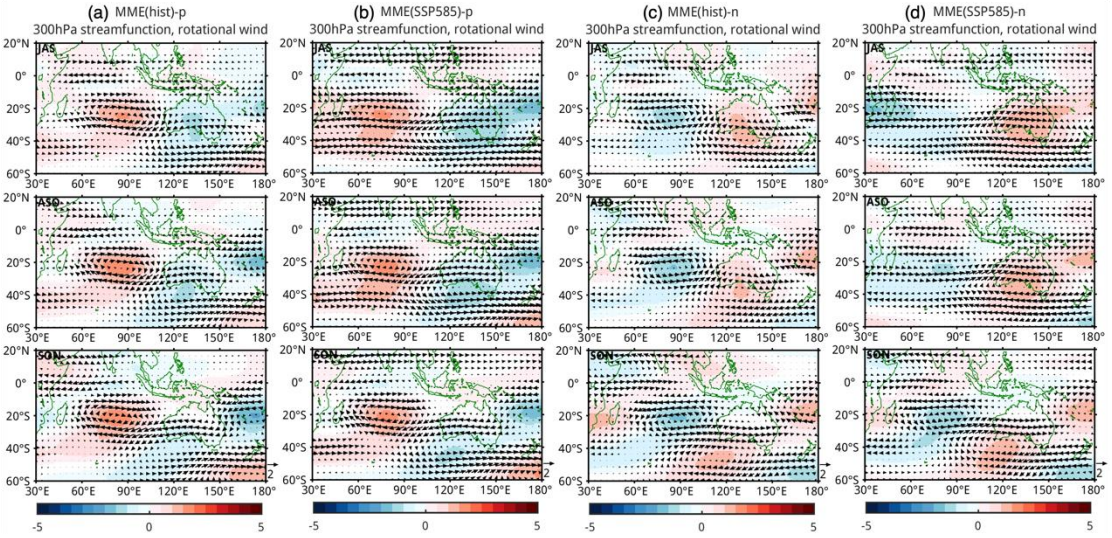


Figure 7.23. Composite 300 hPa streamfunction (unit: 10^6 m^2 s^{-1}) and rotational wind anomalies (see scale vector in lower right; unit: m s^{-1}) during JAS, ASO and SON in (a) historical pIOD, (b) SSP5-8.5 pIOD (c) historical nIOD and (d) SSP5-8.5 nIOD.

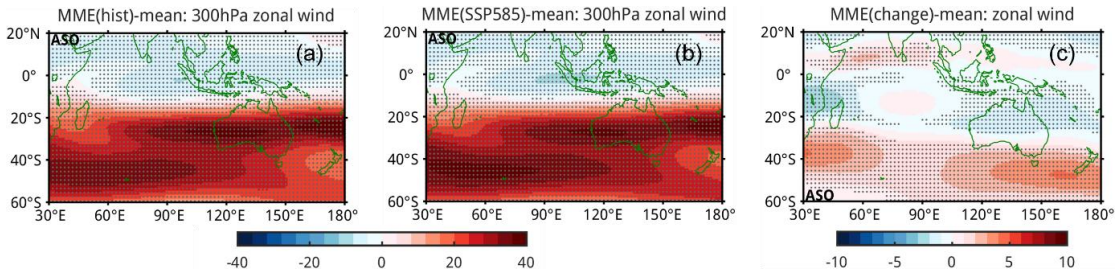


Figure 7.24. (a) Historical mean-state 300 hPa zonal wind, (b) SSP5-8.5 mean-state 300 hPa zonal wind and (c) its changes induced by greenhouse warming. Stippling indicates the 95% significance level based on Student's t-test.

8. Conclusions and discussions

8.1. Major conclusions

8.1.1. Underestimated IOD asymmetry in historical simulations

The IOD is a climate phenomenon that affects weather patterns around the Indian Ocean-rim countries and even worldwide. The IOD exhibits a noticeable amplitude asymmetry, which is particularly evident during extreme IOD events that occur more frequently during positive phases, triggering severer droughts, floods, and wildfires in different regions. In this study, we evaluate the present-day simulation of IOD skewness in CMIP5/6 models and find that most of the recent coupled general circulation models tend to simulate a weaker IOD skewness. Compared to observations, nearly all the selected CMIP5 models produce a smaller IOD skewness except the MPI-ESM-LR model, but 6 out of 20 selected CMIP6 models can simulate a realistic IOD skewness, indicating some improvement in IOD skewness from CMIP5 to CMIP6. To explore the origins of underestimated IOD skewness, the selected CMIP6 models are classified into two groups: the less-skewed CMIP6 model group and the more-skewed CMIP6 model group. Models in the more-skewed CMIP6 model group simulate comparable IOD skewness with observations.

The amplitude asymmetry of observed IOD events is in relation to negative NDH, mainly owing to nonlinear zonal and vertical advection (Hong et al. 2008a, b). In CMIP5/6 models, we find that the NDH simulation is essential to the simulation of IOD skewness. Only the more-skewed CMIP6 model group simulates NDH that is comparable to observations. In the other two less-skewed groups (i.e., CMIP5 model group and less-skewed CMIP6 model group), the simulated NDH is much smaller, which is mainly due to the simulated biases in nonlinear zonal and vertical advection, but the biases in nonlinear meridional advection contribute less to simulated NDH.

Simulated biases of nonlinear zonal advection are related to the mean-state positive IOD-like biases. In observations, the background WTIO SST during JASO is around 27 ℃, with positive net convective response, while the ETIO SST is around 28.5 ℃, with negative net convective response. Models with warmer mean-state WTIO weaken the WTIO's positive net convective response to SSTAs, reducing atmospheric response during pIOD. This leads to weaker surface easterly anomalies during pIOD, which in turn results in weaker ETIO nonlinear zonal advection and less positive IOD skewness. Meanwhile, colder mean-state ETIO induces less negative net convective response,

which is also less favorable for the development of pIOD. The more-skewed CMIP6 model group shows fewer IOD-like biases than the other two groups and thereby simulates more realistic IOD skewness. Furthermore, the positive IOD-like biases are caused by the weaker cross-equatorial summer monsoon in the WTIO and the summer southeasterly wind bias near the Sumatra-Java coast.

Nonlinear vertical advection is another key factor for the IOD asymmetry. Only the more-skewed CMIP6 model group achieves comparable values to observations, which is related to the ETIO stratification. Stronger ocean stratification causes stronger MLT response to thermocline changes, which increases the anomalous vertical temperature gradient and more negative nonlinear vertical advection, favoring the IOD asymmetry. Despite having larger cold biases in the ETIO, the more-skewed CMIP6 model group reproduces better temperature responses and nonlinear vertical advection. These findings imply that models with better simulations of Indian summer monsoon and ETIO oceanic responses perform well in replicating present-day IOD skewness. Therefore, substantial efforts should be undertaken to reduce the monsoon bias as well as to advance the upper-ocean temperature simulation. These present-day findings help to improve our understanding of the present-day model's performances and constitute a step in assessing their predictions for the upcoming changes.

8.1.2. Reduced IOD asymmetry due to global warming

Since the mid-18th century Industrial Revolution, human-induced greenhouse gas emissions have caused rising global temperatures. With ongoing greenhouse gas emissions, further warming is inevitable. Understanding potential IOD changes in this shifting climate is crucial in Earth system science. Under the SSP5-8.5 scenario, which represents a high greenhouse gas emissions future, the IOD is projected to become less asymmetric. This means that the intensity difference between pIOD and nIOD will decrease. The reduction of IOD asymmetry mainly relates to the less negative nonlinear zonal advection in the future. Under a warmer climate, the increased atmospheric static stability will weaken the large-scale atmospheric response to SSTAs. This results in fewer surface zonal wind variations, leading to less negative nonlinear zonal advection and, therefore, less IOD asymmetry. Observations and historical simulations show nonlinear vertical advection as another significant contributor to IOD asymmetry. Under the SSP5-8.5 scenario, the future nonlinear vertical advection matches historical levels. The increased oceanic effect due to the enhanced ETIO stratification will offset

the decreased large-scale atmospheric response due to the intensified atmospheric stability. Hence, the larger vertical temperature gradient response and weaker vertical motion anomalies result in nearly consistent nonlinear vertical advection during IOD. Overall, changes in mean-state conditions, such as increased upper-ocean stratification and atmospheric static stability, play a role in shaping future IOD characteristics.

The reduction in IOD asymmetry corresponds to the increased frequency of extreme nIOD events, with a projected 9% increase in the number of nIOD events evolving into extreme cases under the SSP5-8.5 scenario. Greenhouse warming simulations suggest that the development of nIOD will be less inhibited by negative nonlinear dynamic heating due to reduced negative nonlinear zonal advection. What's more, the weaker thermocline–temperature asymmetry also contributes to the more frequency of extreme nIOD events. These changes in extreme events could significantly impact regional climate patterns. An emergent constraint approach is utilized to establish a correlation between present-day mean-state simulations and future changes in IOD skewness. Models with a weaker present-day westerly tend to exhibit smaller future changes in IOD skewness, aligning with Ng and Cai (2016) using CMIP5. The historical MME IOD skewness is approximately 0.42. The corrected result predicts a greater decrease (–0.48) in IOD asymmetry under a warmer climate compared to the raw change (–0.28), implying an even higher frequency of extreme nIOD events and their impacts. The use of this approach deepens our understanding of projection uncertainties and emphasizes the importance of minimizing positive IOD-like biases in present-day simulations.

8.1.3. Projected northward shift of IOD pattern

In this study, we investigate the potential changes in the IOD pattern under a high greenhouse gas emissions future (SSP5-8.5 scenario), comparing it with historical simulations in CMIP6 models. The ensemble means of CMIP6 projection, both historical and SSP5-8.5 simulations, show significant SSTA variance in the ETIO, with minimal STD changes across the entire ETIO region. Nevertheless, a closer analysis reveals an approximately 10% decrease in SSTA amplitude near the Sumatra coast and a 10% increase along the equatorial ETIO under the SSP5-8.5 scenario. Moreover, individual variances of pIOD show a significant decrease in SSTA amplitude near the Sumatra coast but an increase in the equatorial ETIO. Conversely, individual variances of nIOD exhibit increased SSTA amplitude in the ETIO, along with a minor decrease near the Java coast. These SSTA variance changes align with the composite results of

IOD events, suggesting meaningful alterations in the IOD pattern due to global warming. This suggests a potential future symmetry along the equator in the eastern part of IOD, contrasting with historical runs. The changes in SSTA patterns imply potential modulations of climatic impacts from IOD events and potential risks to society and ecosystems due to greenhouse warming.

The reduction in SSTA variance near the Sumatra coast and the amplification of SSTA variance are both tied to the mean state changes in the Indian Ocean. The reduced SSTA amplitude near the Sumatra coast mainly stems from the restrained development of pIOD events. Under the SSP5-8.5 scenario, the mean-state precipitation in the SETIO is projected to decrease significantly due to the weakened Walker Circulation (Vecchi and Soden 2007; Sharma et al. 2022), consequently making it harder to further reduce the precipitation during pIOD events, resulting in lower efficiency of the thermodynamic air-sea feedback. The weaker atmospheric response, attributed to increased atmospheric static stability, also contributes to the lower efficiency of the thermodynamic air-sea feedback. This limited effect induces a weaker anomalous anticyclone and smaller southeasterly wind anomalies near the Sumatra coast, thereby leading to weaker WES feedback, weaker Ekman-induced upwelling, and ultimately, smaller negative SSTAs. In terms of the amplified SSTA along the eastern equator, it is related to both enhanced atmospheric static stability and upper-ocean stratification (Li et al. 2020). Under a warmer climate, increased atmospheric static stability coincides with weakened Walker Circulation in the TIO, manifesting weaker westerly winds in the northern TIO and stronger easterly winds in the southern TIO in boreal summer and autumn. These changes induce an enhanced westward zonal current within the mixed layer in the mean state compared to the historical simulation, leading to a significant increase in the $-\bar{u}(\partial T'/\partial x)$ term and promoting SSTA development in the equatorial ETIO during IOD events. The linear vertical advection, operating solely in nIOD, also contributes to the increased SSTA amplitude in the equatorial ETIO. Given the increased oceanic stratification, both the mean and variability of the vertical temperature gradient at the MLD are expected to increase in the ETIO. Concerning the $-\bar{w}[(T - T_{-h})/h]'$ term, the weaker atmospheric response and the enhanced wind-driven ocean coupling are likely to balance each other, resulting in a comparable thermocline feedback under the SSP5-8.5 scenario. As for the $-w'\overline{(T - T_{-h})/h}$ term, it increases during nIOD but slightly decreases during pIOD because of the further

reduction in w' near the Sumatra Coast during pIOD. The reduced damping effect from the $-w'\overline{(T-T_{-h})/h}$ term in the off-equatorial region will facilitate the IOD development, but this effect would be counterbalanced by the less negative nonlinear vertical advection during pIOD. Consequently, with the assistance of $-\bar{u}(\partial T'/\partial x)$ and $-w'\overline{(T-T_{-h})/h}$, nIOD will be promoted under global warming.

8.1.4. Overestimated Eastern Africa rainfall responses to IOD

Due to the common bias of Eastern Africa short rain simulation in CMIP6 models, spatial correlation of monthly climatological precipitation between observations and CMIP6 models are explored for model selection. A selection of 16 models, which demonstrate better simulation of both IOD and mean-state precipitation in Eastern Africa, are considered in this study. In observations, pIOD events trigger a significant increase in short-rain precipitation in Eastern Africa, posing severe challenges for the region's developing nations. Conversely, the impact of nIOD is notably less pronounced. These OND precipitation anomalies in Eastern Africa primarily result from the modulation of the Walker Circulation during IOD. The majority of the selected CMIP6 models simulate slightly larger precipitation responses during pIOD, and significantly larger responses during nIOD. This overestimation of precipitation responses to IOD events in Eastern Africa can be attributed to the amplified CVIMF simulation. The dominant factor is the amplification of zonal moisture transport anomaly, resulting from the westward shift of SSTA signals and the larger simulated IOD amplitude. The mean-state precipitation bias also contributes to the enhanced precipitation variabilities in Eastern Africa. CMIP6 models tend to overestimate short-rain precipitation in Eastern Africa, which is associated with the weaker simulation of Walker Circulation and mean-state positive IOD-like biases. These findings highlight the necessity for improved modeling of the IOD and its impacts on short-rain precipitation in Eastern Africa, as well as the region's precipitation climatology. This will enhance our understanding of these intricate processes and facilitate better prediction and management of their impacts on vulnerable regions.

8.1.5. Enhanced IOD impacts on the Horn of Africa under global warming

The Somali Peninsula, also known as the Horn of Africa, experiences significant impacts from the IOD, particularly on its short-rain precipitation characteristics. Under

global warming, pIOD events are projected to have more increased precipitation in the Somali Peninsula, while nIOD events are projected to have more decreased precipitation. This suggests an intensified climatic influence from the IOD on the Somali Peninsula. Notably, the precipitation anomaly changes during nIOD events are significantly larger than those during pIOD events. Conversely, Southeastern Africa is expected to have a reduction in IOD-induced precipitation variability under global warming. The water vapor budget underscores the importance of both the "wet-gets-wetter" (Held and Soden 2006) and "warmer-gets-wetter" (Xie et al. 2010a) mechanisms in comprehending future precipitation changes. The IOD-related precipitation changes in Southeastern Africa are mainly linked to the CVIMF changes due to the IOD-related wind circulation changes. In terms of the Somali Peninsula, the CVIMF changes due to the IOD-related wind circulation changes also contribute to its precipitation response changes, particularly during nIOD events due to the projected larger nIOD amplitude under global warming. Another main contributor to the precipitation anomaly changes in the Somali Peninsula is the CVIMF changes due to the mean-state moisture changes, which are linked to a moister atmosphere under global warming. This increase in atmospheric humidity is attributed to the greenhouse-warming-induced weaker Walker Circulation and the IOD-like warming pattern.

In the context of global warming, our study predicts an increased frequency of extreme nIOD events, resulting in amplified and more frequent dryness in the Horn of Africa. Furthermore, extreme nIOD events also lead to a significant rise in surface air temperature anomalies, implying severe climatic impacts including heightened risks of droughts and heatwaves in the Somali Peninsula. Such conditions may prompt human migration toward rivers or cities, potentially resulting in greater human losses if concurrent flood events occur (Ceola et al. 2023). The emergent constraint results indicate a larger change in short-rain variability in the Horn of Africa under global warming, emphasizing the larger influence of the IOD and associated climatic risks. These findings underscore the necessity for comprehensive climate models that incorporate both thermodynamic and dynamic processes, as well as the influence of IOD on regional precipitation patterns. Moreover, these models should consider the social and human impacts of climate change, including increased human mobility and potential losses. This research provides valuable insights into the climatic influences on Eastern Africa under global warming, contributing to our understanding of regional climate dynamics and informing climate adaptation strategies.

8.1.6. Historical and projected climatic impacts of IOD on Australia

The IOD is one of the key drivers of Australia's weather and climate. It can have a significant impact on agriculture because IOD events generally coincide with the winter crop growing season. The pIOD events typically result in cooler surface air temperatures in Northern Australia and warmer temperatures in Southern Australia, while nIOD events cause the opposite. However, current climate models (CMIP6) only partially replicate these temperature anomalies, and struggle to accurately simulate the temperature center in Southwestern Australia during pIOD events. Rainfall is also impacted by the IOD, with pIOD events causing reduced precipitation in Southeastern Australia, and nIOD events leading to increased rainfall. Again, CMIP6 models fail to fully capture these effects, although they do show some improvement over previous models (CMIP5) in their representation of the IOD's influence on Australian rainfall (Chung et al. 2023). The IOD's effects on Australia's climate are largely due to IOD-induced Rossby waves, which result in anomalous barotropic anticyclone (cyclone) south of Australia during pIOD (nIOD) events. During pIOD, the increased surface air temperature anomalies are linked to a decrease in cold air from the Southern Ocean due to the western part of anomalous anticyclone. While the precipitation anomaly center is generally in Southeastern Australia since this anomalous anticyclone tends to inhibit the storm activity in this region. However, climate models struggle to accurately simulate these Rossby waves, leading to weaker surface air temperature and precipitation responses in their simulations. The weaker simulations of IOD-induced Rossby wave in Australia mainly result from the weaker RWS simulations, attributable to a westward shift of the IOD-induced upper-level divergence/convergence center. Under the SSP5-8.5 scenario, surface air temperature responses to IOD are expected to intensify, particularly in Southeastern Australia. Precipitation responses to the IOD are also expected to increase in Northern Australia, with negligible changes for Southern Australia. The intensified climatic responses to IOD may be related to the slightly increase intensity of Rossby wave trains under global warming, potentially due to the amplification of the eddy-driven jet in the Southern Hemisphere. These projections underscore the need for further research into the mechanisms driving Australia's climate response to the IOD events and strategies to enhance the accuracy of IOD teleconnections to Australia.

8.2. Study limitations

Section 4 mainly focuses on the effect of NDH biases on the simulated IOD skewness. Some thermodynamic processes would also partially contribute to the IOD skewness, such as the SCR feedback (Hong et al. 2008b) and the latent heat flux response in the ETIO. Chen et al. (2016b) acknowledged that while the analysis of mixed-layer heat budget aids in comprehending the respective roles of ocean dynamics and surface heat fluxes in causing asymmetric temperature variations, caution must be exercised when interpreting the budget results due to potential disparities between MLT anomalies and SSTAs. The atmosphere directly influences the SSTA, thus emphasizing the need for heightened focus on heat flux simulations. In observations, notwithstanding that there is no clear evidence linking IOD skewness to the asymmetry of remote ENSO forcing in summer (Hong et al. 2008b), Du et al. (2020) found that the Rossby wave caused by El Niño in spring may enable Bjerknes feedback to occur earlier and facilitate the emergence of the 2019 extreme IOD event. The Indonesian Throughflow, which is closely related to the ENSO (Meyers 1996), could impact the barrier layer in the ETIO and potentially enhance the IOD asymmetry (Cai et al. 2013). An et al. (2023) suggested that ENSO may play a secondary role in IOD asymmetry, alongside local nonlinear processes, as demonstrated by a nonlinear IOD model. Like the IOD, CMIP models also underestimate ENSO skewness (McKenna et al. 2020; Hayashi et al. 2020). The question arises as to whether these biases in ENSO skewness within the models have implications for the accurate simulation of IOD skewness. We also explored the potential link between ENSO skewness (skewness of Niño3.4 index) and IOD skewness (skewness of PC1) within CMIP6 models (Fig. A2). It appears that there was no robust connection, so we paid more attention to the local processes. However, the asymmetric influence of ENSO cannot be ignored and potential impacts of ENSO on IOD asymmetry in climate models need further research. Therefore, it is important to investigate how simulations of pan-tropical interactions (Cai et al. 2019) contribute to the simulated IOD skewness.

Section 5 just focuses on the scenario with the highest greenhouse gas emission, the SSP5-8.5 scenario. To reveal more potential changes in the future, other scenarios should be included in the investigation (Hausfather and Peters 2020). This information will guide us towards more sustainable development approaches. The next aspect is to consider the monsoon-ocean interaction (Meehl 1997; Chang and Li 2000). A pIOD

tends to intensify the South Asian monsoon, whereas the strengthened monsoon often mitigates the pIOD (Chang and Li 2000). Under global warming, the strength of this monsoon is projected to increase (Moon and Ha 2020; Chen et al. 2022). However, it remains uncertain how these enhanced monsoon simulations might impact projected IOD changes. For instance, could a stronger monsoon inhibit the development of pIOD in the future, thereby contributing to a decrease in IOD asymmetry? The third consideration lies in the Pacific's influence on the Indian Ocean. Under global warming, the Pacific mean state change exhibits both "El Niño-like" and "La Niña-like" warming patterns (Collins et al. 2010; Watanabe et al. 2021). These projected changes may influence the mean-state changes in the Indian Ocean, thereby affecting the IOD. Like the IOD, ENSO asymmetry is projected to weaken under global warming (Ham 2017; Kohyama et al. 2018). This raises the question of whether the projected changes in ENSO asymmetry within CMIP models bear implications for the projected changes in IOD asymmetry. As IOD is closely linked to other large-scale climate phenomena like ENSO (Yang et al. 2015; An et al. 2022, 2023), exploring these teleconnections in a warmer climate can provide a more comprehensive understanding of global climate interactions. Such research can enhance our ability to predict complex climate dynamics. Furthermore, the atmospheric response to SSTAs is a complex topic, involving various factors, such as the atmospheric static stability and the SST patterns. Understanding this response becomes even more intricate in coupled models, and the utilization of Atmospheric Model Intercomparison Project (AMIP) models (Gates et al. 1998) can provide further insights into the atmospheric behavior in relation to SSTAs.

Section 6, similar to Section 5, solely examines the highest greenhouse gas emission scenario (SSP5-8.5) in CMIP6 models. However, the response of the IOD pattern may differ under various greenhouse forcings, and this relationship may not follow a linear trend. Therefore, further research is necessary to explore other scenarios or specific societal development pathways (O'Neill et al. 2016) in order to uncover potential future changes and inform sustainable development strategies. In observational studies, the thermodynamic air-sea feedback (Li et al. 2003) results in the eastern core of the IOD being located to the south of the equatorial region. The dominant mechanism for IOD development is the local feedback near the Sumatra-Java coast, followed by the Bjerknes feedback (Bjerknes 1969). Under global warming, the northward shift of the IOD pattern suggests that the basin-wide Bjerknes feedback may be more significant than the local feedback. However, further understanding of this phenomenon is

required. Moreover, in present-day simulations, climate models exhibit significant positive IOD-like biases in the mean state and simulate large errors in the amplitude and frequency of IOD and associated air-sea coupling processes (Li et al. 2015; Long et al. 2020). These biases may cause substantial uncertainty in future climate variability projections under global warming (Li et al. 2016; Wang et al. 2017). Consequently, it remains necessary to investigate how these model biases affect IOD pattern change to reduce uncertainty in climate projections. The utilization of emergent constraints (Cox et al. 2013, 2018) could also assist in refining future climate projections. Prediction uncertainty stems from three primary sources: internal variability, model uncertainty, and scenario uncertainty (Hawkins and Sutton 2009; Dobler et al. 2012; Hingray and Saïd 2014). Model uncertainty is not considered in this section, and large ensemble simulations (Kay et al. 2015) can be employed to further elucidate changes in the IOD pattern.

The assessment of historical simulations in Section 7 mainly focuses on the influences of simulated IOD and mean-state precipitation bias on the overestimated short-rain precipitation variabilities in Eastern Africa. It is noteworthy that Eastern Africa is also significantly influenced by the ENSO (Davey et al. 2014), the Quasi-Biennial Oscillation (QBO; Baldwin et al. 2001), the MJO (Zaitchik 2017; Hagos et al. 2023) and the Atlantic Ocean (Sun et al. 1999). This study primarily focuses on interannual variabilities, leaving extreme weather simulations related to IOD in Eastern Africa (Wainwright et al. 2021) as a topic for future research. Understanding the mechanisms behind extreme weather events, such as heavy rainfall or prolonged droughts (Patil et al. 2023), and their relationship with the IOD would provide valuable insights for climate adaptation and risk management strategies in this region. Additionally, the precise mechanisms leading to overestimated mean-state short rains are still under debate. Some studies suggest this overestimation stems from the warmer WTIO (Yang et al. 2015a, b) and weaker Indian Ocean Walker circulation (King et al. 2020), yet the development processes of such mean-state biases are not fully understood. Almost all CMIP6 models overestimate short-rain precipitation in Eastern Africa, but some still capture reasonable westerly in the TIO. A detailed exploration of the relationship between positive mean-state IOD-like biases, short-rain biases, and the simulated biases of the Indian monsoon in these models would provide a comprehensive understanding of these biases' drivers. This understanding would offer valuable insights into model uncertainties' sources and guide future model improvements. On the other

hand, surface air temperature is an important factor to consider in the study of droughts in Eastern Africa. The partial least squares regression pattern of the surface air temperature anomaly onto the DMI shows significant positive signals in Eastern Africa during JAS and significant negative signals during OND (Figs. 7.1k–o). However, due to the limited number of IOD samples, the surface air temperature anomalies during IOD events show diverse patterns, making it challenging to establish general mechanisms for its variability. Further research is needed to understand how the influences of both IOD-related precipitation and surface air temperature variabilities combine in affecting Eastern Africa. For instance, despite the smaller positive precipitation anomalies during JAS compared to the short-rain season in pIOD events, the increased precipitation, along with higher surface air temperature, can result in humid heat waves that have a significant impact on human health.

In the context of future climate change, the study examines potential shifts in IOD-related precipitation and surface air temperature in Eastern Africa along with their associated mechanisms. A water vapor budget is employed to quantify the contributions from changes in the mean state and IOD variability. Contributions from IOD SST variability can be further segmented into amplitude changes and structural changes (Huang and Xie 2015). The projection of IOD climate impact is a complex subject laden with uncertainties, contingent not only on the IOD simulation but also on the evolving ENSO simulation (Cai et al. 2020). Use climate models and downscaling techniques to assess how the IOD, ENSO, and other climate drivers may evolve in a changing climate and how they will impact rainfall patterns in this region. Additionally, high-resolution climate datasets, remote sensing data, and ground-based observations can be used to constrain the performance of climate models in capturing changes in short-rain precipitation variability (King and Washington 2021). For example, how to use IOD amplitude to constrain the projected changes in Somali Peninsula short rains. Furthermore, in Eastern Africa, water runoff is strongly influenced by precipitation (Chen et al. 2022). The projected increase in extreme nIOD events may result in a significant reduction in potential water availability in the future. Consequently, it is imperative to delve deeper into the effects of IOD fluctuations on Eastern Africa's water runoff. Also, the socioeconomic impacts of short-rain precipitation variabilities in Eastern Africa need further research (IDMC 2020; Ceola et al. 2023), assessing the effects of rainfall pattern changes on agriculture, water resources, food security, and livelihoods. Subsequent studies should also examine the vulnerability of various

communities and probe potential adaptation strategies to mitigate climate variability impacts.

Section 7.4 has shed light on the significant role the IOD plays in shaping Australia's climatic conditions, particularly temperature and rainfall patterns. One limitation lies in the underperformance of the CMIP6 models in precisely replicating the IOD's impact on Australia's climate. This inadequacy stems from the models' weaker simulation of IOD-induced Rossby waves. However, the inter-model analysis reveals a significant diversity concerning IOD characteristics and Australian climate anomalies, necessitating further research. As a subsequent step, it is important to take into account the teleconnections from ENSO and SAM. Di Virgilio et al. (2022) found that some models adept at simulating the ENSO-rainfall teleconnection performed poorly in simulating the IOD-rainfall relationship. Given that nearly all CMIP6 models underestimate the IOD's influence on Australia, it is imperative to constrain the projected climate changes in Australia as much as feasible. Furthermore, the prediction of climate anomalies across Australia during IOD events relies not only on the ability to forecast IOD characteristics in the TIO (Shi et al. 2012), but also on the capability to accurately simulate the subtropical and eddy-driven jets and their associated induced eddy feedback (McIntosh et al. 2018). This highlights the urgent need for ongoing refinement of climate models to better represent the complex interactions between oceanic and atmospheric processes.

8.3. Future directions

(1) Barrier layer thickness

Roles of BLT are also simply explored in CMIP5/6 models. Nearly all the CMIP models fail to capture the nonlinear response of BLT like the observed. Instead, they simulate either a linear response or a larger response during nIOD compared to pIOD. Most of the CMIP models cannot capture the deep BLT near the Sumatra-Java coast (Fig. 8.1). This poor BLT simulation may be attributed to the models' inability to accurately represent enhanced upper-ocean stratification and a shallower thermocline in the ETIO. The precise contributions of BLT to IOD asymmetry are still debated and require further investigation through observational research. While it is suggested that there will be a greater BLT response during pIOD compared to nIOD, the cooling effect resulting from a thinner BLT during pIOD may not necessarily exceed the effect of a

thicker BLT during nIOD. The impact of BLT simulation on the simulated IOD asymmetry remains uncertain. For instance, if the simulation of BLT improves, will the simulation of IOD asymmetry also improve? Under the SSP5-8.5 scenario, the mean BLT is projected to be smaller in the ETIO, particularly in the equatorial ETIO and near the Sumatra-Java coast, compared to historical simulations. This projection may arise from intensified oceanic stratification due to global warming. The projected reduction in mean BLT and its variability suggests that BLT may not be as influential as it is in the present day. Consequently, changes in the thermocline are expected to have a greater influence on MLT.

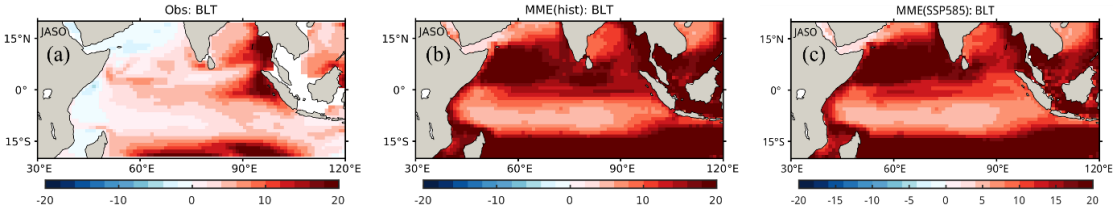


Figure 8.1. Mean-state BLT (unit: m) in (a) observations, (b) historical and (c) SSP5-8.5 simulations.

(2) Pacific mean state simulation

The Pacific Ocean and Indian Ocean are interconnected through the Walker Circulation, and the simulation of the Pacific mean state can influence the simulation of the Indian Ocean mean state and subsequently impact the IOD. A prevalent bias observed in current climate models is the cold tongue bias (Mechoso et al. 1995; Bellenger et al. 2014). This bias may result in a stronger warm pool in the western Pacific through the Bjerknes feedback. Consequently, the intensified warm pool may contribute to stronger westerly winds in the TIO, potentially reducing the mean-state positive IOD-like biases. This hypothesis holds merit. Among the selected CMIP6 models, this relationship appears to be applicable in some models (Fig. 8.2). However, further research is necessary to understand the extent to which present-day simulations of the Pacific mean state affect the Indian Ocean simulation.

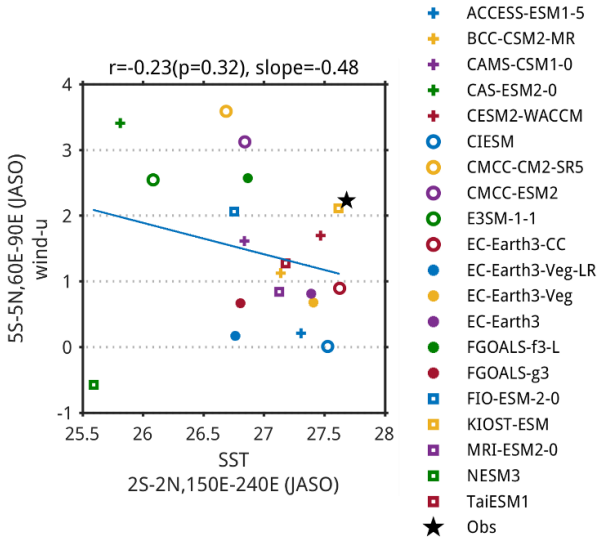


Figure 8.2. Mean-state SST (unit: °C; 2°S–2°N, 150°–240°E; JASO) vs 850 hPa zonal wind (unit: m s^{-1}; 5°S–5°N, 60°–90°E; JASO).

(3) Oceanic wave simulation

In observations, the anomalous wind stress curl in the TIO initiates anomalous Rossby waves in the southern off-equatorial region, which serves as positive feedback for SSTA growth in the WTIO (Webster et al. 1999; Li et al. 2003). Subsequently, these oceanic Rossby waves transform into Kelvin waves upon reaching the western boundary of the TIO. The reflected Kelvin waves can attenuate SST variability along the equatorial ETIO, acting as negative feedback for SSTA growth in the ETIO. However, models may simulate weaker oceanic waves at the equator, resulting in larger SSTA STD along the equatorial ETIO in historical simulations. Furthermore, it is important to investigate whether increased upper-ocean stratification, induced by global warming, would weaken oceanic waves during IOD events. This weakening could contribute to amplified SSTA amplitudes along the equatorial ETIO. These aspects require further research.

(4) Monsoon-IOD interaction

Despite the presence of significant wind anomalies in the Indian Ocean during IOD events, the relationship between the monsoon and IOD remains relatively weak compared to ENSO, both in observations and CMIP models (Jourdain et al. 2013). Nevertheless, the interaction between the monsoon and IOD remains an important topic in climate research. Previous studies have highlighted that the monsoon simulation can influence the simulation of the Indian Ocean mean state (Long et al. 2020), and IOD

events are recognized as a crucial large-scale driving mechanism for the Indian monsoon (Behera et al. 1999; Ashok et al. 2001). Under global warming, shifts in the IOD pattern and changes in the mean-state precipitation pattern, primarily associated with the monsoon, could have significant impacts on weather and climate related to IOD. Understanding these impacts will contribute to improved projections of the climatic effects of IOD.

(5) Climate impacts on East Asia

East Asians, comprising approximately 1.7 billion people, account for 38% of the population in Continental Asia and 20.5% of the global population (Wang et al. 2018). This region is mainly influenced by the Asian-Pacific monsoon that is deeply modulated by the Indo-Pacific climate modes, such as ENSO (McPhaden et al. 2006) and IOD (Saji et al. 1999). These modulations have significant implications for water availability, food security, economics, and social stability, particularly in the context of climate change. However, the precise understanding of future changes in IOD, ENSO and their combined effects on the East Asian monsoon remains incomplete. Further research using CMIP6 models and conducting sensitive experiments can shed light on these changes and identify the dominant processes linking Indo-Pacific climate modes with the East Asian monsoon in future climate projections.

(6) Emergent constraint

Uncertainties persist due to model biases (Hawkins and Sutton 2009; Hui and Zheng 2018), emphasizing the necessity of continuing to develop climate models as well as sustain reliable observations to constrain model projections (Hall et al. 2019). Evaluating models against high-quality observational data should remain a priority to boost confidence in future climate projections. Continual improvement and expansion of observational datasets, especially in the Indian Ocean region (Beal et al. 2020), is essential for validating model projections and enhancing our understanding of historical IOD events. Recent studies have suggested that the pIOD-like warming pattern significantly decreases in the corrected projections using emergent constraints (Li et al. 2016). However, the relationship between model biases and IOD changes is not fully understood. Further investigation is needed to determine how these model biases impact the IOD changes, thereby facilitating the reduction of uncertainty in climate projections.

Except for the emergent constraint, other methods can also be used to reduce the IOD simulation biases. For example, Perturbed Physics Ensembles involve running the same model multiple times with slightly different physics parameters each time. The range of results can then be used to estimate the uncertainty in the projections. In addition, Higher resolution models can often better capture small-scale processes that can have a large impact on the overall climate system. However, these models are computationally expensive and may not be feasible for long-term projections.

Bibliography

Abram, N. J., and Coauthors, 2020: Coupling of Indo-Pacific climate variability over the last millennium. *Nature*, **579**, 385-392, https://doi.org/10.1038/s41586-020-2084-4.

Abram, N. J., M. K. Gagan, J. E. Cole, W. S. Hantoro, and M. Mudelsee, 2008: Recent intensification of tropical climate variability in the Indian Ocean. *Nat. Geosci.*, **1**, 849-853, https://doi.org/10.1038/ngeo357.

Abram, N. J., M. K. Gagan, M. T. McCulloch, J. Chappell, and W. S. Hantoro, 2003: Coral Reef Death During the 1997 Indian Ocean Dipole Linked to Indonesian Wildfires. *Science*, **301**, 952-955, https://doi.org/10.1126/science.1083841.

Adler, R. F., and Coauthors, 2003: The Version-2 Global Precipitation Climatology Project (GPCP) Monthly Precipitation Analysis (1979–Present). *J. Hydrometeorol.*, **4**, 1147-1167, https://doi.org/10.1175/1525-7541(2003)004<1147:TVGPCP>2.0.CO;2.

Adler, R. F., and Coauthors, 2018: The Global Precipitation Climatology Project (GPCP) Monthly Analysis (New Version 2.3) and a Review of 2017 Global Precipitation. *Atmosphere*, **9**, 138, https://doi.org/10.3390/atmos9040138.

An, S.-I., H.-J. Park, S.-K. Kim, J. Shin, S.-W. Yeh, and J.-S. Kug, 2022: Intensity changes of Indian Ocean dipole mode in a carbon dioxide removal scenario. *npj Clim. Atmos. Sci.*, **5**, 20, https://doi.org/10.1038/s41612-022-00246-6.

An, S.-I., H.-J. Park, S.-K. Kim, W. Cai, A. Santoso, D. Kim, and J.-S Kug, 2023: Main drivers of Indian Ocean Dipole asymmetry revealed by a simple IOD model. *npj Clim. Atmos. Sci.*, **6**, 93. https://doi.org/10.1038/s41612-023-00422-2.

Annamalai, H., J. Potemra, R. Murtugudde, and J. P. McCreary, 2005: Effect of Preconditioning on the Extreme Climate Events in the Tropical Indian Ocean. *J. Climate*, **18**, 3450–3469, https://doi.org/10.1175/JCLI3494.1.

Annamalai, H., R. Murtugudde, J. Potemra, S. P. Xie, P. Liu, and B. Wang, 2003: Coupled dynamics over the Indian Ocean: spring initiation of the Zonal Mode. *Deep. Res. Part II Top. Stud. Oceanogr.*, **50**, 2305-2330, https://doi.org/10.1016/S0967-0645(03)00058-4.

Armstrong McKay, D. I., and Coauthors, 2022: Exceeding 1.5°C global warming could trigger multiple climate tipping points. *Science*, **377**, eabn7950, https://www.science.org/doi/abs/10.1126/science.abn7950.

Ashok, K., C. Y. Tam, and W. J. Lee, 2009: ENSO Modoki impact on the Southern Hemisphere storm track activity during extended austral winter. *Geophys. Res. Lett.*, **36**, https://doi.org/10.1029/2009GL038847.

Ashok, K., H. Nakamura, and T. Yamagata, 2007: Impacts of ENSO and Indian Ocean Dipole Events on the Southern Hemisphere Storm-Track Activity during Austral Winter. *J. Climate*, **20**, 3147–3163, https://doi.org/10.1175/JCLI4155.1.

Ashok, K., Z. Guan, and T. Yamagata, 2001: Impact of the Indian Ocean dipole on the relationship between the Indian monsoon rainfall and ENSO. *Geophys. Res. Lett.*, **28**, 4499-4502, https://doi.org/10.1029/2001GL013294.

Ashok, K., Z. Guan, and T. Yamagata, 2003: Influence of the Indian Ocean Dipole on the Australian winter rainfall. *Geophys. Res. Lett.*, **30**, https://doi.org/10.1029/2003GL017926.

Ashok, K., Z. Guan, N. H. Saji, and T. Yamagata, 2004: Individual and Combined Influences of ENSO and the Indian Ocean Dipole on the Indian Summer Monsoon. *J. Climate*, **17**, 3141–3155, https://doi.org/10.1175/1520-0442(2004)017<3141:IACIOE>2.0.CO;2.

Baldwin, M. P., and Coauthors, 2001: The quasi-biennial oscillation. *Rev. Geophys.*, **39**, 179-229, https://doi.org/10.1029/1999RG000073.

Baquero-Bernal, A., and M. Latif, 2005: Wind-Driven Oceanic Rossby Waves in the Tropical South Indian Ocean with and without an Active ENSO. *J. Phys. Oceanogr.*, **35**, 729-746, https://doi.org/10.1175/JPO2723.1.

Beal, L. M., and Coauthors, 2020: A Road Map to IndOOS-2: Better Observations of the Rapidly Warming Indian Ocean. *Bull. Amer. Meteor. Soc.*, **101**, E1891–E1913, https://doi.org/10.1175/BAMS-D-19-0209.1.

Beguería, Santiago; Vicente Serrano, Sergio M.; Reig-Gracia, Fergus; Latorre Garcés, Borja; 2023; SPEIbase v.2.9 [Dataset]; DIGITAL.CSIC; Version 2.9; https://doi.org/10.20350/digitalCSIC/15470.

Behera, S. K., J. J. Luo, S. Masson, S. A. Rao, H. Sakuma, and T. Yamagata, 2006: A CGCM Study on the Interaction between IOD and ENSO. *J. Climate*, **19**, 1688–1705, https://doi.org/10.1175/JCLI3797.1.

Behera, S. K., J. Luo, S. Masson, P. Delecluse, S. Gualdi, A. Navarra, and T. Yamagata, 2005: Paramount Impact of the Indian Ocean Dipole on the East African Short Rains: A CGCM Study. *J. Climate*, **18**, 4514–4530, https://doi.org/10.1175/JCLI3541.1.

Behera, S. K., R. Krishnan, and T. Yamagata, 1999: Unusual ocean-atmosphere conditions in the tropical Indian Ocean during 1994. *Geophys. Res. Lett.*, **26**, 3001-3004, https://doi.org/10.1029/1999GL010434.

Behera, S., J. V. Ratnam, Y. Masumoto, and T. Yamagata, 2013: Origin of extreme summers in Europe: the Indo-Pacific connection. *Clim. Dyn.*, **41**, 663-676, https://doi.org/10.1007/s00382-012-1524-8.

Behringer, D. W., M. Ji, and A. Leetmaa, 1998: An Improved Coupled Model for ENSO Prediction and Implications for Ocean Initialization. Part I: The Ocean Data Assimilation System. *Mon. Weather Rev.*, **126**, 1013-1021, https://doi.org/10.1175/1520-0493(1998)126<1013:AICMFE>2.0.CO;2.

Bellenger, H., E. Guilyardi, J. Leloup, M. Lengaigne, and J. Vialard, 2014: ENSO representation in climate models: From CMIP3 to CMIP5. *Clim. Dyn.*, **42**, 1999–2018, https://doi.org/10.1007/s00382-013-1783-z.

Bjerknes, J., 1969: Atmospheric Teleconnections from the Equatorial Pacific. *Mon. Weather Rev.*, **97**, 163-172, https://doi.org/10.1175/1520-0493(1969)097<0163:ATFTEP>2.3.CO;2.

Black, E., 2005: The relationship between Indian Ocean sea-surface temperature and East African rainfall. Philosophical Transactions. *Phil. Trans. R. Soc. A.*, **363**, 43–47, https://doi.org/10.1098/rsta.2004.1474.

Black, E., J. Slingo, and K. R. Sperber, 2003: An Observational Study of the Relationship between Excessively Strong Short Rains in Coastal East Africa and Indian Ocean SST. *Mon. Wea. Rev.*, **131**, 74–94, https://doi.org/10.1175/1520-0493(2003)131<0074:AOSOTR>2.0.CO;2.

Blau, M. T., and K. J. Ha, 2020: The Indian Ocean Dipole and its Impact on East African Short Rains in Two CMIP5 Historical Scenarios With and Without Anthropogenic Influence. *J. Geophys. Res. Atmos.*, **125**, e2020JD033121, https://doi.org/10.1029/2020JD033121.

Brubaker, K. L., D. Entekhabi, and P. S. Eagleson, 1993: Estimation of Continental Precipitation Recycling. *J. Climate*, **6**, 1077–1089, https://doi.org/10.1175/1520-0442(1993)006<1077:EOCPR>2.0.CO;2.

Budyko, M I., 1974: Climate and Life. Academic Press, 508.

Burgers, G., and D. B. Stephenson, 1999: The “normality” of El Niño. *Geophys. Res. Lett.*, **26**, 1027-1030, https://doi.org/10.1029/1999GL900161.

Cai, W., A. Sullivan, and T. Cowan, 2011: Interactions of ENSO, the IOD, and the SAM in CMIP3 Models. *J. Climate*, **24**, 1688–1704, https://doi.org/10.1175/2010JCLI3744.1.

Cai, W., and Coauthors, 2013: Projected response of the Indian Ocean Dipole to greenhouse warming. *Nat. Geosci.*, **6**, 999-1007, https://doi.org/10.1038/ngeo2009.

Cai, W., and Coauthors, 2014: Increased frequency of extreme Indian Ocean Dipole events due to greenhouse warming. *Nature*, **510**, 254-258, https://doi.org/10.1038/nature13327.

Cai, W., and Coauthors, 2019: Pantropical climate interactions. *Science*, **363**, eaav4236, https://doi.org/10.1126/science.aav4236.

Cai, W., and Coauthors, 2021: Opposite response of strong and moderate positive Indian Ocean Dipole to global warming. *Nat. Clim. Chang.*, **11**, 27-32, https://doi.org/10.1038/s41558-020-00943-1.

Cai, W., and T. Cowan, 2013: Why is the amplitude of the Indian Ocean Dipole overly large in CMIP3 and CMIP5 climate models? *Geophys. Res. Lett.*, **40**, 1200-1205, https://doi.org/10.1002/grl.50208.

Cai, W., and Y. Qiu, 2013: An Observation-Based Assessment of Nonlinear Feedback Processes Associated with the Indian Ocean Dipole. *J. Climate*, **26**, 2880-2890, https://doi.org/10.1175/JCLI-D-12-00483.1.

Cai, W., B. Ng, T. Geng, L. Wu, A. Santoso, and M. J. McPhaden, 2020: Butterfly effect and a self-modulating El Niño response to global warming. *Nature*, **585**, 68-73, https://doi.org/10.1038/s41586-020-2641-x.

Cai, W., P. van Rensch, T. Cowan, and H. H. Hendon, 2012: An Asymmetry in the IOD and ENSO Teleconnection Pathway and Its Impact on Australian Climate. *J. Climate*, **25**, 6318-6329, https://doi.org/10.1175/JCLI-D-11-00501.1.

Cai, W., T. Cowan, and M. Raupach, 2009: Positive Indian Ocean Dipole events precondition southeast Australia bushfires. *Geophys. Res. Lett.*, **36**, L19710, https://doi.org/10.1029/2009GL039902.

Carton, J. A., and B. S. Giese, 2008: A Reanalysis of Ocean Climate Using Simple Ocean Data Assimilation (SODA). *Mon. Wea. Rev.*, **136**, 2999–3017, https://doi.org/10.1175/2007MWR1978.1.

Ceola, S., J. Mård, and G. Di Baldassarre, 2023: Drought and Human Mobility in Africa. *Earth's Future*, **11**, e2023EF003510, https://doi.org/10.1029/2023EF003510.

Chan, R. Y., M. Vuille, D. R. Hardy, and R. S. Bradley, 2008: Intraseasonal precipitation variability on Kilimanjaro and the East African region and its relationship to the large-scale circulation. *Theor. Appl. Climatol.*, **93**, 149-165, https://doi.org/10.1007/s00704-007-0338-9.

Chang, C. P., and T. Li, 2000: A Theory for the Tropical Tropospheric Biennial Oscillation. *Journal of the Atmospheric Sciences*, **57**, 2209-2224, https://doi.org/10.1175/1520-0469(2000)057<2209:ATFTTT>2.0.CO;2.

Chen, G., W. Han, Y. Li, D. Wang, and M. J. McPhaden, 2015: Seasonal-to-Interannual Time-Scale Dynamics of the Equatorial Undercurrent in the Indian Ocean. *J. Phys. Oceanogr.*, **45**, 1532–1553, https://doi.org/10.1175/JPO-D-14-0225.1.

Chen, G., W. Han, Y. Shu, Y. Li, D. Wang, and Q. Xie, 2016a: The role of Equatorial Undercurrent in sustaining the Eastern Indian Ocean upwelling. *Geophys. Res. Lett.*, **43**, 6444-6451, https://doi.org/10.1002/2016GL069433.

Chen, M., T. Li, X. Shen, and B. Wu, 2016b: Relative Roles of Dynamic and Thermodynamic Processes in Causing Evolution Asymmetry between El Niño and La Niña. *J. Climate*, **29**, 2201–2220, https://doi.org/10.1175/JCLI-D-15-0547.1.

Chen, Z., T. Zhou, X. Chen, W. Zhang, L. Zhang, M. Wu, and L. Zou, 2022: Observationally constrained projection of Afro-Asian monsoon precipitation. *Nat. Commun.*, **13**, 2552, https://doi.org/10.1038/s41467-022-30106-z.

Chowdary, J. S., D. Patekar, G. Srinivas, C. Gnanaseelan, and A. Parekh, 2019: Impact of the Indo-Western Pacific Ocean Capacitor mode on South Asian summer monsoon rainfall. *Clim. Dyn.*, **53**, 2327-2338, https://doi.org/10.1007/s00382-019-04850-w.

Chung, C., G. Boschat, A. Taschetto, S. Narsey, S. McGregor, A. Santoso, and F. Delage, 2023: Evaluation of seasonal teleconnections to remote drivers of Australian rainfall in CMIP5 and CMIP6 models. Journal of Southern Hemisphere Earth Systems Science, 73, 219-261, https://doi.org/10.1071/ES23002.

Clark, C. O., J. E. Cole, and P. J. Webster, 2000: Indian Ocean SST and Indian Summer Rainfall: Predictive Relationships and Their Decadal Variability. *J.*

Climate, **13**, 2503–2519, https://doi.org/10.1175/1520-0442(2000)013<2503:IOSAIS>2.0.CO;2.

Clark, C. O., P. J. Webster, and J. E. Cole, 2003: Interdecadal Variability of the Relationship between the Indian Ocean Zonal Mode and East African Coastal Rainfall Anomalies. *J. Climate*, **16**, 548–554, https://doi.org/10.1175/1520-0442(2003)016<0548:IVOTRB>2.0.CO;2.

Clement, A. C., R. Seager, M. A. Cane, and S. E. Zebiak, 1996: An Ocean Dynamical Thermostat. *J. Climate*, **9**, 2190–2196, https://doi.org/10.1175/1520-0442(1996)009<2190:AODT>2.0.CO;2.

Collier, E., T. Mölg, and T. Sauter, 2018: Recent Atmospheric Variability at Kibo Summit, Kilimanjaro, and Its Relation to Climate Mode Activity. *J. Climate*, **31**, 3875–3891, https://doi.org/10.1175/JCLI-D-17-0551.1.

Collins, M., and Coauthors, 2010: The impact of global warming on the tropical Pacific Ocean and El Niño. *Nat. Geosci.*, **3**, 391-397, https://doi.org/10.1038/ngeo868.

Cox, P. M., C. Huntingford, and M. S. Williamson, 2018: Emergent constraint on equilibrium climate sensitivity from global temperature variability. *Nature*, **553**, 319-322, https://doi.org/10.1038/nature25450.

Cox, P. M., D. Pearson, B. B. Booth, P. Friedlingstein, C. Huntingford, C. D. Jones, and C. M. Luke, 2013: Sensitivity of tropical carbon to climate change constrained by carbon dioxide variability. *Nature*, **494**, 341-344, https://doi.org/10.1038/nature11882.

Davey, M. K., A. Brookshaw, and S. Ineson, 2014: The probability of the impact of ENSO on precipitation and near-surface temperature. *Clim. Risk Manag.*, **1**, 5-24, https://doi.org/10.1016/j.crm.2013.12.002.

de Boyer Montégut, C., J. Vialard, S. S. C. Shenoi, D. Shankar, F. Durand, C. Ethé, and G. Madec, 2007: Simulated Seasonal and Interannual Variability of the Mixed Layer Heat Budget in the Northern Indian Ocean. *J. Climate*, **20**, 3249–3268, https://doi.org/10.1175/JCLI4148.1.

Deshpande, A., J. S. Chowdary, and C. Gnanaseelan, 2014: Role of thermocline–SST coupling in the evolution of IOD events and their regional impacts. *Clim. Dyn.*, **43**, 163–174, https://doi.org/10.1007/s00382-013-1879-5.

Di Virgilio, G., and Coauthors, 2022: Selecting CMIP6 GCMs for CORDEX Dynamical Downscaling: Model Performance, Independence, and Climate Change

Signals. *Earth's Future*, **10**, e2021EF002625, https://doi.org/10.1029/2021EF002625.

Dimri, A. P., T. Yasunari, B. S. Kotlia, U. C. Mohanty, and D. R. Sikka, 2016: Indian winter monsoon: Present and past. *Earth-Sci. Rev.*, **163**, 297-322, https://doi.org/10.1016/j.earscirev.2016.10.008.

Ding, Q., and B. Wang, 2005: Circumglobal Teleconnection in the Northern Hemisphere Summer. *J. Climate*, **18**, 3483–3505, https://doi.org/10.1175/JCLI3473.1.

Ding, Y. H., and J. C. L. Chan, 2005: The East Asian summer monsoon: an overview. *Meteor. Atmos. Phys.*, **89**, 117-142, https://doi.org/10.1007/s00703-005-0125-z.

Dobler, C., S. Hagemann, R. L. Wilby, and J. Stötter, 2012: Quantifying different sources of uncertainty in hydrological projections in an Alpine watershed. *Hydrol. Earth Syst. Sci.*, **16**, 4343–4360, https://doi.org/10.5194/hess-16-4343-2012.

Doi, T., S. K. Behera, and T. Yamagata, 2022: On the Predictability of the Extreme Drought in East Africa During the Short Rains Season. *Geophys. Res. Lett.*, **49**, e2022GL100905, https://doi.org/10.1029/2022GL100905.

Doi, T., T. Tozuka, H. Sasaki, Y. Masumoto, and T. Yamagata, 2007: Seasonal and Interannual Variations of Oceanic Conditions in the Angola Dome. *J. Phys. Oceanogr.*, **37**, 2698–2713, https://doi.org/10.1175/2007JPO3552.1.

Du, Y., W. Cai, and Y. Wu, 2013: A New Type of the Indian Ocean Dipole since the Mid-1970s. *J. Climate*, **26**, 959-972, https://doi.org/10.1175/JCLI-D-12-00047.1.

Du, Y., Y. Zhang, L.-Y. Zhang, T. Tozuka, B. Ng, and W. Cai, 2020: Thermocline Warming Induced Extreme Indian Ocean Dipole in 2019. *Geophys. Res. Lett.*, **47**, e2020GL090079, https://doi.org/10.1029/2020GL090079.

Efron, B., 1987: Better Bootstrap Confidence Intervals. *J. Am. Stat. Assoc.*, **82**, 171-185, https://doi.org/10.2307/2289144.

Efron, B., and G. Gong, 1983: A Leisurely Look at the Bootstrap, the Jackknife, and Cross-Validation. *Am. Stat.*, **37**, 36-48, https://doi.org/10.2307/2685844.

Endo, S., and T. Tozuka, 2016: Two flavors of the Indian Ocean Dipole. *Clim. Dyn.*, **46**, 3371-3385, https://doi.org/10.1007/s00382-015-2773-0.

Endris, H. S., C. Lennard, B. Hewitson, A. Dosio, G. Nikulin, and G. A. Artan, 2019: Future changes in rainfall associated with ENSO, IOD and changes in the mean state over Eastern Africa. *Clim. Dyn.*, **52**, 2029-2053, https://doi.org/10.1007/s00382-018-4239-7.

England, M. H., C. C. Ummenhofer, and A. Santoso, 2006: Interannual Rainfall Extremes over Southwest Western Australia Linked to Indian Ocean Climate Variability. J. Climate, 19, 1948–1969, https://doi.org/10.1175/JCLI3700.1.

Enomoto, T., B. J. Hoskins, and Y. Matsuda, 2003: The formation mechanism of the Bonin high in August. *Q. J. R. Meteorol. Soc.*, **129**, 157-178, https://doi.org/10.1256/qj.01.211.

Eyring, V., S. Bony, G. A. Meehl, C. A. Senior, B. Stevens, R. J. Stouffer, and K. E. Taylor, 2016: Overview of the Coupled Model Intercomparison Project Phase 6 (CMIP6) experimental design and organization. *Geosci. Model Dev.*, **9**, 1937-1958, https://doi.org/10.5194/gmd-9-1937-2016.

Fan, L., H. Fu, and Y. Liang, 2024: Two Characteristic Patterns of the Summer Indian Ocean Dipole. *J. Climate*, https://doi.org/10.1175/JCLI-D-23-0534.1, in press.

Fan, L., Q. Liu, C. Wang, and F. Guo, 2017: Indian Ocean Dipole Modes Associated with Different Types of ENSO Development. *J. Climate*, **30**, 2233–2249, https://doi.org/10.1175/JCLI-D-16-0426.1.

Fan, L., S.-I. Shin, Z. Liu, and Q. Liu, 2016: Two-sided impacts of warm pool SSTs on Australian precipitation changes. *Int. J. Climatol.*, **36**, 4697-4704. https://doi.org/10.1002/joc.4661.

Feng, M., G. Meyers, A. Pearce, and S. Wijffels, 2003: Annual and interannual variations of the Leeuwin Current at 32°S. *J. Geophys. Res. Oceans*, **108**, https://doi.org/10.1029/2002JC001763.

Finney, D. L., J. H. Marsham, D. P. Rowell, E. J. Kendon, S. O. Tucker, R. A. Stratton, and L. S. Jackson, 2020: Effects of Explicit Convection on Future Projections of Mesoscale Circulations, Rainfall, and Rainfall Extremes over Eastern Africa. *J. Climate*, **33**, 2701–2718, https://doi.org/10.1175/JCLI-D-19-0328.1.

Fischer, A. S., P. Terray, E. Guilyardi, S. Gualdi, and P. Delecluse, 2005: Two Independent Triggers for the Indian Ocean Dipole/Zonal Mode in a Coupled GCM. *J. Climate*, **18**, 3428–3449, https://doi.org/10.1175/JCLI3478.1.

Foltz, G. R., J. Vialard, B. Praveen Kumar, and M. J. McPhaden, 2010: Seasonal Mixed Layer Heat Balance of the Southwestern Tropical Indian Ocean. *J. Climate*, **23**, 947–965, https://doi.org/10.1175/2009JCLI3268.1.

Gadgil, S., P. N. Vinayachandran, P. A. Francis, and S. Gadgil, 2004: Extremes of the Indian summer monsoon rainfall, ENSO and equatorial Indian Ocean oscillation. *Geophys. Res. Lett.*, **31**, https://doi.org/10.1029/2004GL019733.

Gamoyo, M., C. Reason, and D. Obura, 2015: Rainfall variability over the East African coast. *Theor. Appl. Climatol.*, **120**, 311-322, https://doi.org/10.1007/s00704-014-1171-6.

Gates, W. L., and Coauthors, 1999: An Overview of the Results of the Atmospheric Model Intercomparison Project (AMIP I). *Bull. Amer. Meteor. Soc.*, **80**, 29–56, https://doi.org/10.1175/1520-0477(1999)080<0029:AOOTRO>2.0.CO;2.

Gill, A. E., 1980: Some simple solutions for heat-induced tropical circulation. *Q. J. R. Meteorol. Soc.*, **106**, 447-462, https://doi.org/10.1002/qj.49710644905.

Griffies, S. M., and Coauthors, 2009: Sampling physical ocean fields in WCRP CMIP5 simulations: CLIVAR Working Group on Ocean Model Development (WGOMD) committee on CMIP5 ocean model output (No. 137). Climate Variability and Predictability Programme. http://n2t.net/ark:/85065/d7416zk6.

Guan, Z., and T. Yamagata, 2003: The unusual summer of 1994 in East Asia: IOD teleconnections. *Geophys. Res. Lett.*, **30**, 1544, https://doi.org/10.1029/2002GL016831.

Hagos, S., J. Jung, P.-L. Ma, S. W. Lubis, K. Balaguru, C.-C. Chang, and L. R. Leung, 2023: East African Monsoon as a Drawbridge for the Circumnavigation of Madden–Julian Oscillation Events. *Geophys. Res. Lett.*, **50**, e2023GL102906, https://doi.org/10.1029/2023GL102906.

Hall, A., P. Cox, C. Huntingford, and S. Klein, 2019: Progressing emergent constraints on future climate change. *Nat. Clim. Chang.*, **9**, 269-278, https://doi.org/10.1038/s41558-019-0436-6.

Ham, Y.-G., 2017: A reduction in the asymmetry of ENSO amplitude due to global warming: The role of atmospheric feedback. *Geophys. Res. Lett.*, **44**, 8576-8584, https://doi.org/10.1002/2017GL074842.

Han, W., J. Vialard, M. J. McPhaden, T. Lee, Y. Masumoto, M. Feng, and W. P. de Ruijter, 2014: Indian Ocean Decadal Variability: A Review. *Bull. Amer. Meteor. Soc.*, **95**, 1679–1703, https://doi.org/10.1175/BAMS-D-13-00028.1.

Hausfather, Z., and G. P. Peters, 2020: Emissions – the 'business as usual' story is misleading. *Nature*, **577**, 618–620, https://doi.org/10.1038/d41586-020-00177-3.

Hawkins, E., and R. Sutton, 2009: The Potential to Narrow Uncertainty in Regional Climate Predictions. *Bull. Amer. Meteor. Soc.*, **90**, 1095–1108, https://doi.org/10.1175/2009BAMS2607.1.

Hayashi, M., F.-F. Jin, and M. F. Stuecker, 2020: Dynamics for El Niño-La Niña asymmetry constrain equatorial-Pacific warming pattern. *Nat. Commun.*, **11**, 4230, https://doi.org/10.1038/s41467-020-17983-y.

Held, I. M., and B. J. Soden, 2006: Robust Responses of the Hydrological Cycle to Global Warming. *J. Climate*, **19**, 5686–5699, https://doi.org/10.1175/JCLI3990.1.

Hermes, J. C., and C. J. C. Reason, 2008: Annual cycle of the South Indian Ocean (Seychelles-Chagos) thermocline ridge in a regional ocean model. *J. Geophys. Res. Oceans*, **113**, https://doi.org/10.1029/2007JC004363.

Hermes, J. C., and Coauthors, 2019: A Sustained Ocean Observing System in the Indian Ocean for Climate Related Scientific Knowledge and Societal Needs. *Front. Mar. Sci*., **6**, https://doi.org/10.3389/fmars.2019.00355.

Hingray, B., and M. Saïd, 2014: Partitioning Internal Variability and Model Uncertainty Components in a Multimember Multimodel Ensemble of Climate Projections. *J. Climate*, **27**, 6779–6798, https://doi.org/10.1175/JCLI-D-13-00629.1.

Hirons, L., and A. Turner, 2018: The Impact of Indian Ocean Mean-State Biases in Climate Models on the Representation of the East African Short Rains. *J. Climate*, **31**, 6611–6631, https://doi.org/10.1175/JCLI-D-17-0804.1.

Hoerling, M. P., A. Kumar, and M. Zhong, 1997: El Niño, La Niña, and the Nonlinearity of Their Teleconnections. *J. Climate*, **10**, 1769-1786, https://doi.org/10.1175/1520-0442(1997)010<1769:ENOLNA>2.0.CO;2.

Hoffmann, L., and Coauthors, 2019: From ERA-Interim to ERA5: the considerable impact of ECMWF's next-generation reanalysis on Lagrangian transport simulations. *Atmos. Chem. Phys.*, **19**, 3097-3124, https://doi.org/10.5194/acp-19-3097-2019.

Holgate, C., J. P. Evans, A. S. Taschetto, A. S. Gupta, and A. Santoso, 2022: The Impact of Interacting Climate Modes on East Australian Precipitation Moisture Sources. *J. Climate*, **35**, 3147–3159, https://doi.org/10.1175/JCLI-D-21-0750.1.

Hong, C.-C., and T. Li, 2010: Independence of SST skewness from thermocline feedback in the eastern equatorial Indian Ocean. *Geophys. Res. Lett.*, **37**, L11702, https://doi.org/10.1029/2010GL043380.

Hong, C.-C., T. Li, and J.-J. Luo, 2008a: Asymmetry of the Indian Ocean Dipole. Part II: Model Diagnosis. *J. Climate*, **21**, 4849-4858, https://doi.org/10.1175/2008JCLI2223.1.

Hong, C.-C., T. Li, LinHo, and J.-S. Kug, 2008b: Asymmetry of the Indian Ocean Dipole. Part I: Observational Analysis. *J. Climate*, **21**, 4834-4848, https://doi.org/10.1175/2008JCLI2222.1.

Hoskins, B. J., and T. Ambrizzi, 1993: Rossby Wave Propagation on a Realistic Longitudinally Varying Flow. *J. Atmos. Sci.*, **50**, 1661–1671, https://doi.org/10.1175/1520-0469(1993)050<1661:RWPOAR>2.0.CO;2.

Huang, B., and Coauthors, 2017: Extended Reconstructed Sea Surface Temperature, Version 5 (ERSSTv5): Upgrades, Validations, and Intercomparisons. *J. Climate*, **30**, 8179–8205, https://doi.org/10.1175/JCLI-D-16-0836.1.

Huang, P., and J. Ying, 2015: A Multimodel Ensemble Pattern Regression Method to Correct the Tropical Pacific SST Change Patterns under Global Warming. *J. Climate*, **28**, 4706–4723, https://doi.org/10.1175/JCLI-D-14-00833.1.

Huang, P., and S.-P. Xie, 2015: Mechanisms of change in ENSO-induced tropical Pacific rainfall variability in a warming climate. *Nat. Geosci.*, **8**, 922-926, https://doi.org/10.1038/ngeo2571.

Hui, C., and X.-T. Zheng, 2018: Uncertainty in Indian Ocean Dipole response to global warming: the role of internal variability. *Clim. Dyn.*, **51**, 3597-3611, https://doi.org/10.1007/s00382-018-4098-2.

IDMC. (2020). Global report on internal displacement. Internal Displacement Monitoring Centre. Retrieved from https://www.internal-displacement.org/global-report/grid2020/.

Ihara, C., Y. Kushnir, and M. A. Cane, 2008: Warming Trend of the Indian Ocean SST and Indian Ocean Dipole from 1880 to 2004. *J. Climate*, **21**, 2035–2046, https://doi.org/10.1175/2007JCLI1945.1.

IPCC, 2013: *Climate Change 2013: The Physical Science Basis*. Cambridge University Press, 1535 pp., https://doi.org/10.1017/CBO9781107415324.

Izumo, T., and Coauthors, 2010: Influence of the state of the Indian Ocean Dipole on the following year's El Niño. *Nat. Geosci.*, **3**, 168-172, https://doi.org/10.1038/ngeo760.

Jones, R. M., 1995: On using ambient internal waves to monitor Brunt-Väisälä frequency. *J. Geophys. Res. Oceans*, **100**, 11005-11011, https://doi.org/10.1029/95JC00139.

Jourdain, N. C., A. S. Gupta, A. S. Taschetto, C. C. Ummenhofer, A. F. Moise, and K. Ashok, 2013: The Indo-Australian monsoon and its relationship to ENSO and IOD in reanalysis data and the CMIP3/CMIP5 simulations. *Clim. Dyn.*, **41**, 3073-3102, https://doi.org/10.1007/s00382-013-1676-1.

Jourdain, N. C., M. Lengaigne, J. Vialard, T. Izumo, and A. S. Gupta, 2016: Further Insights on the Influence of the Indian Ocean Dipole on the Following Year's ENSO from Observations and CMIP5 Models. *J. Climate*, **29**, 637–658, https://doi.org/10.1175/JCLI-D-15-0481.1.

Kalnay, E., and Coauthors, 1996: The NCEP/NCAR 40-Year Reanalysis Project. *Bull. Amer. Meteor. Soc.*, **77**, 437–472, https://doi.org/10.1175/1520-0477(1996)077<0437:TNYRP>2.0.CO;2.

Kara, A. B., P. A. Rochford, and H. E. Hurlburt, 2000: An optimal definition for ocean mixed layer depth. *J. Geophys. Res. Oceans*, **105**, 16803-16821, https://doi.org/10.1029/2000JC900072.

Kay, J. E., and Coauthors, 2015: The Community Earth System Model (CESM) Large Ensemble Project: A Community Resource for Studying Climate Change in the Presence of Internal Climate Variability. *Bull. Amer. Meteor. Soc.*, **96**, 1333–1349, https://doi.org/10.1175/BAMS-D-13-00255.1.

Kim, S.-K., H.-J. Park, S.-I. An, C. Liu, W. Cai, A. Santoso, and J.-S. Kug, 2024: Decreased Indian Ocean Dipole variability under prolonged greenhouse warming. *Nat. Commun.*, **15**, 2811, https://doi.org/10.1038/s41467-024-47276-7.

King, J. A., and R. Washington, 2021: Future Changes in the Indian Ocean Walker Circulation and Links to Kenyan Rainfall. *J. Geophys. Res. Atmos.*, **126**, e2021JD034585, https://doi.org/10.1029/2021JD034585.

King, J. A., R. Washington, and S. Engelstaedter, 2020: Representation of the Indian Ocean Walker circulation in climate models and links to Kenyan rainfall. *Int. J. Climatol.*, **41**, E616-E643, https://doi.org/10.1002/joc.6714.

Knauss, J. A., and B. A. Taft, 1964: Equatorial Undercurrent of the Indian Ocean. *Science*, **143**, 354-356, https://www.science.org/doi/10.1126/science.143.3604.354.

Kohyama, T., D. L. Hartmann, and D. S. Battisti, 2018: Weakening of Nonlinear ENSO Under Global Warming. *Geophys. Res. Lett.*, **45**, 8557-8567, https://doi.org/10.1029/2018GL079085.

Kolstad, E. W., D. MacLeod, and T. D. Demissie, 2021: Drivers of Subseasonal Forecast Errors of the East African Short Rains. *Geophys. Res. Lett.*, **48**, e2021GL093292, https://doi.org/10.1029/2021GL093292.

Kumar, B. P., M. F. Cronin, S. Joseph, M. Ravichandran, and N. Sureshkumar, 2017: Latent Heat Flux Sensitivity to Sea Surface Temperature: Regional Perspectives. *J. Climate*, **30**, 129–143, https://doi.org/10.1175/JCLI-D-16-0285.1.

Latif, M., D. Dommenget, M. Dima, and A. Grötzner, 1999: The Role of Indian Ocean Sea Surface Temperature in Forcing East African Rainfall Anomalies during December–January 1997/98. *J. Climate*, **12**, 3497–3504, https://doi.org/10.1175/1520-0442(1999)012<3497:TROIOS>2.0.CO;2.

Lau, N.-C., and M. J. Nath, 2004: Coupled GCM simulation of atmosphere–ocean variability associated with zonally asymmetric SST changes in the tropical Indian Ocean. *J. Climate*, **17**, 245–265, https://doi.org/10.1175/1520-0442(2004)017<0245:Cgsoav>2.0.Co;2.

Le, T., and D.-H. Bae, 2019: Causal Links on Interannual Timescale Between ENSO and the IOD in CMIP5 Future Simulations. *Geophys. Res. Lett.*, **46**, 2820-2828, https://doi.org/10.1029/2018GL081633.

Li, G., L. Cheng, J. Zhu, K. E. Trenberth, M. E. Mann, and J. P. Abraham, 2020: Increasing ocean stratification over the past half-century. *Nat. Clim. Chang.*, **10**, 1116-1123, https://doi.org/10.1038/s41558-020-00918-2.

Li, G., S.-P. Xie, and Y. Du, 2015: Monsoon-Induced Biases of Climate Models over the Tropical Indian Ocean. *J. Climate*, **28**, 3058-3072, https://doi.org/10.1175/JCLI-D-14-00740.1.

Li, G., S.-P. Xie, and Y. Du, 2016: A Robust but Spurious Pattern of Climate Change in Model Projections over the Tropical Indian Ocean. *J. Climate*, **29**, 5589–5608, https://doi.org/10.1175/JCLI-D-15-0565.1.

Li, L., W. Li, and A. P. Barros, 2013: Atmospheric moisture budget and its regulation of the summer precipitation variability over the Southeastern United States. *Clim. Dyn.*, **41**, 613-631, https://doi.org/10.1007/s00382-013-1697-9.

Li, T., B. Wang, C. Chang, and Y. Zhang, 2003: A Theory for the Indian Ocean Dipole–Zonal Mode. *J. Atmos. Sci.*, **60**, 2119–2135, https://doi.org/10.1175/1520-0469(2003)060<2119:ATFTIO>2.0.CO;2.

Lian, X., and Coauthors, 2018: Partitioning global land evapotranspiration using CMIP5 models constrained by observations. *Nat. Clim. Chang.*, **8**, 640-646, https://doi.org/10.1038/s41558-018-0207-9.

Lim, E.-P., and Coauthors, 2021: Tropical forcing of Australian extreme low minimum temperatures in September 2019. *Clim. Dyn.*, **56**, 3625-3641, https://doi.org/10.1007/s00382-021-05661-8.

Liu, L., S.-P. Xie, X.-T. Zheng, T. Li, Y. Du, G. Huang, and W.-D. Yu, 2014: Indian Ocean variability in the CMIP5 multi-model ensemble: the zonal dipole mode. *Clim. Dyn.*, **43**, 1715-1730, https://doi.org/10.1007/s00382-013-2000-9.

Liu, W., K. H. Cook, and E. K. Vizy, 2020: Influence of Indian Ocean SST regionality on the East African short rains. *Clim. Dyn.*, **54**, 4991-5011, https://doi.org/10.1007/s00382-020-05265-8.

Liu, Y., and Y. Ding, 2008: Teleconnection between the Indian summer monsoon onset and the Meiyu over the Yangtze River Valley. *Sci. China Ser. D-Earth Sci.*, **51**, 1021-1035, https://doi.org/10.1007/s11430-008-0073-9.

Long, S.-M., G. Li, K. Hu, and J. Ying, 2020: Origins of the IOD-like Biases in CMIP Multimodel Ensembles: The Atmospheric Component and Ocean–Atmosphere Coupling. *J. Climate*, **33**, 10437-10453, https://doi.org/10.1175/JCLI-D-20-0459.1.

Lorenz, E N., 1956: Empirical Orthogonal Functions and Statistical Weather Prediction. Technical report Statistical Forecast Project Report 1 Department of Meteorology MIT.

Lu, B., and Coauthors, 2018: An extreme negative Indian Ocean Dipole event in 2016: dynamics and predictability. *Clim. Dyn.*, **51**, 89-100, https://doi.org/10.1007/s00382-017-3908-2.

Lukas, R., and E. Lindstrom, 1991: The mixed layer of the western equatorial Pacific Ocean, *J. Geophys. Res.*, **96**, 3343–3357, https://doi.org/10.1029/90JC01951.

Lumpkin, R., and G. C. Johnson, 2013: Global ocean surface velocities from drifters: Mean, variance, El Niño–Southern Oscillation response, and seasonal cycle. *J. Geophys. Res. Oceans*, **118**, 2992-3006, https://doi.org/10.1002/jgrc.20210.

Luo, J.-J., R. Zhang, S. K. Behera, Y. Masumoto, F.-F. Jin, R. Lukas, and T. Yamagata, 2010: Interaction between El Niño and extreme Indian Ocean Dipole. *J. Climate*, **23**, 726–742, https://doi.org/10.1175/2009jcli3104.1.

Luo, J.-J., S. Behera, Y. Masumoto, H. Sakuma, and T. Yamagata, 2008: Successful prediction of the consecutive IOD in 2006 and 2007. *Geophys. Res. Lett.*, **35**, L14S02, https://doi.org/10.1029/2007GL032793.

Lyon, B., 2020: Biases in CMIP5 Sea Surface Temperature and the Annual Cycle of East African Rainfall. *J. Climate*, **33**, 8209–8223, https://doi.org/10.1175/JCLI-D-20-0092.1.

Lyon, B., 2021: Biases in sea surface temperature and the annual cycle of Greater Horn of Africa rainfall in CMIP6. *Int. J. Climatol.*, **42**, 4179-4186, https://doi.org/10.1002/joc.7456.

Mardia, K.V., 1980: Tests of univariate and multivariate normality, in Handbook of Statistics Vol. 1, edited by P.R. Krishnaiah, North Holland Publishing Company, Amsterdam, 279-320.

Masson, S., J.-P. Boulanger, C. Menkes, P. Delecluse, and T. Yamagata, 2004: Impact of salinity on the 1997 Indian Ocean dipole event in a numerical experiment. *J. Geophys. Res. Oceans*, **109**, C02002, https://doi.org/10.1029/2003JC001807.

Masson, S., P. Delecluse, J.-P. Boulanger, and C. Menkes, 2002: A model study of the seasonal variability and formation mechanisms of the barrier layer in the eastern equatorial Indian Ocean. *J. Geophys. Res. Oceans*, **107**, SRF 18-11-SRF 18-20, https://doi.org/10.1029/2001JC000832.

McIntosh, P. C., and H. H. Hendon, 2018: Understanding Rossby wave trains forced by the Indian Ocean Dipole. *Clim. Dyn.*, **50**, 2783-2798, https://doi.org/10.1007/s00382-017-3771-1.

McKay, R. C., J. M. Arblaster, and P. Hope, 2022: Tropical influence on heat-generating atmospheric circulation over Australia strengthens through spring. *Weather Clim. Dynam.*, **3**, 413-428, https://doi.org/10.5194/wcd-3-413-2022.

McKenna, S., A. Santoso, A. S. Gupta, A. S. Taschetto, and W. Cai, 2020: Indian Ocean Dipole in CMIP5 and CMIP6: characteristics, biases, and links to ENSO. *Sci. Rep.*, **10**, 11500, https://doi.org/10.1038/s41598-020-68268-9.

McPhaden, M. J., S. E. Zebiak, and M. H. Glantz, 2006: ENSO as an integrating concept in Earth science. *Science*, **314**, 1740-1745, https://www.science.org/doi/10.1126/science.1132588.

McPhaden, M.J., and M. Nagura, 2014: Indian Ocean dipole interpreted in terms of recharge oscillator theory. *Clim. Dyn.*, **42**, 1569–1586, https://doi.org/10.1007/s00382-013-1765-1.

Mechoso, C. R., and Coauthors, 1995: The seasonal cycle over the tropical Pacific in coupled ocean–atmosphere general circulation models. *Mon. Wea. Rev.*, **123**, 2825–2838, https://doi.org/10.1175/1520-0493(1995)123<2825:TSCOTT>2.0.CO;2.

Meehl, G. A., 1995: Global Coupled General Circulation Models. *Bull. Amer. Meteor. Soc.*, **76**, 951–957, https://doi.org/10.1175/1520-0477-76.6.951.

Meehl, G. A., 1997: The South Asian Monsoon and the Tropospheric Biennial Oscillation. *J. Climate*, **10**, 1921–1943, https://doi.org/10.1175/1520-0442(1997)010<1921:TSAMAT>2.0.CO;2.

Meehl, G. A., and Coauthors, 2007: THE WCRP CMIP3 Multimodel Dataset: A New Era in Climate Change Research. *Bull. Amer. Meteor. Soc.*, **88**, 1383-1394, https://doi.org/10.1175/BAMS-88-9-1383.

Meehl, G. A., G. J. Boer, C. Covey, M. Latif, and R. J. Stouffer, 1997: Intercomparison makes for a better climate model. *Eos., Trans. Amer. Geophys. Union*, **78**, 445-451, https://doi.org/10.1029/97EO00276.

Meyers, G., 1996: Variation of Indonesian throughflow and the El Niño-Southern Oscillation. *J. Geophys. Res. Oceans*, **101**, 12255-12263, https://doi.org/10.1029/95JC03729.

Meyers, G., P. McIntosh, L. Pigot, and M. Pook, 2007: The Years of El Niño, La Niña, and Interactions with the Tropical Indian Ocean. *J. Climate*, **20**, 2872–2880, https://doi.org/10.1175/JCLI4152.1.

Mölg, T., M. Renold, M. Vuille, N. J. Cullen, T. F. Stocker, and G. Kaser, 2006: Indian Ocean zonal mode activity in a multicentury integration of a coupled AOGCM consistent with climate proxy data. *Geophys. Res. Lett.*, **33**, https://doi.org/10.1029/2006GL026384.

Moon, S., and K.-J. Ha, 2020: Future changes in monsoon duration and precipitation using CMIP6. *npj Clim. Atmos. Sci.*, **3**, 45, https://doi.org/10.1038/s41612-020-00151-w.

Nagura, M., and M. J. McPhaden, 2010: Wyrtki Jet dynamics: Seasonal variability. *J. Geophys. Res. Oceans*, **115**, https://doi.org/10.1029/2009JC005922.

Nakazato, M., S. Kido, and T. Tozuka, 2021: Mechanisms of asymmetry in sea surface temperature anomalies associated with the Indian Ocean Dipole revealed by closed heat budget. *Sci. Rep.*, **11**, 22546, https://doi.org/10.1038/s41598-021-01619-2.

Ng, B., and W. Cai, 2016: Present-day zonal wind influences projected Indian Ocean Dipole skewness. *Geophys. Res. Lett.*, **43**, 11,392-311,399, https://doi.org/10.1002/2016GL071208.

Ng, B., W. Cai, and K. Walsh, 2014: The role of the SST-thermocline relationship in Indian Ocean Dipole skewness and its response to global warming. *Sci. Rep.*, **4**, 6034, https://doi.org/10.1038/srep06034.

Nicholson, S. E., 2015: Long-term variability of the East African 'short rains' and its links to large-scale factors. *Int. J. Climatol.*, **35**, 3979-3990, https://doi.org/10.1002/joc.4259.

O'Brien, J. J., and H. E. Hurlburt, 1974: Equatorial Jet in the Indian Ocean: Theory. *Science*, **184**, 1075-1077, https://www.science.org/doi/10.1126/science.184.4141.1075.

Ogata, T., and S. Xie, 2011: Semiannual Cycle in Zonal Wind over the Equatorial Indian Ocean. *J. Climate*, **24**, 6471–6485, https://doi.org/10.1175/2011JCLI4243.1.

Ogata, T., S.-P. Xie, J. Lan, and X. Zheng, 2013: Importance of Ocean Dynamics for the Skewness of the Indian Ocean Dipole Mode. *J. Climate*, **26**, 2145-2159, https://doi.org/10.1175/JCLI-D-11-00615.1.

Ohba, M., and H. Ueda, 2009: Role of Nonlinear Atmospheric Response to SST on the Asymmetric Transition Process of ENSO. *J. Climate*, **22**, 177-192, https://doi.org/10.1175/2008JCLI2334.1.

O'Neill, B. C., and Coauthors, 2016: The Scenario Model Intercomparison Project (ScenarioMIP) for CMIP6. *Geosci. Model Dev.*, **9**, 3461-3482, https://doi.org/10.5194/gmd-9-3461-2016.

Page, S. E., F. Siegert, J. O. Rieley, H.-D. V. Boehm, A. Jaya, and S. Limin, 2002: The amount of carbon released from peat and forest fires in Indonesia during 1997. *Nature*, **420**, 61-65, https://doi.org/10.1038/nature01131.

Palmer, P. I., and Coauthors, 2023: Drivers and impacts of Eastern African rainfall variability. *Nat. Rev. Earth Environ.*, **4**, 254-270, https://doi.org/10.1038/s43017-023-00397-x.

Patil, K. R., T. Doi, and S. K. Behera, 2023: Predicting extreme floods and droughts in East Africa using a deep learning approach. *npj Clim. Atmos. Sci.*, **6**, 108, https://doi.org/10.1038/s41612-023-00435-x.

Picaut, J., F. Masia, and Y. du Penhoat, 1997: An Advective-Reflective Conceptual Model for the Oscillatory Nature of the ENSO. *Science*, **277**, 663-666, http://www.jstor.org/stable/2893263.

Qiu, Y., W. Cai, L. Li, and X. Guo, 2012: Argo profiles variability of barrier layer in the tropical Indian Ocean and its relationship with the Indian Ocean Dipole. *Geophys. Res. Lett.*, **39**, L08605, https://doi.org/10.1029/2012GL051441.

Qiu, Y., W. Cai, X. Guo, and B. Ng, 2014: The asymmetric influence of the positive and negative IOD events on China's rainfall. *Sci. Rep.*, **4**, 4943, https://doi.org/10.1038/srep04943.

Qu, T., and G. Meyers, 2005: Seasonal variation of barrier layer in the southeastern tropical Indian Ocean. *J. Geophys. Res. Oceans*, **110**, https://doi.org/10.1029/2004JC002816.

Rao, S. A., J.-J. Luo, S. K. Behera, and T. Yamagata, 2009: Generation and termination of Indian Ocean dipole events in 2003, 2006 and 2007. *Clim. Dyn.*, **33**, 751-767, https://doi.org/10.1007/s00382-008-0498-z.

Reverdin, G., D. L. Cadet, and D. Gutzler, 1986: Interannual displacements of convection and surface circulation over the equatorial Indian Ocean. *Q. J. R. Meteorol. Soc.*, **112**, 43-67, https://doi.org/10.1002/qj.49711247104.

Riahi, K., and Coauthors, 2017: The Shared Socioeconomic Pathways and their energy, land use, and greenhouse gas emissions implications: An overview. *Glob. Environ. Chang.*, **42**, 153-168, https://doi.org/10.1016/j.gloenvcha.2016.05.009.

Roxy, M. K., P. Dasgupta, M. J. McPhaden, T. Suematsu, C. Zhang, and D. Kim, 2019: Twofold expansion of the Indo-Pacific warm pool warps the MJO life cycle. *Nature*, **575**, 647-651, https://doi.org/10.1038/s41586-019-1764-4.

Saji, N. H., and T. Yamagata, 2003: Possible impacts of Indian Ocean Dipole mode events on global climate. *Clim. Res.*, **25**, 151-169, https://www.jstor.org/stable/24868393.

Saji, N. H., B. N. Goswami, P. N. Vinayachandran, and T. Yamagata, 1999: A dipole mode in the tropical Indian Ocean. *Nature*, **401**, 360-363, https://doi.org/10.1038/43854.

Saji, N. H., T. Ambrizzi, and S. E. T. Ferraz, 2005: Indian Ocean Dipole mode events and austral surface air temperature anomalies. *Dynam. Atmos. Oceans*, **39**, 87-101, https://doi.org/10.1016/j.dynatmoce.2004.10.015.

Sardeshmukh, P. D., and B. J. Hoskins, 1988: The Generation of Global Rotational Flow by Steady Idealized Tropical Divergence. *J. Atmos. Sci.*, **45**, 1228–1251, https://doi.org/10.1175/1520-0469(1988)045<1228:TGOGRF>2.0.CO;2.

Schott, F. A., and J. P. McCreary, 2001: The monsoon circulation of the Indian Ocean. *Prog. Oceanogr.*, **51**, 1–123, https://doi.org/10.1016/S0079-6611(01)00083-0.

Schott, F. A., S.-P. Xie, and J. P. McCreary Jr, 2009: Indian Ocean circulation and climate variability. *Rev. Geophys.*, **47**, RG1002, https://doi.org/10.1029/2007RG000245.

Sharma, S., K.-J. Ha, R. Yamaguchi, K. B. Rodgers, A. Timmermann, and E.-S. Chung, 2023: Future Indian Ocean warming patterns. *Nat. Commun.*, **14**, 1789, https://doi.org/10.1038/s41467-023-37435-7.

Sharma, S., K.-J. Ha, W. Cai, E.-S. Chung, and T. Bódai, 2022: Local meridional circulation changes contribute to a projected slowdown of the Indian Ocean Walker circulation. *npj Clim. Atmos. Sci.*, **5**, 15, https://doi.org/10.1038/s41612-022-00242-w.

Shi, G., J. Ribbe, W. Cai, and T. Cowan, 2007: Multidecadal variability in the transmission of ENSO signals to the Indian Ocean. *Geophys. Res. Lett.*, **34**, https://doi.org/10.1029/2007GL029528.

Shi, L., H. H. Hendon, O. Alves, J. Luo, M. Balmaseda, and D. Anderson, 2012: How Predictable is the Indian Ocean Dipole?. *Mon. Wea. Rev.*, **140**, 3867–3884, https://doi.org/10.1175/MWR-D-12-00001.1.

Singh, D., R. Seager, B. I. Cook, M. Cane, M. Ting, E. Cook, and M. Davis, 2018: Climate and the Global Famine of 1876–78. *J. Climate*, **31**, 9445–9467, https://doi.org/10.1175/JCLI-D-18-0159.1.

Stuecker, M. F., and Coauthors, 2017: Revisiting ENSO/Indian Ocean Dipole phase relationships. *Geophys. Res. Lett.*, **44**, 2481-2492, https://doi.org/10.1002/2016GL072308.

Su, J., R. Zhang, T. Li, X. Rong, J. Kug, and C. Hong, 2010: Causes of the El Niño and La Niña Amplitude Asymmetry in the Equatorial Eastern Pacific. *J. Climate*, **23**, 605–617, https://doi.org/10.1175/2009JCLI2894.1.

Sun, L., F. H. M. Semazzi, F. Giorgi, and L. Ogallo, 1999: Application of the NCAR Regional Climate Model to eastern Africa: 2. Simulation of interannual variability of short rains. *J. Geophys. Res. Atmos.*, **104**, 6549-6562, https://doi.org/10.1029/1998JD200050.

Sun, S., Y. Fang, Y. Zu, L. Liu, and K. Li, 2022: Increased occurrences of early Indian Ocean Dipole under global warming. *Sci. Adv.*, **8**, eadd6025, https://www.science.org/doi/abs/10.1126/sciadv.add6025.

Takaya, Y., I. Ishikawa, C. Kobayashi, H. Endo, and T. Ose, 2020: Enhanced Meiyu-Baiu rainfall in early summer 2020: Aftermath of the 2019 super IOD event, *Geophys. Res. Lett.*, **47**, e2020GL090671, https://doi.org/10.1029/2020GL090671.

Talley, L D, Pickard, G L, Emery, W J, et al. 2011. Chapter 11 - Indian Ocean [M] //L. D. TALLEY, G. L. PICKARD, W. J. EMERY, et al., Descriptive Physical Oceanography (Sixth Edition). Academic Press; Boston: 363-399.

Tanizaki, C., T. Tozuka, T. Doi, and T. Yamagata, 2017: Relative importance of the processes contributing to the development of SST anomalies in the eastern pole of the Indian Ocean Dipole and its implication for predictability. *Clim. Dyn.*, **49**, 1289-1304, https://doi.org/10.1007/s00382-016-3382-2.

Taylor, K. E., R. J. Stouffer, and G. A. Meehl, 2012: An Overview of CMIP5 and the Experiment Design. *Bull. Amer. Meteor. Soc.*, **93**, 485-498, https://doi.org/10.1175/BAMS-D-11-00094.1.

Thielke, A., and T. Mölg, 2019: Observed and simulated Indian Ocean Dipole activity since the mid-19th century and its relation to East African short rains. *Int. J. Climatol.*, **39**, 4467-4478, https://doi.org/10.1002/joc.6085.

Thual, S., B. Dewitte, S. An, S. Illig, and N. Ayoub, 2013: Influence of Recent Stratification Changes on ENSO Stability in a Conceptual Model of the Equatorial Pacific. *J. Climate*, **26**, 4790–4802, https://doi.org/10.1175/JCLI-D-12-00363.1.

Tierney, J. E., C. C. Ummenhofer, and P. B. deMenocal, 2015: Past and future rainfall in the Horn of Africa. *Sci. Adv.*, **1**, e1500682, https://www.science.org/doi/10.1126/sciadv.1500682.

Timmermann, A., J. Oberhuber, A. Bacher, M. Esch, M. Latif, and E. Roeckner, 1999: Increased El Niño frequency in a climate model forced by future greenhouse warming. *Nature*, **398**, 694-697, https://doi.org/10.1038/19505.

Tollefson, J., 2020: How hot will Earth get by 2100? *Nature*, **580**, 443-445, https://doi.org/10.1038/d41586-020-01125-x.

Tozuka, T., J. Luo, S. Masson, and T. Yamagata, 2007: Decadal Modulations of the Indian Ocean Dipole in the SINTEX-F1 Coupled GCM. *J. Climate*, **20**, 2881–2894, https://doi.org/10.1175/JCLI4168.1.

Tozuka, T., J.-J. Luo, S. Masson, and T. Yamagata, 2008: Tropical Indian Ocean variability revealed by self-organizing maps. *Clim. Dyn.*, **31**, 333-343, https://doi.org/10.1007/s00382-007-0356-4.

Trenberth, K. E., and C. J. Guillemot, 1995: Evaluation of the Global Atmospheric Moisture Budget as Seen from Analyses. *J. Climate*, **8**, 2255–2272, https://doi.org/10.1175/1520-0442(1995)008<2255:EOTGAM>2.0.CO;2.

Ummenhofer, C. C., A. Sen Gupta, M. H. England, and C. J. C. Reason, 2009a: Contributions of Indian Ocean Sea Surface Temperatures to Enhanced East African Rainfall. *J. Climate*, **22**, 993–1013, https://doi.org/10.1175/2008JCLI2493.1.m.

Ummenhofer, C. C., and Coauthors, 2009b: What causes southeast Australia's worst droughts? *Geophys. Res. Lett.*, **36**, https://doi.org/10.1029/2008GL036801.

Vecchi, G. A., and B. J. Soden, 2007: Global Warming and the Weakening of the Tropical Circulation. *J. Climate*, **20**, 4316-4340, https://doi.org/10.1175/JCLI4258.1.

Vecchi, G. A., B. J. Soden, A. T. Wittenberg, I. M. Held, A. Leetmaa, and M. J. Harrison, 2006: Weakening of tropical Pacific atmospheric circulation due to anthropogenic forcing. *Nature*, **441**, 73-76, https://doi.org/10.1038/nature04744.

Vinayachandran, P. N., J. Kurian, and C. P. Neema, 2007: Indian Ocean response to anomalous conditions in 2006. *Geophys. Res. Lett.*, **34**, https://doi.org/10.1029/2007GL030194.

Vinayachandran, P. N., N. H. Saji, and T. Yamagata, 1999: Response of the equatorial Indian Ocean to an unusual wind event during 1994. *Geophys. Res. Lett.*, **26**, 1613-1616, https://doi.org/10.1029/1999GL900179.

Wainwright, C. M., D. L. Finney, M. Kilavi, E. Black, and J. H. Marsham, 2021: Extreme rainfall in East Africa, October 2019–January 2020 and context under future climate change. *Weather*, **76**, 26-31, https://doi.org/10.1002/wea.3824.

Wang, B., and S.-I. An, 2005: A method for detecting season-dependent modes of climate variability: S-EOF analysis. *Geophys. Res. Lett.*, **32**, L15710, https://doi.org/10.1029/2005GL022709.

Wang, G., W. Cai, and A. Santoso, 2017: Assessing the Impact of Model Biases on the Projected Increase in Frequency of Extreme Positive Indian Ocean Dipole Events. *J. Climate*, **30**, 2757–2767, https://doi.org/10.1175/JCLI-D-16-0509.1.

Wang, G., W. Cai, and A. Santoso, 2021: Simulated Thermocline Tilt Over the Tropical Indian Ocean and Its Influence on Future Sea Surface Temperature Variability. *Geophys. Res. Lett.*, **48**, e2020GL091902, https://doi.org/10.1029/2020GL091902.

Wang, G., W. Cai, K. Yang, A. Santoso, and T. Yamagata, 2020a: A Unique Feature of the 2019 Extreme Positive Indian Ocean Dipole Event. *Geophys. Res. Lett.*, **47**, e2020GL088615, https://doi.org/10.1029/2020GL088615.

Wang, P., C.-Y. Tam, N.-C. Lau, and K. Xu, 2020b: Future impacts of two types of El Niño on East Asian rainfall based on CMIP5 model projections. *Clim. Dyn.*, **56**, 899–916, https://doi.org/10.1007/s00382-020-05510-0.

Wang, X., and C. Wang, 2014: Different impacts of various El Niño events on the Indian Ocean Dipole. *Clim. Dyn.*, **42**, 991-1005, https://doi.org/10.1007/s00382-013-1711-2.

Wang, Y., D. Lu, Y.-J. Chung, and S. Xu, 2018: Genetic structure, divergence and admixture of Han Chinese, Japanese and Korean populations. *Hereditas*, **155**, 19, https://doi.org/10.1186/s41065-018-0057-5.

Watanabe, M., J.-L. Dufresne, Y. Kosaka, T. Mauritsen, and H. Tatebe, 2021: Enhanced warming constrained by past trends in equatorial Pacific sea surface temperature gradient. *Nat. Clim. Chang.*, **11**, 33-37, https://doi.org/10.1038/s41558-020-00933-3.

Webster, P. J., A. M. Moore, J. P. Loschnigg, and R. R. Leben, 1999: Coupled ocean–atmosphere dynamics in the Indian Ocean during 1997–98. *Nature*, **401**, 356-360, https://doi.org/10.1038/43848.

Weller, E., and W. Cai, 2013: Realism of the Indian Ocean Dipole in CMIP5 Models: The Implications for Climate Projections. *J. Climate*, **26**, 6649–6659, https://doi.org/10.1175/JCLI-D-12-00807.1.

Weller, E., M. Feng, H. Hendon, J. Ma, S. Xie, and N. Caputi, 2012: Interannual Variations of Wind Regimes off the Subtropical Western Australia Coast during Austral Winter and Spring. *J. Climate*, **25**, 5587–5599, https://doi.org/10.1175/JCLI-D-11-00324.1.

Wu, W., Y. Du, Y.-K. Qian, X. Cheng, T. Wang, L. Zhang, and S. Peng, 2020: Structure and Seasonal Variation of the Indian Ocean Tropical Gyre Based on Surface Drifters. *J. Geophys. Res. Oceans*, **125**, e2019JC015483, https://doi.org/10.1029/2019JC015483.

Wyrtki, K., 1973: An equatorial jet in the Indian ocean. *Science*, **181**, 262-264, https://www.science.org/doi/10.1126/science.181.4096.262.

Xie, S. P., Y. Kosaka, Y. Du, K. M. Hu, J. Chowdary, and G. Huang, 2016: Indo-western Pacific Ocean capacitor and coherent climate anomalies in post-ENSO summer: A review. *Adv. Atmos. Sci.*, **33**, 411-432, https://doi.org/10.1007/s00376-015-5192-6.

Xie, S., H. Annamalai, F. A. Schott, and J. P. McCreary, 2002: Structure and Mechanisms of South Indian Ocean Climate Variability. *J. Climate*, **15**, 864–878, https://doi.org/10.1175/1520-0442(2002)015<0864:SAMOSI>2.0.CO;2.

Xie, S.-P., and Coauthors, 2015: Towards predictive understanding of regional climate change. *Nat. Clim. Chang.*, **5**, 921-930, https://doi.org/10.1038/nclimate2689.

Xie, S.-P., and S. G. H. Philander, 1994: A coupled ocean-atmosphere model of relevance to the ITCZ in the eastern Pacific. *Tellus A*, **46**, 340-350, https://doi.org/10.1034/j.1600-0870.1994.t01-1-00001.x.

Xie, S.-P., C. Deser, G. A. Vecchi, J. Ma, H. Teng, and A. T. Wittenberg, 2010a: Global Warming Pattern Formation: Sea Surface Temperature and Rainfall. *J. Climate*, **23**, 966–986, https://doi.org/10.1175/2009JCLI3329.1.

Xie, S.-P., Y. Du, G. Huang, X.-T. Zheng, H. Tokinaga, K. Hu, and Q. Liu, 2010b: Decadal Shift in El Niño Influences on Indo–Western Pacific and East Asian Climate in the 1970s. *J. Climate*, **23**, 3352-3368, https://doi.org/10.1175/2010JCLI3429.1.

Xu, K., H.-Y. Miao, B. Liu, C.-Y. Tam, and W. Wang, 2020: Aggravation of Record-Breaking Drought over the Mid-to-Lower Reaches of the Yangtze River in the Post-monsoon Season of 2019 by Anomalous Indo-Pacific Oceanic Conditions. *Geophys. Res. Lett.*, **47**, e2020GL090847, https://doi.org/10.1029/2020GL090847.

Yamagata, T., S. K. Behera, J.-J. Luo, S. Masson, M. R. Jury, and S. A. Rao, 2004: Coupled Ocean-Atmosphere Variability in the Tropical Indian Ocean. *Earth's Climate*, 189-211. https://doi.org/10.1029/147GM12.

Yang, K., W. Cai, G. Huang, G. Wang, B. Ng, and S. Li, 2020: Oceanic Processes in Ocean Temperature Products Key to a Realistic Presentation of Positive Indian Ocean Dipole Nonlinearity. *Geophys. Res. Lett.*, **47**, e2020GL089396, https://doi.org/10.1029/2020GL089396.

Yang, W., R. Seager, M. A. Cane, and B. Lyon, 2015a: The Annual Cycle of East African Precipitation. *J. Climate*, **28**, 2385–2404, https://doi.org/10.1175/JCLI-D-14-00484.1.

Yang, W., R. Seager, M. A. Cane, and B. Lyon, 2015b: The Rainfall Annual Cycle Bias over East Africa in CMIP5 Coupled Climate Models. *J. Climate*, **28**, 9789–9802, https://doi.org/10.1175/JCLI-D-15-0323.1.

Yang, Y., S.-P. Xie, L. Wu, Y. Kosaka, N.-C. Lau, and G. A. Vecchi, 2015: Seasonality and Predictability of the Indian Ocean Dipole Mode: ENSO Forcing and Internal Variability. *J. Climate*, **28**, 8021–8036, https://doi.org/10.1175/JCLI-D-15-0078.1.

Yu, E., M. P. King, S. Sobolowski, O. H. Otterå, and Y. Gao, 2018: Asian droughts in the last millennium: a search for robust impacts of Pacific Ocean surface temperature variabilities. *Clim. Dyn.*, **50**, 4671-4689, https://doi.org/10.1007/s00382-017-3897-1.

Yu, L., and M. M. Rienecker, 1999: Mechanisms for the Indian Ocean warming during the 1997–98 El Niño. *Geophys. Res. Lett.*, **26**, 735-738, https://doi.org/10.1029/1999GL900072.

Yuan, D., and H. Liu, 2009: Long-Wave Dynamics of Sea Level Variations during Indian Ocean Dipole Events. *J. Phys. Oceanogr.*, **39**, 1115–1132, https://doi.org/10.1175/2008JPO3900.1.

Yuan, J., and J. Cao, 2013: North Indian Ocean tropical cyclone activities influenced by the Indian Ocean Dipole mode. *Sci. China Earth Sci.*, **56**, 855-865, https://doi.org/10.1007/s11430-012-4559-0.

Zaitchik, B. F., 2017: Madden-Julian Oscillation impacts on tropical African precipitation. *Atmos. Res.*, **184**, 88-102, https://doi.org/10.1016/j.atmosres.2016.10.002.

Zhang, C., 2013: Madden–Julian Oscillation: Bridging Weather and Climate. *Bull. Amer. Meteor. Soc.*, **94**, 1849–1870, https://doi.org/10.1175/BAMS-D-12-00026.1.

Zhang, D., M. J. McPhaden, and T. Lee, 2014: Observed interannual variability of zonal currents in the equatorial Indian Ocean thermocline and their relation to Indian Ocean Dipole. *Geophys. Res. Lett.*, **41**, 7933-7941, https://doi.org/10.1002/2014GL061449.

Zhang, L., Y. Du, and W. Cai, 2018: Low-Frequency Variability and the Unusual Indian Ocean Dipole Events in 2015 and 2016. *Geophys. Res. Lett.*, **45**, 1040-1048, https://doi.org/10.1002/2017GL076003.

Zhang, L., Y. Du, W. Cai, Z. Chen, T. Tozuka, and J.-Y. Yu, 2020: Triggering the Indian Ocean Dipole From the Southern Hemisphere. *Geophys. Res. Lett.*, **47**, e2020GL088648, https://doi.org/10.1029/2020GL088648.

Zhang, W., W. Mao, F. Jiang, M. F. Stuecker, F.-F. Jin, and L. Qi, 2021: Tropical Indo-Pacific compounding thermal conditions drive the 2019 Australian extreme drought, *Geophys. Res. Lett.*, **48**, e2020GL090323, https://doi.org/10.1029/2020GL090323.

Zhao, M., and H. H. Hendon, 2009: Representation and prediction of the Indian Ocean dipole in the POAMA seasonal forecast model. *Q. J. R. Meteorol. Soc.*, **135**, 337-352, https://doi.org/10.1002/qj.370.

Zheng, X.-T., J. Lu, and C. Hui, 2021: Response of seasonal phase locking of Indian Ocean Dipole to global warming. *Clim. Dyn.*, **57**, 2737-2751, https://doi.org/10.1007/s00382-021-05834-5.

Zheng, X.-T., S.-P. Xie, G. A. Vecchi, Q. Liu, and J. Hafner, 2010: Indian Ocean Dipole Response to Global Warming: Analysis of Ocean–Atmospheric Feedbacks in a Coupled Model. *J. Climate*, **23**, 1240–1253, https://doi.org/10.1175/2009JCLI3326.1.

Zheng, X.-T., S.-P. Xie, Y. Du, L. Liu, G. Huang, and Q. Liu, 2013: Indian Ocean Dipole Response to Global Warming in the CMIP5 Multimodel Ensemble. *J. Climate*, **26**, 6067-6080, https://doi.org/10.1175/JCLI-D-12-00638.1.

Zheng, Y., C. Tam, K. Xu, and M. Collins, 2024: Origins of Underestimated Indian Ocean Dipole Skewness in CMIP5/6 Models. *J. Climate*, **37**, 837–853, https://doi.org/10.1175/JCLI-D-23-0412.1.

Zhou, Z.-Q., and S.-P. Xie, 2015: Effects of climatological model biases on the projection of tropical climate change. *J. Climate*, **28**, 9909–9917, https://doi.org/10.1175/JCLI-D-15-0243.1.

Zhou, Z.-Q., S.-P. Xie, and R. Zhang, 2021: Historic Yangtze flooding of 2020 tied to extreme Indian Ocean conditions. *Proc. Natl. Acad. Sci. U.S.A.*, **118**, e2022255118, https://www.pnas.org/doi/abs/10.1073/pnas.2022255118.

Zubair, L., S. A. Rao, and T. Yamagata, 2003: Modulation of Sri Lankan Maha rainfall by the Indian Ocean Dipole. *Geophys. Res. Lett.*, **30**, https://doi.org/10.1029/2002GL015639.

Zuo, H., M. A. Balmaseda, and K. Mogensen, 2017: The new eddy-permitting ORAP5 ocean reanalysis: description, evaluation and uncertainties in climate signals. *Clim. Dyn.*, **49**, 791-811, https://doi.org/10.1007/s00382-015-2675-1.

Zuo, H., M. A. Balmaseda, S. Tietsche, K. Mogensen, and M. Mayer, 2019: The ECMWF operational ensemble reanalysis–analysis system for ocean and sea ice: a description of the system and assessment. *Ocean Sci.*, **15**, 779-808, https://doi.org/10.5194/os-15-779-2019.

Appendix

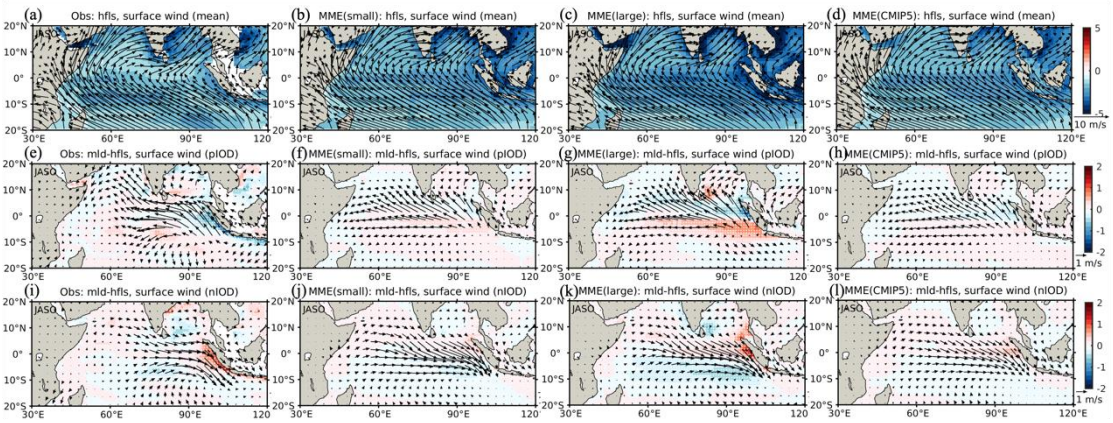


Figure A1. (a, b, c, d) Mean-state latent heat flux (shading; units: W m^{-2}) and sea surface wind (see scale vector in lower right; units: m s^{-1}) during JASO in observations, less-skewed CMIP6 model group, more-skewed CMIP6 model group and CMIP5 models. (e, f, g, h) Positive IOD composites during JASO for latent heat flux forcing anomalies (shading; unit: °C $month^{-1}$) and sea surface wind anomalies (see scale vector in lower right; units: m s^{-1}). (i, j, k, l) are the same as (e, f, g, h), but for negative IOD.

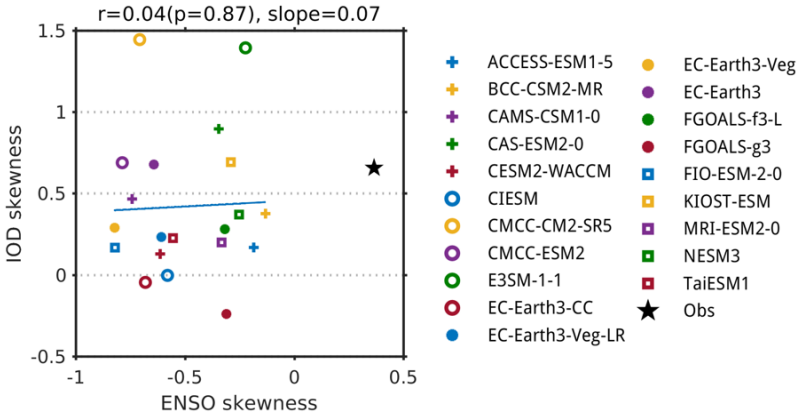


Figure A2. Skewness of Niño3.4 index versus IOD skewness defined by the PC1 skewness.

Model (Hist/SSP585)	PC1		ETIO SSTA		DMI	
	nIOD	extreme nIOD	nIOD	extreme nIOD	nIOD	extreme nIOD
ACCESS-ESM1-5	10/13	**2/3**	7/6	*3/3*	12/10	**1/2**
BCC-CSM2-MR	10/10	3/2	5/7	3/2	12/10	*4/4*
CAMS-CSM1-0	11/10	4/1	4/5	*1/1*	9/6	*0/0*
CAS-ESM2-0	12/14	*1/1*	2/10	**1/2**	9/11	**1/4**
CESM2-WACCM	11/11	**4/5**	10/7	**2/5**	14/9	**3/6**
CIESM	12/10	*4/4*	9/8	**3/4**	14/6	3/2
CMCC-CM2-SR5	9/12	*2/2*	1/8	**0/1**	15/19	*0/0*
CMCC-ESM2	9/11	*2/2*	3/9	**0/2**	10/14	**0/4**
E3SM-1-1	7/12	**1/2**	4/4	*2/2*	8/9	**0/2**
EC-Earth3-CC	10/10	**1/2**	4/8	**0/2**	13/14	**1/5**
EC-Earth3-Veg-LR	11/14	**1/3**	7/10	*1/1*	16/12	**2/5**
EC-Earth3-Veg	10/13	*1/1*	8/4	1/0	15/14	**1/2**
EC-Earth3	14/14	**1/3**	7/5	*1/1*	12/13	**2/3**
FGOALS-f3-L	13/11	**2/6**	7/7	**2/4**	14/10	**1/4**
FGOALS-g3	11/10	**5/7**	9/8	**4/6**	15/10	**3/5**
FIO-ESM-2-0	12/7	*4/4*	9/6	**1/4**	14/7	**2/5**
KIOST-ESM	13/14	**1/3**	4/8	**0/2**	4/12	**0/2**
MRI-ESM2-0	12/13	**4/6**	11/8	**2/6**	13/11	*5/5*
NESM3	13/10	**1/3**	9/7	**1/2**	6/8	*1/1*
TaiESM1	13/12	*3/3*	9/11	**2/4**	15/11	**4/5**
total	223/231	47/63	129/146	30/54	240/216	34/66
extreme/all (%)		21.1/27.3		23.3/37.0		14.2/30.6

Table A1. The same as Table 5.2, but for periods of 1900–1949 and 2050–2099.